UNIVERSITY OF CALIFORNIA,
IRVINE

Preparation and Properties of Mono- and Bimetallic Paramagnetic Co Complexes Supported by Tripodal Ligand Frameworks

DISSERTATION

submitted in partial satisfaction of the requirements
for the degree of

DOCTOR OF PHILOSOPHY

in Chemistry

by

Meghen Elizabeth Goulet

Dissertation Committee
Distinguished Professor Andrew S. Borovik, Chair
Professor Alan F. Heyduk
Professor Jenny Y. Yang

2023

Dedication

To my family, past, present, and future

Table of Contents

	Page
List of Figures	iv
List of Tables	xi
List of Schemes	xiii
List of Equations	xiv
Acknowledgements	xv
Vita	xvii
Abstract of the Dissertation	xix
Chapter 1: Introduction	1
Chapter 2: Preparation, properties, and reactivity of a paramagnetic Co^{III}–OH complex	16
Chapter 3: Preparation and properties of a $[Co^{III}–\mu\text{-}OH–Zn^{II}]^{+}$ from a proposed Co^{II}–IBX-*i*Pr adduct	54
Chapter 4: Modulating magnetic coupling through synthetic control in paramagnetic $Co^{II/III}–\mu\text{-}O(H)–Fe^{III}$ complexes	84
Chapter 5: Magnetic communication in rigorously C_3 symmetric complexes facilitated by N–P=O bridging units	125

List of Figures

Page

Figure 1-1: (A) Representation of the active site found in O_2–Mb, emphasizing how the H–bonding interaction between O_2 and His aids in O_2 binding. N-atoms are represented in blue, C-atoms in light gray, O-atoms in red, and the Fe-atom by an orange sphere. **(B)** Active site of the OEC found in Photosystem II, highlighting the [Mn_4O_5Ca] cubane and the H–bonding network. The dashed lines represent H–bonding interactions in both structures. 1

Figure 1-2: (A) Representation of a structurally characterized Fe–O_2 adduct supported by a picket fence porphyrin ligand.[55–58] **(B)** Fe–O_2 adduct stabilized by a H–bonding interaction in a modified picket fence porphyrin ligand framework, with a phenyl urea moiety incorporated to act as a H–bond donor. 3

Figure 1-3: Representation of *C*$_3$ tripodal pre-ligand developed by the Fout lab. The ligand is isolated as the pyrrole-2-imine tautomer, however the amine-azafulvene tautomer is accessibly upon metallation (top). The bottom shows an example of ligand frameworks developed by the Szymczak lab which incorporates both a pendant Lewis acid and base. 4

Figure 1-4: Examples of *C*$_3$ tripodal ligand frameworks developed by the Borovik lab. 5

Figure 1-5: Representation of [$Co^{III}H_2$pout(OH)]$^-$ and an example of its reactivity with 2,6-di-*t*Bu-4-R-PhOH. 6

Figure 1-6: Synthesis of [poatCo^{III}–μ-OH–$Zn^{II}Me_3$tacn]OTf from K[Co^{II}poat] and IBX-*i*pr in the presence of [$Zn^{II}Me_3$tacn(OTf)$_2$]. 7

Figure 1-7: Synthesis of [poatCo^{III}–μ-OH–$Fe^{III}Me_3$tacn](OTf)$_2$ from [poatCo^{II}–μ-OH–$Fe^{III}Me_3$tacn]OTf and FcOTf and UV-vis spectra following the reaction. 8

Figure 1-8: Preparative method for the synthesis of *C*$_3$ symmetric bimetallic coordination complexes, where M_x = Mn, Co, Zn and M_y = Mn, Fe, Co, Cu, and Zn. 9

Figure 2-1: Examples of *C*$_3$ symmetric tripodal ligand frameworks featuring either H–bond donating or accepting groups. 17

Figure 2-2: A series of Co^{II}–OH complexes supported by unsymmetric, hybrid ligand frameworks. The number of sulfonamido and ureayl donors in the ligands are varied across the series. 18

Figure 2-3: Design scheme of the hybrid ligand framework [H_2pout]$^{3-}$. 19

Figure 2-4: Representations of the 6 structurally characterized Co^{III}–OH species 20

Figure 2-5: Thermal ellipsoid diagrams of **1** and **2**. In **A** and **B**, structural solvent molecules and K^+ counterion(s) were omitted for clarity. **C** and **D** incorporate the K^+ counterion(s) to demonstrate their interactions in the solid state. Thermal ellipsoids are drawn at 50% probability and only hydroxido ligand and urea protons are shown. 22

Figure 2-6: Electronic absorption spectrum of K_2[**1**] (**A**) and K_2[**1**] and K[**2**] (**B**) in DMSO at 25 ºC. 23

Figure 2-7: ATR-FTIR data collected on solid samples of K_2[**1**] (**A**) and K[**2**] (**B**). 24

Figure 2-8: ⊥-mode EPR spectra of 10 mM solutions of K_2[**1**] in DCM:THF, recorded at 12 K. **A** was collected without the use of any 18c6 while **B** was measured in the presence of excess 18c6. 25

Figure 2-9: Cyclic voltammogram of K_2[**1**] in THF. 26

Figure 2-10: Electronic absorption spectra (**A**) and ⊥-mode EPR spectrum (**B**) after reaction of K_2[**1**] with excess O_2 in a 0.4 mM DMSO solution at 25 ºC and 10 mM K_2[**1**] in DCM:THF at 77 K, respectively. 27

Figure 2-11: Representation of possible spin states for a d^6 metal ion in C_3 ligand environments. 30

Figure 2-12: (**A**) UV-vis spectra following the loss of K[**2**] at λ = 400, 478 and 805 nm upon reaction with TEMPO–H at room temperature. (**B**) 77 K ⊥-mode EPR collected after the reaction of **2** with TEMPO–H with g = 4.0, 2.0 consistent with the formation of a Co^{II} species and TEMPO· A, ^{14}N = 119 MHz. 31

Figure 2-13: Reaction of K[**2**] (black trace) with excess DHA. The initial spectrum was collected at 25 ºC and the final spectrum was collected at 40 ºC (blue). 32

Figure 2-14: (**A**) Addition of excess 4-OMe-PhOH to 0.75 mM solution of K[**2**] in DMSO at 25 ºC. New bands were generated at 600 and 660 nm (blue trace, *). (**B**) Plot of substrate $BDFE_{O–H}$ against $logk_2$. The line of best fit is shown by the black dashed trace. The equation is: y = 14.5 – 0.206x, R^2 = 0.835. 33

Figure 2-15: Reaction of 5.75 mM of K_2[**1**] (black) in DMSO with 3 eq of phenol (gray, λ= 371, 434, 548, 605, 636 nm). This species is then treated with $FcBF_4$ (blue, λ_{max}= 604, 655, 746, 832 nm). 35

Figure 2-16: Addition of 2,6-di-^{t}Bu-4-OMe-phenol to a solution of K[**2**] in THF at 25 ºC. (**A**) The initial spectrum is shown in black and the final is shown in blue (λ_{max} = 388, 405, 468(sh), 570, 682 nm). (**B**) 77K ⊥-mode EPR spectrum showing the product of the reaction of K[**2**] with excess 2,6-di-^{t}Bu-4-OMe-phenol, consistent with the formation of a Co^{II} species and an organic radical (10 mM, DCM:THF). 37

Figure 2-S1: Kinetic rate plots from addition of different 4-R-PhOH substrates: R = Br (**A**), R = H (**B**), R = OMe (**C**). 47

Figure 2-S2: (**A**) UV-visible spectra following the reaction of K[**2**] with 2,6-di-^{t}Bu-4-OMe-PhOH, with the final trace shown in blue. (**B**) Plot of 2,6-di-^{t}Bu-4-OMe-PhOH concentration versus k_{obs} values, including the line of best fit and correlation constant. 47

Figure 2-S3: (**A**) UV-visible spectra following the reaction of K[**2**] with 2,6-di-*t*Bu-4-Me-PhOH, with the final trace shown in blue (λ_{max} = 371 (sh), 470, 578, 680 nm). (**B**) Plot of 2,6-di-*t*Bu-4-Me-PhOH concentration versus k_{obs} values, including the line of best fit and correlation constant. 48

Figure 2-S4: (**A**) UV-visible spectra following the reaction of K[**2**] with 2,4,6-tri-*t*Bu-PhOH, with the final trace shown in blue (λ_{max} = 365 (sh), 382, 402, 423, 475, 582, 668 nm). (**B**) Plot of 2,4,6-tri-*t*Bu-PhOH concentration versus k_{obs} values, including the line of best fit and correlation constant. 48

Figure 2-S5: (**A**) UV-visible spectra following the reaction of K[**2**] with 2,6-di-*t*Bu-4-Br-PhOH, with the final trace shown in blue (λ_{max} = 605, 657 nm). (**B**) Plot of 2,6-di-*t*Bu-4-Br-PhOH concentration versus k_{obs} values. 49

Figure 2-S6: Plots of the logarithms of the k_2 values versus BDE (**A**), pKa (**B**), and Hammett Parameter (**C**), with lines of best fit and correlation constants. 49

Figure 3-1: Representation of a synthetic bimetallic complex featuring symmetric ligand fields. 54

Figure 3-2: Examples from the Borovik lab of synthetic bimetallic complexes with unsymmetric ligand fields. 55

Figure 3-3: Representation of the TAML (**A**) and the TMG_3tren (**B**) ligands used by the Nam and Ray labs to prepare LCo^{IV}–O–M^{n+} from Co–OIPh intermediates. 56

Figure 3-4: Molecular structure of the dinuclear $(K[Co^{II}poat])_2$ molecule with thermal ellipsoid representation. Thermal ellipsoids are drawn at 50% probability. 59

Figure 3-5: (**A**) Electronic absorption spectrum of **1** collected in DCM at 25 ºC. (**B**) ⊥-mode EPR spectrum of K[Co^{II}poat], measured with excess 18c6 in DCM:THF at 17 K. 61

Figure 3-6: Cyclic voltammogram showing the full electrochemical profile (**A**) and the isolated first redox event (**B**) in K[Co^{II}poat] measured in DCM, with excess 18c6. 63

Figure 3-7: (**A**) UV-vis spectrum of the proposed Co^{II}–IBX-*i*Pr adduct (black, λ_{max} = 500, 550, 585, 770 nm), overlaid with **1** (blue, λ_{max} = 410, 585, 610, 770 nm). (**B**) Resulting spectrum after adding IBX-*i*Pr to K[Co^{II}poat] and letting react overnight. All spectra were measured at room temperature in DCM. 63

Figure 3-8: Electronic absorption spectra following the reaction of K[Co^{II}poat] with IBX-*i*Pr after addition of $[Zn^{II}Me_3tacn(OTf)_2]$, measured at 25 ºC in DCM. 65

Figure 3-9: Molecular structure of [poatCo^{III}–*μ*-OH–$Zn^{II}Me_3$tacn]OTf with thermal ellipsoids drawn at 50% probability. Only the hydroxido ligand H-atom is shown. Remaining H-atoms, the triflate counterion, and structural solvent molecules were omitted for clarity. 66

Figure 3-10: (**A**) Electronic absorption spectrum of [Co^{III}–μ-OH–Zn^{II}]$^+$ measured at 25 ºC in DCM. * marks a shoulder ~ 880 nm. (**B**) Solid-state vibrational spectrum of [Co^{III}–μ-OH–Zn^{II}]$^+$. The inset shows the O–H vibration. 69

Figure 3-11: (A) Full electrochemical profile and isolated $Co^{III/II}$ reduction **(B)** of [Co^{III}–μ-OH–Zn^{II}]$^+$ measured by CV in DCM. 70

Figure 3-S1: (**A**) Molecular structure view of monomeric K[Co^{II}poat] with thermal ellipsoid representation, drawn to 50% probability. H-atoms were omitted for clarity. (**B**) Solid state ATR-FTIR spectrum of K[Co^{II}poat]. 76

Figure 3-S2: (**A**) CV collected of K[Co^{II}poat] in DCM, without 18c6. (**B**) The isolated second oxidative event of K[Co^{II}poat] measured in DCM in the presence of excess 18c6 77

Figure 3-S3: (**A**) UV-vis spectra following the reaction between AcFcOTF (black trace) with [Co^{III}–μ-OH–Zn^{II}]$^+$. The final spectrum is shown in blue (λ_{max} = 375 (sh), 420, 460, 745 nm). (**B**) UV-vis spectra following the reaction between tris(4-methylphenyl)aminium radical cation (black, λ_{max} = 285, 295, 350, 360, 370, 585, 673 nm) to [Co^{III}–μ-OH–Zn^{II}]$^+$. The final spectrum is shown in blue (λ_{max} = 350, 370, 440*, 580, 675 nm). The band at λ_{max} = 440 nm is the only new feature. The remaining bands appear to be due to excess oxidant. All spectra were collected at –60 ° C in DCM. 77

Figure 4-1: Top: Preparation of a trimetallic sandwich complex using the Kläui ligand. The central metal ion, M, has been shown to be main group, rare earth, and transition metal ions. Bottom: S = 2 Co^{III} complexes supported by bistrimetaphosphate and tris(phosphinimide) ligand fields. 85

Figure 4-2: UV-vis spectra monitoring the reaction between K[Co^{II}poat] (black trace) with O_2 and [$Fe^{II}Me_3$tacn$(OTf)_2$]. The final product spectrum is shown in blue. 88

Figure 4-3: Solid state molecular structure of [poatCo^{II}–μ-OH–$Fe^{III}Me_3$tacn]OTf. Only the hydroxido H-atom is shown. All other H-atoms, the counterion, and structural solvent molecules were omitted for clarity. Thermal ellipsoids were drawn at 50% probability. 90

Figure 4-4: Representation of how the R–P=O resonance structure may affect the [poat]$^{3-}$ ligand framework. 93

Figure 4-5: Proposed bimetallic species which may pre-assemble prior to oxidation. 94

Figure 4-6: (A) UV-vis spectra following the reaction of [Zn^{II}poat]$^-$ (black trace) with O_2 and [$Fe^{II}Me_3$tacn$(OTf)_2$] collected in DCM at room temperature. The final spectrum is shown in blue. **(B)** ⊥-mode EPR spectum collected at 77K in DCM:THF following the reaction of [Zn^{II}poat]$^-$, O_2, and [$Fe^{II}Me_3$tacn$(OTf)_2$]. The inset shows the high field feature. 96

Figure 4-7: (A) Electronic absorbance spectrum of [Co^{II}–μ-OH–Fe^{III}]$^+$ collected in DCM at room temperature. **(B)** [Co^{II}–μ-OH–Fe^{III}]$^+$ (blue) overlaid with K[Co^{II}poat] (black). 97

Fig 4-8: Mössbauer spectra measured on crystalline samples [Co^{II}–μ-OH–Fe^{III}]$^+$ (orange trace, **A**) and [Co^{III}–μ-OH–Fe^{III}]$^{2+}$ (red trace, **B**). Simulations are shown as black traces overlaid with the experimental spectra. 99

Fig 4-9: Overlay of ATR-FTIR spectra measured of crystalline [Co^{II}–μ-OH–Fe^{III}]$^+$ (black trace) and [Co^{III}–μ-OH–Fe^{III}]$^{2+}$ (blue trace). The high energy region is shown in **(A)** while the lower energy region is shown in **(B).** The + and * symbols represent unidentified vibrational features which are discussed in the body of the document. 100

Figure 4-10: (A) $Co^{III}Fe^{III}/Co^{II}Fe^{III}$ (–0.175 V) and $Co^{II}Fe^{III}/Co^{II}Fe^{II}$ (–1.190 V) couples from $[Co^{II}–\mu\text{-}OH–Fe^{III}]^{+}$ together. The $Co^{III}Fe^{III}/Co^{II}Fe^{III}$ couple was isolated in **(B)** and the $Co^{II}Fe^{III}/Co^{II}Fe^{II}$ was isolated in **(C)**. The full voltammogram swept out past +1 V vs $Fc^{+/0}$ including unidentified electrochemical features, denoted by * is shown in **(D)**. 101

Fig 4-11: Solid state molecular structure of $[poatCo^{III}–\mu\text{-}OH–Fe^{III}Me_3tacn](OTf)_2$. Only the hydroxido H-atom is shown. All other H-atoms, counterions, and structural solvent molecules were omitted for clarity. Thermal ellipsoids were drawn at 50% probability. See Table 4-1 for metrical data (*vide supra*). 103

Fig 4-12: (A) Spectra resulting from the reaction of $[Co^{II}–\mu\text{-}OH–Fe^{III}]^{+}$ (black) with FcOTf to form $[Co^{III}–\mu\text{-}OH–Fe^{III}]^{2+}$ (blue). **(B)** Absorbance spectrum from isolated, crystalline $[Co^{III}–\mu\text{-}OH–Fe^{III}]^{2+}$. The * marks a feature which may be due to excess FcOTf. 104

Fig 4-13: ⊥-mode EPR spectrum of $[Co^{III}–\mu\text{-}OH–Fe^{III}]^{2+}$ measured at 7 K in DCM:THF. Simulations of this species to determine rhombicity and other magnetic parameters are still underway. 106

Figure 4-14: Voltammograms obtained from scanning $[Co^{III}–\mu\text{-}OH–Fe^{III}]^{2+}$ oxidatively **(A)** and reductively **(B)**. The * and + mark unidentified electrochemical events which are discussed below. 108

Figure 4-15: (A) UV-vis spectra obtained from reacting $[Co^{III}–\mu\text{-}OH–Fe^{III}]^{2+}$ (black) with LiHMDS (blue), measured at –40 °C in DCM. **(B)** EPR spectra obtained from reacting $[Co^{III}–\mu\text{-}OH–Fe^{III}]^{2+}$ (red) with LiHMDS (blue). Samples were collected at 20 K in DCM:THF. 109

Figure 4-16: Proposed spin state change around the Co^{III} center due to π- donation from an oxido ligand. 110

Fig 4-S1: (A) UV-vis spectra following the reaction between $K[Co^{II}poat]$, $[Fe^{II}Me_3tacn(OTf)_2]$, and FcOTf. The initial spectrum (black) was $K[Co^{II}poat]$, and $[Fe^{II}Me_3tacn(OTf)_2]$. The gray trace was after ~15 minutes. The blue trace was after 48 hours. These spectra are not consistent with $[Co^{II}–\mu\text{-}OH–Fe^{III}]^{+}$.**(B)** UV-vis spectra following the addition of excess O_2 to $[Fe^{II}Me_3tacn(OTf)_2]$ (black trace) after stirring overnight (~15 h, blue trace) in DCM. 118

Fig 4-S2: Overlay of $[Co^{III}–\mu\text{-}OH–Fe^{III}]^{2+}$ (black trace) with $[poatCo^{III}–\mu\text{-}OH–Zn^{II}Me_3tacn]OTf$ (blue trace). Note that these two samples were not the same concentration though both were measured at room temperature in DCM 118

Figure 5-1: Representation of key design principles for C_3 symmetric tripodal ligand frameworks. 125

Figure 5-2: Representation of how C_3 symmetry is maintained in mononuclear metal complexes versus disrupted in bimetallic species. 126

Figure 5-3: Structure of $Ca[Copoat]_2$, with the Ca ion supported only by P=O groups. 126

Figure 5-4: Examples of TMP coordination complexes developed by the Borovik lab which have had their magnetic behavior subsequently studied. Note that the $Me_4N[NiMST]$ system was separately prepared and characterized by the Dunbar lab. 127

Figure 5-5: Molecular structure of the dinuclear $(K[Zn^{II}poat])_2$ molecule with thermal ellipsoid representation. Thermal ellipsoids are drawn at 50% probability. All H-atoms were omitted for clarity. 129

Figure 5-6: Crystalline products obtained from the preparation of $[Co^{II}poat\cdots Zn^{II}Me_3tacn]OTf$ **(A)** and $[Zn^{II}poat\cdots Zn^{II}Me_3tacn]OTf$ **(B)**. 130

Figure 5-7: (A), (C), (E) show the molecular structures of $[Co^{II}\cdots Zn^{II}]^+$, $[Co^{II}\cdots Cu^{II}]^+$, and $[Co^{II}\cdots Co^{II}]^+$. **(B), (D), (F)** depict the view along the C_3 axis of $[Co^{II}\cdots Zn^{II}]^+$, $[Co^{II}\cdots Cu^{II}]^+$, and $[Co^{II}\cdots Co^{II}]^+$. Thermal ellipsoids are drawn at 50% probability. The $^-$OTf ion and H-atoms was omitted for clarity. 133

Figure 5-8: (A), (C), (E) show the molecular structures of $[Co^{II}\cdots Fe^{II}]^+$, $[Co^{II}\cdots Mn^{II}]^+$, and $[Mn^{II}\cdots Mn^{II}]^+$. **(B), (D), (F)** depict the view along the C_3 axis of $[Co^{II}\cdots Fe^{II}]^+$, $[Co^{II}\cdots Mn^{II}]^+$, and $[Mn^{II}\cdots Mn^{II}]^+$. Thermal ellipsoids are drawn at 50% probability. The $^-$OTf ion and H-atoms were omitted for clarity. 134

Figure 5-9: (A), show the molecular structures of $[Zn^{II}\cdots Zn^{II}]^+$. **(B)** depict the view along the C_3 axis of $[Zn^{II}\cdots Zn^{II}]^+$. Thermal ellipsoids are drawn at 50% probability. The OTf ion and H-atoms were omitted for clarity. 135

Figure 5-10: UV-vis spectra following the addition of $[Zn^{II}Me_3tacn(OTf)_2]$ **(A),** $[Fe^{II}Me_3tacn(OTf)_2]$ **(C)**, and $[Mn^{II}Me_3tacn(OTf)_2]$ **(E)** to solutions of $K[Co^{II}poat]$. The baseline jump in **(C)** was likely due to accidental O_2 exposure in the experimental setup. UV-vis spectra obtained from crystalline $[Co^{II}\cdots Zn^{II}]^+$. **(B),** $[Co^{II}\cdots Fe^{II}]^+$ **(D),** and $[Co^{II}\cdots Mn^{II}]^+$ **(F).** The baseline increases in **(E)** and **(F)** were likely due to solubility issues of $[Co^{II}\cdots Mn^{II}]^+$. 137

Figure 5-11: (A) UV-vis spectra following the addition of $K[Co^{II}poat]$ to a solution of $[Cu^{II}Me_3tacn(OTf)_2] \cdot 2$ MeCN. The blue trace was $[Co^{II}\cdots Cu^{II}]^+$ formed *in situ*. **(B)** Molar absorptivity data measured for $[Co^{II}\cdots Cu^{II}]^+$. **(C)** UV-vis spectra following the addition of $[(Co^{II}Me_3tacn)_2(OTf)_3]OTf$ to a solution of $K[Co^{II}poat]$ (black). **(D)** Molar absorptivity data measured for $[Co^{II}\cdots Co^{II}]^+$. All spectra were measured at room temperature in DCM. 138

Figure 5-12: (A) ⊥-mode EPR spectrum obtained from $[Co^{II}\cdots Zn^{II}]^+$ measured in DCM:THF at 15 K. **(B)** ⊥-mode EPR spectrum measured from solid, crystalline $[Co^{II}\cdots Zn^{II}]^+$ at 20 K. 139

Figure 5-13: (A) ZFC thermal magnetic susceptibility plots of $[Co^{II}\cdots Zn^{II}]^+$ collected between 2 – 300 K under varying fields. 100 Oe is shown in blue, 1000 Oe in red, and 5000 Oe in yellow. **(B)** Isothermal magnetization plots shown at 2 K (blue) and 100 K (red). 140

Figure 5-14: (A) ⊥-mode EPR spectrum obtained from $[Co^{II}\cdots Cu^{II}]^+$ measured in DCM:THF at 77 K. The small signals ~ g = 4, 2 were attributed to minimal residual $K[Co^{II}poat]$ and $[Cu^{II}Me_3tacn(OTf)_2] \cdot 2$ MeCN. For reference, **(B)** shows the overlay of ⊥-mode EPR spectra from $[Co^{II}\cdots Cu^{II}]^+$ (black) with $[Cu^{II}Me_3tacn(OTf)_2] \cdot 2$ MeCN (blue) at the same concentrations. 141

Figure 5-15: (A) ZFC thermal magnetic susceptibility plots of $[Co^{II}\cdots Co^{II}]^+$ collected between 2 – 300 K under varying fields. 100 Oe is shown in blue, 1000 Oe in red, and 5000 Oe in yellow. **(B)** Isothermal magnetization plots shown at 2 K (blue) and 100 K (red). 142

Figure 5-16: (A) ⊥-mode EPR spectrum obtained from *in situ* generated $[Co^{II}\cdots Fe^{II}]^+$ measured in DCM:THF. * represents ~14% excess $K[Co^{II}poat]$. **(B)** ⊥-mode EPR spectrum of solid, $[Co^{II}\cdots Fe^{II}]^+$. 143

Figure 5-17: (A) ZFC thermal magnetic susceptibility plots of $[Co^{II}\cdots Fe^{II}]^+$ collected between 2 – 300 K under varying fields. 100 Oe is shown in blue, 1000 Oe in red, and 5000 Oe in yellow. **(B)** Isothermal magnetization plots shown at 2 K (blue) and 100 K (red). 144

Figure 5-18: EPR spectra obtained from *in situ* prepared $[Co^{II}\cdots Mn^{II}]^+$. All spectra were collected at 6 K in DCM:THF. **(A)** The ‖-mode EPR spectrum. **(B)** The full ⊥-mode EPR spectrum of $[Co^{II}\cdots Mn^{II}]^+$. **(C)** Low-field region of the ⊥-mode EPR spectrum. **(D)** The high-field region from the ⊥-mode EPR spectrum of $[Co^{II}\cdots Mn^{II}]^+$. The signal at g = 2.0 was split by hyperfine from both ^{55}Mn and ^{59}Co nuclei. The ^{59}Co hyperfine was less intense and both sets of hyperfine were close to one another, making individual hyperfine features challenging to identify. 145

Figure 5-19: (A) ZFC thermal magnetic susceptibility plots of $[Co^{II}\cdots Mn^{II}]^+$ collected between 2 – 300 K under varying fields. 100 Oe is shown in blue, 1000 Oe in red, and 5000 Oe in yellow. **(B)** Isothermal magnetization plots shown at 2 K (blue) and 100 K (red). 146

Figure 5-20: ‖-mode **(A)** and ⊥-mode **(B)** EPR spectra obtained from redissolved crystalline $[Mn^{II}\cdots Mn^{II}]^+$ in DCM:THF. The ‖-mode EPR spectrum exhibited ^{55}Mn hyperfine on the broad derivative, centered at g = 8.4 (A = 494 MHz). EPR spectra measured from solid $[Mn^{II}\cdots Mn^{II}]^+$, collected in ‖-mode **(C)** and ⊥-mode **(D).** The solution and solid samples were in good agreement with one another, though the spectral features were broadened out in the solid samples. ‖-mode EPR spectra were collected at 6 K and ⊥-mode spectra were measured at 20 K. 148

Figure 5-S1: (A) UV-vis spectrum of $K[Mn^{II}poat]$ in DCM at room temperature. **(B)** ⊥-mode EPR spectrum of $K[Mn^{II}poat]$ collected in DCM:THF at 77 K. 164

Figure 5-S2: Molecular structure of $[(Co^{II}Me_3tacn)_2(OTf)_3]OTf$. Thermal ellipsoids were drawn at 50% probability. The outer sphere triflate ion and all H-atoms were omitted for clarity. 164

Figure 5-S3: (A) UV-vis spectrum from crystalline $[(Co^{II}Me_3tacn)_2(OTf)_3]OTf$ in DCM at room temperature. **(B)** ⊥-mode EPR spectrum of $[(Co^{II}Me_3tacn)_2(OTf)_3]OTf$ collected at 77 K in DCM:THF. 165

Figure 5-S4: ⊥-mode EPR spectrum of $[Co^{II}\cdots Co^{II}]^+$ collected at 77 K in DCM:THF. The signal ~ g = 4 was likely due to a small excess of $K[Co^{II}poat]$. 165

Figure 5-S5: Overlay of ‖-mode EPR spectrum (blue) with ⊥-mode EPR spectrum (black) of $[Co^{II}\cdots Mn^{II}]^+$. Both spectra were collected at 6 K. 165

List of Tables

Page

Table 2-1: Metrical data from the molecular structures of K_2[**1**] and K[**2**]. 22

Table 2-2: Comparison of physical data across a series of Co^{II}–OH complexes with varying ligand fields. Refer to Figure 2-2 for the structure of these compounds. 23

Table 2-3: Comparison of oxidative potentials for $Co^{III/II}$–OH in different solvents. 26

Table 2-4: Summary of data from the reaction of K[**2**]with 4-R substituted phenolic substrates and their thermodynamic parameters. 34

Table 2-5: Summary of data from the reaction of K[**2**] with 2,6-di-^{t}Bu-4-R substituted phenolic substrates and their thermodynamic parameters. BDE values were chosen because the BDFE values have not been reported for all substrates. Thermodynamic data are reported in DMSO, though the reaction was carried out in THF. 37

Table 2-S1: Crystallographic details for K_2[$Co^{II}H_2$pout(OH)], K_2[**1**], (middle column) and K[$Co^{III}H_2$pout(OH)], K[**2**], (right column). 46

Table 3-1: Metrical data obtained from the molecular structure of (K[Co^{II}poat])$_2$. 59

Table 3-2: Metrical data obtained from the molecular structure of [Co^{III}–μ-OH–Zn^{II}]$^+$ τ_5 is the trigonality structural parameter; β and α are the two largest bond angles observed. 67

Table 3-S1: Crystallographic details for (K[Co^{II}poat])$_2$, K[**1**], (middle column) and [poatCo^{III}–μ-OH–Zn^{II}Me$_3$tacn]OTf (right column). 76

Table 4-1: Metrical data obtained from the molecular structures of [Co^{II}–μ-OH–Fe^{III}]$^+$ and [Co^{III}–μ-OH–Fe^{III}]$^{2+}$. 91

Table 4-2: Metrical data obtained from CV of [Co^{II}–μ-OH–Fe^{III}]$^+$, focused on the reversible couples. 102

Table 4-3: Metrical data from marked events from the CV in Figure 15A of [Co^{III}–μ-OH–Fe^{III}]$^{2+}$. 108

Table 4-S1: Crystallographic details for [poatCo^{II}–μ-OH–Fe^{III}Me$_3$tacn]OTf (middle column) and [poatCo^{III}–μ-OH–Fe^{III}Me$_3$tacn]OTf$_2$ (right column). 119

Table 4-S2: Different unit cells obtained for [poatCo^{II}–μ-OH–Fe^{III}Me$_3$tacn]OTf. 119

Table 5-1: Metrical data obtained from the molecular structure of (K[Zn^{II}poat])$_2$. 129

Table 5-2: Metrical data describing relevant bond metrics and atomic distances in the isomorphous molecular structures [M_x^{II}poat···M_y^{II}Me$_3$tacn]$^+$. M_x···N_{eq} describes the distance between M_x from the plane formed by the equatorial N-atoms, N2. 132

Table 5-3: Metrical data describing relevant bond angles in the isomorphous molecular structures $[M_x^{II}poat\cdots M_y^{II}Me_3tacn]^+$. The O1–$M_x$–N3 describes the angle formed between O1 and the N-atom trans to O1 in the Me_3tacn ligand framework 132

Table 5-S1: Metrical data obtained from the molecular structure of $[(Co^{II}Me_3tacn)_2(OTf)_3]OTf$. 164

Table 5-S2: Crystallographic details for $[Co^{II}poat\cdots Zn^{II}Me_3tacn]OTf$ (middle column) and $[Co^{II}poat\cdots Cu^{II}Me_3tacn]OTf$ (right column). 166

Table 5-S3: Crystallographic details for $[(Co^{II}Me_3tacn)_2(OTf)_3]OTf$ (middle column) and $[Co^{II}poat\cdots Co^{II}Me_3tacn]OTf$ (right column). 166

Table 5-S4: Crystallographic details for $[Co^{II}poat\cdots Fe^{II}Me_3tacn]OTf$ (middle column) and $[Co^{II}poat\cdots Mn^{II}Me_3tacn]OTf$ (right column). 167

Table 5-S5: Crystallographic details for $[Mn^{II}poat\cdots Mn^{II}Me_3tacn]OTf$ (second column), $(K[Zn^{II}poat])_2$ (third column), and $[Zn^{II}poat\cdots Zn^{II}Me_3tacn]OTf$ (fourth column). 167

List of Schemes

Page

Scheme 2-1: Preparation of K_2[**1**]. 20

Scheme 2-2: Preparation of K[$Co^{III}H_2$pout(OH)] (K[**2**]). 28

Scheme 2-3: Schematic representations of the proposed pathways through which a ligand substitution event may proceed. 35

Scheme 3-1: Synthetic procedure for preparation of K[Co^{II}poat]. 57

Scheme 3-2: Synthetic scheme describing the preparation of [Co^{III}–μ-OH–Zn^{II}]$^+$. 66

Scheme 4-1: Representation of the lack of reaction between K[Co^{II}poat] and O_2 alone **(A)** and in the presence of [$Zn^{II}Me_3$tacn$(OTf)_2$] **(B)**. 87

Scheme 4-2: Reaction scheme describing the preparation of [poatCo^{II}–μ-OH–$Fe^{III}Me_3$tacn]OTf. 89

Scheme 4-3: Half reactions involved in the reduction of O_2 to either H_2O_2 (**1**) or H_2O (**2**) 93

Scheme 4-4: Reaction scheme describing the preparation of [poatCo^{III}–μ-OH–$Fe^{III}Me_3$tacn$](OTf)_2$. 102

Scheme 5-1: General synthetic procedure for the preparation of trigonal monopyramidal coordination complexes, where M^{II} = Mn, Co, Zn. 128

Scheme 5-2: General synthetic procedure for the preparation of C_3 symmetric bimetallic coordination complexes, where M_x = Mn, Co, Zn and M_y = Mn, Fe, Co, Cu, and Zn. 130

List of Equations

Page

Equation 2-1: Fitting of absorbance data versus time to measure k_{obs}. 33

Acknowledgements

Before beginning my personal acknowledgements, I would like to thank the NIH for funding my work, through GM050781.

My time in grad school has felt far shorter than I ever expected, in part because I have had a strong support system who helped me navigate my journey from day one. First and foremost, I have to thank my advisor, Andy. I was so excited about the work going on in the Borovik lab and so happy to join as a first year. Andy, you have had my back from the start and you have always been so supportive. You gave me the freedom to choose my projects and pursue my interests. You have always worked collaboratively with me and guided me, giving me the room to grow and thrive. You kept me focused and your suggestions always made my work stronger. I have learned so much from you about how to be a thorough scientist. You taught me how to be a strong speaker, the art of chalk talks, and the importance of overlays. As much as I've enjoyed group dinners and parties, my favorite times in the lab have always been the subgroups and group meetings. There is something special about participating in these meetings; they taught me that my lab mates are my friends and collaborators, my greatest resource and biggest allies. You have always supported your group by pushing us in the direction we want to go in, building your program around your students and their talents. I am so grateful I had this opportunity to work with you for the last five years and grateful for all of the support and the opportunities you've given me. You were exactly the advisor I needed.

I would also like to thank my committee, Profs. Alan Heyduk and Jenny Yang, who have been in every one of my exams in the program. You have both had good questions and suggestions for me on my projects and I have always enjoyed talking science with you. You always made me feel like a peer and you were clearly interested and invested in my work, leaving me feeling excited and inspired to try new things. Alan, you have always made me feel welcome and valued in the department, even when you make fun of me for dropping "y'all" in our conversations. Jenny, you and your work were what interested me in UCI for grad school. You were the one who called me to give me my acceptance and I still remember how thrilled I was! I would also like to thank Profs. Bill Evans and Mike Green, who taught several of my courses. Bill was the inorganic area advisor when I was a first year and always gave me good guidance. Mike immensely deepened my understanding of inorganic chemistry, to the point that I could absolutely draw an MO diagram on a napkin at the pub. The entire inorganic division at UCI has always been close and collaborative, and I am so thankful to have been a part of a department where the professors support and encourage this environment.

I would be remiss if I didn't give a shoutout to the Borovik lab members that I've overlapped with. They have been my friends, mentors, collaborators, and biggest cheerleaders. From showing me how to plot and overlay my data (very important), to teaching me how to format my talks and documents, they have always been patient and thorough. Kelsey and Victoria were the senior members when I started and they set the bar for me on what a senior student, scientist, and leader looked like. I have always looked up to them in and out of the lab, and they welcomed me with open arms. Thank you for always giving me guidance and support! J, you were my mentor when I came in as a first year and I can't imagine a better person for the job. You trained me on how to use everything in the lab, from the glovebox to the solvent system to the EPR. You have always been patient, even when I dropped my first recrystallization and cried. I am so glad you trained me on the EPR! Learning how to build a cryostat, train people, and troubleshoot when things inevitably went wrong has been one of the highlights of my time in lab. Even when we would have crazy long days with early starts, I loved

it. Being the EPR person gave me the opportunity to work outside of my comfort zone, collaborate with other researchers, and helped me grow outside of my synthetic work. You have always been willing to chat about science and brainstorm new ideas, which I've loved. Thank you to Dolores for always being supportive and teaching me about persistence. You are one of the most thorough chemists I've ever worked with! Thank you to Sunny Sun for showing me how to be more chill and always making me laugh. To Phan and Jennifer, I am thankful for my time collaborating with you and I have loved watching you grow! Phan and Alec: enjoy the EPR and get some good data for me!

I also want to thank my collaborators at Carnegie Mellon University, Prof. Mike Hendrich and Dr. Saborni Biswas. You have always measured and analyzed my samples so thoroughly. Working with you has helped me understand EPR much better and has been absolutely instrumental in many of my projects. Thank you also to Prof. Jeff Rinehart and Angelica Orlova from UCSD for studying some of my complexes with SQUID. Angelica, thank you in particular for helping me with sample prep and measurements, and answering all of my questions because SQUID is entirely new to me.

Thank you to my friends in the program, who have always been there for me to vent, ask questions, and just hang out when I need the company. Kirsten, Justin, Chuck, Carly, Taylor, Leah, Tyler, and Angelika, y'all have been my friends since the first day and in many instance my family out here. I always had someone to call if I needed help or just wanted to go grab dinner. You all helped ease my transition to CA and manage my homesickness. Thank you also to the Yang lab for letting me crash your office and distract you. Nadia, you helped me prepare for my job interviews and your resources made a huge difference. Kelsey, you've always answered my millions of magnet questions patiently and in a way I understood. You flame sealed my SQUID samples to make sure I didn't carbonize them and I am SO thankful for the help. Tyler, your hard work and persistence as the crystallography fellow strengthened my entire dissertation. Every single structure in this my dissertation was finalized by you! I can't understate how much you helped me. To Allie: thank you for always making me laugh and being so supportive of me, in and out of lab. You and Amanda are two of my favorite people and I wish we had found each other sooner. To Rachel: thank you for Studio Ghibli and always giving me the opportunity to talk about new chemistry.

Finally, to my family: I love you. Thank you for all of your support, from calling me to check in when I've been busy and haven't kept up as well as I'd like, to coming to visit and sending me puppy pictures when I'm stressed. You have always been supportive of me and had unwavering faith in my success. Dad, you always said I couldn't leave school without a PhD and it looks like you were right (again)! Mom, I know you used to tell me that you "didn't need a dissertation" when I wouldn't stop talking and get to the point as a kid, but you're getting one anyway. Hope that's okay! Grace and Josh: thanks for always teasing me and keeping me down to earth. I've missed you both and I'm excited to be closer by soon. To Grandma and Grandpa, the original Drs. Goulet: you were right. Grad school is a marathon! Thank you for all of the reminders and support and always being interested in the ins and outs of my program. Finally, to Nathaniel: thank you for always being proud of me and always knowing how to calm me down or cheer me up in times of stress. You have been a major source of support to me and made a world of difference. I love you and I'm finally coming home.

– MEG

"If I have seen further, it is by standing on the shoulders of giants." – Sir Isaac Newton

Vita

Education

University of California, Irvine (UCI) 2023
Ph.D., Chemistry
A.S. Borovik, Advisor

Texas Christian University (TCU) 2016
B.S., Biochemistry
B.A., Biology

Publications

- Burnett, Marianne E.; Bodiford, Nelli; **Goulet, Meghen E.**; Coffer, Jeffery L.; Green, Kayla N. Environmental effects of chitosan as an immobilization medium for electrochemically active small molecules. Journal of Coordination Chemistry. DOI: 10.1080/00958972.2019.1655550

In Preparation

- **Goulet, Meghen E.**; Oswald, Victoria F.; Hendrich, M.P.; Borovik, A.S. Preparation, properties, and reactivity of a paramagnetic Co^{III}–OH complex.
- **Goulet, Meghen E.**; Hendrich, M.P.; Borovik, A.S. Modulating magnetic coupling through synthetic control in paramagnetic $Co^{II/III}$–μ-O(H)–Fe complexes.
- **Goulet, Meghen E.**; Orlova, Angelica P.; Hendrich, M.P.; Rinehart, J.D.; Borovik, A.S. Magnetic communication in rigorously C_3 symmetric complexes facilitated by N–P=O bridging units
- **Goulet, Meghen E.**; Borovik, A.S. Preparation and reactivity of bimetallic complexes with Co–OH–M cores.

Presentations

- **Goulet, Meghen E.**; Borovik, A.S. The preparation and properties of bimetallic complexes with Co–(μ-OH)–M Cores (M = Fe, Co, Zn) Presented at ACS Spring 2022, San Diego, CA, March 20, 2022. **ACS Inorganic Division 65th Anniversary Symposium Poster Prize- Coordination Chemistry Division.**
- **Goulet, Meghen E.**; Borovik, A.S. Investigating the synthesis and reactivity of bimetallic cobalt complexes. To be presented at Bioinorganic Gordon Research Symposium, January 2022. Cancelled due to Omicron surge of COVID-19 pandemic.
- **Goulet, Meghen E.**; Borovik, A.S. Investigating the Magnetism and Reactivity of Bimetallic Cobalt Complexes. Presented at ACS Fall 2021, Remote, August 24, 2021.
- **Goulet, Meghen E.**; Borovik, A.S. Investigating Electrostatic Effects on Paramagnetic Cobalt Complexes. Presented at ACS Spring Meeting 2021, poster session in honor of Kathy Franz, Remote. April 21, 2021.
- **Goulet, Meghen E.**; Borovik, A.S. Investigating Electrostatic Effects on Paramagnetic Cobalt Complexes. Presented at University of California Chemical Symposium, Remote Poster. March 25, 2021.
- Sun, Chen; Lee, Justin L.; Ross, Dolores, L.; Gomez, Francisco, J.; **Goulet, Meghen E.**; Kneebone, Jared L.; Barman, Suman K.; Oswald, Victoria F.; Borovik, A. S. Bioinspired Inorganic Chemistry: Synthetic Models. Presented at Southern California Bioinorganic Conference, UCLA, Los Angeles, CA, December 7, 2019.
- Sun, Chen; Lee, Justin L.; Ross, Dolores, L.; Gomez, Francisco, J.; **Goulet, Meghen E.**; Kneebone, Jared L.; Barman, Suman K.; Oswald, Victoria F.; Borovik, A. S. Bioinspired Inorganic Chemistry: Synthetic Models. Presented at Southern California Bioinorganic Conference, Cal Tech, Pasadena, CA, December 8, 2018.

- Burnett, Marianne; **Goulet, Meghen E.**; Green, Kayla N. Investigation into the synthesis and characterization of derivatized electrochemical biosensors utilizing a biotin-ferrocene platform. Presented at TCU Student Research Symposium, Fort Worth, TX, April 2016.
- **Goulet, Meghen E.** Optimizing immobilization of ferrocene peptide bioconjugates for biosensor development. Presented at *Proteins, Enzymes, and Model Systems.* 251st ACS National Meeting & Exposition, San Diego, CA, March 16, 2016.
- Burnett, Marianne; **Goulet, Meghen E.**; Green, Kayla N. Investigation into the synthesis and characterization of derivatized electrochemical biosensors utilizing a biotin-ferrocene platform. Presented at 251st ACS National Meeting & Exposition, San Diego, CA, March 13, 2016.
- **Goulet, Meghen E.**; Burnett, Marianne E.; Green, Kayla N. Optimizing Immobilization of Ferrocene Peptide Bioconjugates for Biosensor Development. Presented at Gulf Coast Undergraduate Research Symposium, Houston, TX, October 15, 2015.

Awards

UCI Department of Chemistry Dissertation Fellowship	2022
American Chemical Society Division of Inorganic Chemistry Poster Presentation Award	2022
American Chemical Society Division of Inorganic Chemistry Travel Grant	2022
Research Translation Group Fellowship, Beall Applied Innovation	2021 – 2022
UCI Department of Chemistry Travel Grant	2020
TCU John V. Roach Honor's College Dean's Scholarship	2012 – 2016
TCU Science and Engineering Research Center Grant	2015

Professional Affiliations

UCI Graduate Professional Success in STEM	2020 – Present
Iota Sigma Pi– Women in Chemistry Society, Calcium Chapter	2017 – Present
American Chemical Society, Member	2016 – Present

Abstract of the Dissertation

Preparation and Properties of Mono- and Bimetallic Paramagnetic

Co Complexes Supported by Tripodal Ligand Frameworks

by

Meghen Elizabeth Goulet

Doctor of Philosophy in Chemistry

University of California, Irvine, 2023

Distinguished Professor Andrew S. Borovik, Chair

Many important and synthetically challenging chemical reactions are carried out by metalloenzymes, including water oxidation, nitrogen fixation, O_2 reduction, and oxidation of C–H bonds in substrates such as methane, fatty acids, and pharmaceutical products. Metalloenzymes are able to catalyze these reactions in part due to their ability to access reactive intermediates which is facilitated by the protein host. To replicate these effects synthetically, the Borovik lab designs organic ligands that incorporate both primary and secondary coordination sphere interactions to control the local environment within metal complexes. This dissertation presents research that employs these ligand frameworks in both mono- and bimetallic small molecule Co complexes.

Chapter 1 provides a brief introduction to key features of metalloenzyme active sites that support their reactivity. A concise overview of relevant synthetic ligand designs is given, in addition to summaries of the following chapters.

Chapter 2 describes the preparation of mononuclear Co^{II}– and Co^{III}–OH complexes within an unsymmetric, hybrid tripodal ligand framework: $[H_2pout]^{3-}$. The characterization of these complexes is discussed, including the molecular structure of $K[Co^{III}H_2pout(OH)]$.

$K[Co^{III}H_2pout(OH)]$ is paramagnetic, an unusual trait for a Co^{III} center. The reactivity of $K[Co^{III}H_2pout(OH)]$ towards substrates with an O–H bonds is also examined. This work is the first reactivity study of a Co^{III}–OH complex.

Chapter 3 describes the preparation of a trigonal monopyramidal, four-coordinate Co complex supported by the C_3 symmetric $[poat]^{3-}$ ligand framework. This complex, $K[Co^{II}poat]$ is used in Chapter 3 – 5 to prepare unsymmetric bimetallic species. Chapter 3 focuses specifically on the formation of a $[poatCo^{III}–\mu\text{-}OH–Zn^{II}Me_3tacn]^+$ complex via a proposed Co^{II}–oxidant adduct that reacts in the presence of $[Zn^{II}Me_3tacn(OTf)_2]$, where Me_3tacn is a heterocyclic N-based ligand.

In Chapter 4, the preparation of a $[poatCo^{II}–\mu\text{-}OH–Fe^{III}Me_3tacn]^+$ complex from $K[Co^{II}poat]$ and O_2 in the presence of $[Fe^{II}Me_3tacn(OTf)_2]$ is discussed. The $[poatCo^{II}–\mu\text{-}OH–Fe^{III}Me_3tacn]^+$ complex is subsequently oxidized to $[poatCo^{III}–\mu\text{-}OH–Fe^{III}Me_3tacn]^{2+}$ and the changes in the magnetic coupling between the Co and Fe centers are examined. Mössbauer and EPR spectroscopies support antiferromagnetic coupling in $[poatCo^{II}–\mu\text{-}OH–Fe^{III}Me_3tacn]^+$, but ferromagnetic coupling in $[poatCo^{III}–\mu\text{-}OH–Fe^{III}Me_3tacn]^{2+}$.

Finally, Chapter 5 describes the development of a new series of bimetallic species, $[M_x^{II}poat\cdots M_y^{II}Me_3tacn]^+$, ($M_x$ = Mn, Co, Zn; M_y = Mn, Fe, Co, Cu, Zn). The metal ion coordinated in the $[poat]^{3-}$ ligand backbone is in a trigonal monopyramidal geometry, which is shielded by the binding of a $[M_y^{II}Me_3tacn]^{2+}$ solely through the P=O groups. The two metal ions interact through three, triple-atom N–P=O bridging units and are highly symmetric, crystallizing in the $R\bar{3}$ space group. The metal ions were found to couple ferromagnetically to one another through the N–P=O bridges and the magnetism of these complexes was studied to determine if the complexes exhibit single molecule magnetic behavior. While the $[Co^{II}poat\cdots M_y^{II}Me_3tacn]^+$ complexes were most thoroughly investigated, the $[M_x^{II}poat\cdots M_y^{II}Me_3tacn]^+$ have also been prepared where M_x = Mn, Zn and M_y = Mn, Zn, suggesting that these complexes could be expanded to a wide array of metal ion.

Chapter 1: Introduction

Biological Inspiration

Nature utilizes metalloproteins to perform chemical transformations under ambient conditions and in aqueous environments, at efficiencies that are unmatched by synthetic systems.[1–11] This efficiency is attributed to the tight control that metalloproteins impose over the metal ion(s) at the active site.[12–15] This control is due to both the primary (1°) coordination sphere, which includes ligands covalently bound to the metal center(s), as well as the secondary (2°) coordination sphere which involves non-covalent interactions distal to the metal site(s). 2° sphere effects include hydrogen-bonding (H–bonding) interactions and electrostatic effects. Both coordination spheres comprise the microenvironment within the protein host. While influence of the 1° coordination sphere over the reactivity of metalloenzymes is well established, recent efforts have established the importance of the 2° coordination sphere in regulating reactivity and stabilizing key reactive intermediates.[16–25]

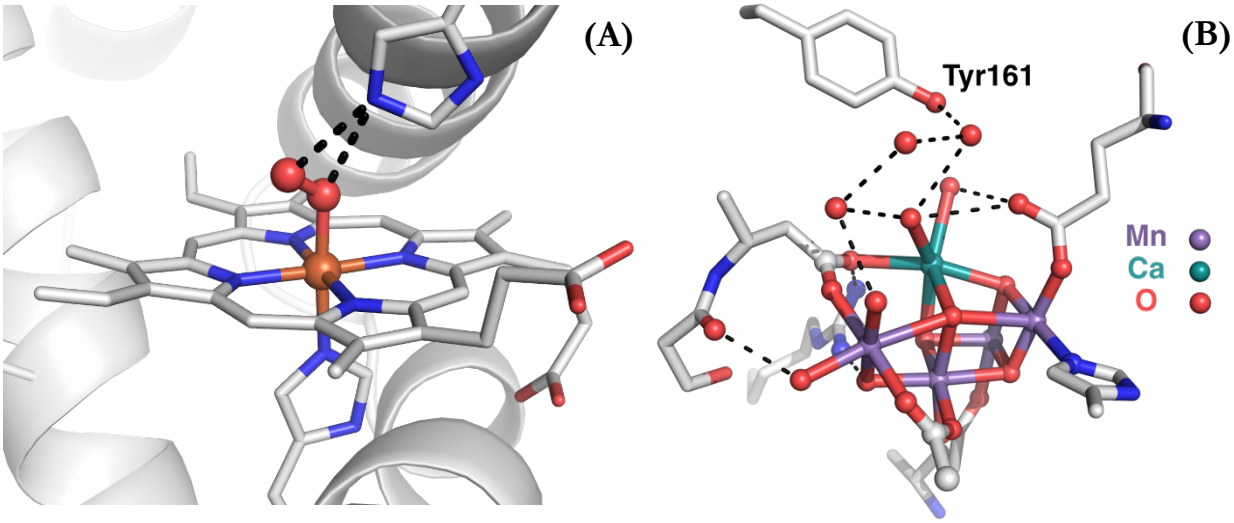

Oxymyoglobin (O_2–Mb)
PDB: 1A6M

Oxygen Evolving Complex (OEC)
PDB: 3WU2

Figure 1-1: (A) Representation of the active site found in O_2–Mb, emphasizing how the H–bonding interaction between O_2 and His aids in O_2 binding. N-atoms are represented in blue, C-atoms in light gray, O-atoms in red, and the Fe-atom by an orange sphere.[26] **(B)** Active site of the OEC found in Photosystem II, highlighting the [Mn_4O_5Ca] cubane and the H–bonding network.[28] The dashed lines represent H–bonding interactions in both structures.

Two biological systems that emphasize the significance of controlling the microenvironment within the protein are the oxygen evolving complex (OEC) of Photosystem II and myoglobin (Mb; Fig 1-1).[26–30] The structure of Mb highlights the importance of 2° sphere effects as well as the role of the protein host. Mb is a

respiratory protein found in the muscles of vertebrates that stores O_2 by reversibly binding it to the Fe center of a heme cofactor. Oxygen binding is mediated by a H–bonding interaction with an nearby histidine (His64) amino acid residue (Fig 1-1A).[3,26,31] Both the steric bulk provided by the protein host and the H–bonding interaction between the O_2 unit and His64 are key for function; when either is disrupted, the heme cofactor is irreversibly oxidized and loses function.[1,32,33]

The OEC features a $[Mn_4O_5Ca]$ cluster at the active site, arranged in a cubane orientation that uses multiple redox active metal ions to oxidize H_2O to O_2 in a four-proton, four-electron process.[34–36] The cluster is held in place by several endogenous amino acid residues bound to the Mn ions, as well as an extensive H–bonding network (Fig 1-1B). The bridging oxido units in the 1º coordination sphere are implicated in the stabilization of the high-valent Mn centers due to their anionic nature.[37] In addition to the H–bonding interactions that aid in the transfer of proton and electron equivalents, the electrostatic interaction of the Ca^{II} ion within the cubane is also important for driving the oxidation of H_2O to O_2.[28,29,34,35,38–48] Substitution of Ca^{II} with a different metal ion not only changes the structure of the OEC, but also limits its reactivity.[37,49–52] Much like substitution of the Ca^{II} ion, disruption of the H–bonding network through site-directed mutagenesis studies effectively quenched reactivity at the OEC, limiting O_2 evolution.[53,54] The profound disruption of enzymatic function caused by alterations to the 2º coordination sphere in both the OEC and Mb emphasizes the key role noncovalent interactions play in biological systems.

Synthetic Systems

Outside Work

While nature excels at directing the chemistry carried out by metalloenzymes by manipulation of the microenvironment within the protein host, replicating these effects in synthetic systems has been challenging. One successful approach to include 2º sphere interactions into synthetic metal complexes is the design of ligand frameworks which feature appended functional groups to provide H–bonding interactions. The earliest examples of these principles originated in the Collman lab, where they designed modifiable "picket fence porphyrin" ligand frameworks. The 1º coordination sphere of the porphyrin ligand was designed to emulate structural features of the heme cofactor, while the pendant functional groups could be synthetically modulated

(Fig 1-2).[55–58] Incorporation of the sterically bulky pivalamide groups to the porphyrin backbone resulted in the formation of a "fence" around the Fe–O_2 unit. The picket fence facilitated the preparation and characterization of mononuclear complexes by preventing irreversible oxidation and formation of dinuclear complexes, as observed in earlier examples of synthetic porphyrin complexes.[59–63] At first glance, the amide N–H moieties appear promising to form intramolecular H–bonds in the 2º coordination sphere with the bound O_2 unit, however the pivalamide functional groups ultimately were found to be too far away to interact (Fig 1-2A). Exchanging one of the pivalamide arms for a phenyl urea group improved the complex's affinity for O_2, which was attributed to the proposed formation of an intramolecular H–bond between the phenyl urea N–H group and the O_2 unit (Fig 1-2B).[64] While this interaction was never structurally confirmed, it represents one of the earliest examples of 2º sphere interactions in a synthetic complex.

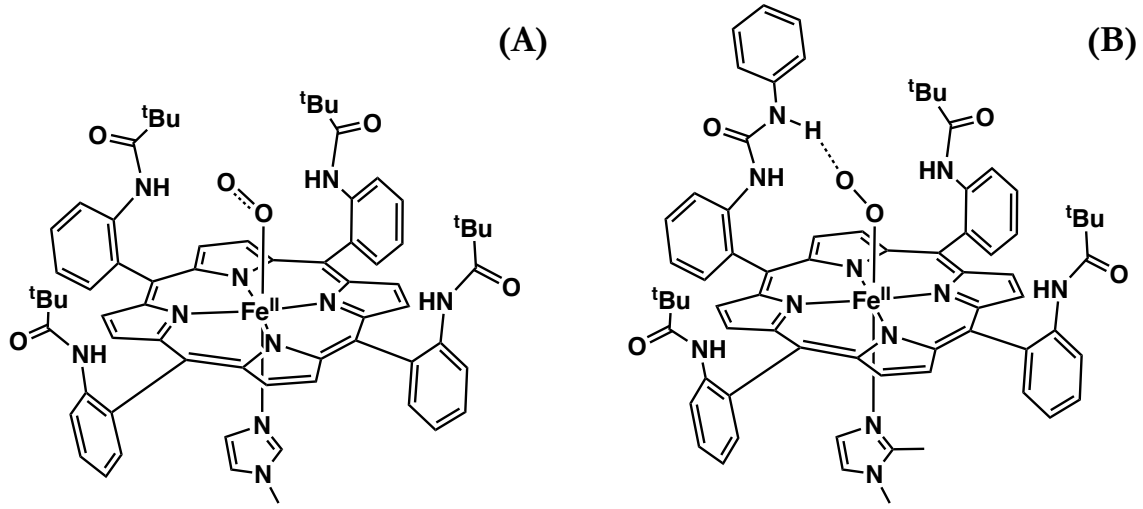

Figure 1-2: (A) Representation of a structurally characterized Fe–O_2 adduct supported by a picket fence porphyrin ligand.[59–63] **(B)** Fe–O_2 adduct stabilized by a H–bonding interaction in a modified picket fence porphyrin ligand framework, with a phenyl urea moiety incorporated to act as a H–bond donor.[64]

Since Collman's seminal work, significant strides have been made towards the development of ligand frameworks that incorporate intramolecular 2º sphere interactions. The Fout lab has developed ligand frameworks that feature 2º sphere interactions from tautomeric functional groups that can act either as a H–bond donor or a H–bond acceptor depending on the tautomer: amine-azafulvene or pyrrole-2-imine (Fig 1-3). Both tripodal and tetrapodal ligands have been prepared with these tautomeric functional groups and support metal complexes with a varying exogenous ligands.[65–72] The *C_3* symmetric ligand developed by the group (Fig 1-3, top) was found to support a rare Fe^{III}–O unit due to H–bond donation from three amine-azafulvene

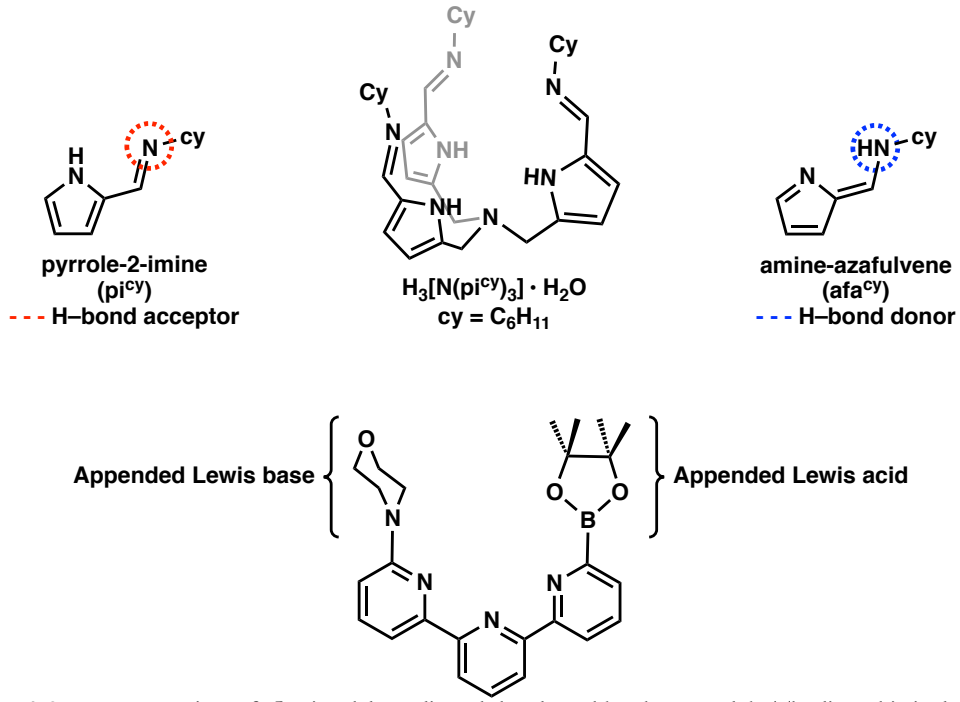

Figure 1-3: Representation of C_3 tripodal pre-ligand developed by the Fout lab. The ligand is isolated as the pyrrole-2-imine tautomer, however the amine-azafulvene tautomer is accessibly upon metallation (top). The bottom shows an example of ligand frameworks developed by the Szymczak lab which incorporates both a pendant Lewis acid and base.

donors and the steric bulk provided by the cyclohexyl groups.[73] Furthermore, it was found that each arm tautomerizes independently, providing diversity in the 2º coordination sphere to support a wide range of exogenous ligands.[65] In addition to the Fout lab, the Szymczak lab has also focused on the design of ligand frameworks which feature intramolecular H–bonding interactions.[74–80] The Szymczak lab has further expanded their study of 2º sphere effects to include pendant Lewis acidic and basic groups (Fig 1-3, bottom).[81–89] Incorporation of Lewis acidic and basic groups in the 2º coordination sphere has been shown to enhance N_2 uptake and activation.[90] The Yang group has developed a salen ligand with an auxiliary crown ether moiety to facilitate the incorporation of Lewis acidic metal ions.[91,92] The electrostatic effects induced by incorporation of a Lewis acidic metal ion in the appended crown ether was found to affect the hydrogen-atom transfer reactivity carried out by a Mn^{V}–imido complex supported by the salen. These examples demonstrate the synthetic utility of incorporating 2º sphere effects, as inspired by biological environments.

Previous Work from the Borovik Lab

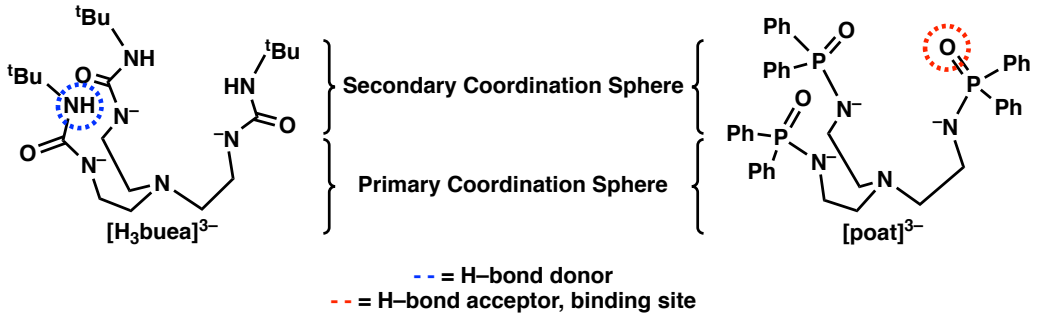

Figure 1-4: Examples of C_3 tripodal ligand frameworks developed by the Borovik lab.

In addition to the systems discussed above, the Borovik lab has pioneered the incorporation of 2º sphere effects in synthetic ligand design. Given that biological systems typically access high-valent, high-spin metal centers to catalyze chemical transformations, several design considerations were taken into account to replicate these features. To access high-spin metal complexes, a C_3 symmetric ligand field was targeted because C_3 symmetry has been found to favor high-spin states over tetragonal fields.[93] Therefore, ligand frameworks were designed by modifying a tris(2-aminoethyl)amine (tren) backbone. The tren backbone is readily functionalized to provide 2º sphere interactions and the derivatized framework can then be deprotonated to provide a trianionic ligand environment. The trianionic nature of the ligand backbone supports both high-spin and high-valent metal complexes. When the modified ligand framework coordinates to a metal ion, it provides a rigid ligand framework, stabilizing the metal complex through the chelate effect and placing the appended functional groups in an appropriate position to participate in intramolecular H–bonding interactions (Fig 1-4).[94,95] These design principles have afforded ligand platforms that support the formation and characterization of molecules that are both biologically relevant and synthetically interesting, including multiple examples of M–O(H) species,[94–103] M–O_2 adducts,[104–106] and unsymmetric bimetallic complexes.[95,107–114] Focusing on incorporating these 2º sphere effects has also led to the development of several unsymmetric tripodal ligand frameworks, where each tripod arm can be systematically modified to more specifically understand the contributions of individual 2º sphere interactions.[106,115–117] Rigorous synthetic control has supported the preparation of biologically relevant complexes in past work, however this dissertation focuses on how biologically inspired design principles can be used to develop and support synthetic coordination complexes.

Overview of Following Chapters

The work described in this dissertation focused on synthetic control of both the 1º and 2º coordination spheres to design paramagnetic mono- and bimetallic Co coordination complexes. One chapter describes the use of a hybrid, unsymmetric tripodal ligand framework to prepare mononuclear hydroxido complexes. The remaining three chapters focus on the use of a trigonal monopyramidal (TMP) Co complex, supported by a C_3 symmetric tripodal ligand framework, to prepare bimetallic systems with single- and triple-atom bridging interactions.

Chapter 2: Preparation, properties, and reactivity of a paramagnetic Co^{III}–OH complex

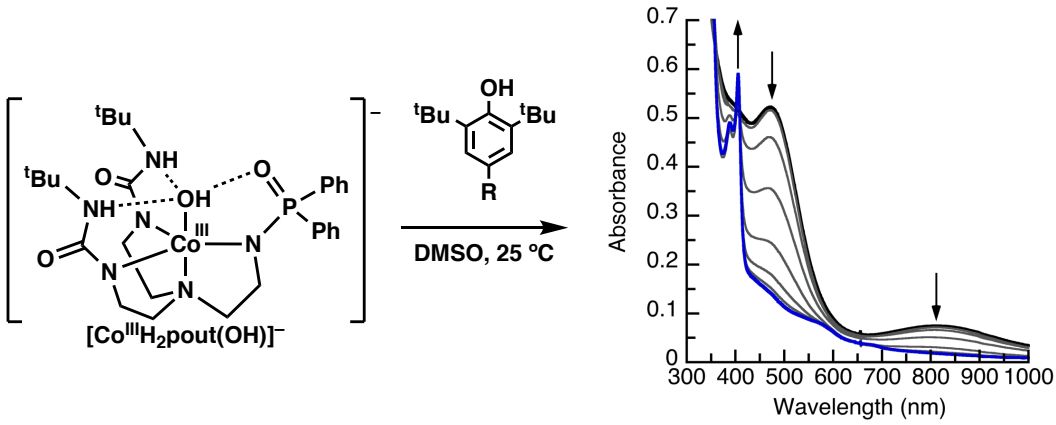

Figure 1-5: Representation of $[Co^{III}H_2pout(OH)]^-$ and an example of its reactivity with 2,6-di-^{t}Bu-4-R-PhOH.

This chapter employed a hybrid, unsymmetric ligand framework, $[H_2pout]^{3-}$, to prepare a pair of paramagnetic $Co^{II/III}$–OH complexes. $[H_2pout]^{3-}$ was designed to favor M–OH complexes through the incorporation of two H–bond donating groups and one H–bond accepting group. Previously, $[H_2pout]^{3-}$ was used to prepare and study $Mn^{II/III/IV}$–OH and $Fe^{II/III}$–OH complexes.[116,118] A pair of $Co^{II/III}$–OH complexes were prepared and characterized spectroscopically and structurally, accessing a rare example of a crystallographically validated Co^{III}–OH complex. The Co^{III}–OH complex was paramagnetic, with a $S = 1$ spin state, and was found to be moderately unstable in solution. The reactivity of the complex was subsequently investigated with different substrates and $[Co^{III}H_2pout(OH)]^-$ was found to be competent to cleave O–H bonds (Fig 1-5). This chapter describes the first study on the reactivity of a Co^{III}–OH complex, to the best of my knowledge.

Chapter 3: Preparation and properties of a $[Co^{III}–\mu\text{-}OH–Zn^{II}]^+$ complex from a proposed Co^{II}–IBX-^{i}Pr adduct

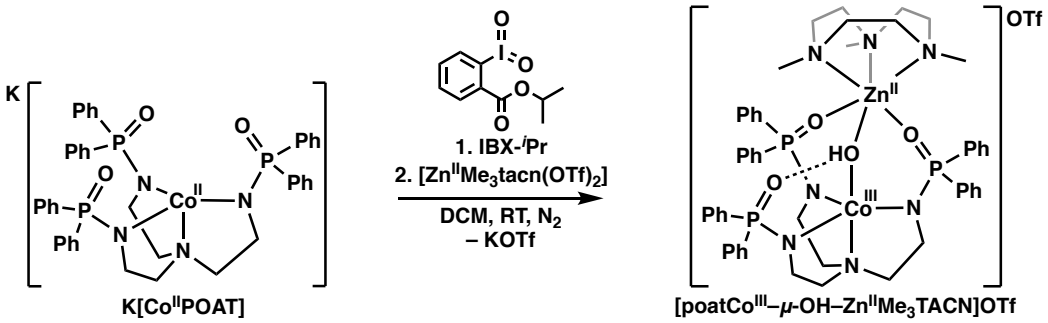

Figure 1-6: Synthesis of [poatCo^{III}–μ-OH–Zn^{II}Me$_3$tacn]OTf from K[Co^{II}poat] and IBX-^{i}pr in the presence of [Zn^{II}Me$_3$tacn(OTf)$_2$].

Work in this chapter focused on the preparation of a TMP Co^{II} complex, K[Co^{II}poat]. The synthesis and characterization of K[Co^{II}poat] was described and the complex was characterized. The utility of K[Co^{II}poat] towards the preparation of bimetallic complexes was then investigated. K[Co^{II}poat] was used in Chapter 3 and all remaining chapters as the starting synthon to access multiple bimetallic species. Chapter 3 specifically focused on the synthesis and characterization of [poatCo^{III}–μ-OH–Zn^{II}Me$_3$tacn]OTf (Fig 1-6) from a proposed adduct formed between K[Co^{II}poat] and an O-atom transfer reagent, isopropyl 2-iodoxybenzoate (IBX-^{i}Pr). The proposed adduct persisted in dilute solutions and subsequently reacted in the presence of [Zn^{II}Me$_3$tacn(OTf)$_2$], forming [poatCo^{III}–μ-OH–Zn^{II}Me$_3$tacn]OTf which was characterized both structurally and spectroscopically. The spectroscopic characterization provided important information about Co^{III}–OH units in bimetallic systems due to the incorporation of the redox-inert, diamagnetic Zn^{II} center. Furthermore, the d^{10} Zn^{II} ion did not affect the magnetic behavior of the complex and was unlikely to have a significant effect on the electronic absorption spectrum.

Chapter 4: Modulating magnetic coupling through synthetic control in paramagnetic $Co^{II/III}$–μ-O(H)–Fe^{III} complexes

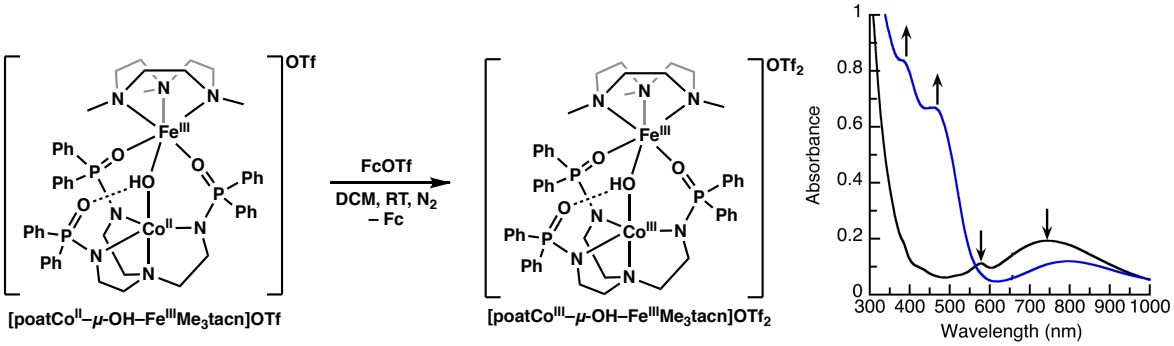

Figure 1-7: Synthesis of [poatCo^{III}–μ-OH–$Fe^{III}$$Me_3$tacn](OTf)$_2$ from [poatCo^{II}–μ-OH–$Fe^{III}$$Me_3$tacn]OTf and FcOTf and UV-vis spectra following the reaction.

Chapter 4 focused on the preparation of bimetallic complexes with a M–μ-OH–M' core from O_2. K[Co^{II}poat] was found to react with O_2 in the presence of a redox active metal complex, [$Fe^{II}$$Me_3$tacn(OTf)$_2$]. This reaction resulted in the formation of [poatCo^{II}–μ-OH–$Fe^{III}$$Me_3$tacn]OTf. Interestingly, the Fe center was oxidized to Fe^{III} while the Co^{II} center did not change oxidation states. The mechanism of formation for this complex was investigated to better understand why the Fe^{II} center was preferentially oxidized, though a definitive conclusion could not be drawn. [poatCo^{II}–μ-OH–$Fe^{III}$$Me_3$tacn]OTf was subsequently characterized and was found to exhibit a one electron oxidation negative of the ferrocenium/ferrocene ($Fc^{+/0}$) couple. Therefore, [poatCo^{II}–μ-OH–$Fe^{III}$$Me_3$tacn]OTf treated with FcOTf, leading to the formation of [poatCo^{III}–μ-OH–$Fe^{III}$$Me_3$tacn](OTf)$_2$. Upon oxidation of the Co center, the spin state of the Co center was found to change from S = 3/2 for the Co^{II} center to S = 1 to the Co^{III} center. The change in spin state affected the mode of magnetic coupling between the Co and Fe centers, from antiferromagnetic coupling in [poatCo^{II}–μ-OH–$Fe^{III}$$Me_3$tacn]OTf to ferromagnetic coupling in [poatCo^{III}–μ-OH–$Fe^{III}$$Me_3$tacn](OTf)$_2$. The magnetic interactions were confirmed with electron paramagnetic resonance (EPR) and Mössbauer spectroscopies. There is preliminary evidence that introducing a base may result in the formation of [poatCo^{III}–μ-O–$Fe^{III}$$Me_3$tacn]OTf, where the hydroxido bridging ligand is deprotonated to an oxido ligand. The proposed incorporation of an oxido ligand once again led to a change in the coupling between the two metal ions, back to antiferromagnetic coupling.

Chapter 5: Magnetic communication in rigorously *C*$_3$ symmetric complexes facilitated by N–P=O bridging units

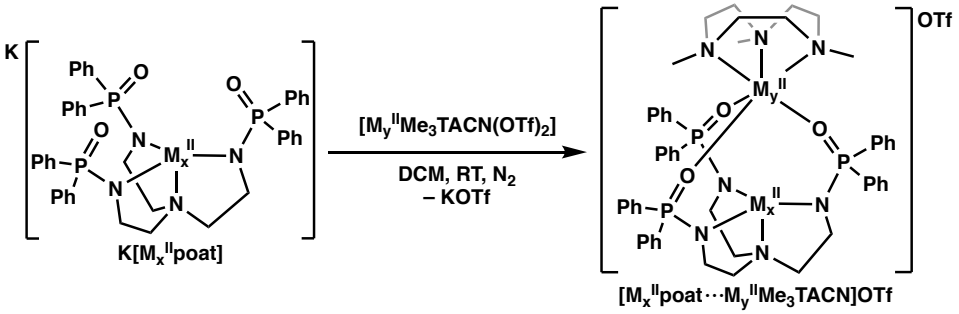

Figure 1-8: Preparative method for the synthesis of *C*$_3$ symmetric bimetallic coordination complexes, where M_x = Mn, Co, Zn and M_y = Mn, Fe, Co, Cu, and Zn.

Chapter 5 describes the preparation of *C*$_3$ symmetric bimetallic complexes, where a second metal ion was added to a TMP K[M_x^{II}poat] starting complex to form [M_x^{II}poat···M_y^{II}Me$_3$tacn]$^+$ (M_x = Mn, Co, Zn; M_y = Mn, Fe, Co, Cu, Zn). The second metal ion coordinated to the [poat]$^{3-}$ ligand backbone through the P=O units to form three, triple atom N–P=O bridges between the two metal centers. Binding of the second metal ion to the [poat]$^{3-}$ P=O groups effectively shields the [M_x^{II}poat]$^-$ unit, preserving the TMP coordination geometry. These complexes all crystallized isomorphous to one another in the $R\bar{3}$ space group. Following structural characterization, the [M_x^{II}poat···M_y^{II}Me$_3$tacn]$^+$ complexes where studied spectroscopically with an eye towards understanding the role the N–P=O bridging units played in facilitating magnetic coupling between the two metal centers. The complexes were characterized by ⊥- and ∥-mode EPR spectroscopy, which revealed that the N–P=O bridges led to ferromagnetic interactions between the two metal centers. The coupling between the two metal centers appeared weak, leading to complex EPR spectra with multiple features which were the same in both solution and solid EPR samples. The origins of these spectral features are still under investigation. Finally, SQUID measurements were collected which supported antiferromagnetic interactions between the two metal centers of the [M_x^{II}poat···M_y^{II}Me$_3$tacn]$^+$ complexes. The SQUID data did not indicate that any of the complexes exhibited single molecule magnetism.

References

(1) Kurtz, D. M. Oxo- and Hydroxo-Bridged Diiron Complexes: A Chemical Perspective on a Biological Unit. *Chem. Rev.* **1990**, *90*, 585–606.

(2) Holm, R. H.; Kennepohl, P.; Solomon, E. I. Structural and Functional Aspects of Metal Sites in Biology. *Chem. Rev.* **1996**, *96*, 2239–2314.

(3) Poulos, T. L. Heme Enzyme Structure and Function. *Chem. Rev.* **2014**, *114*, 3919–3962.

(4) Kurtz, D. M. Structural Similarity and Functional Diversity in Diiron-Oxo Proteins. *J. Biol. Inorg. Chem.* **1997**, *2*, 159–167.

(5) Tommos, C.; Babcock, G. T. Oxygen Production in Nature: A Light-Driven Metalloradical Enzyme Process. *Acc. Chem. Res.* **1998**, *31*, 18–25.

(6) Que, L. J.; Tolman, W. B. Biologically Inspired Oxidation Catalysis. *Nature* **2008**, *455*, 333–340.

(7) Stone, K. L.; Borovik, A. S. Lessons from Nature: Unraveling Biological C–H Bond Activation. *Curr. Opin. Chem. Biol.* **2009**, *13*, 114–118.

(8) Borovik, A. S. Role of Metal–Oxo Complexes in the Cleavage of C–H Bonds. *Chem. Soc. Rev.* **2011**, *40*, 1870–1874.

(9) Cook, S. A.; Borovik, A. S. Molecular Designs for Controlling the Local Environments around Metal Ions. *Acc. Chem. Res.* **2015**, *48*, 2407–2414.

(10) Lee, J. L.; Ross, D. L.; Barman, S. K.; Ziller, J. W.; Borovik, A. S. C-H Bond Cleavage by Bioinspired Nonheme Metal Complexes. *Inorg. Chem.* **2021**, *60*, 13759–13783.

(11) Liu, J.; Chakraborty, S.; Hosseinzadeh, P.; Yu, Y.; Tian, S.; Petrik, I.; Bhagi, A.; Lu, Y. Metalloproteins Containing Cytochrome, Iron–Sulfur, or Copper Redox Centers. *Chem. Rev.* **2014**, *114*, 4366–4469.

(12) Dawson, J. H. Probing Structure-Function Relations in Heme-Containing Oxygenases and Peroxidases. *Sci.* **1988**, *240*, 433–439.

(13) Hegg, E. L.; Que, L. The 2-His-1-Carboxylate Facial Triad - An Emerging Structural Motif in Mononuclear Non-Heme Iron(II) Enzymes. *Eur. J. Biochem.* **1997**, *250*, 625–629.

(14) Que, L.; Ho, R. Y. N. Dioxygen Activation by Enzymes with Mononuclear Non-Heme Iron Active Sites. *Chem. Rev.* **1996**, *96*, 2607–2624.

(15) Solomon, E. I.; Zhang, Y. The Electronic Structures of Active Sites in Non-Heme Iron Enzymes. *Acc. Chem. Res.* **1992**, *25*, 343–352.

(16) Borovik, A. S. Bioinspired Hydrogen Bond Motifs in Ligand Design: The Role of Noncovalent Interactions in Metal Ion Mediated Activation of Dioxygen. *Acc. Chem. Res.* **2005**, *38*, 54–61.

(17) Shook, R. L.; Borovik, A. S. The Effects of Hydrogen Bonds on Metal-Mediated O2 Activation and Related Processes. *Chem. Commun.* **2008**, 6095–6107.

(18) Shaw, W. J. The Outer-Coordination Sphere: Incorporating Amino Acids and Peptides as Ligands for Homogeneous Catalysts to Mimic Enzyme Function. *Catal. Rev. Sci. Eng.* **2012**, *54*, 489–550.

(19) Costas, M.; Mehn, M. P.; Jensen, M. P.; Que, L. Dioxygen Activation at Mononuclear Nonheme Iron Active Sites: Enzymes, Models, and Intermediates. *Chem. Rev.* **2004**, *104*, 939–986.

(20) Casadei, C. M.; Gumiero, A.; Metcalfe, C. L.; Murphy, E. J.; Basran, J.; Concilio, M. G.; Teixeira, S. C. M.; Schrader, T. E.; Fielding, A. J.; Ostermann, A.; Blakeley, M. P.; Raven, E. L.; Moody, P. C. E. Neutron Cryo-Crystallography Captures the Protonation State of Ferryl Heme in a Peroxidase. *Science* **2014**, *345*, 193–197.

(21) Berggren, G.; Adamska, A.; Lambertz, C.; Simmons, T. R.; Esselborn, J.; Atta, M.; Gambarelli, S.; Mouesca, J. M.; Reijerse, E.; Lubitz, W.; Happe, T.; Artero, V.; Fontecave, M. Biomimetic Assembly and Activation of [FeFe]-Hydrogenases. *Nature* **2013**, *499*, 66–69.

(22) Boussac, A.; Rappaport, F.; Carrier, P.; Verbavatz, J. M.; Gobin, R.; Kirilovsky, D.; Rutherford, A. W.; Sugiura, M. Biosynthetic Ca2+/Sr2+ Exchange in the Photosystem II Oxygen-Evolving Enzyme of Thermosynechococcus Elongatus. *J. Biol. Chem.* **2004**, *279*, 22809–22819.

(23) Pushkar, Y.; Yano, J.; Sauer, K.; Boussac, A.; Yachandra, V. K. Structural Changes in the Mn4Ca Cluster and the Mechanism of Photosynthetic Water Splitting. *Proc. Natl. Acad. Sci. USA* **2008**, *105*, 1879–1884.

(24) Rapatskiy, L.; Cox, N.; Savitsky, A.; Ames, W. M.; Sander, J.; Nowaczyk, M. M.; Rögner, M.; Boussac, A.; Neese, F.; Messinger, J.; Lubitz, W. Detection of the Water-Binding Sites of the Oxygen-Evolving Complex of Photosystem II Using W-Band 17O Electron–Electron Double Resonance-Detected NMR Spectroscopy. *J. Am. Chem. Soc.* **2012**, *134*, 16619–16634.
(25) Groves, J. T. High-Valent Iron in Chemical and Biological Oxidations. *J. Inorg. Biochem.* **2006**, *100*, 434–447.
(26) Vojtěchovský, J.; Chu, K.; Berendzen, J.; Sweet, R. M.; Schlichting, I. Crystal Structures of Myoglobin-Ligand Complexes at near-Atomic Resolution. *Biophys. J.* **1999**, *77,* 2153–2174.
(27) Lee, J. L. Synthetic Models for Metalloenzyme Active Sites: Accessing High-Valent Bimetallic Complexes with [M–(μ-OH)–M'] Cores, University of California, Irvine, 2021.
(28) Barber, J. Crystal Structure of the Oxygen-Evolving Complex of Photosystem II. *Inorg. Chem.* **2008**, *47*, 1700–1710.
(29) Barber, J.; Murray, J. W. Revealing the Structure of the Mn-Cluster of Photosystem II by X-Ray Crystallography. *Coord. Chem. Rev.* **2008**, *252*, 233–243.
(30) Chen Sun. Secondary Coordination Sphere Effects on Properties and Reactivities of Metal Complexes, University of California, Irvine, Irvine, CA, 2021.
(31) Paoli, M.; Liddington, R.; Tame, J.; Wilkinson, A.; Dodson, G. Crystal Structure of T State Haemoglobin with Oxygen Bound At All Four Haems. *J. Mol. Biol.* **1996**, *256*, 775–792.
(32) Cohen, I. A.; Caughey, W. S. Substituted Deuteroporphyrins. IV. Kinetics and Mechanism of Reactions of Iron(II) Porphyrins with Oxygen. *Biochemistry* **1968**, *7*, 636–641.
(33) Shikama, K. Stability Properties of Dioxygen-Iron(II) Porphyrins: An Overview from Simple Complexes to Myoglobin. *Coord. Chem. Rev.* **1988**, *83*, 73–91.
(34) Siegbahn, P. E. M. Structures and Energetics for O_2 Formation in Photosystem II. *Acc. Chem. Res.* **2009**, *42*, 1871–1880.
(35) Yano, J.; Yachandra, V. Mn4Ca Cluster in Photosynthesis: Where and How Water Is Oxidized to Dioxygen. *Chem. Rev.* **2014**, *114*, 4175–4205.
(36) Kern, J.; Chatterjee, R.; Young, I. D.; Fuller, F. D.; Lassalle, L.; Ibrahim, M.; Gul, S.; Fransson, T.; Brewster, A. S.; Alonso-Mori, R.; Hussein, R.; Zhang, M.; Douthit, L.; de Lichtenberg, C.; Cheah, M. H.; Shevela, D.; Wersig, J.; Seuffert, I.; Sokaras, D.; Pastor, E.; Weninger, C.; Kroll, T.; Sierra, R. G.; Aller, P.; Butryn, A.; Orville, A. M.; Liang, M.; Batyuk, A.; Koglin, J. E.; Carbajo, S.; Boutet, S.; Moriarty, N. W.; Holton, J. M.; Dobbek, H.; Adams, P. D.; Bergmann, U.; Sauter, N. K.; Zouni, A.; Messinger, J.; Yano, J.; Yachandra, V. K. Structures of the Intermediates of Kok's Photosynthetic Water Oxidation Clock. *Nature* **2018**, *563*, 421–425.
(37) Cox, N.; Pantazis, D. A.; Neese, F.; Lubitz, W. Biological Water Oxidation. *Acc. Chem. Res.* **2013**, *46*, 1588–1596.
(38) Cady, C. W.; Crabtree, R. H.; Brudvig, G. W. Functional Models for the Oxygen-Evolving Complex of Photosystem II. *Coord. Chem. Rev.* **2008**, *252*, 444–455.
(39) Brudvig, G. W. Water Oxidation Chemistry of Photosystem II. *Philos. Trans. R. Soc. B Biol. Sci.* **2008**, *363*, 1211–1219.
(40) Mullins, C.; Pecoraro, V. Reflections on Small Molecule Manganese Models That Seek to Mimic Photosynthetic Water Oxidation Chemistry. *Coord. Chem. Rev.* **2008**, *252*, 416–443.
(41) Betley, T. A.; Wu, Q.; Van Voorhis, T.; Nocera, D. G. Electronic Design Criteria for O-O Bond Formation via Metal-Oxo Complexes. *Inorg. Chem.* **2008**, *47*, 1849–1861.
(42) Vogt, L.; Vinyard, D. J.; Khan, S.; Brudvig, G. W. Oxygen-Evolving Complex of Photosystem II: An Analysis of Second-Shell Residues and Hydrogen-Bonding Networks. *Curr. Opin. Chem. Biol.* **2015**, *25*, 152–158.
(43) Umena, Y.; Kawakami, K.; Shen, J.-R.; Kamiya, N. Crystal Structure of Oxygen-Evolving Photosystem II at a Resolution of 1.9 Å. *Nature* **2011**, *473*, 55–60.
(44) Ferreira, K. N.; Iverson, T. M.; Maghlaoui, K.; Barber, J.; Iwata, S. Architecture of the Photosynthetic Oxygen-Evolving Center. *Science* **2004**, *303*, 1831–1838.

(45) Yano, J.; Kern, J.; Sauer, K.; Latimer, M. J.; Pushkar, Y.; Biesiadka, J.; Loll, B.; Saenger, W.; Messinger, J.; Zouni, A.; Yachandra, V. K. Where Water Is Oxidized to Dioxygen: Structure of the Photosynthetic Mn4Ca Cluster. *Science* **2006**, *314*, 821–825.

(46) Sauer, K.; Yano, J.; Yachandra, V. K. X-Ray Spectroscopy of the Photosynthetic Oxygen-Evolving Complex. *Coord. Chem. Rev.* **2008**, *252*, 318–335.

(47) Guskov, A.; Kern, J.; Gabdulkhakov, A.; Broser, M.; Zouni, A.; Saenger, W. Cyanobacterial Photosystem II at 2.9-Å Resolution and the Role of Quinones, Lipids, Channels and Chloride. *Nat. Struct. Mol. Biol.* **2009**, *16*, 334–342.

(48) Pecoraro, V. L.; Baldwin, M. J.; Caudle, M. T.; Hsieh, W.-Y.; Law, N. A. A Proposal for Water Oxidation in Photosystem II. *Pure Appl. Chem.* **1998**, *70*, 925–929.

(49) McEvoy, J. P.; Brudvig, G. W. Water-Splitting Chemistry of Photosystem II. *Chem. Rev.* **2006**, *106*, 4455–4483.

(50) Tsui, E. Y.; Tran, R.; Yano, J.; Agapie, T. Redox-Inactive Metals Modulate the Reduction Potential in Heterometallic Manganese–Oxido Clusters. *Nat. Chem.* **2013**, *5*, 293–299.

(51) Tsui, E. Y.; Kanady, J. S.; Agapie, T. Synthetic Cluster Models of Biological and Heterogeneous Manganese Catalysts for O_2 Evolution. *Inorg. Chem.* **2013**, *52*, 13833–13848.

(52) Liang, W.; Roelofs, T. A.; Cinco, R. M.; Rompel, A.; Latimer, M. J.; Yu, W. O.; Sauer, K.; Klein, M. P.; Yachandra, V. K. Structural Change of the Mn Cluster during the S2→S3 State Transition of the Oxygen-Evolving Complex of Photosystem II. Does It Reflect the Onset of Water/Substrate Oxidation? Determination by Mn X-Ray Absorption Spectroscopy. *J. Am. Chem. Soc.* **2000**, *122*, 3399–3412.

(53) Oyala, P. H.; Stich, T. A.; Debus, R. J.; Britt, R. D. Ammonia Binds to the Dangler Manganese of the Photosystem II Oxygen-Evolving Complex. *J. Am. Chem. Soc.* **2015**, *137*, 8829–8837.

(54) Navarro, M. P.; Ames, W. M.; Nilsson, H.; Lohmiller, T.; Pantazis, D. A.; Rapatskiy, L.; Nowaczyk, M. M.; Neese, F.; Boussac, A.; Messinger, J.; Lubitz, W.; Cox, N. Ammonia Binding to the Oxygen-Evolving Complex of Photosystem II Identifies the Solvent-Exchangeable Oxygen Bridge (μ-Oxo) of the Manganese Tetramer. *Proc. Natl. Acad. Sci. USA* **2013**, *110*, 15561–15566.

(55) Collman James, P.; Gagne, R. R.; Halbert, T. R.; Marchon, J. C.; Reed, C. A.; Collman, J. P.; Gagne, R. R.; Halbert, T. R.; Marchon, J. C.; Reed, C. A. Reversible Oxygen Adduct Formation in Ferrous Complexes Derived from a Picket Fence Porphyrin. Model for Oxymyoglobin. *J. Am. Chem. Soc.* **1973**, *95*, 7868–7870.

(56) Collman James, P.; Reed, C. A.; Collman, J. P.; Reed, C. A.; Coliman, J. P.; Reed, C. A. Syntheses of Ferrous-Porphyrin Complexes. Hypothetical Model for Deoxymyoglobin. *J. Am. Chem. Soc.* **1973**, *95* (6), 2048–2049. https://doi.org/10.1021/ja00787a075.

(57) Collman, J. P.; Gagne, R. T.; Reed, C. A.; Collman James, P.; Gagne, R. T.; Reed, C. A. Paramagnetic Dioxygen Complex of Iron(II) Derived from a Picket Fence Porphyrin. Further Models for Hemoproteins. *J. Am. Chem. Soc.* **1974**, *96* (8), 2629–2631. https://doi.org/10.1021/ja00815a060.

(58) Collman, J. P.; Gagne, R. R.; Reed, C. A.; Robinson, W. T.; Rodley, G. A. Structure of an Iron(II) Dioxygen Complex; a Model for Oxygen Carrying Hemeproteins. *Proc. Natl. Acad. Sci. U. S. A.* **1974**, *71* (4), 1326–1329.

(59) Fleischer, E. B.; Srivastava, T. S. The Structure and Properties of μ-Oxo-Bis(Tetraphenylporphineiron(III)). *J. Am. Chem. Soc.* **1969**, *91*, 2403–2405.

(60) Baldwin, J. E.; Huff, J.; Balwin, J. S.; Huff, J. Binding of Dioxygen to Iron(II). Reversible Behavior in Solution. *J. Am. Chem. Soc.* **1973**, *95*, 5757–5759.

(61) Anderson, D. L.; Weschler, C. J.; Basolo, F. Reversible Reaction of Simple Ferrous Porphyrins with Molecular Oxygen at Low Temperatures. *J. Am. Chem. Soc.* **1974**, *96*, 5599–5600.

(62) Wagner, G. C.; Kassner, R. J. Spectroscopic Properties of Protoheme Complexes Undergoing Reversible Oxygenation. *J. Am. Chem. Soc.* **1974**, *96*, 5593–5595.

(63) Basolo, F.; Hoffman, B. M.; Ibers, J. A. Synthetic Oxygen Carriers of Biological Interest. *Acc. Chem. Res.* **1975**, *8*, 384–392.

(64) Wuenschell, G. E.; Tetreau, C.; Lavalette, D.; Reed, C. A. H-Bonded Oxyhemoglobin Models with Substituted Picket-Fence Porphyrins - the Model-Compound Equivalent of Site-Directed Mutagenesis. *J. Am. Chem. Soc.* **1992**, *114*, 3346–3355.
(65) Matson, E. M.; Bertke, J. A.; Fout, A. R. Isolation of Iron(II) Aqua and Hydroxyl Complexes Featuring a Tripodal H-Bond Donor and Acceptor Ligand. *Inorg. Chem.* **2014**, *53*, 4450–4458.
(66) Matson, E. M.; Park, Y. J.; Fout, A. R. Facile Nitrite Reduction in a Non-Heme Iron System: Formation of an Iron(III)-Oxo. *J. Am. Chem. Soc.* **2014**, *136*, 17398–17401.
(67) Park, Y. J.; Matson, E. M.; Nilges, M. J.; Fout, A. R. Exploring Mn–O Bonding in the Context of an Electronically Flexible Secondary Coordination Sphere: Synthesis of a Mn(III)–Oxo. *Chem. Commun.* **2015**, *51*, 5310–5313.
(68) Gordon, Z.; Drummond, M. J.; Matson, E. M.; Bogart, J. A.; Schelter, E. J.; Lord, R. L.; Fout, A. R. Tuning the Fe(II/III) Redox Potential in Nonheme Fe(II)-Hydroxo Complexes through Primary and Secondary Coordination Sphere Modifications. *Inorg. Chem.* **2017**, *56*, 4852–4863.
(69) Ford, C. L.; Miller, T. J.; Park, Y. J.; Iranmanesh, N.; Gray, D. L.; Fout, A. R. Varying the Secondary Coordination Sphere: Synthesis of Cobalt and Iron Complexes of a Tripodal Ligand Featuring Two Hydrogen-Bond Donors or Acceptors. *J. Coord. Chem.* **2020**, *73*, 2195–2208.
(70) Drummond, M. J.; Ford, C. L.; Gray, D. L.; Popescu, C. V.; Fout, A. R. Radical Rebound Hydroxylation Versus H-Atom Transfer in Non-Heme Iron(III)-Hydroxo Complexes: Reactivity and Structural Differentiation. *J. Am. Chem. Soc.* **2019**, *141*, 6639–6650.
(71) Gordon, Z.; Miller, T. J.; Leahy, C. A.; Matson, E. M.; Burgess, M.; Drummond, M. J.; Popescu, C. V.; Smith, C. M.; Lord, R. L.; Rodríguez-López, J.; Fout, A. R. Characterization of Terminal Iron(III)-Oxo and Iron(III)-Hydroxo Complexes Derived from O2 Activation. *Inorg. Chem.* **2019**, *58*, 15801–15811.
(72) Drummond, M. J.; Miller, T. J.; Ford, C. L.; Fout, A. R. Catalytic Perchlorate Reduction Using Iron: Mechanistic Insights and Improved Catalyst Turnover. *ACS Catal.* **2020**, *10*, 3175–3182.
(73) Ford, C. L.; Park, Y. J.; Matson, E. M.; Gordon, Z.; Fout, A. R. A Bioinspired Iron Catalyst for Nitrate and Perchlorate Reduction. *Science.* **2016**, *354*, 741–743.
(74) Moore, C. M.; Szymczak, N. K. 6,6'-Dihydroxy Terpyridine: A Proton-Responsive Bifunctional Ligand and Its Application in Catalytic Transfer Hydrogenation of Ketones. *Chem. Commun.* **2013**, *49*, 400–402.
(75) Moore, C. M.; Szymczak, N. K. Redox-Induced Fluoride Ligand Dissociation Stabilized by Intramolecular Hydrogen Bonding. *Chem. Commun.* **2014**, *51*, 5490–5492.
(76) Moore, C. M.; Quist, D. A.; Kampf, J. W.; Szymczak, N. K. A 3-Fold-Symmetric Ligand Based on 2-Hydroxypyridine: Regulation of Ligand Binding by Hydrogen Bonding. *Inorg. Chem.* **2014**, *53*, 3278–3280.
(77) Moore, C. M.; Szymczak, N. K. Nitrite Reduction by Copper through Ligand-Mediated Proton and Electron Transfer. *Chem. Sci.* **2015**, *6*, 3373–3377.
(78) Dahl, E. W.; Szymczak, N. K. Hydrogen Bonds Dictate the Coordination Geometry of Copper: Characterization of a Square-Planar Copper(I) Complex. *Angew. Chemie* **2016**, *128*, 3153–3157.
(79) Dahl, E. W.; Kiernicki, J. J.; Zeller, M.; Szymczak, N. K. Hydrogen Bonds Dictate O2Capture and Release within a Zinc Tripod. *J. Am. Chem. Soc.* **2018**, *140*, 10075–10079.
(80) Dahl, E. W.; Dong, H. T.; Szymczak, N. K. Phenylamino Derivatives of Tris(2-Pyridylmethyl)Amine: Hydrogen-Bonded Peroxodicopper Complexes. *Chem. Commun.* **2018**, *54*, 892–895.
(81) Kiernicki, J. J.; Shanahan, J. P.; Zeller, M.; Szymczak, N. K. Tuning Ligand Field Strength with Pendent Lewis Acids: Access to High Spin Iron Hydrides. *Chem. Sci.* **2019**, *10*, 5539–5545.
(82) Kiernicki, J. J.; Zeller, M.; Szymczak, N. K. Requirements for Lewis Acid-Mediated Capture and N-N Bond Cleavage of Hydrazine at Iron. *Inorg. Chem.* **2019**, *58*, 1147–1154.
(83) Geri, J. B.; Shanahan, J. P.; Szymczak, N. K. Testing the Push-Pull Hypothesis: Lewis Acid Augmented N2 Activation at Iron. *J. Am. Chem. Soc.* **2017**, *139*, 5952–5956.
(84) Kiernicki, J. J.; Zeller, M.; Szymczak, N. K. Hydrazine Capture and N-N Bond Cleavage at Iron Enabled by Flexible Appended Lewis Acids. *J. Am. Chem. Soc.* **2017**, *139*, 18194–18197.
(85) Kiernicki, J. J.; Zeller, M.; Szymczak, N. K. Examining the Generality of Metal-Ligand Cooperativity across a Series of First-Row Transition Metals: Capture, Bond Activation, and Stabilization. *Inorg. Chem.* **2020**, *59*, 9279–9286.

(86) Kiernicki, J. J.; Norwine, E. E.; Lovasz, M. A.; Zeller, M.; Szymczak, N. K. Mobility of Lewis Acids within the Secondary Coordination Sphere: Toward a Model for Cooperative Substrate Binding. *Chem. Commun.* **2020**, *56*, 13105–13108.
(87) Kiernicki, J. J.; Norwine, E. E.; Zeller, M.; Szymczak, N. K. Substrate Specific Metal-Ligand Cooperative Binding: Considerations for Weak Intramolecular Lewis Acid/Base Pairs. *Inorg. Chem.* **2021**, *60*, 1380–13810.
(88) Norwine, E. E.; Kiernicki, J. J.; Zeller, M.; Szymczak, N. K. Distinct Reactivity Modes of a Copper Hydride Enabled by anIntramolecular Lewis Acid. *J. Am. Chem. Soc.* **2022**, *144*, 15038–15046.
(89) Wang, B.; Seo, C. S. G.; Zhang, C.; Chu, J.; Szymczak, N. K. A Borane Lewis Acid in the Secondary Coordination Sphere of a Ni(II) Imido Imparts Distinct C−H Activation. *J. Am. Chem. Soc.* **2022**, *144*, 15793–15802.
(90) Tutusaus, O.; Ni, C.; Szymczak, N. K. A Transition Metal Lewis Acid/Base Triad System for Cooperative Substrate Binding. *J. Am. Chem. Soc.* **2013**, *135*, 3403–3406.
(91) Chantarojsiri, T.; Reath, A. H.; Yang, J. Y. Cationic Charges Lead to Inverse Free-Energy Relationship for N–N Bond Formation by MnVI Nitrides. *Angew. Chemie Int. Ed.* **2018**, *57*, 14037–14042.
(92) Léonard, N. G.; Chantarojsiri, T.; Ziller, J. W.; Yang, J. Y. Cationic Effects on the Net Hydrogen Atom Bond Dissociation Free Energy of High-Valent Manganese Imido Complexes. *J. Am. Chem. Soc.* **2022**, *144*, 1503–1508.
(93) Mayer, J. M.; Thorn, D. L.; Tulip, T. H. Synthesis, Reactions, and Electronic Structure of Low-Valent Rhenium−oxo Compounds. Crystal and Molecular Structure of $Re(O)I(MeCCMe)_2$. *J. Am. Chem. Soc.* **1985**, *107*, 7454–7462.
(94) Hammes, B. S.; Young, V. G.; Borovik, A. S. Hydrogen-Bonding Cavities about Metal Ions: A Redox Pair of Coordinatively Unsaturated Paramagnetic Co-OH Complexes. *Angew. Chemie Int. Ed.* **1999**, *38*, 666–669.
(95) Oswald, V. F.; Lee, J. L.; Biswas, S.; Weitz, A. C.; Mittra, K.; Fan, R.; Li, J.; Zhao, J.; Hu, M. Y.; Alp, E. E.; Bominaar, E. L.; Guo, Y.; Green, M. T.; Hendrich, M. P.; Borovik, A. S. Effects of Noncovalent Interactions on High-Spin Fe(IV)–Oxido Complexes. *J. Am. Chem. Soc.* **2020**, *142*, 11804–11817.
(96) MacBeth, C. E.; Golombek, A. P.; Young, V. G.; Yang, C.; Kuczera, K.; Hendrich, M. P.; Borovik, A. S. O_2 Activation by Nonheme Iron Complexes: A Monomeric Fe(III)–Oxo Complex Derived From O_2. *Science* **2000**, *289* (5481), 938–941.
(97) MacBeth, C. E.; Gupta, R.; Mitchell-Koch, K. R.; Young, V. G.; Lushington, G. H.; Thompson, W. H.; Hendrich, M. P.; Borovik, A. S. To Stabilize M−O(H) Units: Synthesis and Properties of Monomeric Iron and Manganese Complexes with Terminal Oxo and Hydroxo Ligands. *J. Am. Chem. Soc.* **2004**, *126*, 2556–2567.
(98) Shirin, Z.; Hammes, B. S.; Young, V. G.; Borovik, A. S. Hydrogen Bonding in Metal Oxo Complexes: Synthesis and Structure of a Monomeric Manganese(III)−Oxo Complex and Its Hydroxo Analogue. *J. Am. Chem. Soc.* **2000**, *122*, 1836–1837.
(99) Lacy, D. C.; Gupta, R.; Stone, K. L.; Greaves, J.; Ziller, J. W.; Hendrich, M. P.; Borovik, A. S. Formation, Structure, and EPR Detection of a High Spin Fe^{IV}−Oxo Species Derived from Either an Fe^{III}−Oxo or Fe^{III}−OH Complex. *J. Am. Chem. Soc.* **2010**, *132*, 12188–12190..
(100) Parsell, T. H.; Behan, R. K.; Green, M. T.; Hendrich, M. P.; Borovik, A. S. Preparation and Properties of a Monomeric Mn(IV)-Oxo Complex. *J. Am. Chem. Soc.* **2006**, *128*, 8728–8729.
(101) Taguchi, T.; Stone, K. L.; Gupta, R.; Kaiser-Lassalle, B.; Yano, J.; Hendrich, M. P.; Borovik, A. S. Preparation and Properties of an MnIV-Hydroxide Complex: Proton and Electron Transfer at a Mononuclear Manganese Site and Its Relationship to the Oxygen Evolving Complex within Photosystem II. *Chem. Sci.* **2014**, *5*, 3064–3071.
(102) Gupta, R.; Taguchi, T.; Borovik, A. S.; Hendrich, M. P. Characterization of Monomeric Mn(II/III/IV)-Hydroxo Complexes from X- and Q-Band Dual Mode Electron Paramagnetic Resonance (EPR) Spectroscopy. *Inorg. Chem.* **2013**, *52*, 12568–12575.
(103) Gupta, R.; Taguchi, T.; Lassalle-Kaiser, B.; Bominaar, E. L.; Yano, J.; Hendrich, M. P.; Borovik, A. S. High-Spin Mn–Oxo Complexes and Their Relevance to the Oxygen-Evolving Complex within Photosystem II. *Proc. Natl. Acad. Sci.* **2015**, *112*, 5319–5324.

(104) Shook, R. L.; Gunderson, W. A.; Greaves, J.; Ziller, J. W.; Hendrich, M. P.; Borovik, A. S. A Monomeric MnIII−Peroxo Complex Derived Directly from Dioxygen. *J. Am. Chem. Soc.* **2008**, *130*, 8888–8889.
(105) Shook, R. L.; Peterson, S. M.; Greaves, J.; Moore, C.; Rheingold, A. L.; Borovik, A. S. Catalytic Reduction of Dioxygen to Water with a Monomeric Manganese Complex at Room Temperature. *J. Am. Chem. Soc.* **2011**, *133*, 5810–5817.
(106) Lucas, R. L.; Zart, M. K.; Murkerjee, J.; Sorrell, T. N.; Powell, D. R.; Borovik, A. S. A Modular Approach toward Regulating the Secondary Coordination Sphere of Metal Ions: Differential Dioxygen Activation Assisted by Intramolecular Hydrogen Bonds. *J. Am. Chem. Soc.* **2006**, *128*, 15476–15489.
(107) Park, Y. J.; Ziller, J. W.; Borovik, A. S. The Effects of Redox-Inactive Metal Ions on the Activation of Dioxygen: Isolation and Characterization of a Heterobimetallic Complex Containing a MnIII–(μ-OH)–CaII Core. *J. Am. Chem. Soc.* **2011**, *133*, 9258–9261.
(108) Lacy, D. C.; Park, Y. J.; Ziller, J. W.; Yano, J.; Borovik, A. S. Assembly and Properties of Heterobimetallic Co(II/III)/Ca(II) Complexes with Aquo and Hydroxo Ligands. *J. Am. Chem. Soc.* **2012**, *134*, 17526–17535.
(109) Park, Y. J.; Cook, S. A.; Sickerman, N. S.; Sano, Y.; Ziller, J. W.; Borovik, A. S. Heterobimetallic Complexes with M^{III}-(μ-OH)-M^{II} Cores (M^{III} = Fe, Mn, Ga; M^{II} = Ca, Sr, and Ba): Structural, Kinetic, and Redox Properties. *Chem. Sci.* **2013**, *4*, 717–726.
(110) Sano, Y.; Lau, N.; Weitz, A. C.; Ziller, J. W.; Hendrich, M. P.; Borovik, A. S. Models for Unsymmetrical Active Sites in Metalloproteins: Structural, Redox, and Magnetic Properties of Bimetallic Complexes with M^{II}-(*μ*-OH)-Fe^{III} Cores. *Inorg. Chem.* **2017**, *56*, 14118–14128.
(111) Lau, N.; Sano, Y.; Ziller, J. W.; Borovik, A. S. Modular Bimetallic Complexes with a Sulfonamido-Based Ligand. *Dalt. Trans.* **2018**, *47*, 12362–12372.
(112) Sano, Y.; Weitz, A. C.; Ziller, J. W.; Hendrich, M. P.; Borovik, A. S. Unsymmetrical Bimetallic Complexes with M^{II}–(*μ*-OH)–M^{III} Cores ($M^{II}M^{III}$ = $Fe^{II}Fe^{III}$, $Mn^{II}Fe^{III}$, $Mn^{II}Mn^{III}$): Structural, Magnetic, and Redox. *Inorg. Chem.* **2013**, *52*, 10229–10231.
(113) Lee, J. L.; Oswald, V. F.; Biswas, S.; Hill, E. A.; Ziller, J. W.; Hendrich, M. P.; Borovik, A. S. Stepwise Assembly of Heterobimetallic Complexes: Synthesis, Structure, and Physical Properties. *Dalt. Trans.* **2021**, *50*, 8111–8119.
(114) Lee, J. L.; Biswas, S.; Sun, C.; Ziller, J. W.; Hendrich, M. P.; Borovik, A. S. Bioinspired Di-Fe Complexes: Correlating Structure and Proton Transfer over Four Oxidation States. *J. Am. Chem. Soc.* **2022**, *144*, 4559–4571.
(115) Jones, J. R.; Ziller, J. W.; Borovik, A. S. Modulating the Primary and Secondary Coordination Spheres within a Series of CoII-OH Complexes. *Inorg. Chem.* **2017**, *56*, 1112–1120.
(116) Oswald, V. F.; Weitz, A. C.; Biswas, S.; Ziller, J. W.; Hendrich, M. P.; Borovik, A. S. Manganese−Hydroxido Complexes Supported by a Urea/Phosphinic Amide Tripodal Ligand. *Inorg. Chem.* **2018**, *57*, 13341–13350.
(117) Barman, S. K.; Jones, J. R.; Sun, C.; Hill, E. A.; Ziller, J. W.; Borovik, A. S. Regulating the Basicity of Metal−Oxido Complexes with a Single Hydrogen Bond and Its Effect on C−H Bond Cleavage. *J. Am. Chem. Soc.* **2019**, *141*, 11142–11150.
(118) Oswald, V. F. Tripodal Phosphoryl Amide Frameworks: Investigating The Relationship Between High Valent Metal–Oxido And Metal–Hydroxido Complexes, University of California, Irvine, 2018.

Chapter 2: Preparation, properties, and reactivity of a paramagnetic Co^{III}–OH complex

Introduction

Metal hydroxido (M–OH) species are important intermediates in both biological and synthetic systems for the functionalization of external substrates.[1–8] Biological systems utilize M–OH moieties in both heme and non-heme environments to activate C–H bonds, halogenate substrates, and hydroxylate carbon-centered radicals.[9,10] The ability of biological systems to access reactive intermediates, such as M–O(H) species, is frequently attributed to tight regulation within the active site.[11,12] This control extends to both the primary (1º) coordination sphere, which consists of ligands directly bound to the metal ion(s) in the active site, and to the secondary (2º) coordination sphere, which includes non-covalent interactions such as electrostatic effects, hydrogen–bonds (H–bonds), and pi–stacking interactions. Because these M–OH intermediates are highly reactive, it is difficult to characterize and study these species in their biological environments. To meet this challenge, scientists have targeted synthetic systems to model the properties and reactivity of proposed M–OH species; however, the acidic nature of the O–H bond in high-valent ($M^{III,IV}$) M–OH complexes makes it difficult to synthesize and isolate these reactive species.[13,14]

The Borovik Lab has addressed the challenges associated with stabilizing high-valent M–O(H) complexes through the design of multidentate ligands that regulate both the 1º and 2º coordination spheres to promote chemistry.[15] The core design feature is a tris(2-aminoethyl)amine (tren) backbone, which provides four N-donors to the metal center to coordinate to a metal ion in a tetradentate fashion. The 1º amines of the tren backbone are readily derivatized to incorporate functional groups that provide intramolecular 2º sphere interactions, primarily H–bond donor or acceptor groups. Following functionalization of the tren platform, the pre-ligand can be deprotonated and subsequently metallated. Deprotonation provides three anionic N-donor atoms capable of binding a metal ion and supporting high-spin, high-valent metal centers. The tren motif enforces local C_3 symmetry and further favors high-spin states. Chelation of a metal ion results in formation of a well-defined, rigid tripodal complex with a fifth coordination site available to bind an exogenous ligand in proximity to the 2º sphere functional groups of the tripodal ligand, facilitating formation of intramolecular H–bonds. For example, *N,N′,N″*-[nitrilotris(ethane-2,1-diyl)]tris(*tert*-butylureaylato) incorporates ureayl functional

groups to act as H–bond donors and has been found to support high-valent M–O(H) complexes (Fig 2-1, $[H_3buea]^{3-}$, left).[16] Similar C_3 symmetric ligand frameworks have been designed to incorporate H–bond accepting groups, such as (*N,N′,N″*-[nitrilotris(ethane-2,1-diyl)]tris(P,P-diphenylphosphinic amido)) $[poat]^{3-}$ (Fig 2-1, middle)[17] and *N,N′,N″*-[2,2',2"-nitrilotris(ethane-2,1-diyl)]-tris-({R-Ph}-sulfonamido), $[RST]^{3-}$ where R is a substituted aryl ring (Fig 2-1, right).[18–20] Note that $[poat]^{3-}$ features phosphinic amido groups within the 2º coordination sphere while $[RST]^{3-}$ features substituted aryl sulfonamido groups.

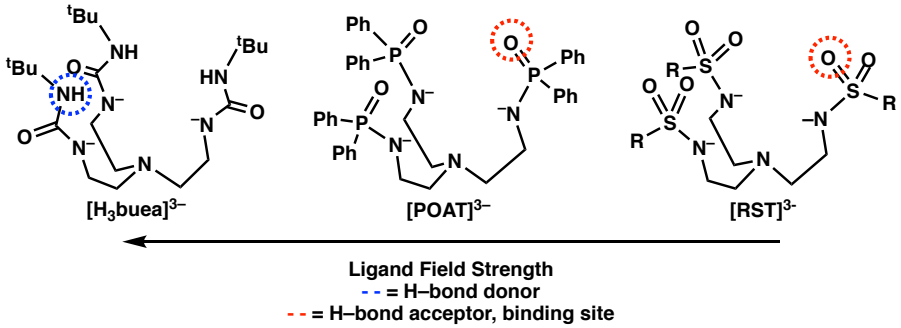

Figure 2-1: Examples of C_3 symmetric tripodal ligand frameworks featuring either H–bond donating or accepting groups.

While the three aforementioned ligand frameworks have supported M–OH complexes, none of the 2º coordination spheres are optimally designed to favor M–OH species. $[H_3buea]^{3-}$ provides H–bond donating groups to the O-atom of the HO^- unit but cannot interact with the O–H bond. Conversely, $[poat]^{3-}$ and $[RST]^{3-}$ accept a H–bond from the proton of the HO^- unit but cannot H–bond with the O-atom. To optimize the H-bond interactions for a M–OH unit, the Borovik Lab designed "hybrid" unsymmetric tripodal ligand frameworks to allow for selective modification of one of the tripod arms (Figs 2-2, 2-3). Two of the most notable examples include $[H_2tol]^{3-}$ (Fig 2-2)[21] and $[H_2pout]^{3-}$ (Fig 2-3, *vide infra*).[22] Both $[H_2tol]^{3-}$ and $[H_2pout]^{3-}$ have 2º coordination spheres that incorporate two H–bond donors from the ureayl arms and one H–bond accepting group from a phosphinic amido or sulfonamido donor. This unsymmetric cavity is optimized to support M–OH units, by donating two H–bonds to the hydroxido oxygen while providing one H–bond acceptor to interact with the hydroxido proton.

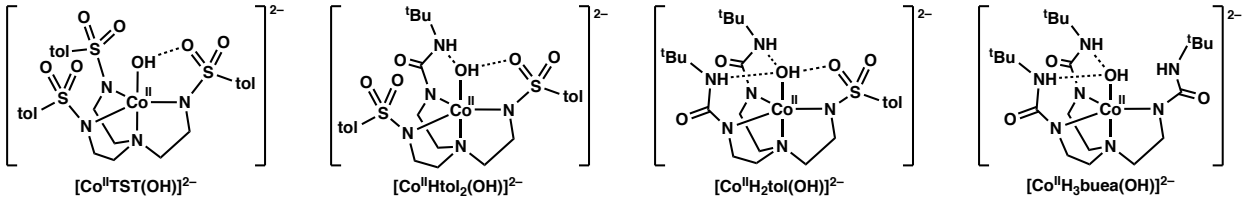

Figure 2-2: A series of Co^{II}–OH complexes supported by unsymmetric, hybrid ligand frameworks. The number of sulfonamido and ureayl donors in the ligands are varied across the series.

In a 2017 paper, the hybrid ureayl-sulfonamido ligand frameworks described above were used to prepare a series of Co^{II}–OH complexes with an eye towards investigating the differences in the 1º coordination sphere donor strength between deprotonated sulfonamido and deprotonated ureayl N-donors (Fig 2-2).[21] In the electronic absorption spectra of these compounds, a low energy *d–d* band was found to be sensitive to equatorial ligand donor strength. Systematically increasing the number of deprotonated ureayl donors resulted in a shift of the *d–d* band to higher energy, confirming that ureayl groups are stronger 1º coordination sphere donors than sulfonamido donors, a claim that was supported by additional spectroscopic data. Furthermore, the prepared Co^{II}–OH metal complexes were treated with a chemical oxidant to determine if the Co^{III}–OH species could be accessed. By following these reactions spectroscopically, it was found that decreasing the number of ureayl donor arms destabilized the oxidized Co^{III}–OH species. The $[Co^{III}H_3buea(OH)]^-$ analogue was stable enough to crystallographically characterize, while Co^{III}–OH units coordinated by ligands that contain sulfonamido group(s) were destabilized and molecular structures could not be obtained. This finding was consistent with previous work on the $[RST]^{3-}$ framework, which has shown that sulfonamido based systems do not support metals in oxidation states beyond +3.[19,23–27] Given the desire to access more highly oxidized metal complexes, the more donating $[poat]^{3-}$ ligand was designed and prepared.

In contrast to $[RST]^{3-}$, $[poat]^{3-}$supports more highly oxidized metal centers. Previous work from the Borovik lab has shown that $[poat]^{3-}$ can support metal oxidation states up to +4.[17,28] The phosphinic amido donor arms featured in $[poat]^{3-}$ have also been incorporated into a hybrid ligand framework, $[H_2pout]^{3-}$ (Fig 2-3).[22] As stated above, $[H_2pout]^{3-}$ is optimized in the 2º coordination sphere to support M–OH complexes with a more strongly donating H–bond donor arm, suggesting that $[H_2pout]^{3-}$ may be employed to access higher valent M–OH. Bolstering this premise, previous work utilized $[H_2pout]^{3-}$ to prepare a series of Mn–OH

complexes, spanning oxidation states between Mn^{II-IV}. This work employs $[H_2pout]^{3-}$ to support Co–OH metal complexes and study their reactivity.

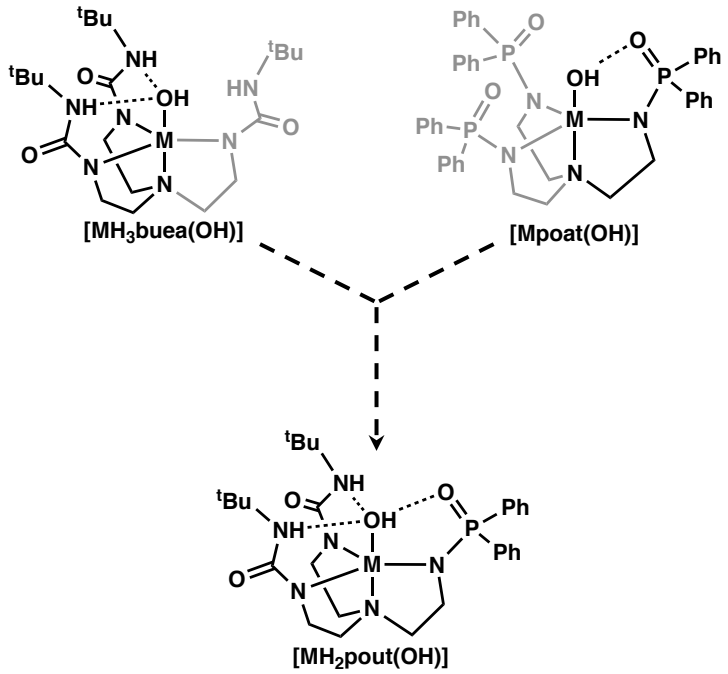

Figure 2-3: Design scheme of the hybrid ligand framework $[H_2pout]^{3-}$.

My specific interest in Co–OH systems stems from their suggested role as reactive intermediates in a variety of chemical reactions. High-valent Co species have been implicated as the competent oxidants in an array of reactions, including synthetic water oxidation catalysis[29–37] and C–H bond activation.[38–43] Co^{IV}–O moieties are most commonly invoked in these processes, because of the presumed stability of low-spin Co^{III} species.[44] While the stability of Co^{III} species may be apparent for six–coordinate compounds, examples from the Anderson and the Borovik groups suggest that Co^{III} complexes in coordinatively unsaturated environments could be more reactive.[16,21,41,45] Work within the Anderson group focused on the pK_a driven asynchronous C–H bond activation reactivity of a four-coordinate Co^{III}–O, while work within the Borovik group has shown that terminal, five-coordinate Co^{III}–OH species appear to be unstable.[16,21,24] To date there are only six examples of structurally characterized, mononuclear Co^{III}–OH complexes (Fig 2-4).[16,41,46–50] The rareness of this type of structure suggests the Co^{III}–OH unit may be inherently unstable, possibly due to the acidity of the O–H bond.

The instability of the Co^{III}–OH species could be redirected towards productive chemistry within the correct ligand framework.

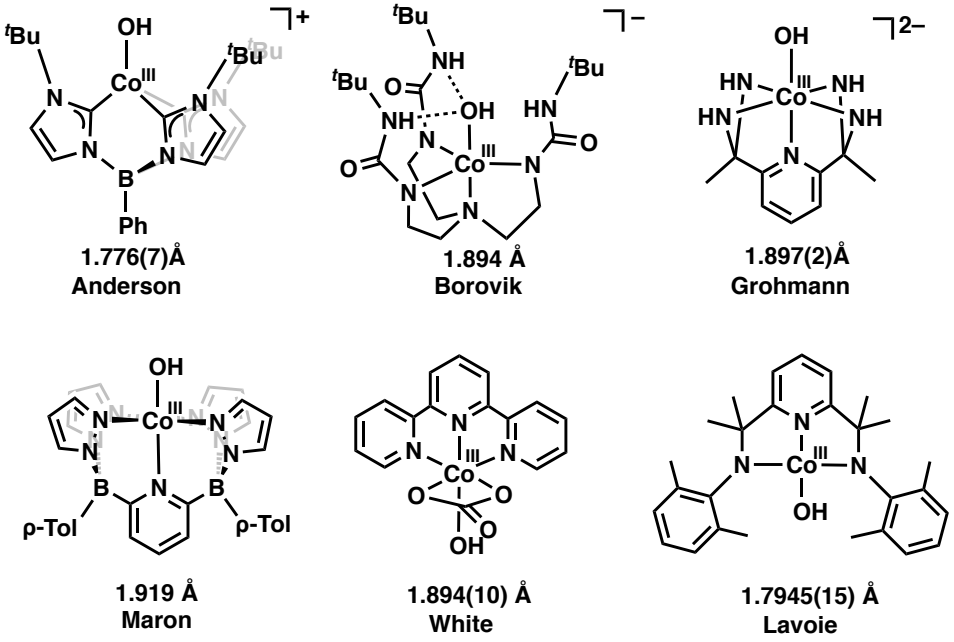

Figure 2-4: Representations of the 6 structurally characterized Co^{III}–OH species.

This chapter describes efforts taken to prepare and characterize $Co^{II/III}$–OH complexes supported by the $[H_2pout]^{3-}$ ligand. The reactivity of the Co^{III}–OH complexes towards external substrates is further examined. To the best of our knowledge, the ability of Co^{III}–OH complexes to perform X–H bond activation has yet been reported.

Results and Discussion

Synthesis and Characterization of $K_2[Co^{II}H_2pout(OH)]$, (K_2[**1**])

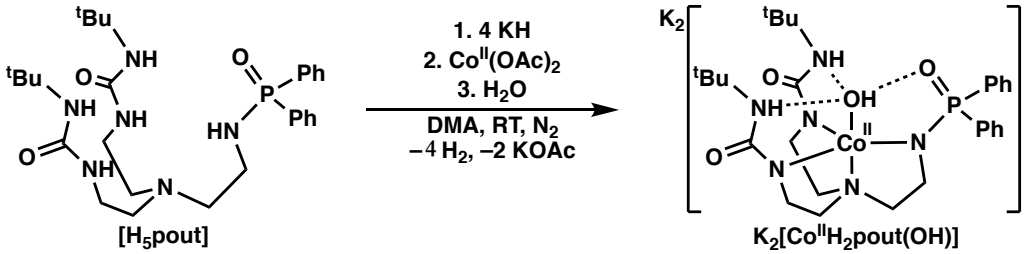

Scheme 2-1: Preparation of K_2[**1**].

Synthesis: $K_2[Co^{II}H_2pout(OH)]$ (K_2[**1**]) was prepared following literature procedures for the synthesis of the Mn analogue, $K_2[Mn^{II}H_2pout(OH)]$ (Scheme 2-1).[22] H_5pout was suspended and stirred in *N,N′*-dimethylacetamide

(DMA) in the presence of four equivalents of potassium hydride (KH), to ensure full deprotonation of the equatorial N–donor atoms and deprotonate one of the 2º coordination sphere urea groups. This strategy provided an internal basic site for preparation of the $^{-}$OH ligand in a future step. Following deprotonation of the ligand, $Co^{II}(OAc)_2$ was added to the reaction and stirred until a purple solution formed. Then one equivalent of degassed water was added directly into solution, yielding a new pink-purple color. The addition of water lends to its being deprotonated by the internal basic site to form a hydroxido ligand, which causes reprotonation of urea NH groups within the 2º coordination sphere. The reaction was filtered and subsequently diluted with DMA until any cloudiness dissipated. Single crystals suitable for X-ray diffraction (XRD) studies were subsequently grown by vapor diffusion of Et_2O into the filtrate.

Structural Properties: The molecular structure of K_2[**1**] revealed a five-coordinate Co-complex in a trigonal bipyramidal (TBP) coordination geometry with a τ_5 value of 0.92 (Fig 2-5, A and C; Table 2-1).[51] The 1º coordination sphere is made up of four N-atom donors from the $[H_2pout]^{3-}$ ligand and an exogenous O-atom, derived from the hydroxido ligand. The bond lengths within the 1º coordination sphere are similar to previously published Co^{II}–OH molecules in TBP geometries.[16,21,24,52] The H-atoms associated with N5, N6, and O1 were all located in the Fourier-difference map and the molecular structure reveals the formation of two intramolecular H–bonds, with the hydroxido ligand acting as a H–bond acceptor (O1···N5 = 2.707(2), O1···N6 = 2.927(2), Table 1). Based on the ligand design concept, a third intramolecular H–bond was expected to be present between the hydroxido ligand (O1) and the phosphinic amido O-atom (O2); however in the solid state one K^+ counterion (K1) interacts with both O1 and O2, blocking the formation of the intramolecular H–bonding interaction. A similar structural motif was observed in the isomorphous Mn^{II} and Fe^{II}–OH analogues.[22,53,54] In addition to the intramolecular interactions of the K^+ counterions with O1 and O2, the K^+ counterions also interacted with the ligand O-atoms from nearby $[\mathbf{1}]^{2-}$ molecules forming extensive intermolecular interactions in the solid state.

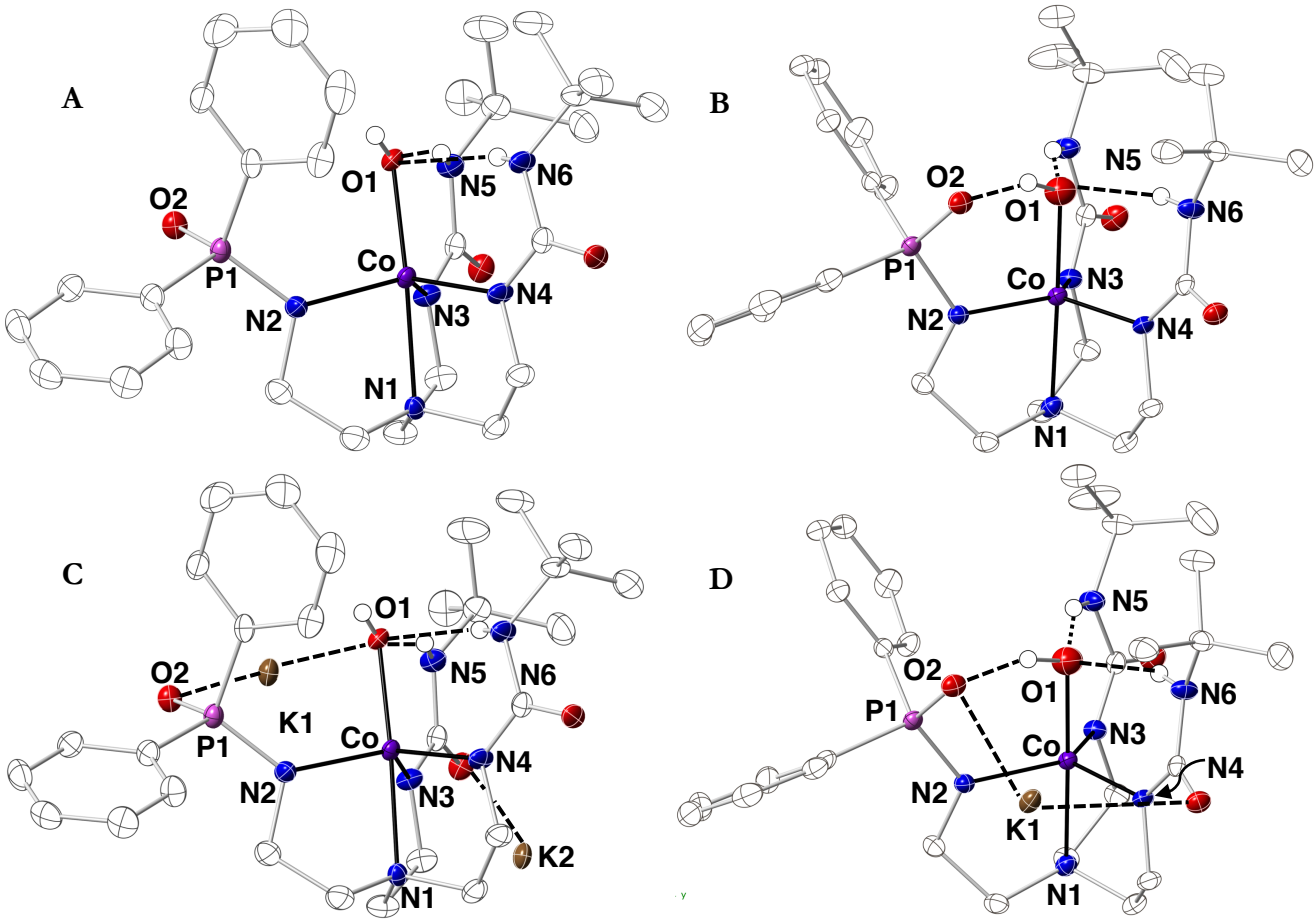

Figure 2-5: Thermal ellipsoid diagrams of K_2[**1**] and K[**2**]. In **A** and **B**, structural solvent molecules and K^+ counterion(s) were omitted for clarity. **C** and **D** incorporate the K^+ counterion(s) to demonstrate their interactions in the solid state. Thermal ellipsoids are drawn at 50% probability and only hydroxido ligand and urea protons are

Table 2-1: Metrical data from the molecular structures of K_2[**1**] and K[**2**].

	Distance, 1 (Å)	**Distance, 2 (Å)**
Co1–O1	2.020(1)	1.895(1)
Co1–N1	2.217(2)	2.014(1)
Co1–N2	2.120(2)	1.978(1)
Co1–N3	2.108(2)	1.944(1)
Co1–N4	2.035(2)	1.952(1)
O1···N5	2.707(2)	2.606(2)
O1···N6	2.927(2)	2.668(2)
O1···O2	3.856(2)	2.749(2)
O1···K1	2.700(2)	3.944(2)
	Angles, 1 (º)	**Angles, 2 (º)**
N1–Co1–O1	171.66(6)	178.72(6)
N2–Co1–N3	121.01(7)	124.23(6)
N2–Co1–N4	113.63(7)	112.80(6)
N3–Co1–N4	116.73(7)	120.76(6)
	τ_5* = 0.92	τ_5* = 0.91

* τ_5 is the trigonality structural parameter. α and β are the two largest angles in the molecule. $\tau_5 = (\beta - \alpha)/60°$

Spectroscopic Characterization: The electronic and magnetic properties of K_2[**1**] were characterized using electronic absorption (UV-vis), attenuated total reflectance-Fourier transform infrared (ATR-FTIR), and electron paramagnetic resonance (EPR) spectroscopies, respectively. K_2[**1**] is weakly colored and exhibits low-energy, low-intensity features arising from *d–d* transitions at λ_{max} [nm(ε, $M^{-1}cm^{-1}$)] = 491 (185), 524 (180), 583 (75), 753 (44) (Fig 2-6, A), consistent with previous Co^{II} complexes in TBP environments and specific to Co^{II} ions in C_3 symmetric ligand fields.[16,21,24,55,56] The lowest energy band in these systems, between 700 and 900 nm, arises from a $^4A_1 \longrightarrow {}^4E$ transition and can be used to evaluate the donor atom strength for ligands coordinated in the equatorial plane.[21] In previous work, the ligand field strength was evaluated using a σ-only approach and it was found that for stronger donor atoms, such as deprotonated ureayl donors, this low energy feature shifted to higher energies. In comparison to the low energy band arising from $[Co^{II}H_2tol(OH)]^{2-}$ and $[Co^{II}H_3buea(OH)]^{2-}$ (Fig 2-2, *vide supra*), the 753 nm transition of K_2[**1**] falls in between the two, further bolstering claims that deprotonated phosphinic amido donors are stronger than the sulfonamido counterparts but weaker than the ureayl donors (Table 2-2).

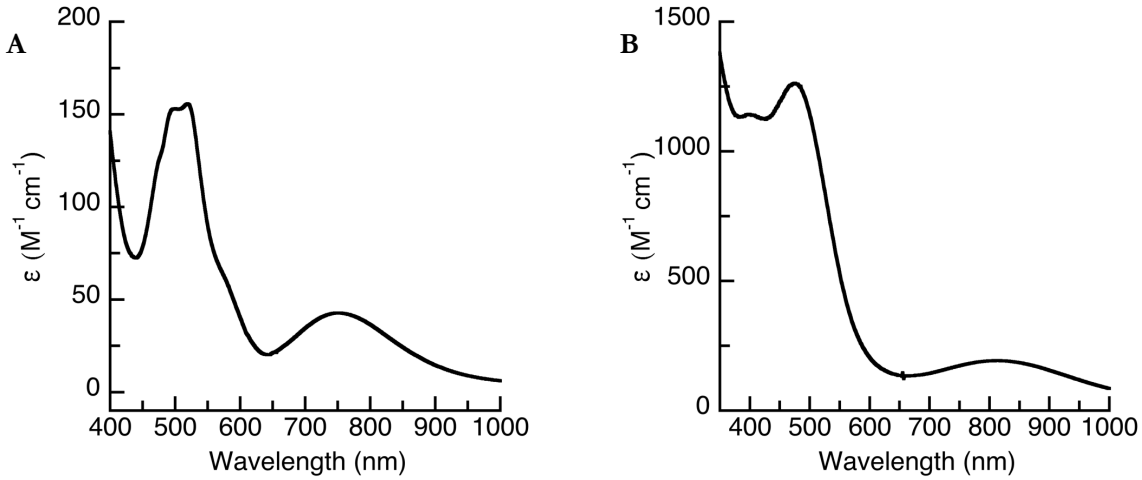

Figure 2-6: Electronic absorption spectrum of K_2[**1**] (**A**) and K[**2**] (**B**) in DMSO at 25 ºC.

Table 2-2: Comparison of physical data across a series of Co^{II}–OH complexes with varying ligand fields. Refer to Figure 2-2 for the structure of these compounds.

Compound	λ_{max}(nm)	ν_{O-H}, (cm^{-1})	Co–O1 (Å)
$[Co^{II}TST(OH)]^{2-}$	890	3574	1.935(4)
$[Co^{II}Htol_2(OH)]^{2-}$	820	3602, 3581	——
$[Co^{II}H_2tol(OH)]^{2-}$	767	3625	2.015(2)
$[Co^{II}H_2pout(OH)]^{2-}$	753	3640	2.020(1)
$[Co^{II}H_3buea(OH)]^{2-}$	710	N/A	2.051(4)

K_2[**1**] was further examined by solid-state ATR-FTIR spectroscopy. **1** exhibited an O–H vibration at 3640 cm^{-1}, consistent with literature examples of M^{II}–OH vibrations, and N–H vibrations at 3230 and 3130 cm^{-1} (Fig 2-7, black).[21,22,24] The $\boldsymbol{\nu}_{O-H}$ vibration of K_2[**1**] was noticeably sharp, likely due to a free O–H vibration rather than a H–bonded one. In the solid-state molecular structure of **1**, the HO^- ligand is not H–bonded to the P=O oxygen atom due to interaction between a K^+ counterion and the P=O group. The disruption of the H–bonding network in K_2[**1**] complicates direct comparison of the O–H vibration with the aforementioned series of Co^{II}–OH complexes because the shape and width of the O–H vibration is significantly different (Table 2-2).[21]

The energy of the O–H vibrations can be compared and further correlated to the Co–O1 bond length. In the sulfonamido-ureayl hybrid series (Fig 2-2), the Co–O1 bond length increased as the number of ureayl donor arms increased, where $[Co^{II}H_3buea(OH)]^{2-}$ had the longest bond and $[Co^{II}TST(OH)]^{2-}$ the shortest. Deprotonated ureayl ligands were determined to be stronger than the sulfonamido ligands, effectively providing a more electron rich ligand field. It can therefore be extrapolated that Co^{II} ions supported by stronger ligand fields, such as ureayl donors, are more electron-rich. Consequently, Co^{II} ions in more strongly donating, electron-rich fields would likely withdraw less electron density from an exogenous hydroxido ligand and have a longer, weaker Co–O bond. The weakening of the Co–O bond leads to a complementary strengthening of the O–H bond, shifting the O–H bond vibration to higher energy. This trend was empirically observed and correlated once again with the σ-only approach to the ligand field analysis discussed above. $[Co^{II}TST(OH)]^{2-}$ exhibited the shortest Co–O1 bond length and the weakest, lowest energy O–H vibration. $[Co^{II}H_3buea(OH)]^{2-}$ had the longest Co–O1 bond length, but did not

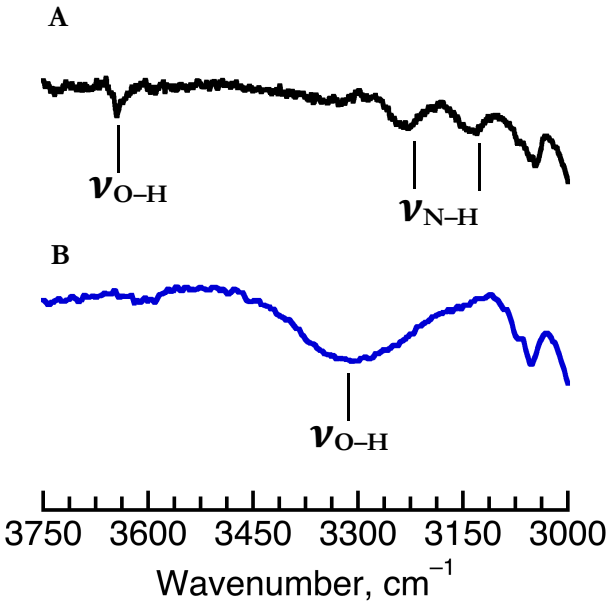

Figure 2-7: ATR-FTIR data collected on solid samples of K_2[**1**] (**A**) and K[**2**] (**B**).

exhibit an O–H bond vibration. The lack of vibration has previously been attributed to the H–bond donation from the ureayl functional groups, however an increase in the O–H bond strength due to the ligand field may play a role in its apparent absence. Further evaluation would be needed to confirm this hypothesis, as this analysis does not take into account variations in the H–bonding networks which has a significant effect on bond length and vibration. Finally, the structural and vibrational data collected from $[Co^{II}H_2pout(OH)]^{2-}$ followed the proposed qualitative trend of ligand field strength which supported that phosphinic amido donors are stronger than sulfonamido donors but weaker than ureayl donors.

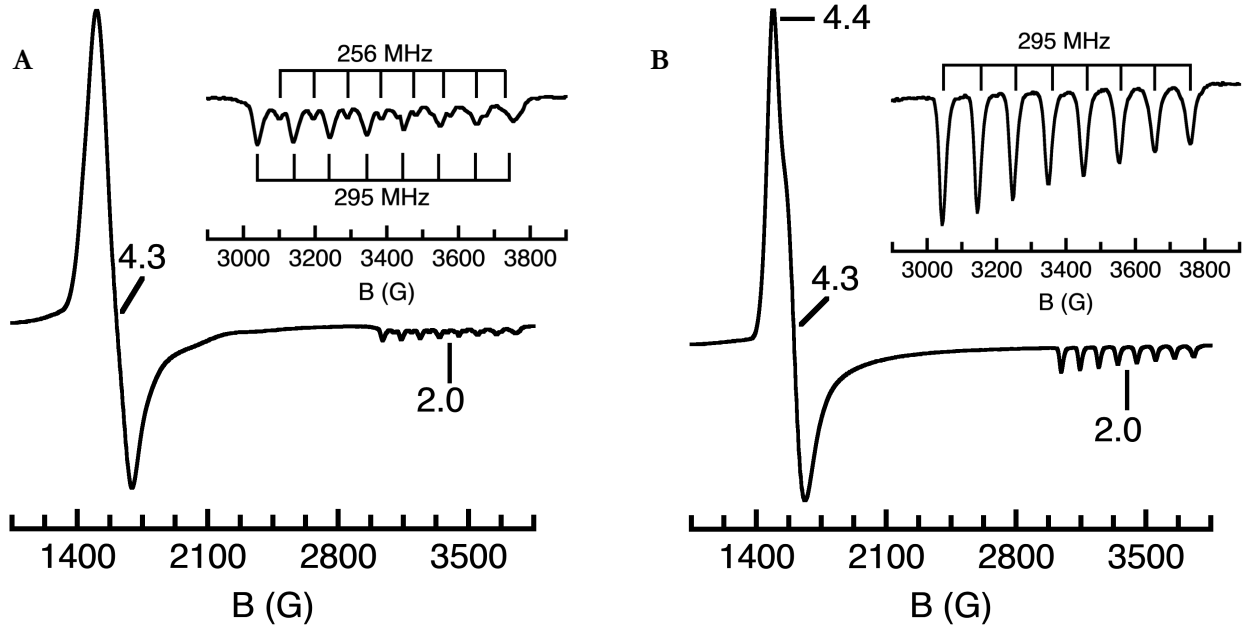

Figure 2-8: ⊥-mode EPR spectra of 10 mM solutions of K_2[**1**] in DCM:THF, recorded at 12 K. **A** was collected without the use of any 18c6 while **B** was measured in the presence of excess 18c6.

The perpendicular-mode (⊥-mode) EPR spectrum of K_2[**1**] showed a derivative signal at g = 4.3 and a high-field feature at g = 2.0 (Fig 2-8, A). The feature at g = 2.0 is split by hyperfine from the nuclear spin active ^{59}Co nucleus (I = 7/2). Two sets of 8-line hyperfine patterns were observed, which suggested that there may be multiple species in solution. Given how K_2[**1**] was found to interact with the K^+ counterions in the solid state, forming both intra- and intermolecular interactions, it is possible that crystalline K_2[**1**] did not fully dissociate into separate units of [**1**]$^{2-}$ in solution but rather the intermolecular interactions between multiple equivalents of K_2[**1**] remained intact. To probe this idea, 18-crown-6 ether (18c6) was added as an encapsulating reagent for the K^+ ions. The EPR spectrum then appeared sharper and more intense and only one set of ^{59}Co

hyperfine was present at g = 2.0 (Fig 2-8, B). The distinctive 8-line hyperfine pattern imposed on the g = 2.0 feature had a hyperfine coupling constant of A_z = 295 MHz, ^{59}Co. These data were consistent with formation of $[Co^{II}H_2pout(OH)]^{2-}$ complex without K^+ ion ionteractions.[24,57,58] The spectrum was simulated and fit with an E/D value of 0.0069, indicating nearly axial symmetry around the Co center. Additionally, an Evans method room temperature effective magnetic moment was measured to b μ_{eff} = 4.14 μ_B. This value is larger than the theoretical spin-only magnetic moment for three unpaired electrons (μ_s = 3.87 μ_B) likely due to contributions from spin-orbit coupling, which is consistent with other examples of S = 3/2 Co^{II} systems.[59–61]

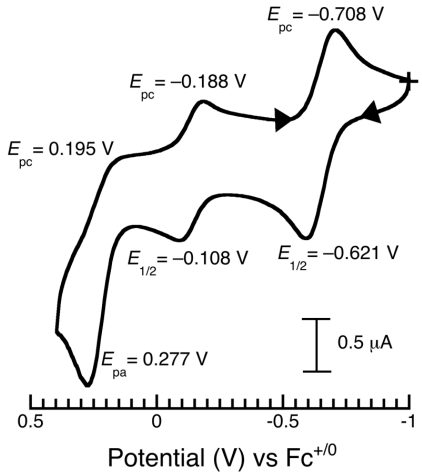

Figure 2-9: Cyclic voltammogram of K_2[**1**] in THF.

Table 2-3: Comparison of oxidative potentials for $Co^{III/II}$–OH in different solvents.

Solvent	E_{pa} (V vs $Fc^{+/0}$)	$E_{1/2}$ (V vs $Fc^{+/0}$)
DMSO	–1.159	–1.204
DCM	–0.779	–0.812
THF	–0.568	–0.621

Electrochemical Properties and Oxidation Studies: The electrochemical properties of K_2[**1**] were investigated by cyclic voltammetry (CV) to determine what potential the corresponding Co^{III}–OH species could be accessed. As discussed in the Introduction, no ligands which incorporated sulfonamido donors could support a Co^{III}–OH complex at room temperature and this species was only observed spectroscopically at lower temperatures.[21] Given that $[H_2pout]^{3-}$ has been previously used in the prepartion of $Mn^{III/IV}$–OH and Fe^{III}–OH complexes, it was hypothesized that a Co^{III}–OH species could also be prepared.[22,53,54] The electrochemical behavior was studied in multiple solvents, including *N,N′*-dimethylsulfoxide (DMSO), dichloromethane (DCM), and tetrahydrofuran (THF), all of which indicated that K_2[**1**] exhibits an oxidation at potentials negative of the ferrocenium/ferrocene ($Fc^{+/0}$) couple (Table 2-3). However, the reversibility of the oxidation and subsequent return reduction varied based on the solvent. K_2[**1**] exhibited a reversible one-electron event at –0.621 V versus $Fc^{+/0}$ in THF, which was assigned as the $Co^{III/II}$–OH couple, as well as two additional oxidative events observed

at $E_{1/2}$ = –0.108, +0.245 V versus $Fc^{+/0}$. The relatively low potential for the $Co^{III/II}$–OH redox couple and its reversibility suggested that a Co^{III}–OH could be accessed through the use of a Fc^{+} salt. Furthermore, the potential of this redox couple as well as literature precedent for previously characterized Co^{II}–OH species in C_3 symmetry suggests that K_2[**1**] could be oxidized by O_2 (E^o, V versus $Fc^{+/0}$ = +1.21, MeCN; +0.60, DMF).[16,57,62,63] Because the CV of K_2[**1**] appeared most reversible in THF, this solvent was chosen for bulk oxidation studies (Fig 2-9).

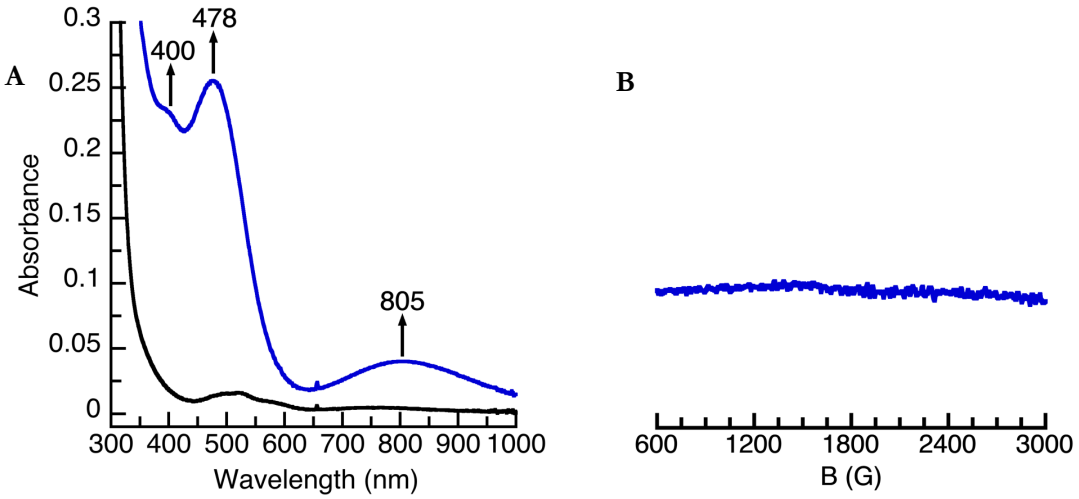

Figure 2-10: Electronic absorption spectra (**A**) and ⊥-mode EPR spectrum (**B**) after reaction of K_2[**1**] with excess O_2 in a 0.4 mM DMSO solution at 25 ºC and 10 mM K_2[**1**] in DCM:THF at 77 K, respectively.

Oxidation of K_2[**1**] with O_2 was studied by UV-vis spectroscopy. The addition of excess O_2 to a solution of K_2[**1**] was followed by electronic absorption spectrscopy. The reaction showed a rapid color change from pink-purple to dark red-orange (blue trace Fig 2-10, A). These bands were consistent in shape and energy with previously characterized Co^{III}–OH complexes.[16,24,57] This reaction was also monitored with ⊥-mode EPR spectroscopy and the resulting product of this reaction was EPR silent, further supporting the proposed assignment of this new species as a Co^{III}–OH complex (Fig 2-10, B). Reaction of K_2[**1**] with an equimolar amount of $FcBF_4$ also gave the same Co^{III}–OH product. Given that the spectroscopic data suggested formation of a Co^{III}–OH species upon reacting K_2[**1**] with an oxidant, bulk synthetic experiments were undertaken to obtain a solid-state molecular structure and confirm the identity of this new species.

Synthesis and Characterization of K[Co^{III}H$_2$pout(OH)] (K[2])

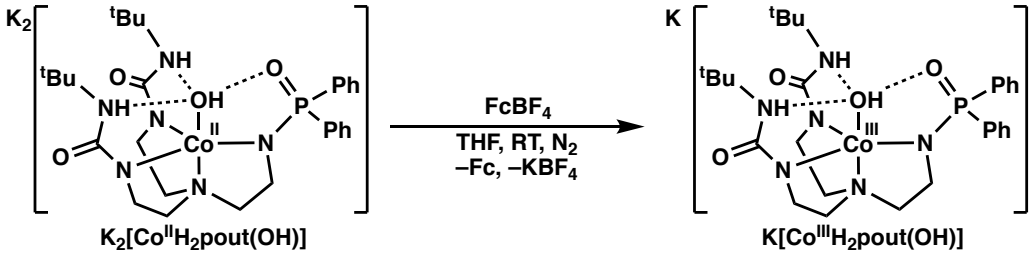

Scheme 2-2: Preparation of K[Co^{III}H$_2$pout(OH)] (K[**2**]).

Synthesis: For bulk syntheses, $FcBF_4$ was chosen as an oxidant over O_2 as it the byproducts of this reaction, such as KBF_4 or Fc, can be removed easily. Additionally, Fc^+ is well known for acting as a mild, one-electron reagent.[64–66]

K_2[**1**] was suspended in THF and treated with one equivalent of $FcBF_4$. Addition of $FcBF_4$ caused an immediate color change, from a purple-pink suspension to a deep red-orange solution. The reaction mixture was dried *in vacuo*. The resulting solid was redissolved in acetonitrile (MeCN) and filtered. The deep red-orange filtrate was recrystallized via vapor diffusion of Et_2O into the mother liquor, resulting in few deep red crystals suitable for XRD studies. It should be noted that despite repeated attempts, the yield of K[**2**] remained consistently low, with less than ~ 10% yields of crystalline materials, if any was obtained.

Structural Properties: Upon oxidation of K_2[**1**] to K[**2**], the TBP coordination geometry about the Co center was preserved (τ_5 = 0.91), with all 1° coordination sphere bond lengths contracted from K_2[**1**] to K[**2**] by ~0.2 Å (Table 2-1, *vide supra*), consistent with oxidation of the Co center. Furthermore, oxidation of the Co center in K[**2**] resulted in the formation of a monoanionic metal complex and loss of one K^+ counterion relative to K_2[**1**], causing a profound change in the 2° coordination sphere (Fig 2-5, B and D, *vide supra*). In the molecular structure of K_2[**1**], K2 interacts with the carbonyl O-atom on one of the urea arms (O3) while K1 interacts directly with the O-atoms from both the hydroxido ligand (O1) and the P=O arm (O2), preventing the formation of an intramolecular H–bond between O1 and O2. In the molecular structure of K[**2**], K1 interacts with the O-atoms from a carbonyl and the P=O arm (O4, O2 respectively) but no longer interacts with the hydroxido ligand (K1···O1 = 3.944(2), Table 2-1). The attenuated interactions between K1 and O1/O2 led to formation of the

H–bonding network around the hydroxido ligand and incorporation of three intramolecular H–bonds, as designed in the $[H_2pout]^{3-}$ framework.

Spectroscopic Characterization: As discussed above, *in situ* oxidation of **1** with $FcBF_4$, a new, deep red-orange species formed with features at λ_{max}, [nm (ε, $M^{-1}cm^{-1}$)] = 400 (sh), 478 (1030), and 805 (171) in DMSO, consistent with previously characterized Co^{III}–OH species in TBP geometry.[16,21,24,57] These features are in good agreement with redissolved solid K[**2**] in DMSO (λ_{max}, nm = 400, 478, 810). The energies of these transitions were consistent between *in situ* generated and isolated solids of K[**2**], however the absorbance values obtained from solutions of redissolved solids were lower than expected based on the molar absorptivity values obtained via *in situ* oxidation. The discrepancy in molar absorptivity was attributed to the isolation of impure solids due to solution instability of K[**2**] producing unknown byproducts during its degradation, most likely some Co^{II} species. Because Co^{II} complexes are typically weakly colored due to low absorbing *d–d* transitions, any residual Co^{II} species would absorb below the baseline of any transitions arising from a Co^{III}–OH complex.

Following oxidation of K_2[**1**] to K[**2**], additional vibrational data was obtained. The $\boldsymbol{\nu}_{O–H}$ vibration was found at 3310 cm^{-1}, shifted to lower energy from the 3640 cm^{-1} O–H vibration exhibited by K_2[**1**], consistent with oxidation of the metal center in K[**2**] (Fig 2-7, *vide supra*). Oxidation of the metal center from Co^{II} to Co^{III} leads to a weakening of the O–H bond, similar to the $[Mn^{III}H_2pout(OH)]^-$ analogue.[22] Additionally, the O–H feature is broader in K[**2**] than in K_2[**1**], consistent with the presence of the H–bonding interaction between the HO^- ligand and the P=O group in the solid state. The energetic shift and broadness of the $\boldsymbol{\nu}_{O–H}$ vibration effectively overlapped with the expected N–H vibrations from the urea ligand backbone, therefore these features could not be identified. As addressed throughout this chapter, solids isolated from the oxidation of K_2[**1**] to K[**2**] were frequently impure. However the vibrational spectrum appeared clean and the identified $\boldsymbol{\nu}_{O–H}$ vibration did not appear in the vibrational spectrum of K_2[**1**] nor in the ligand precursor, H_5pout, which further supports the assignment of the O–H vibration.

K[**2**] was also studied by EPR and was silent in both ⊥- and ∥-modes, suggesting that this species was likely $S = 1$ because of the difficulties associated with detecting $S = 1$ species by X–band EPR spectroscopy.[67] Given how the *d*–orbitals split in pseudo-C_3 symmetric ligand environments (Fig 2-11), d^6 species may take on

either $S = 1$ or 2 spin states. While $S = 2$ spin states can be more readily observed by ǁ-mode EPR spectroscopy than $S = 1$ spin states, integer spin species are frequently challenging to measure. Therefore, an Evans' Method spectrum was collected to confirm the spin state of K[**2**]. A paramagnetic solvent shift was observed and used to calculate an effective magnetic moment: $\mu_{eff} = 2.96\ \mu_B$, consistent with a spin state of $S = 1$ ($\mu_s = 2.83\ \mu_B$). This μ_{eff} value is consistent with literature precedent for $S = 1$ Co^{III} species and further supports the assignment of an $S = 1$ spin state for K[**2**].[16]

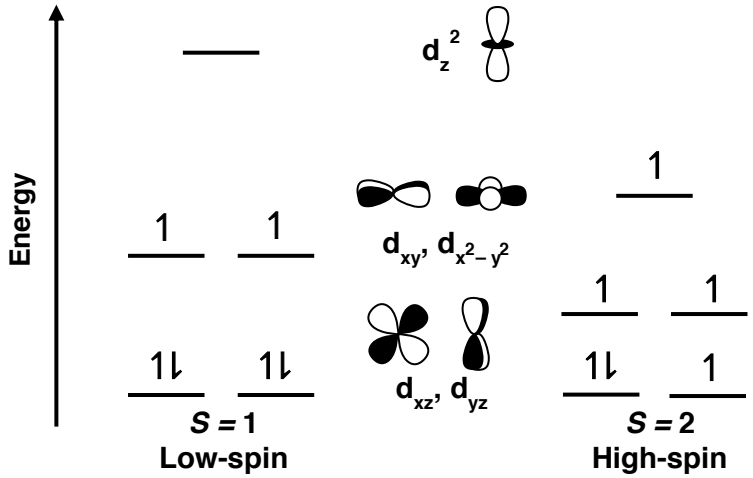

Figure 2-11: Representation of possible spin states for a d^6 metal ion in C_3 ligand environments.

Reactivity of K[$Co^{III}H_2$pout(OH)] Towards External Substrates

Initial Substrates Investigated: Spectroscopic studies of K[**2**] revealed that the Co^{III}–OH species was moderately unstable in solution. This instability was corroborated in initial attempts to crystallize and isolate K[**2**]; bulk reactions performed in less volatile solvents (e.g. DMA) often exhibited notable loss of the signature red-orange color of K[**2**] before solvents could be removed *in vacuo* and no product could be isolated from these syntheses. Further attempts to crystallize K[**2**] ultimately led to isolation of single crystals suitable for XRD studies in poor yield. As discussed above, when bulk solids of K[**2**] were isolated, electronic absorption spectra of the redissolved powder exhibited features with the appropriate wavelengths and shapes, but far lower absorbance values than expected based on the calculated concentration. The solution instability of K[**2**] ($t_{1/2}$ = 10 h, THF) suggested that the Co^{III}–OH moiety may be reactive towards external substrates. In subsequent studies, K[**2**] was screened for its potential to activate O–H and C–H bonds.

To test this hypothesis, different substrates were added to solutions of K[**2**] in DMSO at 25 ºC and monitored via electronic absorbance spectroscopy. The first substrate chosen was 1-hydroxy-2,2,6,6-tetramethylpiperdine (TEMPO–H) due to its weak O–H bond dissociation free energy ($BDFE_{O-H}$, DMSO = 67.5 kcal/mol) and advantageous spectroscopic handles; specifically, if the O–H bond of TEMPO–H is cleaved, TEMPO· forms and is detectable by ⊥-mode EPR spectroscopy.[68] When K[**2**] was treated with TEMPO–H, the resulting spectra showed a loss of features associated with K[**2**] and the generation of a new, weakly absorbing spectrum (λ_{max} = 390, 580 nm, Fig 2-12, A). The feature at 390 nm is consistent with literature examples of TEMPO· species,[69] while the 580 nm band is similar in energy and absorbance to previously characterized Co^{II} complexes and K_2[**1**].[16,21,24,57,59] The reaction was also monitored at 77 K by ⊥-mode EPR spectroscopy, which showed generation of TEMPO· (Fig 2-12, B) and an increase in a signal around g = 4, consistent with an S = 3/2 spin system that arises from a Co^{II} center.

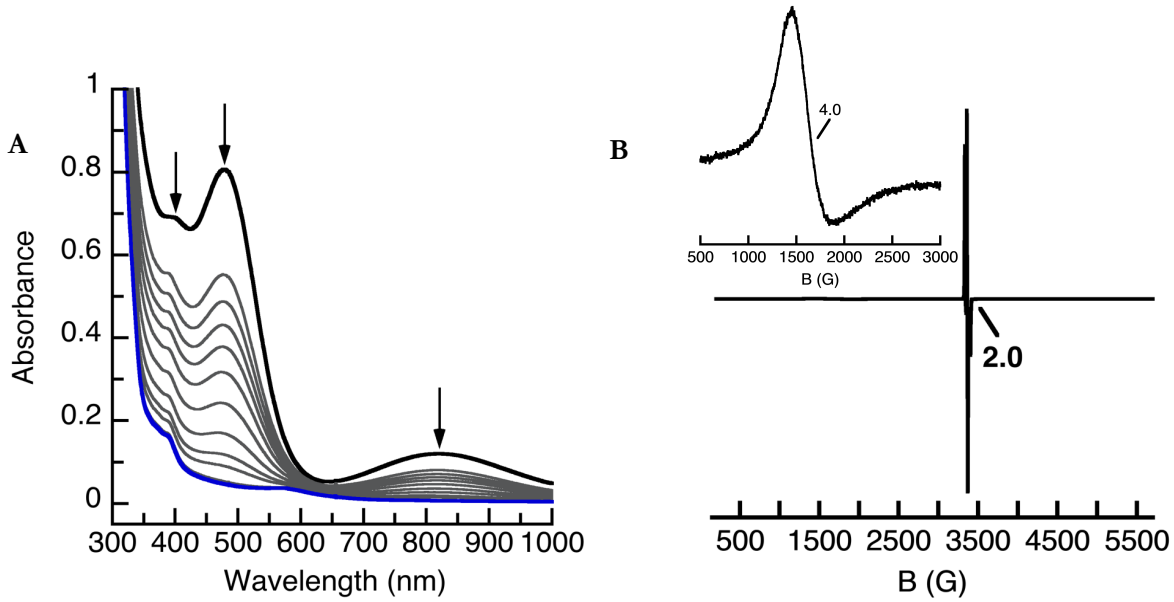

Figure 2-12: (**A**) UV-vis spectra following the loss of K[**2**] at λ = 400, 478 and 805 nm upon reaction with TEMPO–H at room temperature. (**B**) 77 K ⊥-mode EPR collected after the reaction of **2** with TEMPO–H with g = 4.0, 2.0 consistent with the formation of a Co^{II} species and TEMPO· A, ^{14}N = 119 MHz.

The next substrate studied was 9,10-dihydroanthracene (DHA; $BDFE_{C-H}$, DMSO = 76.0 kcal/mol).[68] Cleavage of the weak C–H bond in DHA results in the formation of anthracene, which has sharp and distinctive features in the electronic absorption spectrum between 340-380 nm.[70,71] Addition of excess DHA to K[**2**] resulted in no significant spectral changes at room temperature. The solution was then gently warmed from 25

ºC to 40 ºC. After several hours at elevated temperature, no anthracene bands were observed in the spectra, though there was a loss of the features associated with K[**2**] (Fig 2-13). It could not be definitively concluded whether the spectral changes were due to the reaction of K[**2**] with DHA or the solution instability of K[**2**], though the absence of anthracene formation suggests the latter.

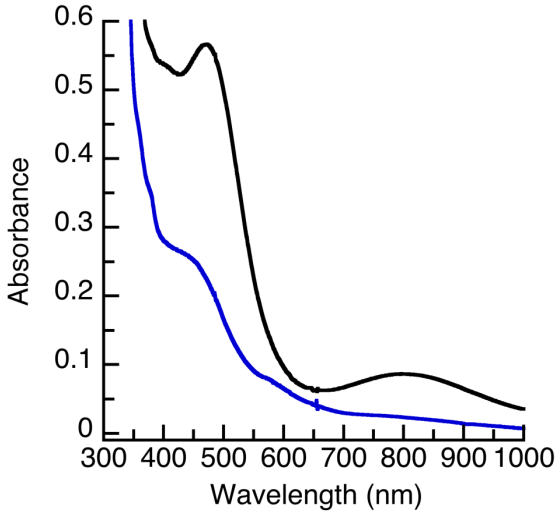

Figure 2-13: Reaction of K[**2**] (black trace) with excess DHA. The initial spectrum was collected at 25 ºC and the final spectrum was collected at 40 ºC (blue).

Reactivity with para-Substituted Phenolic Compounds: Given that K[**2**] was competent to cleave the O–H bond of TEMPO–H but not the C–H bond of DHA, it was decided to pursue kinetic studies with phenolic substrates, which feature O–H bonds. Initially, the kinetics of the reaction between K[**2**] and a series of 4-substituted phenolic substrates was investigated. Varying the substituent at the para position of the phenolic substrates allows the $BDFE_{O–H}$ to be systematically changed. Three phenolic substrates were analyzed (4-OMe, 4-H and 4-Br-phenol; PhOH) under pseudo-first order conditions where K[**2**] was treated with greater than 10 equivalents of substrate. The substrate concentration was varied between ~10 and ~65 equivalents relative to a 0.75 mM solution of K[**2**] in DMSO, which was generated by oxidation of K_2[**1**] with one equivalent of $FcBF_4$ *in situ* and monitored by UV-vis spectroscopy at 25 ºC. The reaction progress was monitored following the decrease in absorbance of the *d–d* band associated with K[**2**] (λ_{max} = 805 nm) and the final spectra from all reactions had bands at λ_{max} = 600, 660 nm. Equation 1 was plotted against the reaction time traces at 805 nm for at least three half-lives of the reaction to obtain the pseudo-first order rate constant, k_{obs}. A_i is the initial absorbance at, A_t is the absorbance at time t, and A is the absorbance at the end of the reaction (Fig 2-14).

Plotting this data yielded a line with a slope consistent with k_{obs} (s^{-1}). The k_{obs} values were plotted against the concentration of substrate and the resulting slope was the second order rate constant, k_2 (Table 2-4).

$$k_{obs} = \ln\left[\frac{(A_t - A_\infty)}{(A_i - A_\infty)}\right] \textbf{ (Equation 2-1)}$$

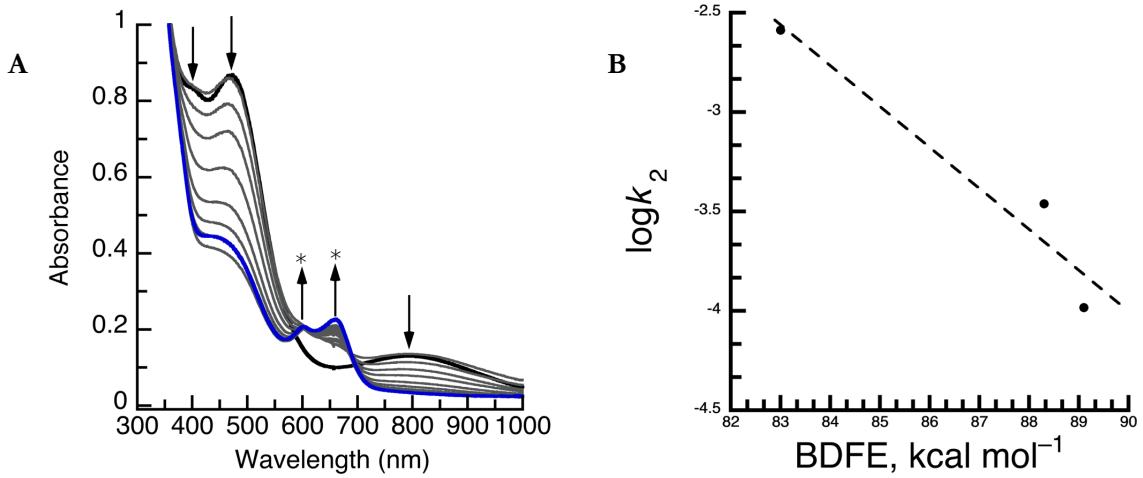

Figure 2-14: (**A**) Addition of excess 4-OMe-PhOH to 0.75 mM solution of K[**2**] in DMSO at 25 °C. New bands were generated at 600 and 660 nm (blue trace, *). (**B**) Plot of substrate $BDFE_{O-H}$ against $logk_2$. The line of best fit is shown by the black dashes. The equation is: y = 14.5 – 0.206x, R^2 = 0.935.

While the obtained kinetic data suggested that the rate of the reaction between K[**2**] and the selected phenolic substrates was correlated to the substrate $BDFE_{O-H}$ (Fig 2-14, B), further data interpretation proved to be a challenge. When the decrease in absorbance at λ = 805 nm was plotted against time during substrate addition following Equation 1, the resulting plots did not appear linear but rather exhibited a curve. This led to low R^2-values between substrate concentration and the pseudo-first order rate constant, k_{obs}, calling the validity of the measured k_2 values into question. The distinctive curve of the time trace plots suggested that the reaction between the 4-R-phenols and K[**2**] may not follow first order conditions, potentially undergoing a mechanism other than homolytic X–H bond cleavage (Fig 2-14). It was expected that the products of these reactions would be a phenoxyl radical (PhO·) and some Co^{II} species, likely $[Co^{II}H_2pout(OH_2)]^-$. However, the 4-R-PhOH compounds were not sterically bulky, leading to quenching of the proposed PhO· through radical coupling, which rendered the radical intermediates undetectable by EPR spectroscopy. While a Co^{II} product would be EPR active, the EPR spectra measured after addition of excess phenol did not have a definitive Co^{II} signal so no clear conclusion could be drawn. In reexamining the raw data from these reactions, new bands formed at

λ_{max} = 600, 660 nm (Fig 2-14A, marked with *) which grew in as the reaction proceeded. The molar absorptivity values (~300 $M^{-1}cm^{-1}$) were larger than is typical for other characterized Co^{II}–OH and Co^{II}–OH_2 complexes, suggesting that the inorganic product of these reactions was not either one of those species.

Table 2-4: Summary of data from the reaction of K[**2**]with 4-R substituted phenolic substrates and their thermodynamic parameters.[69]

Substrate	$BDFE_{O–H}$ (kcal mol^{-1})	pK_a	k_2 ($M^{-1}s^{-1}$)	R^2
4-OMe	83.0	19.1	$2.59*10^{-3}$	0.945
4-H	88.3	18.0	$3.46*10^{-4}$	0.695
4-Br	89.1	16.4	$1.04*10^{-4}$	0.757

Given that these studies were performed in the presence of excess substrate, it is plausible that some competitive binding event or ligand substitution may occur along the course of the reaction pathway, which may account for these new bands. There are a few likely pathways through which a binding event could proceed. In the first possible scenario, the O–H bond of the 4-R-PhOH is first cleaved to form 4-R-PhO· and a Co^{II} species, at which point excess 4-R-PhOH could bind to form a Co^{II}–OHPh complex where the 4-R-PhOH is bound in the fifth coordination site (Scheme 2-3, Pathway A). Based on the acidity of the phenolic substrates chosen (Table 2-4), it is also feasible that K[**2**] could deprotonate the 4-R-PhOH to form a phenolate ion and a Co^{III}–OH_2 complex, followed by displacement of the OH_2 ligand to form a Co^{III}–OPh complex (Scheme 2-3, Pathway B). Lastly, it is possible that the O–H bond of the 4-R-PhOH could be homolytically cleaved first, yielding a 4-R-PhO· and a Co^{II} species. At this point, the 4-R-PhO· could coordinate to the Co center and oxidize the Co ion to form a Co^{III}–OPh species (Scheme 2-3, Pathway C).

Pathway A:

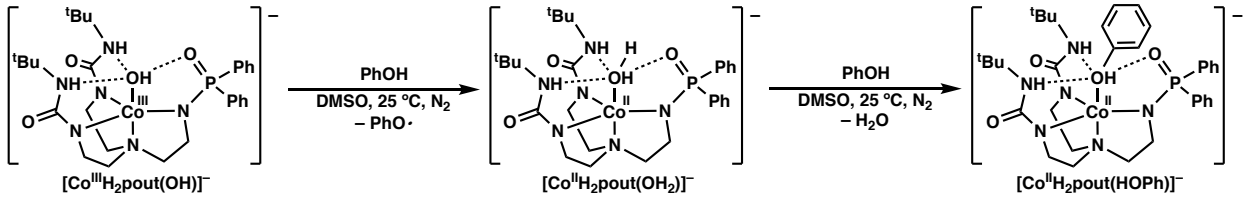

Pathway B:

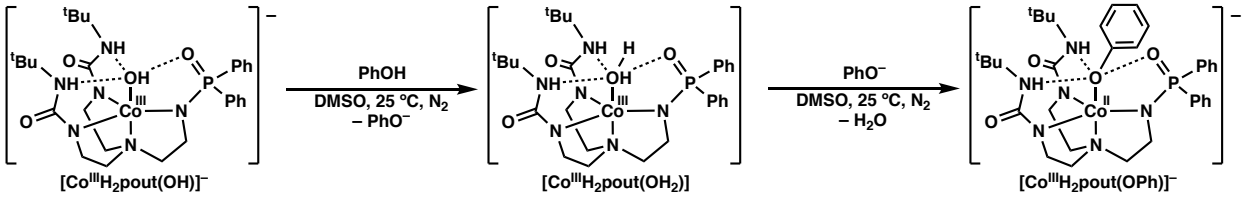

Pathway C:

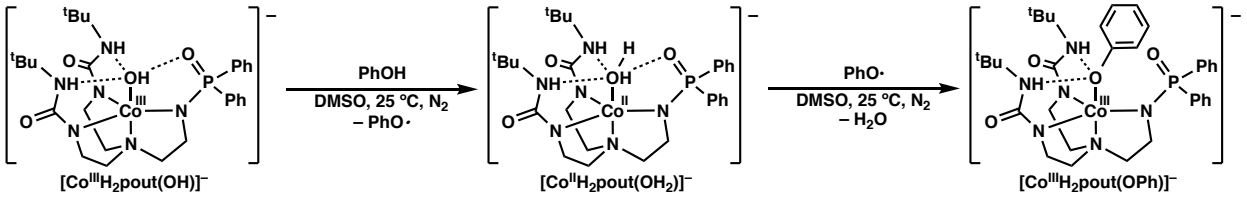

Scheme 2-3: Schematic representations of the proposed pathways through which a ligand substitution event may proceed.

To test the above hypotheses, a solution of K_2[**1**] was prepared in DMSO and treated with 3 eq of PhOH, to form a proposed Co^{II}–OHPh complex. This reaction resulted in the formation of an intense blue solution, distinct from K_2[**1**] (Figure 2-14, gray trace). The bands associated with this new species were also not consistent with the product that grows into solution following reaction of K[**2**] with 4-R-PhOH substrates, suggesting that a Co^{II}–O(H)Ph was not the likely product of the reaction. The solution was then treated with $FcBF_4$ in an attempt to oxidize the new species, to form a proposed Co^{III}–OHPh. Addition of $FcBF_4$ resulted in the formation of a dark green mixture with some unidentified precipitate, which may have contributed to the increase in absorbance of the spectrum (Fig 2-15, blue trace). This spectrum featured bands at 603 and 655 nm, similar

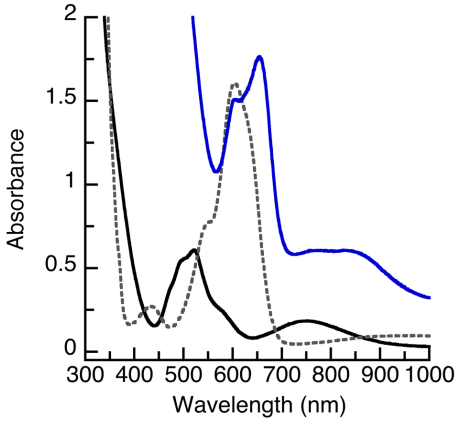

Figure 2-15: Reaction of 5.75 mM of K_2[**1**] (black) in DMSO with 3 eq of phenol (gray, λ= 371, 434, 548, 605, 636 nm). This species is then treated with $FcBF_4$ (blue, λ_{max}= 604, 655, 746, 832 nm).

to the product of the reaction of K[**2**] with 4-R-phenolic substrates (Figure 2-14, A). The similarity in these spectra further suggests that ligand substitution may play a role, however the mechanism of the proposed substitution is still unclear as is the precise identity of the inorganic product. While efforts were made to prepare the proposed Co–OHPh or Co–OPh species in bulk, ultimately attempts to isolate crystalline solids and confirm their identity were unsuccessful.

Reactivity with tri-Substituted Phenolic Compounds: The underlying complications identified in the reactivity studies between K[**2**] and the 4-R-PhOH substrates could largely be attributed to the lack of steric bulk of the substrates. Given that these substrates were relatively small and sterically unencumbered, the 4-R-PhOH compounds could feasibly coordinate to the Co center. Furthermore, potential radical products typically quench through radical coupling pathways making them more difficult to identify by spectroscopic methods. To probe the ability of K[**2**] to perform a O–H bond activation in a more straightforward manner, a series of bulkier 2,6-di-^{t}Bu-4-R-PhOH substrates were chosen. Addition of *tert*-butyl groups at the 2 and 6 positions on the aromatic ring provide steric bulk that effectively stabilizes the radical species by preventing radical coupling.

K[**2**] was treated with a series of 2,6-di-^{t}Bu-4-R phenolic compounds (R = OMe, ^{t}Bu, Br, Me) to examine its competence towards O–H bond cleavage. Because the radical species are stabilized by the bulky *tert*-butyl groups, potential phenoxyl radical products are detectable by ⊥-mode EPR spectroscopy. Initial studies were performed in DMSO, however the reaction(s) proceeded rapidly which made spectra difficult to fit to Equation 1. Therefore, the reaction conditions were modified. A 0.5 mM solution of **2** in THF was treated with excess 2,6-di-^{t}Bu-4-R-phenol at 10 ºC which resulted in the formation of sharp bands above 400 nm and the loss of features associated with **2** in the UV-vis spectra. The high energy bands at λ_{max} = 388, 405 nm (Fig 2-16, A; 2,6-di-^{t}Bu-4-OMe-PhOH) were similar in shape and energy to literature examples of phenoxyl radicals (λ_{max} = 383, 400, 626 nm, MeCN).[68,72,73] These reactions were followed by monitoring the band at λ_{max} = 805 nm. The data was fit following Equation 1 and plotted against time to determine a k_{obs} value. The slope of the lines generated by plotting k_{obs} values versus substrate concentration gave the k_2 values of the reaction (Table 2-5, Fig 2-S2 to 2-S5). Additionally, these reactions were followed by ⊥-mode EPR spectroscopy, which

revealed formation of a radical signal at g = 2 and a broad signal at g = 4, consistent with the formation of a Co^{II} species (Fig 2-16, B).

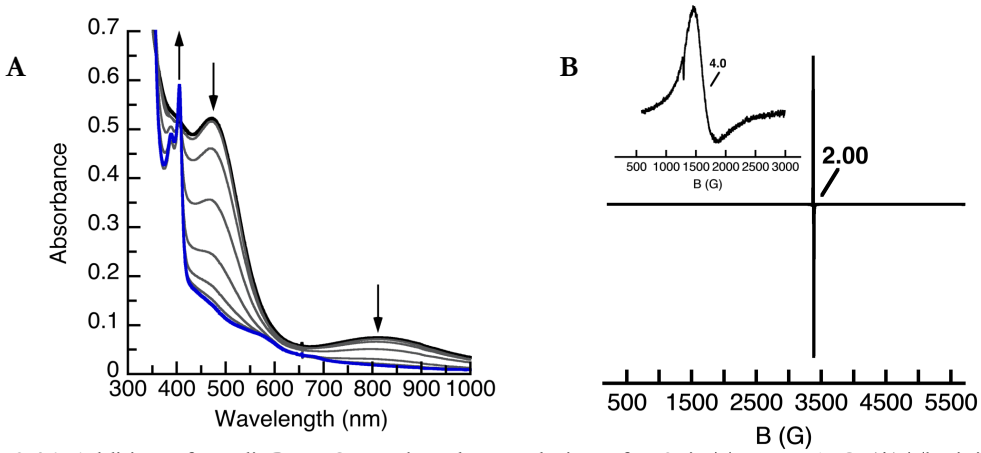

Figure 2-16: Addition of 2,6-di-^{t}Bu-4-OMe-phenol to a solution of K[**2**] in THF at 25 °C. (**A**) The initial spectrum is shown in black and the final is shown in blue (λ_{max} = 388, 405, 468(sh), 570, 682 nm). (**B**) 77K ⊥-mode EPR spectrum showing the product of the reaction of K[**2**] with excess 2,6-di-^{t}Bu-4-OMe-phenol, consistent with the formation of a Co^{II} species and an organic radical (10 mM, DCM:THF).

Table 2-5: Summary of data from the reaction of K[**2**] with 2,6-di-^{t}Bu-4-R substituted phenolic substrates and their thermodynamic parameters.[68,73] BDE values were chosen because the BDFE values have not been reported for all substrates. Thermodynamic data are reported in DMSO, though the reaction was carried out in THF.

R =	BDE_{O-H} (kcal mol^{-1})	pK_a	k_2 ($M^{-1}s^{-1}$)	R^2
OMe	78.3	18.2	1.28	0.952
Me	81.0	17.7	1.77	0.988
^{t}Bu	81.2	17.8	9.16	0.972
Br	83.2	-	6.49	0.997

After the data was collected and analyzed, the logarithm of the k_2 values ($\log k_2$) were plotted against BDE, pKa, and Hammett parameter values to gain a better understanding of the thermodynamic driving force behind these reactions. The thermodynamic values used were obtained in DMSO because these values have not been reported in THF. While it was clear that K[**2**] was competent to cleave O–H bonds, the $\log k_2$ values of these reactions did not appear to follow a trend with any of the aforementioned parameters, complicating data analysis and preventing a clear conclusion regarding the mechanism of reaction (Figure 2-S6). Initial kinetic analyses (i.e. determining k_{obs} and k_2 values) resulted in linear plots which suggested a concerted bond cleavage mechanism, however conclusive mechanistic insights require further experiments.

Summary and Conclusion

This chapter includes the successful syntheses and characterization of a redox pair of paramagnetic Co–OH complexes. The Co^{II}–OH complex, $K_2[Co^{II}H_2pout(OH)]$ (K_2[**1**]), was isomorphous to the Mn^{II}– and Fe^{II}–OH analogues.[22,53,54] The 2º coordination sphere of all three complexes have strong interactions between one of the K^+ counterions with the hydroxido ligand, which prevents formation of an intramolecular H–bond between the $^-$OH ligand proton and the P=O groups. Additionally, K_2[**1**] can be related to a set of Co^{II}–OH complexes supported by a series of unsymmetric ureayl-sulfonamido ligand frameworks. The spectroscopic characteristics of these complexes were compared, which concluded that ureayl functional groups act as stronger σ-donors in the 1º coordination sphere than sulfonamido units. When K_2[**1**] was evaluated against this series, the spectroscopic data fit in with the trend established by the prior study, supporting a previously established hypothesis that phosphinic amido groups are stronger donor ligands than the sulfonamido analogues but are weaker than the ureayl moieties. Furthermore, it was found that K_2[**1**] could be oxidized by O_2 or Fc^+, as established by the electrochemical profile of K_2[**1**].

In a further testament to the superior supportive nature of phosphinic amido donors versus sulfonamido groups, K_2[**1**]was oxidized to $K[Co^{III}H_2pout(OH)]$ (K[**2**]) and a molecular structure was obtained, which none of the sulfonamido based systems had achieved. K[**2**] was subsequently spectroscopically characterized and the data was in good agreement with previously characterized examples of Co^{III}–OH species in C_3 symmetric environments. The magnetic moment of K[**2**] was measured by Evans' Method NMR spectroscopy and found to be μ_{eff} = 2.96 μ_B, indicating a spin state of S = 1 for the Co^{III} center. This paramagnetism is uncommon for Co^{III} species, which are typically diamagnetic. It was observed that K[**2**] was unstable in solution and its diagnostic color faded over time, with a half-life of 10 h in THF. The solution instability taken in conjunction with the paramagnetism suggested that the compound may be reactive towards external substrates.

The reactivity of K[**2**] was subsequently investigated with various substrates. In these kinetic studies, K[**2**] was generated spectroscopically due to issues with poor purity and yields during bulk synthesis. K[**2**] was treated with TEMPO–H and found to cleave the O–H bond. However when treated with C–H bond substrates,

like DHA, K[**2**] did not cleave the C–H bond. To further study its reactivity, K[**2**] was treated with other substrates featuring O–H bonds, including a series of para-substituted phenolic compounds. While it was clear that K[**2**]reacted with these phenols in some manner, fitting the raw time traces using Equation 1 generated curved plots rather than straight lines, suggesting that the reaction was not a homolytic bond cleavage event but rather that some other reaction(s) were also occurring. The final spectra did not look like typical Co^{II}–OH or OH_2 complexes in C_3 symmetry, suggesting that a competitive binding event may occur. To examine this possibility, PhOH was added to solutions of K_2[**1**]. This product was then oxidized. These reactions did exhibit color changes, but a clear conclusion regarding the identity of these species could not be drawn from the data. Lastly, K[**2**] was treated with a series of tri-substituted phenols, 2,6-di-*t*Bu-4-R-PhOH, to follow the organic radical product which would result from homolytic bond cleavage while also eliminating potential competitive binding events. Following these reactions by UV-vis and EPR spectroscopies, it was clear that the products of this reaction were a phenoxyl radical and some Co^{II} species. However, when the measured k_2 values were plotted against the Hammett parameters, pKa, and BDE values, a linear correlation was not observed. Fitting the time traces from these reactions to Equation 2-1 generated linear fits, suggesting that K[**2**] homolytically cleaves the O–H bond of the phenolic substrates. However, given that the k_2 values could not be correlated to the aforementioned thermodynamic parameters, the driving force behind this reaction was not clear and requires further study.

Outlook

Should studies with these complexes continue, there are a few potential directions the work could be taken in. Firstly, K_2[**1**] was compared to a series of unsymmetric ureayl-sulfonamido ligand frameworks which concluded the following regarding ligand field strength: ureayl > phosphinic amido > sulfonamido groups. The empirical data measured throughout these studies is supportive of this. However, it may be interesting to moderately expand this study through an EPR analysis. The He-temperature EPR spectrum of K_2[**1**] has been measured, which revealed a hyperfine coupling constant of A, ^{59}Co = 295 MHz. Meanwhile this data for other Co^{II}–OH complexes in these series has not been measured. The hyperfine coupling constants could be

measured and compared to determine if ligand field strength affects the magnitude of the A-values, which could be used as another handle to evaluate ligand donorability.

Lastly, the reactions between K[**2**] and the tri-substituted phenolic substrates occurred rapidly in DMSO, which affected reproducibility. The reactions were then studied in THF at 10 ºC which effectively slowed the reaction and made fitting the data more straightforward. However, when the k_2 values did not correlate with various thermodynamic parameters, including BDE, pKa, and Hammett parameters. The reactivity studies could be optimized by screening different solvents, temperature ranges, or other conditions to obtain more in-depth kinetic analyses.

Experimental

General Procedures

Unless otherwise noted, all experiments were performed and reagents stored under a N_2 atmosphere in a VAC dry box. BHT-stabilized Et_2O, DCM stabilized with amylene, pentane, MeCN, and THF were purchased from Fisher, sparged with argon, and purified using a JC Meyer Co. solvent purification system with columns containing Q-5 and molecular sieves. Sure-seal bottles of DMSO and DMA were purchased respectively from Honeywell- Burdick & Jackson and Acros Organics (99.5% purity). KH was bought from Sigma Aldrich as a 30% suspension in mineral oil and washed on a 15 mL fine porosity frit with pentane and Et_2O, then dried under vacuum. $Co^{II}(OAc)_2$ was purchased from Sigma Aldrich in 99.995% purity and dried briefly in an oven until a purple powder was obtained. Fc was obtained from TCI Chemicals in 98.0% purity, recrystallized by sublimation, and immediately used to prepare $FcBF_4$ according to literature procedure.[65] DHA, PhOH (>99% purity), 4-^{t}Bu-PhOH (99% purity), 4-Br-PhOH, and 4-OMe-PhOH (98% purity) were purchased from Sigma Aldrich and used as obtained. All para-substituted phenolic compounds were brought into a dry-box and stored appropriately to prevent prolonged exposure to light. 2,4,6-tri-^{t}Bu-phenol was purchased from Sigma Aldrich and purified via sublimation. 2,6-di-^{t}Bu-4-Br-PhOH and 2,6-di-^{t}Bu-4-Me-PhOH were purchased from Aldrich and used as provided. 2,6-di-^{t}Bu-4-OMe-PhOH was purchased from Acros and used as provided.

Physical Methods

^{1}H–NMR spectra were recorded at 500 MHz using a Bruker DRX500 spectrometer with a TCI cryoprobe. Chemical shifts were reported in ppm and referenced to an internal trimethylsilane standard in deuterated solvents. Electronic absorption (UV-vis) spectra were collected in a 1 cm quartz cuvette fitted with a 4 mm magnetic stir bar. Spectra were recorded on a Cary-60 spectrophotometer or an 8453E Agilent UV-vis spectrophotometer fitted with a Unisoku Unispeks cryostat for temperature-controlled spectroscopy. Cyclic voltammetry was performed with a CHI600C potentiostat. Voltammograms were collected from a ~1 mM stock solution of analyte in ~100 mM tetrabutylammonium hexafluorophosphate in dry, air-free solvent and measured in a 4-neck, double-walled cell. A 1 mm glassy carbon electrode acted as the working electrode with Pt wire counter and Ag wire reference electrodes. All voltammograms were referenced to an internal $Fc^{+/0}$ standard. Elemental analyses were measured on a Perkin-Elmer 2400 Series II CHNS elemental analyzer. He-temperature EPR spectra were collected on an X-Band (9.64 GHz) Bruker spectrometer fitted with an Oxford liquid helium cryostat. Signals were referenced and quantified to a $[CuEDTA]^{2-}$ spin standard. The magnetic field was calibrated with an NMR gaussmeter and the microwave frequency of the instrument was calibrated with a frequency counter. 77K EPR experiments were recorded on a Bruker EMX X-band spectrometer with the following parameters, unless otherwise noted: microwave frequency of 9.64 GHz, a modulation frequency of 100 kHz, a modulation amplitude of 10 G, a microwave power of 2 mW, an attenuation of 20 dB, a time constant of 82 msec, and a conversion time of 41 msec. All EPR samples were prepared under a nitrogen atmosphere in 4 mm quartz EPR tubes, capped with a septum, and flash frozen in liquid nitrogen. Attenuated Total Reflectance-Fourier Transform Infrared (ATR-FTIR) spectra were measured on a Thermo Scientific Nicolet iS5 spectrometer fitted with an iD5 ATR attachment. Elemental analyses were measured on a Perkin-Elmer 2400 Series II CHNS elemental analyzer.

Kinetic studies for the oxidation of substrates

Kinetic experiments studying the activation of 4-R-PhOH substrates were performed with 0.75 mM $K[Co^{III}H_2pout(OH)]$ in DMSO at 25 ºC, generated *in situ*. 2.0 mL DMSO were transferred into a 1 cm quartz cuvette equipped with a 4 mm stir bar, capped with a septum, and placed in cryostat. A concentrated stock

solution of $K_2[Co^{II}H_2pout(OH)]$ was prepared by dissolving crystalline $K_2[Co^{II}H_2pout(OH)]$ in 1.0 mL of DMSO in the presence of excess 18c6. 85 μL of the concentrated $(K\subset18c6)_2[Co^{II}H_2pout(OH)]$ stock solution was added to 2.0 mL of DMSO in the cuvette and a spectrum was collected. To this solution, 35 μL of concentrated $FcBF_4$ (~1 equivalent relative to $(K\subset18c6)_2[Co^{II}H_2pout(OH)]$) was prepared in DCM, added to the cuvette and the solution was allowed to mix for ~1 minute. A spectrum was then collected to confirm generation of $(K\subset18c6)[Co^{III}H_2pout(OH)]$. Stock solutions of each substrate (~650 mM) were then prepared in DMSO and the substrate was added to the cuvette in 25 μL increments (25 μL to 100 μL). These experiments were performed under pseudo first order reaction conditions in the presence of at least 10 equivalents of substrate.

When studying the activation of 2,6-di-*t*Bu-4-R-PhOH substrates, kinetic experiments were performed with 0.54 mM *in situ* generated $K[Co^{III}H_2pout(OH)]$ in THF at 10 ºC. 2.0 mL of THF were transferred into a 1 cm quartz cuvette equipped with a 4 mm stir bar, capped with a septum, and cooled in the cryostat. A concentrated stock solution of $K_2[Co^{II}H_2pout(OH)]$ was prepared by dissolving pure $K_2[Co^{II}H_2pout(OH)]$ in 1.0 mL of THF in the presence of excess 18c6. 75 μL of concentrated $(K\subset18c6)_2[Co^{II}H_2pout(OH)]$ was added to 2.0 mL of chilled THF in the cuvette and a spectrum was collected. To this solution, 25 μL of concentrated $FcBF_4$ (~1 equivalent relative to $(K\subset18c6)_2[Co^{II}H_2pout(OH)]$, prepared in MeCN) was added to the cuvette and allowed to mix for ~1 minute. A spectrum was then collected to confirm generation of $(K\subset18c6)[Co^{III}H_2pout(OH)]$. Stock solutions of each substrate (~450 mM) were then prepared in THF and the substrate was added to the cuvette in 25 μL increments (25 μL to 100 μL). Please note that for 2,6-di-*t*Bu-4-Me-PhOH, titrations were only followed between 25 – 75 μL. These experiments were performed under pseudo first order reaction conditions in the presence of at least 10 equivalents of substrate.

$$k_{obs} = \ln\left[\frac{(A_t - A_\infty)}{(A_i - A_\infty)}\right]$$ **Equation 2-1**

The reaction progress for both the activation of 4-R-PhOH and 2,6-di-*t*Bu-4-R-PhOH were monitored by following the decrease in absorbance of the *d–d* band at λ_{max} = 805 nm. Equation 1 was plotted against the time traces at 805 nm for at least three half-lives of each reaction. For each reaction, the observed pseudo first-

order rate constant (k_{obs}, s^{-1}) was found from the slope of the line generated by fitting with Equation 2-1. When k_{obs} was plotted against substrate concentrations, the second order rate constant was found (k_{obs}= [Substrate]k_2; k_2, $M^{-1}s^{-1}$). These plots and k_2 values can be found in the supplementary information.

Preparative Methods

*K_2[$Co^{II}H_2$pout(OH)] (K_2[**1**]):* 0.1268 g (0.2330 mmol) of H_5pout were dissolved in 5 mL of DMA with 4.00 eq of KH (0.0374 g, 0.932 mmol). These reagents were stirred for 30 minutes until all bubbling ceased, resulting in a clear, pale yellow solution. To this solution, 0.0452 g (0.255 mmol, 1.09 eq) of solid $Co^{II}(OAc)_2$ were added and stirred for 30 minutes, yielding a blueish-purple mixture. 5.0 μL (0.28 mmol, 1.2 eq) of air-free H_2O were added to the reaction mixture, causing an immediate color change to a purple-pink mixture, and stirred for 15 minutes. The reaction was then filtered with a 15 mL medium-porosity glass frit and washed with 3 mL of DMA followed by 2 mL Et_2O to yield 0.0480 g of a blueish-white solid (0.0457 g theoretical yield of KOAc) and a purple filtrate. The resulting purple solution was briefly dried under vacuum to remove residual Et_2O and was further diluted with DMA until residual cloudiness abated. The complex was recrystallized from vapor diffusion of Et_2O into the crude DMA solution to give 142.1 mg (0.2042 mmol, 87.66 % yield) of K_2[$Co^{II}H_2$pout(OH)] as purple crystals suitable for X-ray diffraction. H1, H5, and H6 were located from a difference-Fourier map and refined (x, y, z and U_{iso}). FTIR: $\boldsymbol{\nu}$ (cm^{-1}) = 3640 (O–H); 3130, 3230 (N–H); 2950-2800 (C–H); 1647, 1635 (CO). UV-vis (DMSO, λ_{max} [nm (ε $M^{-1}cm^{-1}$)] = 491 (185), 524 (180), 583 (75), 753 (44). EPR (X-band, ⊥-mode, 12 K, g = 4.4, 4.3, 2.0, A = 295 MHz). μ_{eff}, Evans' Method, DMSO = 4.142 μ_B. Cyclic voltammetry (THF, V vs $Fc^{+/0}$) $E_{1/2}$= –0.621 ($Co^{III/II}$), E_{pa}= –0.108, E_{pa}= +0.277. Elemental Analysis calculated for $3(C_{28}H_{43}CoK_2N_6O_5P) \cdot C_4H_9NO$; C, 50.59, H, 6.91, N, 13.16; found C, 50.25, H, 7.27, N, 13.18.

*K[$Co^{III}H_2$pout(OH)] (K[**2**]):* 0.0570 g (0.0819 mmol) of K_2[$Co^{II}H_2$pout(OH)] was suspended in 4 mL of THF. To this pale purple suspension, 0.0224 g (0.0821 mmol, 1.00 eq) of $FcBF_4$ was added in 1 mL DCM to aid in solubility. The addition of $FcBF_4$ afforded an immediate color change to a deep red-orange solution. This solution was stirred for 45 minutes and the solvent was removed under vacuum to yield a red-orange residue. This residue was triturated briefly with Et_2O and dried under vacuum again to yield a red-orange solid. The solid was re-dissolved in 15 mL of MeCN and filtered to yield a deep red-orange filtrate and 0.0180 g of a pale

orange solid (0.0152 g, 0.0103 g theoretical yield of Fc, KBF_4). The filtrate was concentrated and recrystallized via vapor diffusion of Et_2O into the crude MeCN filtrate, resulting in small, deep-red crystals suitable for X-ray diffraction. Despite best efforts, yields of pure solids were low, making it difficult to characterize K[**2**] in bulk. To address these challenges, K[**2**] was largely characterized spectroscopically via *in situ* generation. No elemental analysis or high-resolution mass spectrometry measurements were obtained. H5 and H6 were located from a difference-Fourier map and refined (x,y,z, and U_{iso}). H1 was refined (x,y,z) with d (O–H) = 0.85 and riding U_{iso}. FTIR: $\boldsymbol{\nu}$ (cm^{-1}) = 3310 (O–H); 3051, 3061 (N–H); 2960–2840 (C–H), 1640 (CO). UV-vis (DMSO, λ_{max} nm (ε $M^{-1}cm^{-1}$)) = 400 (sh), 478 (1030), 805 (171). EPR (X-Band, $\perp$, $\parallel$-mode = silent). Evans' Method NMR: μ_{eff}, DMSO = 2.96 μ_B.

X-ray Crystallographic Methods

K_2[$Co^{II}H_2$pout(OH)]: The data for $K_2[Co^{II}H_2pout(OH)]\cdot 2DMA$ were collected from a shock-cooled single crystal at 88(2) K on a Bruker SMART APEX II three-circle diffractometer with a sealed X-ray tube using a equatorial mounted graphite as monochromator and a Bruker Apex II CCD detector. The diffractometer was equipped with a Cryo Industries low temperature device and used MoK_a radiation (λ = 0.71073 Å). All data were integrated with SAINT and a multi-scan absorption correction using SADABS was applied.[74–76] The structure was solved by direct methods using SHELXS and refined by full-matrix least-squares methods against F^2 by SHELXL-2018/3 using ShelXle.[77–79] All non-hydrogen atoms were refined with anisotropic displacement parameters. All hydrogen atoms were refined with isotropic displacement parameters. Some were refined freely and some on calculated positions using a riding model with their U_{iso} values constrained to 1.5 times the U_{eq} of their pivot atoms for terminal sp^3 carbon atoms and 1.2 times for all other carbon atoms. Disordered moieties were refined using bond lengths restraints and displacement parameter restraints. This report and the CIF file were generated using FinalCif.[80] *Refinement Details*: All non-hydrogen atoms were refined anisotropically. All main molecule and ordered DMA hydrogen atom positions were freely refined with displacement parameters constrained to 1.2x the ADP of the connecting atom for all CH_2, NH, and OH groups and 1.5x the ADP for CH_3 groups. On one slightly disordered (91:9) DMA molecule, bond lengths and angles were restrained to

similar values between the two parts, ADPs were constrained to the same value for each unique atom, and hydrogen atoms were added using a riding model.

K[Co^{III}H$_2$pout(OH)]: The data for K[Co^{III}H$_2$pout(OH)]·MeCN were collected from a shock-cooled single crystal at 133(2) K on a Bruker SMART APEX II three-circle diffractometer with a fine-focus sealed tube using a equatorial mounted graphite as monochromator and a Bruker Apex II CCD detector. The diffractometer was equipped with a Cryo Industries low temperature device and used MoK_a radiation (λ = 0.71073 Å). All data were integrated with SAINT and a multi-scan absorption correction using SADABS was applied.[74–76] The structure was solved by direct methods using SHELXT and refined by full-matrix least-squares methods against F^2 by SHELXL-2018/3 using ShelXle.[77,79,81] All non-hydrogen atoms were refined with anisotropic displacement parameters. All hydrogen atoms were refined with isotropic displacement parameters. Some were refined freely and some on calculated positions using a riding model with their U_{iso} values constrained to 1.5 times the U_{eq} of their pivot atoms for terminal sp^3 carbon atoms and 1.2 times for all other carbon atoms. This report and the CIF file were generated using FinalCif.[80] *Refinement Details:* All non-hydrogen atoms were refined anisotropically without restraints or constraints. All methylene and sp2 hydrogen atom positions were refined freely with ADPs constrained to 1.2x the ADP of the connecting atom. Methyl hydrogen atoms were refined using a riding model. The H6 position was refined freely with ADP 1.2x that of N6. H1 and H5 positions were refined with the distances restrained to 0.83A to O1 and 0.93A to N5, respectively and ADPs 1.2x the connecting atoms. All refined hydrogen atoms connecting to hetero atoms were found in the difference map.

Supplemental Information

Table 2-S1: Crystallographic details for $K_2[Co^{II}H_2pout(OH)]$, K_2[**1**], (middle column) and $K[Co^{III}H_2pout(OH)]$, K[**2**], (right column).

Compound	$K_2[Co^{II}H_2pout(OH)]\cdot 2$ DMA	$K[Co^{III}H_2pout(OH)]\cdot$MeCN
Empirical formula	$C_{36}H_{61}CoK_2N_8O_6P$	$C_{30}H_{46}CoKN_7O_4P$
Formula weight	870.02	697.74
Temperature [K]	88(2)	133(2)
Crystal system	orthorhombic	monoclinic
Space group (number)	$Pbca$ (61)	$P2_1/n$ (14)
a [Å]	17.8053(18)	10.0313(6)
b [Å]	21.167(2)	23.4096(15)
c [Å]	23.491(2)	14.4563(9)
α [°]	90	90
β [°]	90	92.0090(10)
γ [°]	90	90
Volume [Å^3]	8853.6(15)	3392.7(4)
Z	8	4
ϱ_{calc} [gcm^{-3}]	1.305	1.366
Independent reflections	9786	8261
Goodness-of-fit on F^2	1.008	1.035
R_1, $[I \geq 2\sigma(I)]$	0.0369	0.0332
wR_2, [all data]	0.0852	0.0859

$R_1 = \Sigma \; | \; |F_o| - |F_c| \; | \; / \; \Sigma \; |F_o|$
$wR_2 = [\Sigma[w(F_o^2 - F_c^2)^2] \; / \; \Sigma[w(F_o^2)^2]]^{1/2}$

Thermal ellipsoids are shown at 50% probability.

Goof (Goodness-of-fit) = $S = [\Sigma[w(F_o^2 - F_c^2)^2] \; / \; (n - p)]^{1/2}$, where n = number of reflections and p = total number of parameters refined.

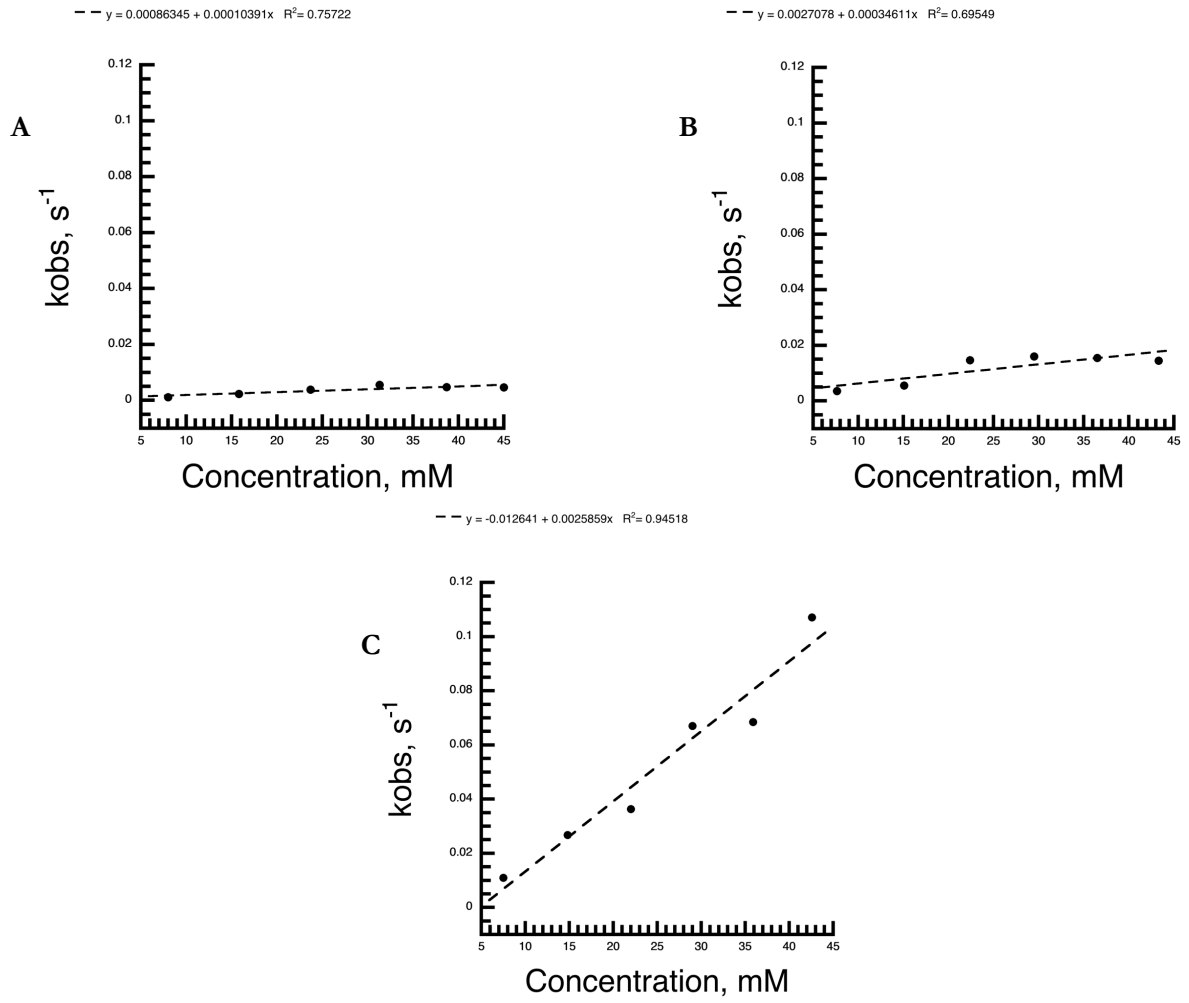

Figure 2-S1: Kinetic rate plots from addition of different 4-R-PhOH substrates: R = Br (**A**), R = H (**B**), R = OMe (**C**).

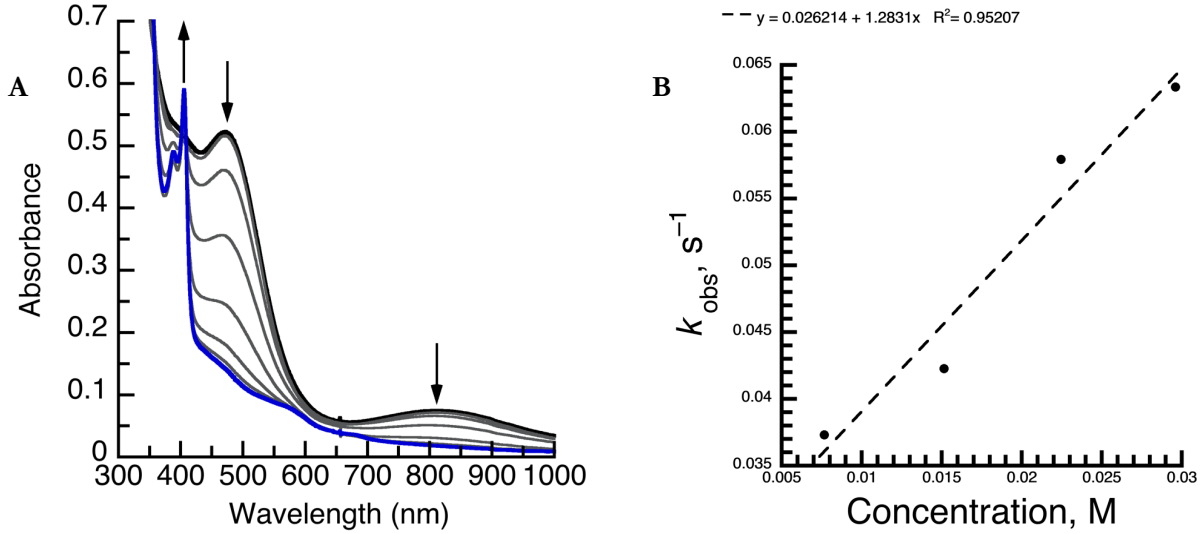

Figure 2-S2: (**A**) UV-visible spectra following the reaction of K[**2**] with 2,6-di-*t*Bu-4-OMe-PhOH, with the final trace shown in blue. (**B**) Plot of 2,6-di-*t*Bu-4-OMe-PhOH concentration versus k_{obs} values, including the line of best fit and correlation constant.

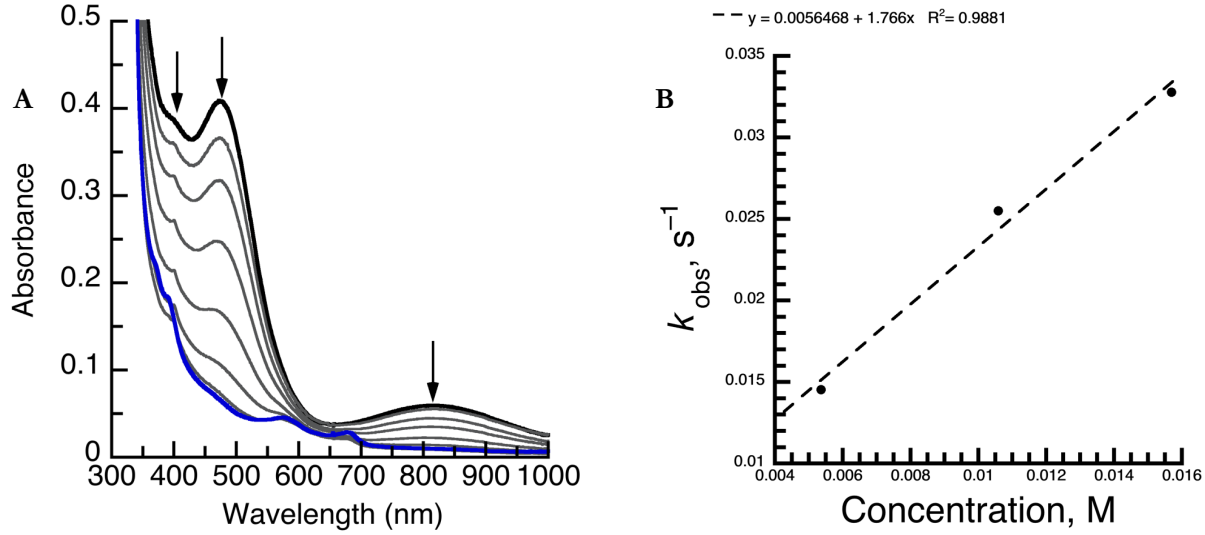

Figure 2-S3: (**A**) UV-visible spectra following the reaction of K[**2**] with 2,6-di-*t*Bu-4-Me-PhOH, with the final trace shown in blue (λ_{max} = 371 (sh), 470, 578, 680 nm). (**B**) Plot of 2,6-di-*t*Bu-4-Me-PhOH concentration versus k_{obs} values, including the line of best fit and correlation constant.

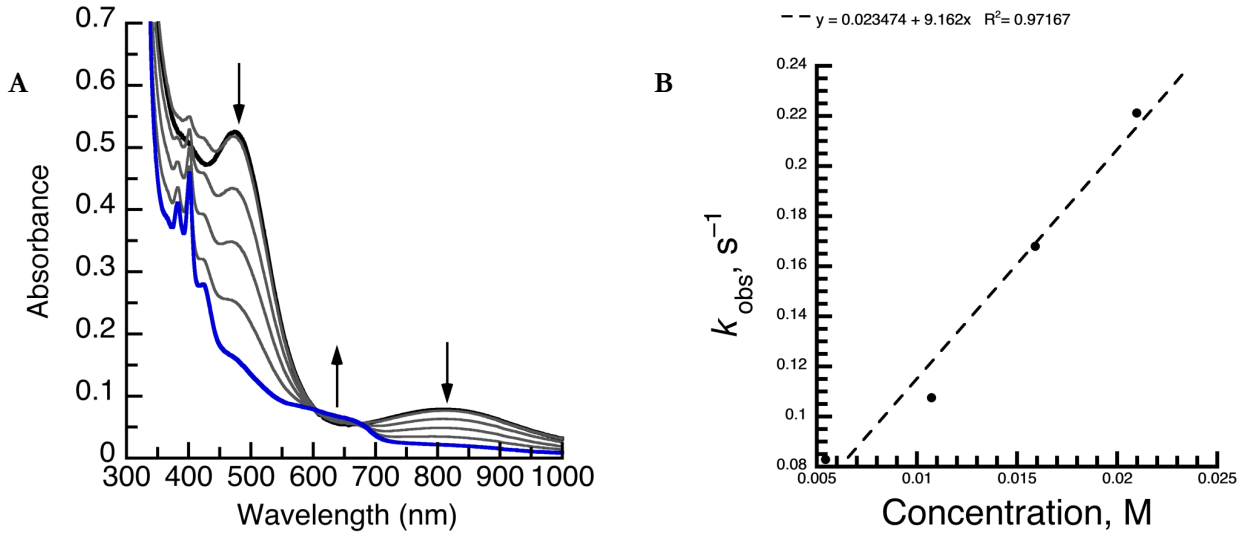

Figure 2-S4: (**A**) UV-visible spectra following the reaction of K[**2**] with 2,4,6-tri-*t*Bu-PhOH, with the final trace shown in blue (λ_{max} = 365 (sh), 382, 402, 423, 475, 582, 668 nm). (**B**) Plot of 2,4,6-tri-*t*Bu-PhOH concentration versus k_{obs} values, including the line of best fit and correlation constant.

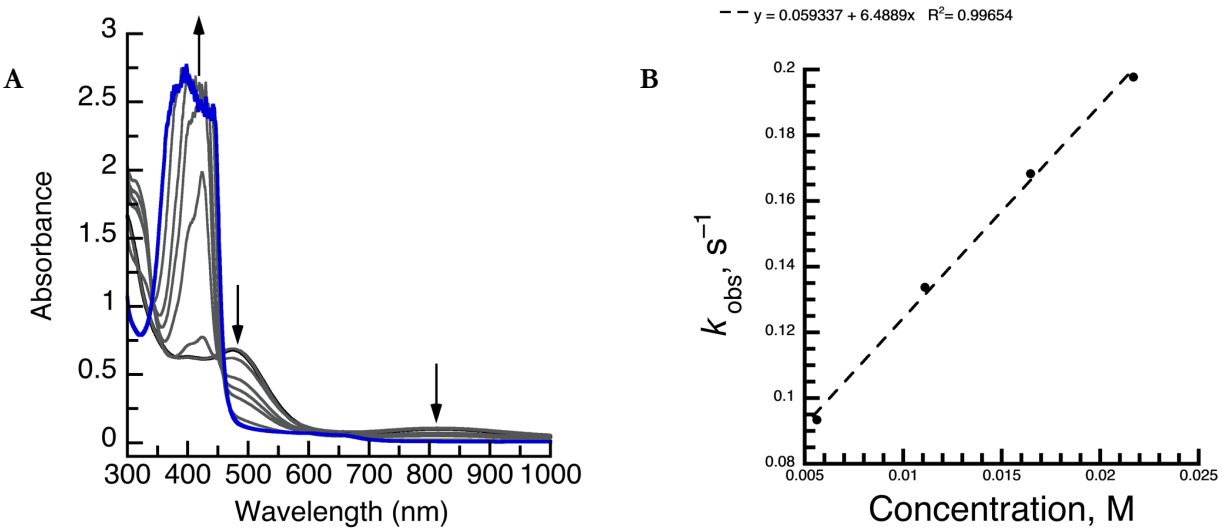

Figure 2-S5: (**A**) UV-visible spectra following the reaction of K[**2**] with 2,6-di-*t*Bu-4-Br-PhOH, with the final trace shown in blue (λ_{max} = 605, 657 nm). (**B**) Plot of 2,6-di-*t*Bu-4-Br-PhOH concentration versus k_{obs} values.

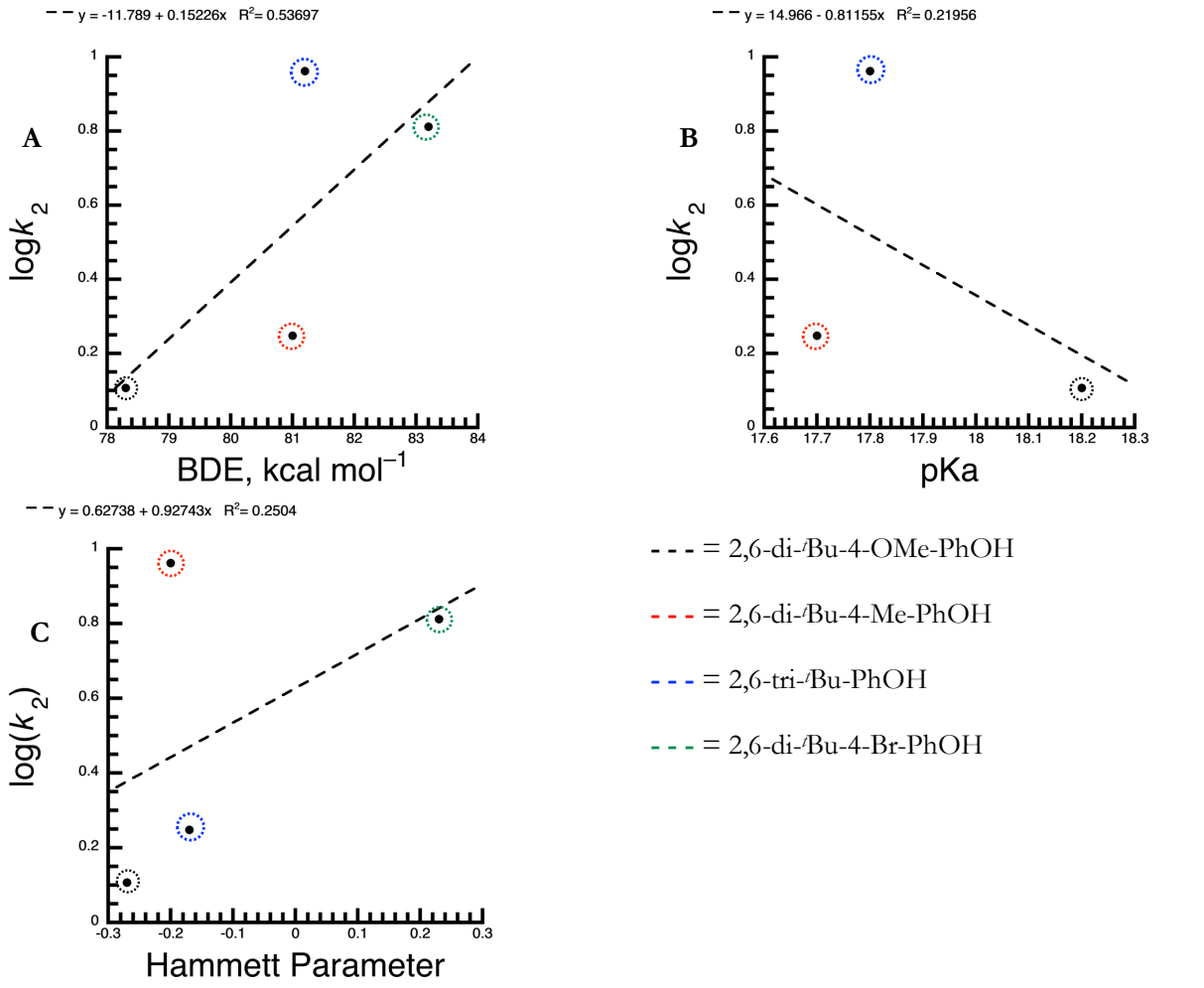

Figure 2-S6: Plots of the logarithms of the k_2 values versus BDE (**A**), pKa (**B**), and Hammett Parameter (**C**), with lines of best fit and correlation constants.

References

(1) Rittle, J.; Green, M. T. Cytochrome P450 Compound I: Capture, Characterization, and C-H Bond Activation Kinetics. *Science.* **2010**, *330*, 933–937.

(2) Green, M. T.; Dawson, J. H.; Gray, H. B. Oxoiron(IV) in Chloroperoxidase Compound II Is Basic: Implications for P450 Chemistry. *Science.* **2004**, *304*, 1653–1656.

(3) Yosca, T. H.; Rittle, J.; Krest, C. M.; Onderko, E. L.; Silakov, A.; Calixto, J. C.; Behan, R. K.; Green, M. T. Iron(IV)Hydroxide pK_a and the Role of Thiolate Ligation in C–H Bond Activation by Cytochrome P450. *Science.* **2013**, *342*, 825–829.

(4) Kurtz, D. M. Oxo- and Hydroxo-Bridged Diiron Complexes: A Chemical Perspective on a Biological Unit. *Chem. Rev.* **1990**, *90*, 585–606.

(5) Solomon, E. I.; Sundaram, U. M.; Machonkin, T. E. Multicopper Oxidases and Oxygenases. *Chem. Rev.* **1996**, *96*, 2563–2606.

(6) Holm, R. H.; Kennepohl, P.; Solomon, E. I. Structural and Functional Aspects of Metal Sites in Biology. *Chem. Rev.* **1996**, *96*, 2239–2314.

(7) Solomon, E. I.; Brunold, T. C.; Davis, M. I.; Kemsley, J. N.; Lee, S.-K.; Lehnert, N.; Neese, F.; Skulan, A. J.; Yang, Y.-S.; Zhou, J. Geometric and Electronic Structure/Function Correlations in Non-Heme Iron Enzymes. *Chem. Rev.* **2000**, *100*, 235–350.

(8) McEvoy, J. P.; Brudvig, G. W. Water-Splitting Chemistry of Photosystem II. *Chem. Rev.* **2006**, *106*, 4455–4483.

(9) Abu-Omar, M. M.; Loaiza, A.; Hontzeas, N. Reaction Mechanisms of Mononuclear Non-Heme Iron Oxygenases. *Chem. Rev.* **2005**, *105*, 2227–2252.

(10) Krest, C. M.; Onderko, E. L.; Yosca, T. H.; Calixto, J. C.; Karp, R. F.; Livada, J.; Rittle, J.; Green, M. T. Reactive Intermediates in Cytochrome P450 Catalysis. *J. Biol. Chem.* **2013**, *288*, 17074–17081.

(11) Cook, S. A.; Borovik, A. S. Molecular Designs for Controlling the Local Environments around Metal Ions. *Acc. Chem. Res.* **2015**, *48*, 2407–2414.

(12) Lee, J. L.; Ross, D. L.; Barman, S. K.; Ziller, J. W.; Borovik, A. S. C-H Bond Cleavage by Bioinspired Nonheme Metal Complexes. *Inorg. Chem.* **2021**, *60*, 13759–13783.

(13) Costas, M.; Mehn, M. P.; Jensen, M. P.; Que, L. Dioxygen Activation at Mononuclear Nonheme Iron Active Sites: Enzymes, Models, and Intermediates. *Chem. Rev.* **2004**, *104*, 939–986.

(14) Pecoraro, V. L.; Baldwin, M. J.; Gelasco, A. Interaction of Manganese with Dioxygen and Its Reduced Derivatives. *Chem. Rev.* **1994**, *94*, 807–826.

(15) Borovik, A. S. Bioinspired Hydrogen Bond Motifs in Ligand Design: The Role of Noncovalent Interactions in Metal Ion Mediated Activation of Dioxygen. *Acc. Chem. Res.* **2005**, *38*, 54–61.

(16) Hammes, B. S.; Young, V. G.; Borovik, A. S. Hydrogen-Bonding Cavities about Metal Ions: A Redox Pair of Coordinatively Unsaturated Paramagnetic Co-OH Complexes. *Angew. Chemie Int. Ed.* **1999**, *38*, 666–669.

(17) Oswald, V. F.; Lee, J. L.; Biswas, S.; Weitz, A. C.; Mittra, K.; Fan, R.; Li, J.; Zhao, J.; Hu, M. Y.; Alp, E. E.; Bominaar, E. L.; Guo, Y.; Green, M. T.; Hendrich, M. P.; Borovik, A. S. Effects of Noncovalent Interactions on High-Spin Fe(IV)–Oxido Complexes. *J. Am. Chem. Soc.* **2020**, *142*, 11804–11817.

(18) Schwarz, A. D.; Chu, Z.; Mountford, P. Sulfonamide-Supported Aluminum Catalysts for the Ring-Opening Polymerization of Rac-Lactide. *Organometallics* **2010**, *29*, 1246–1260.

(19) Park, Y. J.; Ziller, J. W.; Borovik, A. S. The Effects of Redox-Inactive Metal Ions on the Activation of Dioxygen: Isolation and Characterization of a Heterobimetallic Complex Containing a MnIII–(μ-OH)–CaII Core. *J. Am. Chem. Soc.* **2011**, *133*, 9258–9261.

(20) Lau, N.; Ziller, J. W.; Borovik, A. S. Sulfonamido Tripods: Tuning Redox Potentials via Ligand Modifications. *Polyhedron* **2015**, *85*, 777–782.

(21) Jones, J. R.; Ziller, J. W.; Borovik, A. S. Modulating the Primary and Secondary Coordination Spheres within a Series of CoII-OH Complexes. *Inorg. Chem.* **2017**, *56*, 1112–1120.

(22) Oswald, V. F.; Weitz, A. C.; Biswas, S.; Ziller, J. W.; Hendrich, M. P.; Borovik, A. S. Manganese−Hydroxido Complexes Supported by a Urea/Phosphinic Amide Tripodal Ligand. *Inorg. Chem.* **2018**, *57*, 13341–13350.

(23) Cook, S. A.; Ziller, J. W.; Borovik, A. S. Iron(II) Complexes Supported by Sulfonamido Tripodal Ligands: Endogenous versus Exogenous Substrate Oxidation. *Inorg. Chem.* **2014**, *53*, 11029–11035.
(24) Lacy, D. C.; Park, Y. J.; Ziller, J. W.; Yano, J.; Borovik, A. S. Assembly and Properties of Heterobimetallic Co(II/III)/Ca(II) Complexes with Aquo and Hydroxo Ligands. *J. Am. Chem. Soc.* **2012**, *134*, 17526–17535.
(25) Park, Y. J.; Cook, S. A.; Sickerman, N. S.; Sano, Y.; Ziller, J. W.; Borovik, A. S. Heterobimetallic Complexes with M^{III} -(μ-OH)-M^{II} Cores (M^{III} = Fe, Mn, Ga; M^{II} = Ca, Sr, and Ba): Structural, Kinetic, and Redox Properties. *Chem. Sci.* **2013**, *4*, 717–726.
(26) Sano, Y.; Weitz, A. C.; Ziller, J. W.; Hendrich, M. P.; Borovik, A. S. Unsymmetrical Bimetallic Complexes with M^{II}–(*μ*-OH)–M^{III} Cores ($M^{II}M^{III}$ = $Fe^{II}Fe^{III}$, $Mn^{II}Fe^{III}$, $Mn^{II}Mn^{III}$): Structural, Magnetic, and Redox. *Inorg. Chem.* **2013**, *52*, 10229–10231.
(27) Lau, N.; Sano, Y.; Ziller, J. W.; Borovik, A. S. Modular Bimetallic Complexes with a Sulfonamido-Based Ligand. *Dalt. Trans.* **2018**, *47*, 12362–12372.
(28) Lee, J. L.; Oswald, V. F.; Biswas, S.; Hill, E. A.; Ziller, J. W.; Hendrich, M. P.; Borovik, A. S. Stepwise Assembly of Heterobimetallic Complexes: Synthesis, Structure, and Physical Properties. *Dalt. Trans.* **2021**, *50*, 8111–8119.
(29) Kanan, M. W.; Nocera, D. G. In Situ Formation of an Oxygen-Evolving Catalyst in Neutral Water Containing Phosphate and Co2+. *Science.* **2008**, *321*, 1072–1075.
(30) Kanan, M. W.; Yano, J.; Surendranath, Y.; Dincă, M.; Yachandra, V. K.; Nocera, D. G. Structure and Valency of a Cobalt−Phosphate Water Oxidation Catalyst Determined by in Situ X-Ray Spectroscopy. *J. Am. Chem. Soc.* **2010**, *132*, 13692–13701.
(31) McAlpin, J. G.; Surendranath, Y.; Dinca, M.; Stich, T. A.; Stoian, S. A.; Casey, W. H.; Nocera, D. G.; Britt, R. D. EPR Evidence for Co (IV) Species Produced During Water Oxidation at Neutral PH. *J. Am. Chem. Soc.* **2010**, *132*, 6882–6883.
(32) Surendranath, Y.; Kanan, M. W.; Nocera, D. G. Mechanistic Studies of the Oxygen Evolution Reaction by a Cobalt-Phosphate Catalyst at Neutral PH. *J. Am. Chem. Soc.* **2010**, *132*, 16501–16509.
(33) Bediako, D. K.; Ullman, A. M.; Nocera, D. G. Catalytic Oxygen Evolution by Cobalt Oxido Thin Films. In *Topics in Current Chemistry*; Springer Verlag, 2015; Vol. 371, pp 173–214.
(34) Ullman, A. M.; Liu, Y.; Huynh, M.; Bediako, D. K.; Wang, H.; Anderson, B. L.; Powers, D. C.; Breen, J. J.; Abruña, H. D.; Nocera, D. G. Water Oxidation Catalysis by Co(II) Impurities in $Co(III)_4$ O_4 Cubanes. *J. Am. Chem. Soc.* **2014**, *136*, 17681–17688.
(35) Brodsky, C. N.; Hadt, R. G.; Hayes, D.; Reinhart, B. J.; Li, N.; Chen, L. X.; Nocera, D. G. In Situ Characterization of Cofacial Co(IV) Centers in Co4 O4 Cubane: Modeling the High-Valent Active Site in Oxygen-Evolving Catalysts. *Proc. Natl. Acad. Sci. USA* **2017**, *114*, 3855–3860.
(36) Song, F.; Hu, X. Ultrathin Cobalt−Manganese Layered Double Hydroxide Is an Efficient Oxygen Evolution Catalyst. *J. Am. Chem. Soc.* **2014**, *136*, 16481–16484.
(37) Zhang, X.; Chen, Q.-F.; Deng, J.; Xu, X.; Zhan, J.; Du, H.-Y.; Yu, Z.; Li, M.; Zhang, M.-T.; Shao, Y. Identifying Metal-Oxo/Peroxo Intermediates in Catalytic Water Oxidation by In Situ Electrochemical Mass Spectrometry. *J. Am. Chem. Soc.* **2022**, *144*, 17748–17752.
(38) Egan, J. W.; Theopold, K. H. Trans-Tetrakis(3-Tert-Butyl-5-Methylpyrazole)Bis(Tetrafluoroborato) Cobalt(II), a Complex with Two Coordinated Tetrafluoroborate Anions. *Acta Crystallogr., Sect. C Cryst. Struct. Commun.* **1990**, *C46*, 1013–1015.
(39) Reinaud, O. M.; Theopold, K. H. Hydrogen Tunneling in the Activation of Dioxygen by a Tris(Pyrazolyl)Borate Cobalt Complex. *J. Am. Chem. Soc.* **1994**, *116*, 6979–6980.
(40) Nam, W.; Kim, I.; Kim, Y.; Kim, C. Biomimetic Alkane Hydroxylation by Cobalt(III) Porphyrin Complex and m-Chloroperbenzoic Acid. *Chem. Commun.* **2001**, *14*, 1262–1263.
(41) Goetz, M. K.; Hill, E. A.; Filatov, A. S.; Anderson, J. S. Isolation of a Terminal Co(III)-Oxo Complex. *J. Am. Chem. Soc.* **2018**, *140*, 13176–13180.
(42) Goetz, M. K.; Anderson, J. S. Experimental Evidence for pK_a-Driven Asynchronicity in C−H Activation by a Terminal Co(III)−Oxo Complex. *J. Am. Chem. Soc.* **2019**, *141*, 4051–4062.

(43) Andris, E.; Navrátil, R.; Jašík, J.; Srnec, M.; Rodríguez, M.; Costas, M.; Roithová, J. M−O Bonding Beyond the Oxo Wall: Spectroscopy and Reactivity of Cobalt(III)-Oxyl and Cobalt(III)-Oxo Complexes. *Angew. Chemie Int. Ed.* **2019**, *58*, 9619–9624.
(44) Miessler, G. L.; Fischer, P. J.; Tarr, D. A. *Inorganic Chemistry*, Fifth.; Pearson: Upper Saddle River, NJ, 2014.
(45) Goetz, M. K.; Anderson, J. S. Experimental Evidence for PKa-Driven Asynchronicity in C-H Activation by a Terminal Co(III)-Oxo Complex. *J. Am. Chem. Soc.* **2019**, *141*, 4051–4062.
(46) Nurdin, L.; Spasyuk, D. M.; Fairburn, L.; Piers, W. E.; Maron, L. Oxygen–Oxygen Bond Cleavage and Formation in Co(II)-Mediated Stoichiometric O2 Reduction via the Potential Intermediacy of a Co(IV) Oxyl Radical. *J. Am. Chem. Soc.* **2018**, *140*, 16094–16105.
(47) Bigotto, A; Zangrando, E.; Randaccio, L. Structural Chemistry of Alkylcobaloximes. Structural Evidence for a Hydroxocobaloxime and Molecular Structure of Trans-Bis(Dimethyl-Glyoximato) Methylpyridinecobalt(III) and Trans-Bis(Dimethylglyoximato)-Methyl(3-N-Methyl Imidazole)Cobalt (III). *J. Chem. Soc., Dalton Trans.* **1976,** *2*, 96–104.
(48) Hana, F.; Lough, A. J.; Lavoie, G. G. Coordinatively- and Electronically-Unsaturated Square Planar Cobalt(III) Complexes of a Pyridine Dianionic Pincer Ligand. *Dalt. Trans.* **2017**, *46*, 16228.
(49) Poth, T.; Paulus, H.; Elias, H.; Eldik, R. van; Grohmann, A. Kinetics and Mechanism of Base Hydrolysis in Cobalt(III) Complexes – The Case of a Complex CoLCl2+ Where L Has the Novel Topology of a Square-Pyramidal NN4 Coordination Cap. *Eur. J. Inorg. Chem.* **1999**, *1999*, 643–650.
(50) Kucharski, E. S.; Skelton, B. W.; White, A. H. Crystal Structure of Carbonatohydroxo- (2, 2', 6', 2''-Terpyridyl)Cobalt(III) Tetrahydrate. *Aust. J. Chem.* **1978**, *31*, 47–51.
(51) Addison, A. W.; Rao, T. N.; Reedijk, J.; van Rijn, J.; Verschoor, G. C. Synthesis, Structure, and Spectroscopic Properties of Copper(II) Compounds Containing Nitrogen-Sulphur Donor Ligands; the Crystal and Molecular Structure of Aqua[1,7-Bis(N-Methylbenzimidazol-2[Prime or Minute]-Yl)-2,6-Dithiaheptane]Copper(II) Perchlorate. *J. Chem. Soc., Dalt. Trans.* **1984**, *7*, 1349–1356.
(52) Wilson, R. J.; Jones, J. R.; Bennett, M. V. Unprecedented Gallium-Nitrogen Anions: Synthesis and Characterization of [(Cl3Ga)3N]3- and [(Cl3Ga)2NSnMe3]2-. *Chem. Commun.* **2013**, *49*, 5049–5051.
(53) Weitz, A. C.; Hill, E. A.; Oswald, V. F.; Bominaar, E. L.; Borovik, A. S.; Hendrich, M. P.; Guo, Y. Probing Hydrogen Bonding Interactions to Iron-Oxido/Hydroxido Units by ^{57}Fe Nuclear Resonance Vibrational Spectroscopy. *Angew. Chemie Int. Ed.* **2018**, *57*, 16010–16014.
(54) Oswald, V. F. Tripodal Phosphoryl Amide Frameworks: Investigating The Relationship Between High Valent Metal–Oxido And Metal–Hydroxido Complexes, University of California, Irvine, 2018.
(55) Morassi, R.; Bertini, I.; Sacconi, L. Five-Coordination in Iron(II); Cobalt(II) and Nickel(II) Complexes. *Coord. Chem. Rev.* **1973**, *11*, 343–402.
(56) Sickerman, N. S.; Park, Y. J.; Ng, G. K.-Y.; Bates, J. E.; Hilkert, M.; Ziller, J. W.; Furche, F.; Borovik, A. S. Synthesis, Structure, and Physical Properties for a Series of Trigonal Bipyramidal MII–Cl Complexes with Intramolecular Hydrogen Bonds. *Dalt. Trans.* **2012**, *41*, 4358.
(57) Lucas, R. L.; Zart, M. K.; Murkerjee, J.; Sorrell, T. N.; Powell, D. R.; Borovik, A. S. A Modular Approach toward Regulating the Secondary Coordination Sphere of Metal Ions: Differential Dioxygen Activation Assisted by Intramolecular Hydrogen Bonds. *J. Am. Chem. Soc.* **2006**, *128*, 15476–15489.
(58) Pfaff, F. F.; Kundu, S.; Risch, M.; Pandian, S.; Heims, F.; Pryjomska-Ray, I.; Haack, P.; Metzinger, R.; Bill, E.; Dau, H.; Comba, P.; Ray, K. An Oxocobalt(IV) Complex Stabilized by Lewis Acid Interactions with Scandium(III) Ions. *Angew. Chemie Int. Ed.* **2010**, *50*, 1711–1715.
(59) Ray, M.; Hammes, B. S.; Yap, G. P. A.; Rheingold, A. L.; Borovik, A. S. Structure and Physical Properties of Trigonal Monopyramidal Iron(II), Cobalt(II), Nickel(II), and Zinc(II) Complexes. *Inorg. Chem.* **1998**, *37*, 1527–1532.
(60) Dori, Z.; Gray, H. B. High-Spin, Five-Coordinate Cobalt(II) Complexes. *Inorg. Chem.* **1968**, *7*, 889–892.
(61) Ciampolini, M.; Nardi, N.; Speroni, G. P. Five-Coordinated Complexes of 3d Bivalent Metal Ions with Polyamines. *Coord. Chem. Rev.* **1966**, *1*, 222–233.
(62) Pegis, M. L.; Roberts, J. A. S.; Wasylenko, D. J.; Mader, E. A.; Appel, A. M.; Mayer, J. M. Standard Reduction Potentials for Oxygen and Carbon Dioxide Couples in Acetonitrile and N,N-Dimethylformamide. *Inorg. Chem.* **2015**, *54*, 11883–11888.

(63) Pegis, M. L.; Roberts, J. A. S.; Wasylenko, D. J.; Mader, E. A.; Appel, A. M.; Mayer, J. M. Erratum: Standard Reduction Potentials for Oxygen and Carbon Dioxide Couples in Acetonitrile and N, N-Dimethylformamide *Inorg. Chem.* **2020**, *59*, 8638.
(64) Carney, M. J.; Lesniak, J. S.; Likar, M. D.; Pladziewicz, J. R. Ferrocene Derivatives as Metalloprotein Redox Probes: Electr on-Transfer Reactions of Ferrocene and Ferricenium Ion Derivatives with Cytochrome C. *J. Am. Chem. Soc.* **1984**, *10*, 2565–2569.
(65) Connelly, N. G.; Geiger, W. E. Chemical Redox Agents for Organometallic Chemistry. *Chem. Rev.* **1996**, *96*, 877–910.
(66) Pegis, M. L.; Wise, C. F.; Martin, D. J.; Mayer, J. M. Oxygen Reduction by Homogeneous Molecular Catalysts and Electrocatalysts. *Chem. Rev.* **2018**, *118*, 2340–2391.
(67) Que, L. J. *Physical Methods in Bioinorganic Chemistry - Spectroscopy and Magnetism*; 2000.
(68) Warren, J. J.; Tronic, T. A.; Mayer, J. M. Thermochemistry of Proton-Coupled Electron Transfer Reagents and Its Implications. *Chem. Rev.* **2010**, *110*, 6961–7001.
(69) Lloveras, V.; Liko, F.; Pinto, L. F.; Muñoz-Gómez, J. L.; Veciana, J.; Vidal-Gancedo, J. Tuning Spin-Spin Interactions in Radical Dendrimers. *ChemPhysChem* **2018**, *19*, 1895–1902.
(70) Barman, S. K.; Jones, J. R.; Sun, C.; Hill, E. A.; Ziller, J. W.; Borovik, A. S. Regulating the Basicity of Metal−Oxido Complexes with a Single Hydrogen Bond and Its Effect on C−H Bond Cleavage. *J. Am. Chem. Soc.* **2019**, *141*, 11142–11150.
(71) Jones, R. N. The Ultraviolet Absorption Spectra of Anthracene Derivatives. *Chem. Rev.* **1947**, *41*, 353–371.
(72) Fisher, K. J.; Feuer, M. L.; Lant, H. M. C.; Mercado, B. Q.; Crabtree, R. H.; Brudvig, G. W. Concerted Proton-Electron Transfer Oxidation of Phenols and Hydrocarbons by a High-Valent Nickel Complex. *Chem. Sci.* **2020**, *11*, 1683–1690.
(73) Manner, V. W.; Markle, T. F.; Freudenthal, J. H.; Roth, J. P.; Mayer, J. M. The First Crystal Structure of a Monomeric Phenoxyl Radical: 2,4,6-Tri-Tert-Butylphenoxyl Radical. *Chem. Commun.* **2007**, *2*, 256–258.
(74) Sheldrick, G. M. SADABS. Bruker AXS, Inc: Madison 2014.
(75) Bruker AXS Inc, SAINT Version 8.34a. Madison, WI 2013.
(76) Krause, L.; Herbst-Irmer, R.; Sheldrick, G. M.; Stalke, D. Comparison of Silver and Molybdenum Microfocus X-Ray Sources for Single-Crystal Structure Determination. *J. Appl. Crystallogr.* **2015**, *48*, 3–10.
(77) Sheldrick, G. M.; IUCr. Crystal Structure Refinement with SHELXL. *Acta Crystallogr. Sect. A Found. Crystallogr.* **2015**, *71*, 3–8.
(78) Sheldrick, G. M. A Short History of SHELX. *Acta Crystallogr. Sect. A Found. Crystallogr.* **2008**, *64*, 112–122.
(79) Hübschle, C. B.; Sheldrick, G. M.; Dittrich, B. ShelXle: A Qt Graphical User Interface for SHELXL. *J. Appl. Crystallogr.* **2011**, *44*, 1281–1284.
(80) Kratzert, D. FinalCif.
(81) Sheldrick, G. M.; IUCr. Crystal Structure Refinement with SHELXL. *Acta Crystallogr., Sect. C Cryst. Struct. Commun.* **2015**, *71*, 3–8.

Chapter 3: Preparation and properties of a $[Co^{III}–\mu\text{-}OH–Zn^{II}]^+$ complex from a proposed Co^{II}–IBX-^{i}Pr adduct

Introduction

Multimetallic systems are of importance in both biology and synthetic chemistry. These systems can efficiently carry out challenging molecular transformations and drive multi-proton/electron reactivity through metal-metal cooperativity.[1–5] In many biological examples, the multimetallic active sites feature high-valent metal ions in unsymmetric coordination environments, such as the di-Fe site in the hydroxylase component of methane monooxygenase,[4,6–14] MnFe-based ribonucleotide reductase (RNR),[15–17] and the oxygen evolving complex (OEC) of photosystem II featuring the tetranuclear Mn cubane.[18] While natural systems have evolved unsymmetric binding sites within the active sites of metalloproteins, synthesizing unsymmetric bimetallic complexes is more challenging. These challenges largely arise from the propensity of synthetic bimetallic systems to form highly symmetric species with the same ligand frameworks about both metal ions[19–36] (Fig 3-1).[35] In order to break this symmetry, it is necessary to design molecular complexes that support differentiation within their ligand fields. Researchers have found success with designing ligand frameworks that incorporate unique binding sites to support the formation of unsymmetrical bimetallic species.[37–49]

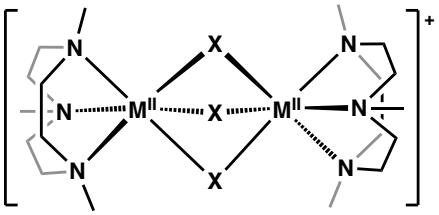

Figure 3-1: Representation of a synthetic bimetallic complex featuring symmetric ligand fields.

In the Borovik Lab, we have focused on the design of ligand frameworks that support secondary (2°) coordination sphere interactions through the incorporation of hydrogen-bond (H–bond) donating and accepting groups. Work with a previous ligand framework, $[MST]^{3-}$ (*N,N′,N″*-[2,2′,2″-nitrilotris(ethane-2,1-diyl)]tris(2,4,6-trimethylbenzenesulfonamido), showed that the sulfonamido groups introduced as H–bond acceptors can also act as an auxiliary binding site for a second metal ion.[50–55] While the sulfonamido-based

ligand frameworks proved adept at supporting unsymmetric bimetallic complexes, it was found that metal ions coordinated by the tris-2-amino ethylamine (tren) backbone were unable to access oxidation states above M^{III} (Fig 3-2).[56] Given the desire to study higher-valent metal complexes, the group turned to a new ligand framework, *N,N′,N″*-[nitrilotris(ethane-2,1-diyl)]tris(P,P-diphenylphosphinic amido), $[poat]^{3-}$.[57] The phosphinic amido (P=O) groups featured within the 2º coordination sphere act both as H–bond acceptors and a second binding site for an additional metal ion, similar to $[MST]^{3-}$, while supporting metal ions in oxidation states up to M^{IV} (Fig 3-2).[57] Recent work within the group has explored the bimetallic chemistry of $[poat]^{3-}$ resulting in the successful preparation of several unsymmetric bimetallic complexes.[57–60] The work described in this chapter focuses on the preparation of unsymmetric bimetallic complexes from a Co^{II} complex within $[poat]^{3-}$, an oxygen-atom transfer reagent, and $[Zn^{II}Me_3tacn(OTf)_2]$ to act as the auxiliary metal ion (OTf^- = trifluoromethanesulfonate, Me_3tacn = 1,4,7-trimethyl-1,4,7-triazacyclononane).

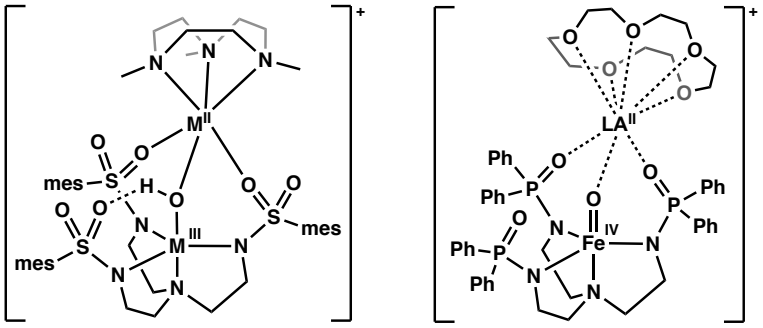

Figure 3-2: Examples from the Borovik lab of synthetic bimetallic complexes with unsymmetric ligand fields.

In addition to designing unsymmetric bimetallic species, the preparation of high-valent metal complexes is of interest to chemists. To access higher-valent oxidation states, starting metal complexes may be oxidized in a variety of ways. One method to efficiently oxidize metal complexes is through the use of oxygen-atom (O-atom) transfer reagents. O-atom transfer reagents typically catalyze a two-electron oxidation of a metal ion concomitant to the two-electron reduction of the oxygen atom and its binding to the metal ion as an oxido ligand.[61] Hypervalent iodine reagents, such as idosoylbenzene (PhIO) and related iodosylarene derivatives, have acted as competent oxidants for the formation of high-valent metal-oxido species via O-atom transfer to a

lower-valent starting synthon.[51,57,62–69] In these examples, the iodosylarene reagent is proposed to first coordinate to the metal center, then transfer its O-atom resulting in the formation of a M–O or –OH complex. In addition to reactions where a M–O or –OH species is formed upon addition of an O-atom transfer reagent, there are further examples where metal-oxidant adducts are formed.[70–78] These adducts have been shown to be competent oxidants for C–H bond activations, epoxidations, hydroxylations, and O-atom transfer to substrates. However, metal-oxidant adducts are typically characterized spectroscopically and cannot be crystallized due to their instability. Recent work by Hill and coworkers resulted in the successful crystallization and structural characterization of a series of Co^{II}–OIPh adducts.[70] Reactivity studies were also performed, which confirmed that the Co^{II}–OIPh oxidant adduct was the competent oxidant to drive C–H bond activation.

While Hill *et al* found that Co^{II}–OIPh adducts were isolable without oxidation of the metal center, work from the Nam and Ray labs found that the addition of Lewis acidic, redox-inactive metal ions led to activation of proposed intermediate Co^{II}–OIPh adducts.[62,69,70] Addition of redox-inactive metal ions further acted to stabilize the proposed high-valent Co–O product via formation of bimetallic species with Co–O–M cores. While the oxidative load of these reactions is borne by the Co-center and the second metal ion serves to activate the Co^{II}–OIPh adduct, both metal ions are needed for the overall reaction to proceed. In the examples from the Nam and Ray labs, the identity of the bimetallic product was assigned as LCo^{IV}–O–M^n, where L was a tetraamido macrocyclic ligand (TAML) and tris[2-(N-tetramethylguanidyl)ethyl]amine (TMG_3tren) respectively (Fig 3-3).[62,69] In both examples, the Co oxidation state was assigned based on spectroscopic data including EPR and X-ray absorption spectroscopies (XAS), however crystallographic evidence of these species was not obtained. Furthermore, a re-examination of the data collected by Pfaff *et al* found that the EPR spectra

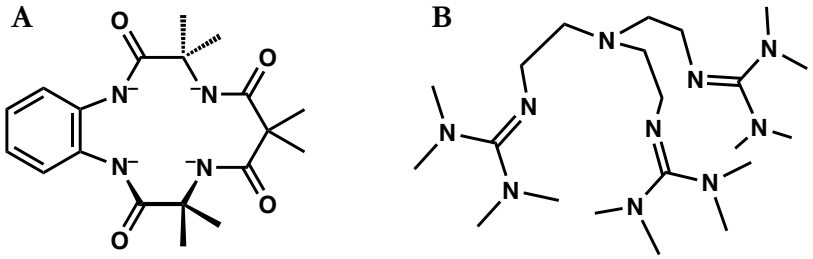

Figure 3-3: Representation of the TAML (**A**) and the TMG_3tren (**B**) ligands used by the Nam and Ray labs to prepare LCo^{IV}–O–$M^{n+}$from Co–OIPh intermediates.

showed few changes between the [Co^{II}TMG$_3$tren(OTf)]OTf starting synthon and the proposed [TMG$_3$trenCo^{IV}–O–Sc^{III}]$^{5+}$ product.[62] Additionally, the electronic absorption spectra were more consistent with examples of Co^{III}–OH species in C_3 symmetric ligand fields,[51,79–81] leading to the suggestion that the bimetallic species formed was not [TMG$_3$trenCo^{IV}–O–Sc^{III}]$^{5+}$ but was likely [TMG$_3$trenCo^{III}–OH–Sc^{III}]$^{4+}$.[51,62,68] Additionally, the oxidation state of the Co center in the proposed [(TAML)Co^{IV}–O–M^n]$^{m+}$ complex cannot be unambiguously assigned due to the potential redox active nature of the TAML ligand backbone, which may play a role in the formation of this complex.[69,82] Therefore, there are still questions regarding the reactivity between Co^{II} metal complexes with O-atom transfer reagents in the presence of secondary metal ions, including whether the product of these types of reactions is a Co^{IV}–O–M^n or some Co^{III}–O(H)–M^n species.

This chapter discusses a high-valent bimetallic complex containing a Co–O(X)–M core that was prepared from the reaction of a starting Co^{II} synthon with an O-atom transfer reagent, in the presence of a redox inactive metal ion. A four-coordinate trigonal monopyramidal Co^{II} complex was first prepared with the [poat]$^{3-}$ ligand. Upon treatment with an O-atom transfer reagent, isopropyl 2-iodoxybenzoate (IBX-*i*Pr), a proposed Co^{II}–IBX-*i*Pr adduct was formed, which readily converted to a [Co^{III}–μ-OH–Zn^{II}]$^+$ species in the presence of a Zn^{II} complex, [Zn^{II}Me$_3$tacn(OTf)$_2$].

Results and Discussion

Synthesis and Characterization of K[Co^{II}poat]

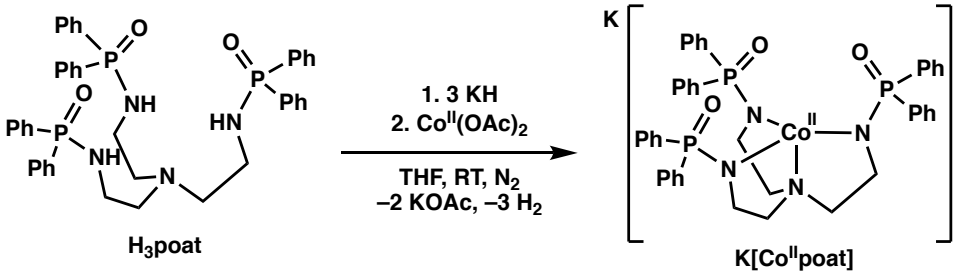

Scheme 3-1: Synthetic procedure for preparation of K[Co^{II}poat].

Synthesis: K[Co^{II}poat] (K[**1**]) was prepared according to the reaction shown in Scheme 3-1, adapted from a previously reported procedure.[83] K[**1**] can be prepared either from *N,N'*-dimethylacetamide (DMA) or tetrahydrofuran (THF) following the same basic procedures. In the initial syntheses, THF was chosen as the solvent for this reaction because it is more easily removed *in vacuo* than DMA and metal complexes supported

by $[poat]^{3-}$ had been previously prepared in THF.[57,59] In typical preparation, H_3poat was dissolved in THF and stirred with KH until bubbling ceased and a clear, colorless solution was obtained. At this point, $Co^{II}(OAc)_2$ was added as a solid, giving a suspension with purple chunks. The reaction mixture was stirred overnight and a bright blue powder precipitated. The resulting suspension was filtered to give a faintly blue filtrate with blue solids remaining on the frit. The solids were washed with dichloromethane (DCM) until all blue powder had been dissolved to give a bright blue filtrate and white powder (KOAc), which was further washed. The blue filtrate was subsequently dried to a solid, redissolved in DCM, and layered under *n*-pentane. This layering resulted in bright blue, block shaped single crystals suitable for study by X-ray diffraction methods to obtain the molecular structure of K[**1**].

While H_3poat was soluble in THF, $[poat]^{3-}$ was significantly less so. If the metal salt was not rapidly introduced to the reaction after bubbling ceased following addition of KH, white solids precipitated out faster than the metal salt dissolved into solution to form the metal complex. The white solids were likely $K_3[poat]$ or some similar potassium salt of the pre-ligand H_3poat and were insoluble, precipitating rapidly. If the metal salt was introduced after a small amount of white precipitate formed, it was found that metallation did not proceed, leading to isolation of large quantities of solids. Furthermore, the resulting solids were a mixture of white and purple powders, consistent with isolation of the proposed $K_3[poat]$ salt or the pre-ligand and $Co^{II}(OAc)_2$. These observations suggested that the metallation was unsuccessful. In addition to the observed solubility issues with $[poat]^{3-}$, $Co^{II}(OAc)_2$ also exhibited poor solubility in THF which likely contributed to the ineffective metallation reactions.

To avoid solubility issues, the solvent was changed from THF to DMA. While DMA is significantly less volatile than THF, $K_3[poat]$ was far more soluble in DMA. The synthetic procedures described above in THF remained unchanged, except for the solvent. Following deprotonation which yielded a clear, faintly yellow solution, $Co^{II}(OAc)_2$ was added as a solid to the reaction to give a cloudy, dark blue mixture. The reaction was left to stir overnight and gave a cloudy, paler blue suspension with far less precipitate than reactions performed in THF. This suspension was subsequently filtered to give a pale blue filtrate and faintly blue solid. The solid was washed with DCM until the washings appeared colorless and a white solid persisted. The color and mass

balance of this solid was consistent with the isolation of two equivalents of KOAc, rather than K_3[poat] or $Co^{II}(OAc)_2$. The blue filtrate was then washed and the solution was dried to a blue solid. This solid was immediately redissolved in DCM and layered under pentane to obtain blocky, blue single crystals suitable for X-ray diffraction (XRD) studies. Despite carrying out the reactions in different solvents, there was no difference in the crystalline product isolated from layering of DCM and *n*-pentane.

Structural Properties: The molecular structure of K[**1**] revealed a four-coordinate trigonal monopyramidal (TMP) Co ion, coordinated to the four N-atoms from the tren backbone of the $[poat]^{3-}$ ligand (Fig 3-3). The bond lengths were consistent with those expected for a four-coordinate Co^{II} ion in C_3 symmetric ligand environments ranging between 1.94 – 1.97 Å, while the Co–N_{ax} bond lengths were longer than 2 Å (Table 3-1).[51,81,84] The N_{ax}–Co–N_{eq} bond angles of K[**1**] were less than 90º, the ideal angle expected for a TMP coordination

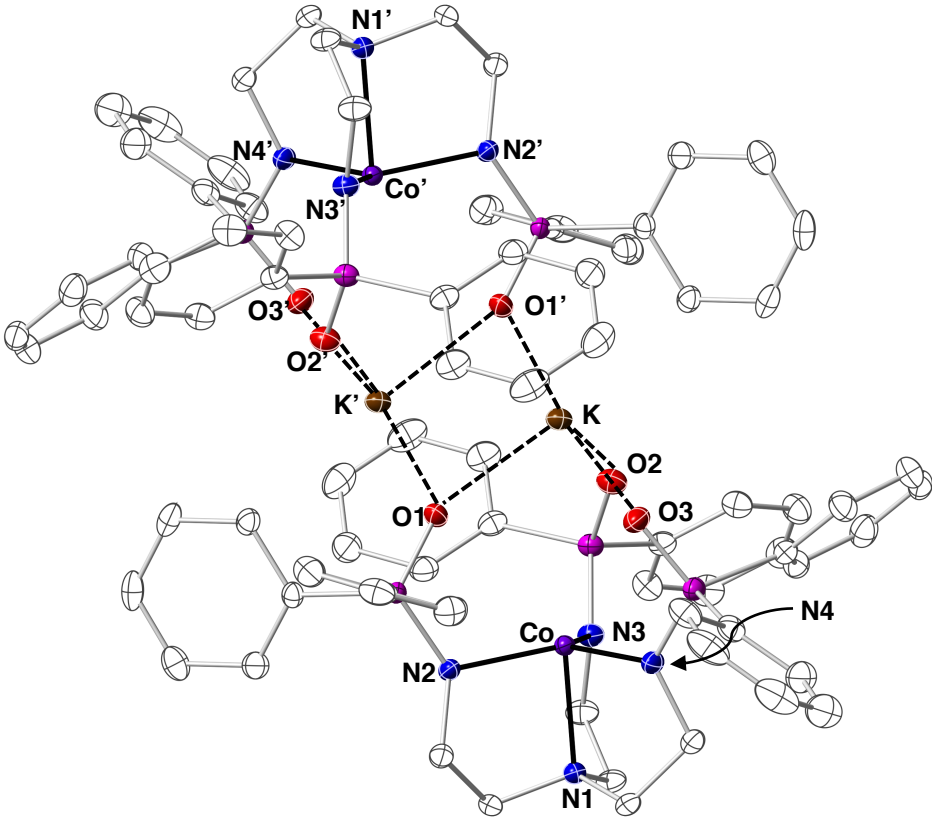

Table 3-1: Metrical data obtained from the molecular structure of $(K[Co^{II}poat])_2$.

Bond	Distance, Å
Co–N1	2.124(1)
Co–N2	1.973(1)
Co–N3	1.948(1)
Co–N4	1.957(1)
Co···K	3.7880(4)
Atoms	**Angles, º**
N1–Co–N2	84.70(5)
N1–Co–N3	85.03(5)
N1–Co–N4	84.82(5)
N2–Co–N3	115.80(5)
N2–Co–N4	122.27(5)
N3–Co–N4	119.54(5)
N_{eq}···Co, 0.176 Å	

Figure 3-4: Molecular structure of the dinuclear $(K[Co^{II}poat])_2$ molecule with thermal ellipsoid representation. Thermal ellipsoids are drawn at 50% probability.

environment. Despite the discrepancies in these bond angles, the Co atom was only puckered up out of the plane formed by the three N_{eq} atoms by 0.176 Å.

Perhaps the most notable aspect of this structure is that K[**1**] does not crystallize as a single unit, but rather as a cluster, $(K[Co^{II}poat])_2$. In this cluster, two $[Co^{II}poat]^-$ anions are held together by electrostatic interactions with K^+ ions. In examining one $K[Co^{II}poat]$ unit (Fig 3-S1), each of the P=O group O-atoms (O1, O2, and O3) interact with a single K^+ ion. This K^+ ion then bridges to another unit of $[Co^{II}poat]^-$ through O1'. Overall, each K^+ interacts with four O-atoms. In early synthetic attempts, Me_4NOAc was added to the reaction to metathesize the K^+ counterion. Whether or not the metathesis was successful in solution, the product which crystallized out of solution was $(K[Co^{II}poat])_2$. Given how closely the K^+ ions interact with the $[Co^{II}poat]^-$ anions, it is unsurprising that metathesis was unsuccessful. Furthermore, attempts to prepare putative Co^{II}–OH or Co^{II}–OH_2 complexes were made either by adding water to act as an exogenous ligand to the Co^{II} center *in situ* or to redissolved, crystalline $(K[Co^{II}poat])_2$. While a color change from bright blue to a pink-purple solution could be qualitatively observed, any attempts to crystallize the product(s) of these reactions resulted once again in the formation of crystalline $(K[Co^{II}poat])_2$ rather than the expected species. These observations suggest that $(K[Co^{II}poat])_2$ may be exceedingly stable in the solid state, perhaps due to the propensity for $[poat]^{3-}$ to form bimetallic species. Furthermore, the strong interaction between the K^+ ion and the P=O units confirm that this functional group acts as a scaffold to assemble discrete bimetallic complexes.

Spectroscopic and Electrochemical Characterization: Following structural studies, $(K[Co^{II}poat])_2$ was characterized spectroscopically. Studies were performed in DCM unless otherwise specified, because $(K[Co^{II}poat])_2$ was soluble without needing to employ an encapsulating reagent, such as 18-crown-6 (18c6) ether. Nevertheless, all spectroscopic studies were performed in the presence of excess (greater than 2 equivalents) 18c6 to ensure full encapsulation of the K^+ ion. The ⊥-mode EPR spectrum of dissolved $(K[Co^{II}poat])_2$ was measured in DCM:THF with excess 18c6 at 17 K (Fig 3-4, B). The spectrum revealed a near-axial $S = 3/2$ signal from a high-spin Co^{II} center, with features at g = 4.5, 4.3, and 2.0. This signal is consistent with literature precedent for Co^{II} ions in C_3 symmetric ligand fields, which largely appear near perfect axiality regardless of the presence or absence of a fifth ligand.[51,62,81,85] This signal was simulated with an E/D of 0.0029 and an estimated D value

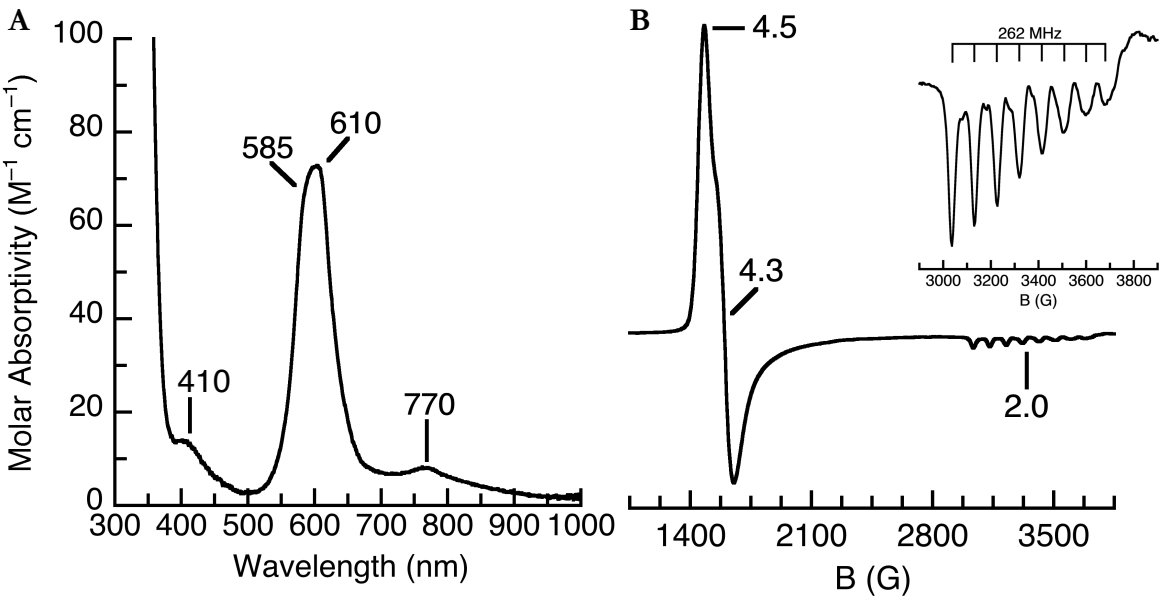

Figure 3-5: (**A**) Electronic absorption spectrum of **1** collected in DCM at 25 ºC. (**B**) ⊥-mode EPR spectrum of K[Co^{II}poat], measured with excess 18c6 in DCM:THF at 17 K.

of +3.6 cm^{-1}. The feature at g = 2.0 was split into an 8-line hyperfine pattern consistent with a single Co ion in solution (^{59}Co, I = 7/2; A = 262 MHz). For spectra featuring a mononuclear Co ion, an 8-line hyperfine pattern is expected. If (K[Co^{II}poat])$_2$ remained intact in solution, then it is possible that multiple sets of hyperfine may have been observed, similar to K$_2$[Co^{II}H$_2$pout(OH)] (see Chapter 2). Because only one set of ^{59}Co hyperfine was observed, the EPR spectrum supported the dissociation of (K[Co^{II}poat])$_2$ in solution in the presence of 18c6. From here on the mononuclear representation, K[Co^{II}poat] (K[**1**]), will be used to describe this molecule.

In addition to characterizing the magnetic properties of K[**1**] with ⊥-mode EPR spectroscopy, a room temperature effective magnetic moment was measured. The μ_{eff} value, 4.28 μ_B, was obtained via Evans' Method NMR spectroscopy in DCM. The theoretical spin-only magnetic moment for a S = 3/2 spin system is 3.87 μ_B. While the experimental magnetic moment is higher than the spin-only magnetic moment, it is well within the range of values reported for previously reported Co^{II} ions in TMP environments.[84,86] Both the ⊥-mode EPR spectrum and the Evans' Method data support the assignment of the Co^{II} spin state as high-spin, S = 3/2.

The electronic absorption (UV-vis) spectrum of K[**1**] was collected. A solution of K[Co^{II}poat] appeared blue with absorbance features at λ_{max} = 410, 585, 610, 770 nm (Fig 3-4, A). These features were weak in intensity, between ~ 10 – 70 M^{-1} cm^{-1} consistent with *d–d* transitions as expected for a Co^{II} ion in TMP geometry.

Furthermore, the energies and shapes of these absorption features were similar to literature examples of TMP Co^{II} complexes.[51,81,84,86–91] Specifically, Banci *et al* and Ray *et al* assigned the electronic transitions in TMP Co^{II} complexes, assuming local C_{3v} symmetry.[84,87,92] K[**1**] exhibited a similar absorption profile, with a relatively symmetrical band at λ_{max} = 358 nm, an unsymmetric band spanning 585 – 610 nm, and a smaller feature at λ_{max} = 770 nm. The band at λ_{max} = 358 nm was assigned as a $^4A_2 \longrightarrow {}^4A_2$ transition. The features at λ_{max} = 585 and 770 nm were assigned as $^4A_2 \longrightarrow {}^4E$ transitions based on the literature assignments discussed above.

The electrochemical properties of K[Co^{II}poat] were studied by cyclic voltammetry (CV). The voltammogram of K[Co^{II}poat] was first measured in DCM without 18c6. In the absence of 18c6, the full voltammogram exhibited multiple electrochemical events (Fig 3-S2, A). These events did not appear reversible. They were difficult to identify and assign and the electrochemical events could not be isolated from the whole voltammogram without losing significant current intensity. The poor reversibility and larger number of electrochemical events likely stemmed from the clustering of K[**1**] in the solid state. As discussed above, the K^+ ion interacts with the P=O units of the ligand and may not dissociate fully in solution without the use of 18c6.

To further understand the electrochemical behavior of **1**, cyclic voltammograms were collected in the presence of 18c6. Upon introduction of excess 18c6, the open circuit potential of the complex shifts to a more negative potential, consistent with dissociation of the K^+ cation from the [Co^{II}poat]$^-$ anion and more localization of the negative charge on the Co complex. The full voltammogram exhibited a redox couple as well as an irreversible oxidation (Fig 3-5). The couple was identified at $E_{1/2}$ = –0.495 V versus ferrocene ($Fc^{+/0}$), which has been assigned as the $Co^{III/II}$ couple. This event is reversible, with a peak-to-peak separation of 80 mV and a current ratio of 0.96 (i_{pa}/i_{pc}), in comparison to the internal $Fc^{+/0}$ reference couple (ΔE = 70 mV, i_{pa}/i_{pc} = 0.92). The second electrochemical event was an irreversible oxidative wave at E_{pa} = +0.440 mV versus $Fc^{+/0}$, which did not exhibit a return reduction (Fig 3-S2, B).

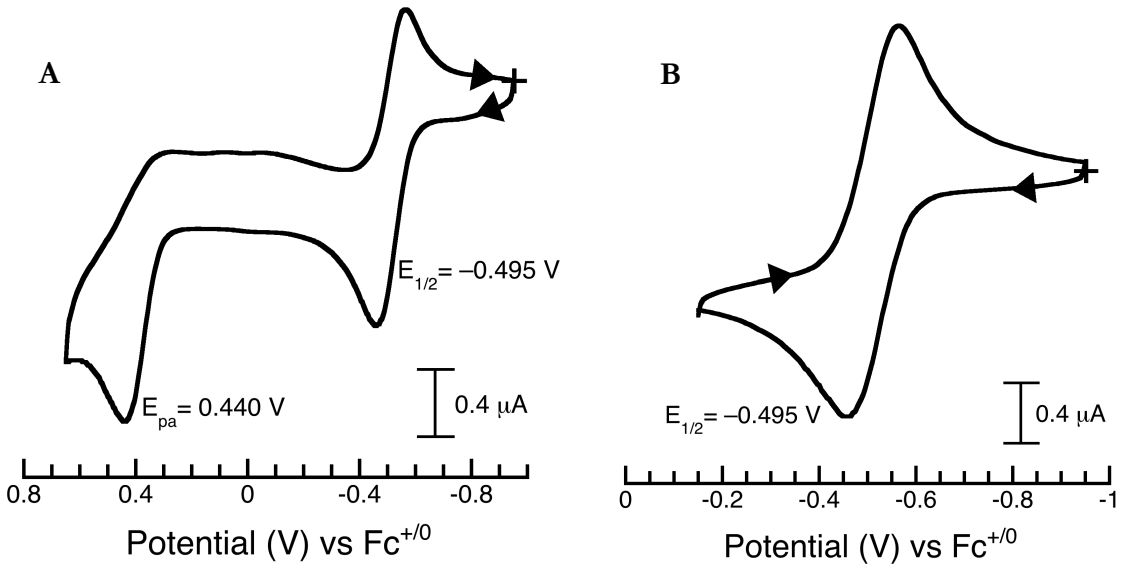

Figure 3-6: Cyclic voltammogram showing the full electrochemical profile (**A**) and the first redox event (**B**) in K[Co^{II}poat] measured in DCM, with excess 18c6.

Addition of an Oxygen Atom Transfer Reagent to 1

Spectroscopic Studies: Given the desire to access high-valent intermediates, **1** was treated with IBX-*i*Pr with the intention of preparing a proposed Co^{IV}–oxido complex. As discussed above, IBX-*i*Pr acts as an O-atom transfer reagent and has been shown to successfully prepare M^{IV}–O intermediates.[51,57,61–69] Immediately upon addition of IBX-*i*Pr to **1**, a new, pale-pink species formed with a distinct UV-vis spectrum with features at λ_{max} = 500, 550, 600, 770 nm (Fig 3-6, A). The shift in these bands is similar to the energetic differences observed in the

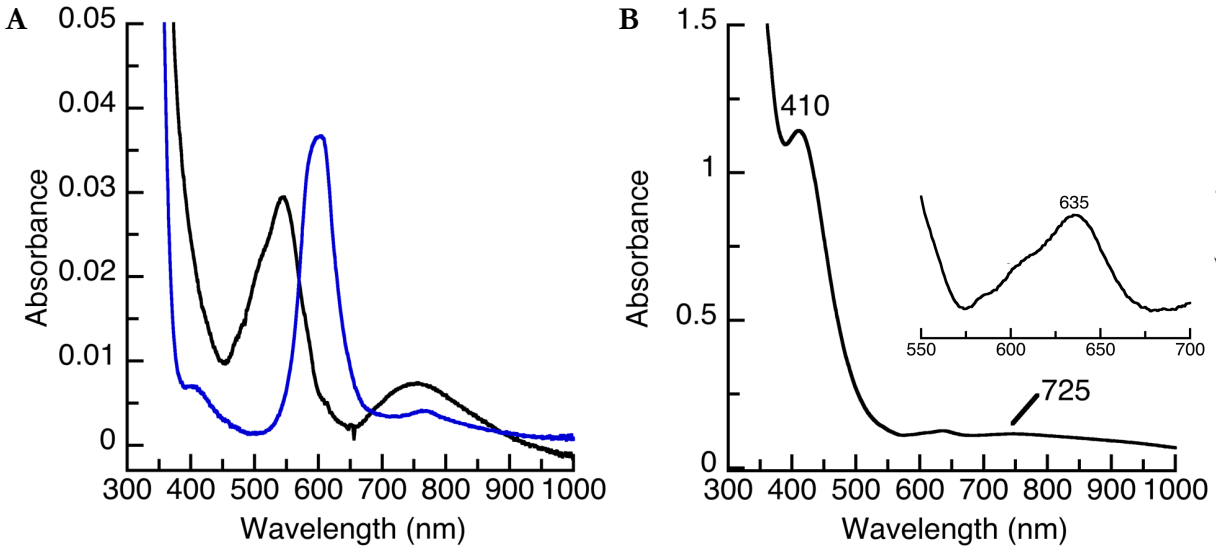

Figure 3-7: (**A**) UV-vis spectrum of the proposed Co^{II}–IBX-*i*Pr adduct (black, λ_{max} = 500, 550, 585, 770 nm), overlaid with **1** (blue, λ_{max} = 410, 585, 610, 770 nm). (**B**) Resulting spectrum after adding IBX-*i*Pr to K[Co^{II}poat] and letting react overnight. All spectra were measured at room temperature in DCM.

electronic transitions of four-coordinate TMP versus 5-coordinate trigonal bipyramidal complexes.[80,84,86,88,91,92] Furthermore, the molar absorptivity values of this new species were small and consistent with *d*–*d* transitions observed in the electronic absorption spectra of Co^{II} complexes. Based on the shape and energies of the bands observed, it was initially proposed that the product of this reaction was a Co^{II}–IBX-*i*Pr adduct rather than some further oxidized Co–O(H) species. Additionally, when IBX-*i*Pr was added to a solution of K[Co^{II}poat] and quickly frozen in an EPR tube, the ⊥-mode EPR spectrum did not change, which is not surprising given the insensitivity of high-spin Co^{II} ions in trigonal symmetry to the identity of the fifth ligand.[51,62,81,85] Perhaps more significantly, there was no loss of signal intensity from the Co^{II} center which suggested that an oxidation had not occurred.

Following spectroscopic studies of the proposed Co^{II}–IBX-*i*Pr adduct, attempts were made to prepare this complex in bulk and crystallize the product. In a representative experiment, K[Co^{II}poat] was dissolved in DCM to give a bright blue solution. One equivalent of IBX-*i*Pr was dissolved in a minimal amount of DCM and added slowly to the solution of K[Co^{II}poat], leading to a color change from light, bright blue to purple to pink. After roughly 5 minutes of stirring, the solution was pipet-filtered and set up to recrystallize via layering or vapor diffusion with a variety of anti-solvents, including Et_2O and *n*-pentane. However, no solids were isolated and the remaining solution was deeper yellow, rather than the pale pink color which appeared immediately after addition of IBX-*i*Pr. This experiment was replicated spectroscopically by adding IBX-*i*Pr to a solution of K[Co^{II}poat] in DCM and stirring overnight. The resulting solution was yellow in color and a UV-vis spectrum was collected, which revealed bands at λ_{max} = 410, 585 (sh), 610 (sh), 635, 725 nm (Fig 3-6, B). The lower-absorbing features, with shoulder $\lambda \sim$ 585, 610 nm and a band at λ_{max} = 635 nm appeared to share features with both K[**1**] and the proposed Co^{II}–IBX-*i*Pr adduct, however the features at 410 and 725 nm were unique. While this spectrum was reproducible, this species has not been successfully isolated nor definitively identified.

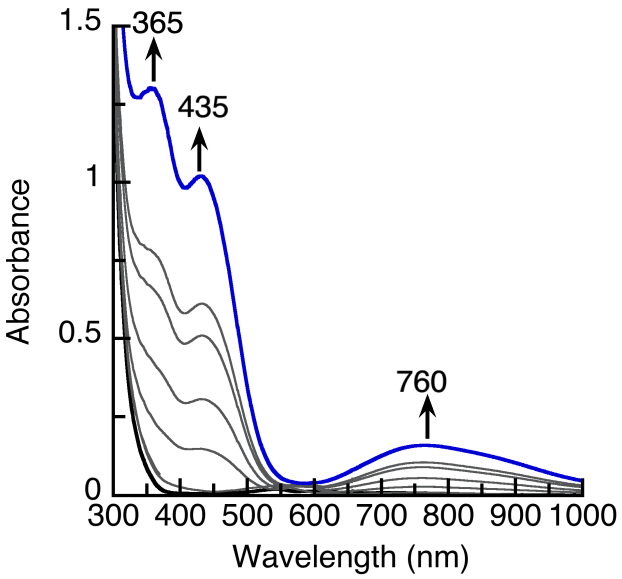

Figure 3-8: Electronic absorption spectra following the reaction of K[Co^{II}poat] with IBX-*i*Pr after addition of [Zn^{II}Me$_3$tacn(OTf)$_2$], measured at 25 °C in DCM.

In investigating the reactivity of K[Co^{II}poat] towards IBX-*i*Pr, it was observed that a potential metal-oxidant adduct formed. There is literature precedent for the activation of metal-oxidant adducts in the presence of Lewis acids, including redox inactive metal ions.[62,68,69] To activate the proposed adduct, [Zn^{II}Me$_3$tacn(OTf)$_2$] was added. This complex was chosen because [Zn^{II}Me$_3$tacn(OTf)$_2$] can be cleanly prepared and the triflate ligands are readily displaced while the Me$_3$tacn ligand framework remains coordinated, effectively leaving three open coordination sites. Previous work with metal complexes supported by [poat]$^{3-}$ demonstrated that the P=O units and exogenous $^{-}$OH ligand are competent to coordinate to the Zn^{II} center.[59] When K[**1**] was treated first with IBX-*i*Pr, then with [Zn^{II}Me$_3$tacn(OTf)$_2$], a deep red-orange solution formed. Monitoring this reaction by electronic absorption spectroscopy revealed that this new species had bands at λ_{max} = 365, 435, 760 nm (Fig 3-7). These absorption features appeared similar to previously characterized mono- and bimetallic Co^{III}–OH species in C_3 symmetric ligand fields based on the bands observed between λ_{max} ~ 350 – 500 nm, as well as the broad, lower energy feature centered around 760 nm.[51,79–81]

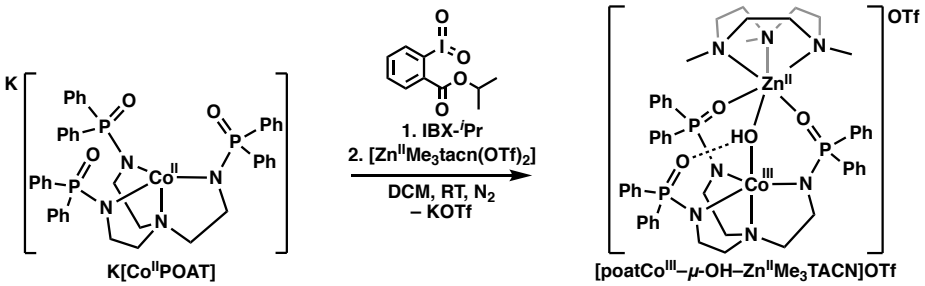

Scheme 3-2: Synthetic scheme describing the preparation of $[Co^{III}–\mu\text{-}OH–Zn^{II}]^{+}$.

Synthesis and Characterization of the Bimetallic Complex: Following the UV-visible studies discussed above, bulk syntheses were performed in an attempt to isolate the product of this reaction and identify its molecular structure. As outlined in Scheme 3-2, **1** was weighed into a vial without 18c6. Crown ether was avoided in this synthesis to aid in the precipitation of KOTf as a byproduct and make it easier to isolate via filtration. IBX-*i*Pr was added as a solid to the vial containing K[Co^{II}poat] and both reagents were dissolved in ~3 mL of DCM and stirred to yield a pink solution. After all solids were consumed, [Zn^{II}Me$_3$tacn(OTf)$_2$] was dissolved in ~1 mL of DCM and added slowly to the reaction, resulting in a color change to a deep, red-orange solution. This solution was stirred for approximately 30 minutes, at which point it was filtered to isolate any remaining solids. The filtrate was layered under *n*-pentane, which resulted in the formation of crystals suitable for X-ray diffraction studies (Fig 3-8).

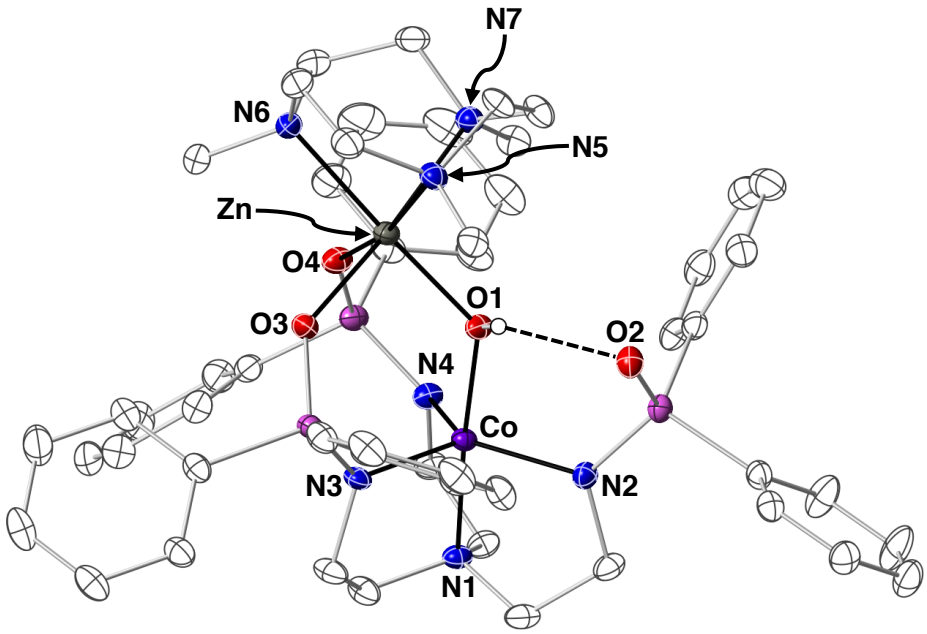

Figure 3-9: Molecular structure of [poatCo^{III}–μ-OH–Zn^{II}Me$_3$tacn]OTf with thermal ellipsoids drawn at 50% probability. Only the hydroxido ligand H-atom is shown. Remaining H-atoms, the triflate counterion, and structural solvent molecules were omitted for clarity.

Table 3-2: Metrical data obtained from the molecular structure of $[Co^{III}–\mu\text{-}OH–Zn^{II}]^+$ τ_5 is the trigonality structural parameter; β and α are the two largest bond angles observed.

Bond	Distance, Å	Bond	Distance, Å
Co–N1	1.951(1)	**Zn–O1**	1.987(1)
Co–N2	1.936(2)	**Zn–O3**	2.090(1)
Co–N3	1.959(2)	**Zn–O4**	2.085(1)
Co–N4	1.981(2)	**Zn–N5**	2.251(2)
Co–O1	1.884(1)	**Zn–N6**	2.185(2)
O1···O2	2.777(2)	**Zn–N7**	2.223(2)
Atoms	**Angles, °**	**Atoms**	**Angles, °**
N1–Co–N2	84.30(6)	**Co–O1–Zn**	127.88(7)
N1–Co–N3	85.20(6)	**O1–Zn–O3**	89.98(5)
N1–Co–N4	83.29(6)	**O1–Zn–O4**	88.52(5)
N1–Co–O1	176.29(6)	**O3–Zn–O4**	95.14(5)
N2–Co–N3	124.08(6)	**N5–Zn–N6**	80.87(6)
N2–Co–N4	123.37(6)	**N5–Zn–N7**	79.79(6)
N3–Co–N4	109.56(6)	**N6–Zn–N7**	80.96(6)
N_{eq}···Co = 0.197 Å		**Co···Zn = 3.4774(4)**	
τ_5 = 0.87		**$\tau_5 = (\beta - \alpha)/60°$**	

The molecular structure obtained from the above reaction revealed a bimetallic coordination complex formulated as $[poatCo^{III}–\mu\text{-}OH–Zn^{II}Me_3tacn]OTf$, (abbreviated: $[Co^{III}–\mu\text{-}OH–Zn^{II}]^+$, Fig 3-8). The Co ion remained coordinated to the $[poat]^{3-}$ ligand and was also bound to a hydroxido ligand to form an overall 5-coordinate Co center. The ligands were arranged around the Co center in a near-trigonal bipyramidal arrangement with a τ_5 value of 0.87.[93] The hydroxido ligand formed a single-atom bridge between the Co and Zn ions, while also participating in an intramolecular H–bonding interaction with the O-atom from one of the phosphinic amido groups, O2 (O1···O2 = 2.777(2) Å, Table 3-2). The Zn ion was further coordinated to O3 and O4, the O-atoms from the remaining phosphinic amido groups. O1, O3, and O4 coordinated to the Zn center in a facial manner and the remaining coordination sites on the Zn ion were occupied by the three N-atom donors of the Me_3tacn ligand. The overall complex had a charge of +1, with a single OTf^- counterion.

The ligand field incorporated in this complex provided a charge of –4, from the trianionic $[poat]^{3-}$ ligand backbone and the monoanionic ^-OH ligand. In order to prepare a complex with an overall +1 charge,

the metal ions must add up to charge of +5. Given that Zn^{II} is treated as a redox inert metal ion and was introduced during synthesis as a Zn^{II} salt, the remaining positive charge was accounted for with the cobalt center. Therefore, the Co ion was assigned an oxidation state of +3. The Co–L bond lengths observed in the molecular structure further supported the assignment of a Co^{III} oxidation state. The bonds around the Co^{III} ion were significantly contracted in length versus the starting Co^{II} salt. Of particular note was the decrease of the Co–N1 bond length between the two molecules and the formation of a relatively short Co–O1 bond length (1.884(1) Å, Table 3-2). These bond lengths were similar to other crystallographically characterized Co^{III}–OH complexes.[51,79,94–98]

To corroborate the oxidation state of the Co center, the magnetic properties of $[Co^{III}–\mu\text{-}OH–Zn^{II}]^{+}$ were investigated. The complex was silent by both ⊥- and ∥-mode EPR spectroscopy. As discussed in the previous chapter, Co^{III} ions in C_3 symmetric ligand fields may either have spin states of $S = 1$ or $S = 2$ based on how the *d*-orbitals split. Given that it is typically difficult to observe integer spin states by ∥-mode EPR spectroscopy, an Evans' Method NMR spectrum was collected to ascertain the μ_{eff} value via the paramagnetic solvent resonance shift. The μ_{eff} was determined to be 2.57 μ_B, which was consistent with the theoretical spin-only magnetic moment for a $S = 1$ system ($\mu_S = 2.83\ \mu_B$). The spin state of the Co center was therefore concluded to be $S = 1$, further supporting assignment of the Co^{III} oxidation state.

Following the structural and magnetic analysis, further spectroscopic studies were undertaken. $[Co^{III}–\mu\text{-}OH–Zn^{II}]^{+}$ was redissolved in DCM and its electronic absorption spectrum was studied. Following dissolution of $[Co^{III}–\mu\text{-}OH–Zn^{II}]^{+}$, a deep red-orange species was obtained and the molar absorptivity values were determined: λ_{max}, nm (ε, $M^{-1}cm^{-1}$) = 365 (3260), 435 (2690), 760 (498), (Fig 3-9, A). The spectrum which resulted from the redissolved $[Co^{III}–\mu\text{-}OH–Zn^{II}]^{+}$ was consistent with the *in situ* generated species discussed above and the features were similar with previously studied Co^{III}–OH species in C_3 symmetric ligand fields.[51,79–81] In comparing the electronic absorption features of $[Co^{III}H_3buea(OH)]^{-}$ versus $[Co^{III}–\mu\text{-}OH–Zn^{II}]^{+}$, the absorption bands were all blue shifted. It was not clear whether the differences in these absorption features are due to differences in the 1° or 2° coordination sphere traits of the $[poat]^{3-}$ and $[H_3buea]^{3-}$ ligands or the interaction of the $[Zn^{II}Me_3tacn]^{2+}$ unit with the Co^{III}–OH species. It was also observed that the 760 nm band,

which has previously been assigned as a *d–d* band was unsymmetric with a weak shoulder at roughly 880 nm. The asymmetry in this band was not observed in monometallic examples of Co^{III}–OH complexes, though it was observed absorption spectrum of [MSTCo^{III}–μ-OH–Ca^{II}⊂15-crown-5]$^{+}$.[51] Additionally, the complex was studied by solid state attenuated total reflectance-Fourier transform infrared spectroscopy (ATR-FTIR). The vibrational spectrum exhibited a broad feature at 3230 cm^{-1} which was assigned as an O–H vibration (Fig 3-9, B). This vibration was consistent in energy and shape with previously characterized [M^{III}–μ-OH–M^{II}]$^{n+}$ species.[52–54]

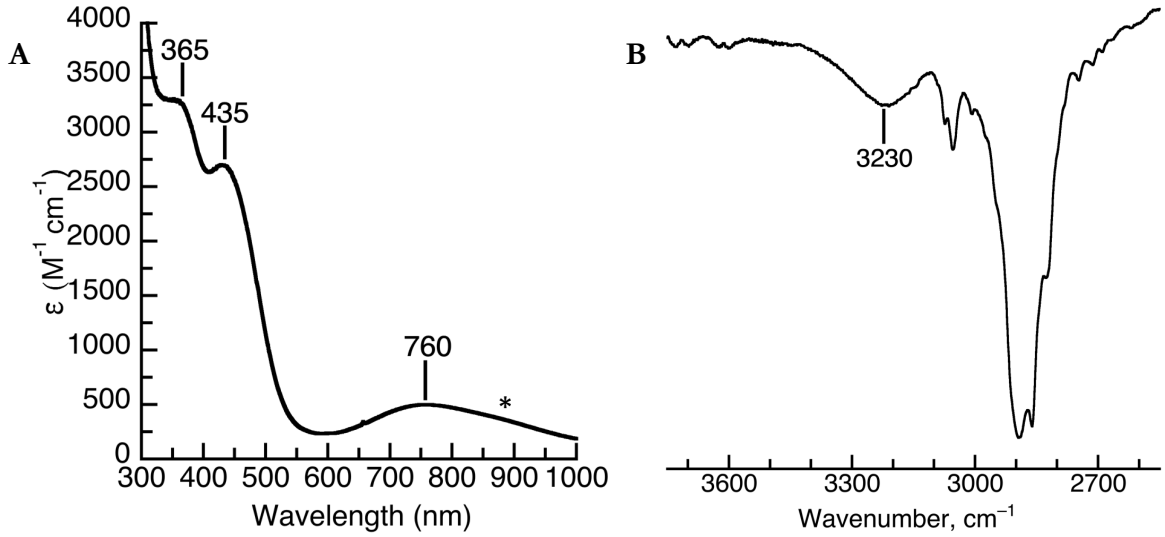

Figure 3-10: (**A**) Electronic absorption spectrum of [Co^{III}–μ-OH–Zn^{II}]$^{+}$ measured at 25 ºC in DCM. * marks a shoulder ~ 880 nm. (**B**) Solid-state vibrational spectrum of [Co^{III}–μ-OH–Zn^{II}]$^{+}$. The inset shows the O–H vibration.

Finally, [Co^{III}–μ-OH–Zn^{II}]$^{+}$ was studied by CV. The complex exhibited a reversible, one electron redox event at –0.645 V versus $Fc^{+/0}$ in DCM, assigned as the $Co^{III/II}$ couple, as well as two irreversible oxidative events at +0.290 V and +0.625 V versus $Fc^{+/0}$. Initial attempts to oxidize this compound were made using 1-acetylferrocenium triflate (AcFcOTF) and tris(4-methylphenyl)aminium hexafluoroantimonate ($E_{1/2}$ = +0.27, +0.37 V versus $Fc^{+/0}$ respectively in DCM).[99] These studies were performed at –60 ºC in DCM and monitored by UV-vis spectroscopy. AcFcOTf appeared to be consumed based on spectral changes (Fig 3-S3) however the product bands were similar to the starting [Co^{III}–μ-OH–Zn^{II}]$^{+}$ complex. When [Co^{III}–μ-OH–Zn^{II}]$^{+}$ was treated with the tris(4-methylphenyl)aminium radical cation, the absorption features from the radical species were only partly consumed and the inorganic product was not clear due to overlap with the intensely absorbing

radical species (Fig 3-S3). Lastly, AgOTF ($E_{1/2}$ = +0.65 V versus $Fc^{+/0}$) was added to the complex in bulk and pipet filtered, then layered under *n*-pentane. This recrystallization was stored in a dry-box freezer, and did not exhibit a clear color change from $[Co^{III}–\mu\text{-}OH–Zn^{II}]^+$ by UV-vis spectroscopy. A conclusion regarding whether $[Co^{III}–\mu\text{-}OH–Zn^{II}]^+$ can be further oxidized could not be drawn. Additional studies would be needed in order to optimize experimental conditions and definitively determine if the complex could be oxidized.

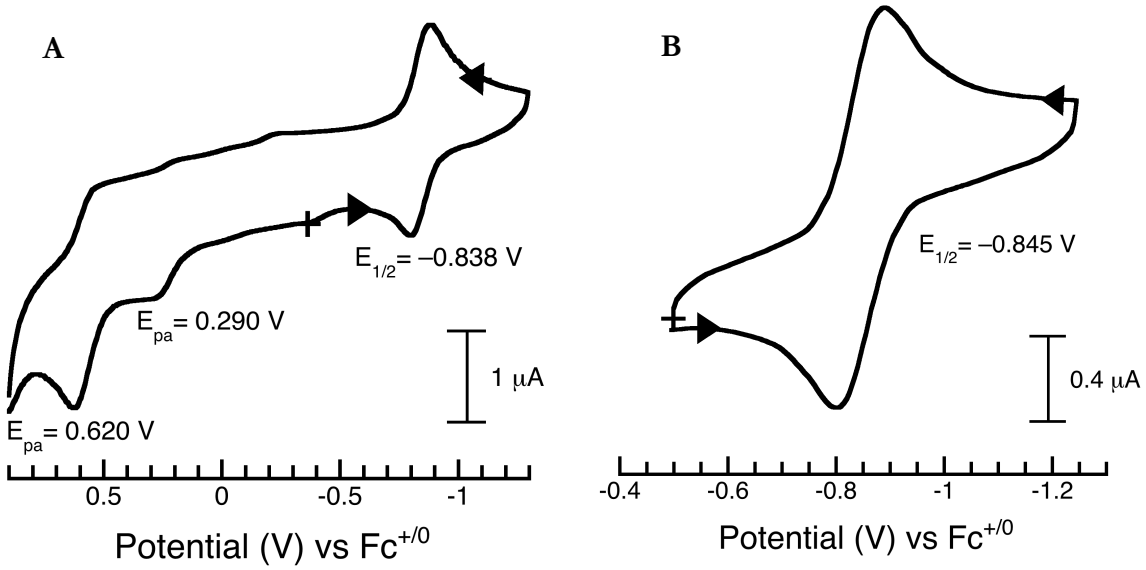

Figure 3-11: (**A**) Full electrochemical profile and isolated $Co^{III/II}$ reduction (**B**) of $[Co^{III}–\mu\text{-}OH–Zn^{II}]^+$ measured by CV in DCM.

Summary and Conclusion

This chapter described the preparation and properties of a TMP Co^{II} complex supported by the $[poat]^{3-}$ ligand framework and its utility as a scaffold for the assembly of bimetallic systems, which will be further explored in subsequent chapters. $K[Co^{II}poat]$ was crystallized and the molecular structure was successfully obtained. The complex was found to crystallize as a dinuclear cluster, formulated as $(K[Co^{II}poat])_2$ where the $[Co^{II}poat]^-$ anions were held together via electrostatic interactions with the K^+ counterions. $K[Co^{II}poat]$ was then studied by UV-vis, $\perp$-mode EPR, and Evans' method NMR spectroscopies. The EPR spectrum, measured in the presence of excess 18c6, exhibited a $S = 3/2$ signal and had hyperfine features consistent with a mononuclear species in solution, suggesting that 18c6 is sufficient to break up the crystalline dinuclear cluster in solution. The spectral features observed were all consistent with literature examples of other Co^{II} TMP species, corroborating the structural data. The electrochemical properties of $K[Co^{II}poat]$ were studied by CV,

in both the presence and absence of 18c6. The CV features appeared different when measured with excess 18c6 and there were fewer electrochemical events. The wealth of features observed in the CVs without 18c6 were difficult to analyze and suggests that the encapsulating reagent is necessary to guarantee full dissociation of the crystalline materials in order to treat the $[Co^{II}poat]^-$ molecule as a mononuclear species.

K[Co^{II}poat] was treated with IBX-*i*Pr and a proposed Co^{II}–IBX-*i*Pr adduct was observed. To this species, [$Zn^{II}Me_3tacn(OTf)_2$] was added in an effort to activate the metal-oxidant adduct. The product of this reaction was determined to be [poatCo^{III}–μ-OH–$Zn^{II}Me_3$tacn]OTf by X-ray diffraction studies as well as UV-vis, EPR, Evans Method, and ATR-FTIR spectroscopies. This data confirmed the oxidation state of the Co ion, as well as the spin state, which suggested that the product of the reaction between K[Co^{II}poat], IBX-*i*Pr, and [$Zn^{II}Me_3tacn(OTf)_2$] was a bimetallic complex featuring a bridging hydroxido ligand. Despite carrying this reaction out at different temperatures, the reaction profile appeared the same. There were not any intermediate species detectable under the various reaction conditions screened, including any proposed Co^{IV} species. It is not immediately clear how an O-atom transfer reagent known for carrying out two electron oxidations with metal centers proceeded directly to a Co^{III}–OH species without observing an intermediate.

Lastly the CV collected of $[Co^{III}$–μ-OH–$Zn^{II}]^+$ had two irreversible oxidative events at +0.29 and +0.62 V versus $Fc^{+/0}$. The identity of the oxidized species events could not be determined from electrochemical studies alone, though one of the features could be associated with a $Co^{IV/III}$ oxidation. To prepare and identify the oxidized product(s), $[Co^{III}$–μ-OH–$Zn^{II}]^+$ was treated with different oxidants including AcFcOTf, AgOTf, and tris(4-methylphenyl)aminium radical cation. The product(s) of these reactions were unclear and further investigation is necessary to draw any conclusions.

Outlook

Should this work be continued, there are a few suggested directions. To confirm that the hydroxido O-atom in $[Co^{III}$–μ-OH–$Zn^{II}]^+$ derived from IBX-*i*Pr, an isotopic labeling experiment could be performed where IBX-*i*Pr is prepared from $Na^{18}OCl$. The high resolution-mass spectrometry (HR-MS) data could then be recollected to determine if the ^{18}O atom was successfully incorporated into the complex. Additionally, the ^{18}O–H vibration could be measured to obtain an isotopic shift from the natural abundance complex.

The oxidation chemistry of $[Co^{III}–\mu\text{-}OH–Zn^{II}]^{+}$ could be further investigated. There are two relatively intense, irreversible oxidative events present in the voltammogram of $[Co^{III}–\mu\text{-}OH–Zn^{II}]^{+}$ at high, but accessible potentials versus $Fc^{+/0}$. There is a question about whether the product of a one electron oxidation of this compound would be a proposed $[poatCo^{IV}–\mu\text{-}OH–Zn^{II}Me_3tacn]^{+}$ species or if an intramolecular proton transfer may occur to form a species such as $[HpoatCo^{IV}–\mu\text{-}O–Zn^{II}Me_3tacn]^{2+}$, where one of the anionic N-groups of the $[poat]^{3-}$ ligand framework is protonated rather than the ^{-}OH bridge. This type of chemistry has been previously observed in other examples of bimetallic complexes supported by $[poat]^{3-}$ and Me_3tacn, so there is precedent for protonation of one of the $[poat]^{3-}$ arms.[58,60]

Finally, a few attempts were made to treat the $[Co^{III}–\mu\text{-}OH–Zn^{II}]^{+}$ complex with a base in order to deprotonate the bridging ^{-}OH unit and prepare a proposed bridging O^{2-} ligand. In these studies, it was unclear whether the deprotonation was successful, though not much time was spent on this line of inquiry. The viability of the deprotonation event could still be determined.

Experimental Section

General Procedures

Unless otherwise specified, all reagents were purchased and used from commercially available sources and stored under a N_2 atmosphere in a VAC dry box. Sure-seal bottles of DMA were purchased from Honeywell, Burdick, & Jackson (99.5% purity). All other solvents were sparged with argon and purified with a JC Meyer Co. solvent purification system with Q-5 columns and molecular sieves. Potassium hydride (KH) was bought as a 30% suspension in mineral oil, washed on a fine porosity frit 5 times with *n*-pentane and diethyl ether (Et_2O), dried under vacuum, and stored under N_2. 18c6 was purchased in 99% purity from Acros Organics, ground with a mortar and pestle to a powder, and dried under vacuum. Cobalt (II) acetate ($Co^{II}(OAc)_2$) was purchased from Sigma Aldrich as a pink-purple solid and dried in an oven until a purple powder was obtained. H_3poat,[57] Me_3tacn,[100,101] $[Zn^{II}Me_3tacn(OTf)_2]$,[59] and IBX-iPr[102,103] were prepared following literature procedures. $Zn^{II}(OTf)_2{\cdot}2MeCN$[104] was prepared by adapting previous literature reports.

Physical Methods

Electronic absorption spectra were collected in a 1 cm quartz cuvette, fitted with a magnetic stir bar. Spectra were recorded on a Cary-60 spectrophotometer or an 8453E Agilent UV-vis spectrophotometer fitted with a Unisoku Unispeks cryostat for temperature-controlled spectroscopy. Cyclic voltammetry was performed with a CHI600C potentiostat. Voltammograms were measured from a ~1 mM stock solution of analyte in at least 100-fold excess of tetrabutylammonium hexafluorophosphate in dry, air-free DCM collected in 4-neck, double-walled cell. A 1 mm glassy carbon electrode acted as the working electrode with a Pt wire counter electrode and a Ag wire reference electrode. All voltammograms were referenced to an internal $Fc^{+/0}$ standard. He-temperature EPR spectra were collected on an X-Band Bruker spectrometer fitted with an Oxford liquid helium cryostat. Signals were referenced and quantified to a CuEDTA spin standard. The magnetic field was calibrated with an NMR gaussmeter. The microwave frequency of the instrument was calibrated with a frequency counter. 77 K EPR experiments were recorded on a Bruker EMX X-band spectrometer with the following parameters, unless otherwise noted: microwave frequency of 9.64 GHz, a modulation frequency of 100 kHz, a modulation amplitude of 10 G, a microwave power of 2 mW, an attenuation of 20 dB, a time constant of 82 msec, and a conversion time of 41 msec. All EPR samples were prepared under a nitrogen atmosphere in 4 mm quartz EPR tubes, capped with a septum, and flash frozen in liquid nitrogen. EPR spectra were simulated and fit using SpinCount software.[105] ATR-FTIR spectra were measured on a Thermo Scientific Nicolet iS5 spectrometer fitted with an iD5 ATR attachment. Evans' Method NMR spectra were recorded at 500 MHz using a Bruker DRX500 spectrometer with a TCI cryoprobe. Chemical shifts were reported in ppm and referenced to an internal trimethylsilane standard in deuterated solvents. Elemental analyses were measured on a Perkin-Elmer 2400 Series II CHNS elemental analyzer.

Preparative Methods

$K[Co^{II}poat]$: 0.1426 g (0.1910 mmol) of H_3poat were dissolved in 4 mL of DMA. To this solution, 0.0280 g (0.698 mmol) KH were added, yielding a bubbling, cloudy solution. The reaction mixture was stirred till bubbling ceased and the solution was clear and colorless. Then, 0.0348 g (0.197 mmol) of $Co^{II}(OAc)_2$ were added as a purple powder suspension in 2 mL of DMA. The reaction mixture was allowed to stir overnight and

resulted in formation of a bright, cloudy blue suspension. The reaction mixture was filtered to yield solid blue powder and a bright blue solution. The solid on the frit was washed with minimal DCM, followed by *n*-pentane and Et_2O until the blue color washed away and 0.0345 g of dry, off-white solid remained (92.0% yield; theoretical yield, KOAc = 0.0375 g, 0.382 mmol). The blue filtrate was subsequently dried under vacuum to give bright blue powder. This powder was redissolved in DCM and layered under *n*-pentane to yield 0.1170 g (0.1390 mmol, 72.8% yield) of bright blue, blocky single crystals, suitable for X-ray diffraction analysis. UV-vis (DCM, λ_{max} nm (ε, $M^{-1}cm^{-1}$)) = 410 (13), 585 (67), 610 (71), 770 (8). ATR-FTIR, selected bands (cm^{-1}) = 3050, 2949, 2838, 2342, 1720, 1589, 1481, 1433, 1271, 1232, 1192, 1155, 1118, 1026, 965, 918, 851, 801, 746, 717, 696. EPR (X-Band, ⊥-mode, 20 K, DCM:THF, excess 18c6), g = 4.5, 4.3, 2.0 (A = 262 MHz), E/D = 0.0029, D = +3.6 cm^{-1}. μ_{eff}, Evans Method, DCM = 4.28 μ_B. Cyclic Voltammetry (100 mV/s, DCM, V vs $Fc^{+/0}$) = $E_{1/2}$ = –0.495, E_{pa} = +0.365. Elemental Analysis calculated for $4(C_{42}H_{42}CoKN_4O_3P_3) \cdot C_5H_{12}$; C, 60.42, H, 5.28, N, 6.52; found C, 60.6, H, 4.87, N, 6.71.

[poatCo^{III}(–μ-OH–)$Zn^{II}Me_3$tacn]OTf: 0.1226 g (0.1456 mmol) of K[Co^{II}poat] was weighed. To this solid, 0.0474 g (0.147 mmol) of 2-iodoxy benzoate isopropyl ester (IBX-iPr) were added and the two reagents were dissolved together in ~5 mL of DCM, immediately forming a clear, purple-pink solution. To this solution, 0.0783 g (0.146 mmol) of [$Zn^{II}Me_3$tacn$(OTf)_2$] dissolved in ~1 mL of DCM was added slowly, affording a deep red-orange solution. The reaction was stirred for 30 minutes, then pipet filtered to remove any residual solids. This solution was layered under *n*-pentane and after roughly a week, dark red-brown crystals suitable for study by X-ray diffraction analysis were grown in a 85.90% yield (0.1505 g, 0.1250 mmol). UV-vis (DCM, λ_{max} nm (ε, $M^{-1}cm^{-1}$)) = 365 (3260), 435 (2690), 760 (498), 880 (sh). ATR-FTIR, selected bands (cm^{-1}) = 3230 (OH), 3055, 2894, 2860, 2364, 2250, 1974, 1673, 1590, 1437, 1352, 1263, 1224, 1145, 1104, 1067, 1030, 961, 838, 803, 752, 721, 698. EPR Silent, ⊥- and ∥-modes. μ_{eff}, Evans Method, DCM = 2.57 μ_B. Cyclic Voltammetry (100 mV/s, DCM, V vs $Fc^{+/0}$) = $Co^{III}Zn^{II}/Co^{II}Zn^{II}$, $E_{1/2}$= –0.845, E_{pa} = +0.290, +0.620. HRMS (ES+, *m/z*): Exact mass calculated for $C_{51}H_{64}CoN_7O_4P_3Zn$: 1054.2856, Found: 1054.2845.

X-ray Crystallographic Methods

(K[Co^{II}poat])$_2$: The data for asb622 were collected from a shock-cooled single crystal at 133(2) K on a Bruker SMART APEX II three-circle diffractometer with a fine-focus sealed tube using a equatorial mounted graphite as monochromator and a Bruker Apex II CCD detector. The diffractometer was equipped with a low temperature device and used MoK_a radiation (λ = 0.71073 Å). All data were integrated with SAINT and a multi-scan absorption correction using SADABS was applied.[106,107] The structure was solved by direct methods using SHELXS and refined by full-matrix least-squares methods against F^2 by SHELXL-2018/3 using ShelXle.[108–110] All non-hydrogen atoms were refined with anisotropic displacement parameters. All hydrogen atoms were refined isotropic on calculated positions using a riding model with their U_{iso} values constrained to 1.5 times the U_{eq} of their pivot atoms for terminal sp^3 carbon atoms and 1.2 times for all other carbon atoms. This report and the CIF file were generated using FinalCif.[111] *Refinement Details:* All non-hydrogen atoms were refined freely without constraints or restraints. All hydrogen atoms were refined using a riding model.

[poatCo^{III}–μ-OH–Zn^{II}Me$_3$tacn]OTf: single crystal at 93(2) K on a Bruker SMART APEX II three-circle diffractometer with a sealed X-ray tube using a equatorial mounted graphite as monochromator and a Bruker Apex II CCD detector. The diffractometer was equipped with a low temperature device and used MoK_a radiation (λ = 0.71073 Å). All data were integrated with SAINT and a multi-scan absorption correction using SADABS was applied.[106,107] The structure was solved by direct methods using SHELXT and refined by full-matrix least-squares methods against F^2 by SHELXL-2018/3 using ShelXle.[109,110,112] All non-hydrogen atoms were refined with anisotropic displacement parameters. All hydrogen atoms were refined with isotropic displacement parameters. Some were refined freely and some on calculated positions using a riding model with their U_{iso} values constrained to 1.5 times the U_{eq} of their pivot atoms for terminal sp^3 carbon atoms and 1.2 times for all other carbon atoms. This report and the CIF file were generated using FinalCif.[111] *Refinement Details:* All main molecule non-hydrogen atoms were freely refined without restraints. The half triflate ion in the asymmetric unit was constrained to 50% occupancy, and being located on the inversion center, F1-F3 were constrained to the same positions and ADPs as O5-O7, and C52 and S1 were treated the same. Most non-hydrogen atoms were refined using a riding model. The position for H1 was refined freely with ADP

constrained to 1.5x that of O1. In initial refinements, another half triflate was found in the asymmetric unit with what was possibly a half occupancy acetonitrile that shared the same position. Additionally, a heavily disordered chloroform molecule, and pentane molecule were found. SQUEEZE,[113] as an implementation of Platon,[113–115] was used to remove the electron density from these heavily disordered areas.

Supplemental Information

Table 3-S1: Crystallographic details for (K[Co^{II}poat])$_2$, K[**1**], (middle column) and [poatCo^{III}–μ-OH–Zn^{II}Me$_3$tacn]OTf (right column).

Compound	**(K[Co^{II}poat])$_2$**	**[poatCo^{III}–μ-OH–Zn^{II}Me$_3$tacn](OTf)$_{1/2}$**
Empirical formula	$C_{84}H_{84}Co_2K_2N_8O_6P_6$	$C_{51.5}H_{64}CoF_{1.5}N_7O_{5.5}P_3S_{0.5}Zn$
Formula weight	1683.47	1130.83
Temperature [K]	133(2)	93(2)
Crystal system	monoclinic	triclinic
Space group (number)	$P2_1/n$ (14)	$P\overline{1}$ (2)
a [Å]	14.4988(11)	14.5057(14)
b [Å]	16.2701(12)	14.9985(15)
c [Å]	16.8941(13)	16.9225(16)
α [°]	90	71.826(2)
β [°]	90.0432(12)	66.289(2)
γ [°]	90	82.932(2)
Volume [Å^3]	3985.3(5)	3202.8(5)
Z	2	2
ϱ_{calc} [gcm^{-3}]	1.403	1.173
Independent reflections	9176	19332
Goodness-of-fit on F^2	1.032	1.046
R_1, [$I \geq 2\sigma(I)$]	0.0272	0.0437
wR_2, [all data]	0.0736	0.1035

$R_1 = \Sigma \; | \; |F_o| - |F_c| \; | \; / \; \Sigma \; |F_o|$
$wR_2 = [\Sigma[w(F_o^2 - F_c^2)^2] \; / \; \Sigma[w(F_o^2)^2]]^{1/2}$

Goof (Goodness-of-fit) = S = $[\Sigma[w(F_o^2 - F_c^2)^2] \; / \; (n - p)]^{1/2}$, where n = number of reflections and p = total number of parameters refined.

Thermal ellipsoids are shown at 50% probability.

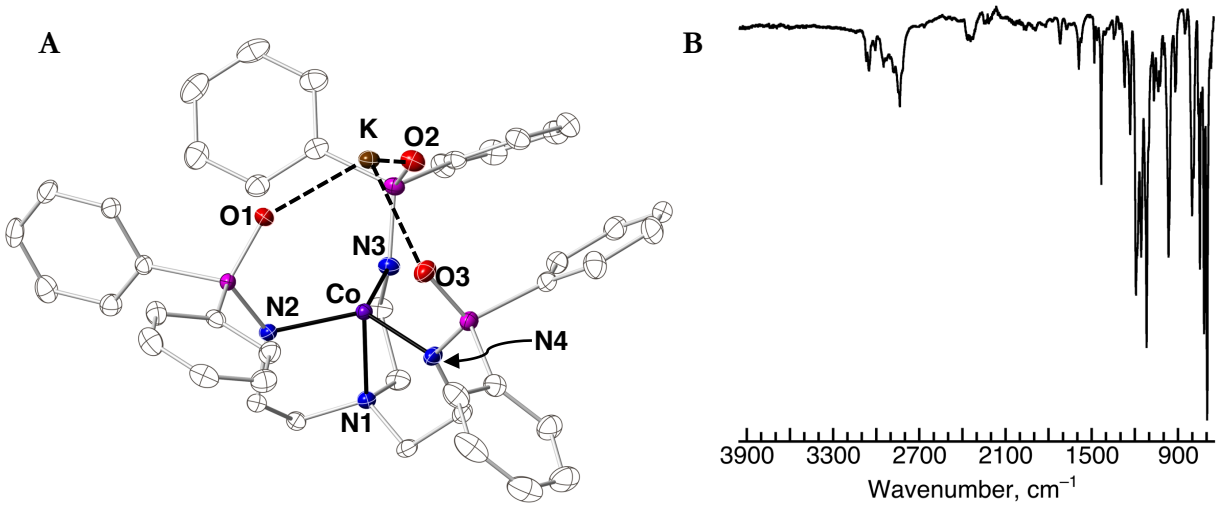

Figure 3-S1: (**A**) Molecular structure view of monomeric K[Co^{II}poat] with thermal ellipsoid representation, drawn to 50% probability. H-atoms were omitted for clarity. (**B**) Solid state ATR-FTIR spectrum of K[Co^{II}poat].

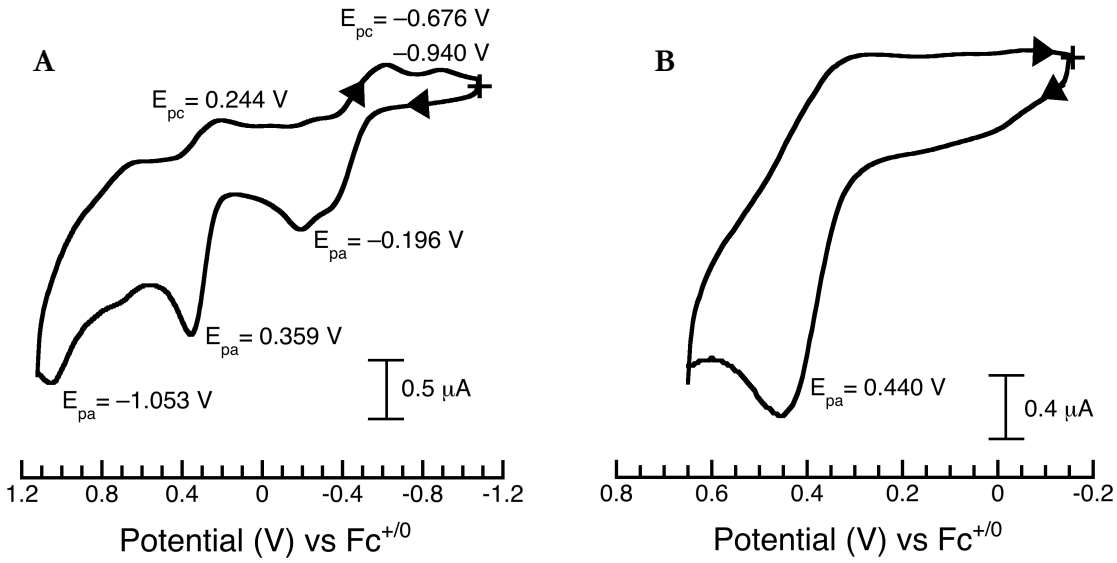

Figure 3-S2: (**A**) CV collected of K[Co^{II}poat] in DCM, without 18c6. (**B**) The isolated second oxidative event of K[Co^{II}poat] measured in DCM in the presence of excess 18c6

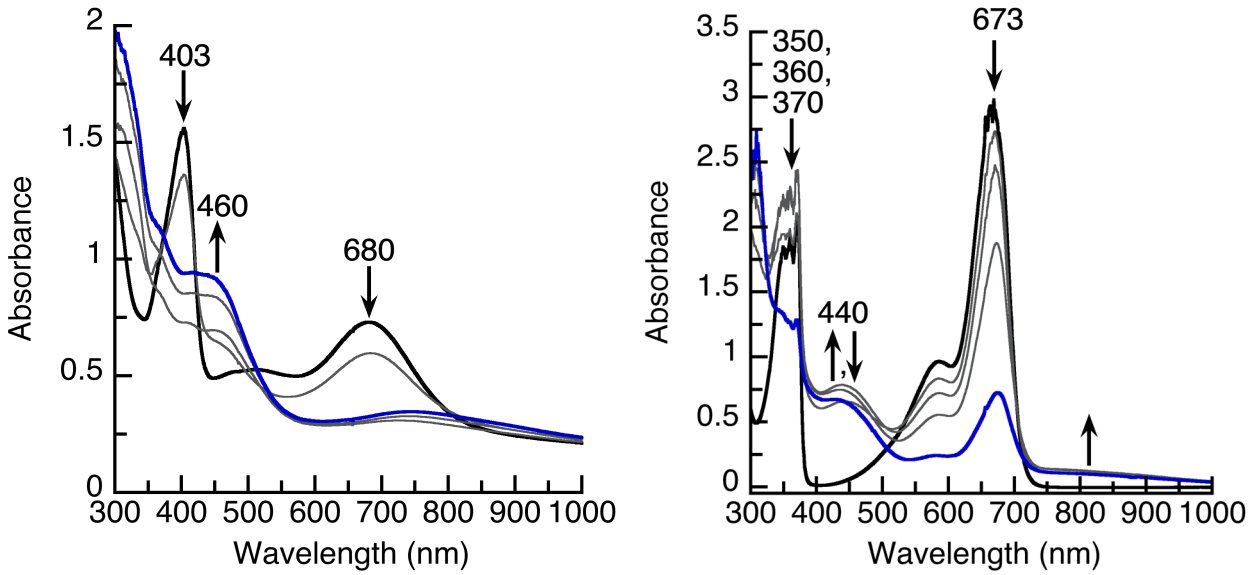

Figure 3-S3: (**A**) UV-vis spectra following the reaction between AcFcOTF (black trace) with [Co^{III}–μ-OH–Zn^{II}]$^+$. The final spectrum is shown in blue (λ_{max} = 375 (sh), 420, 460, 745 nm). (**B**) UV-vis spectra following the reaction between tris(4-methylphenyl)aminium radical cation (black, λ_{max} = 285, 295, 350, 360, 370, 585, 673 nm) to [Co^{III}–μ-OH–Zn^{II}]$^+$. The final spectrum is shown in blue (λ_{max} = 350, 370, 440*, 580, 675 nm). The band at λ_{max} = 440 nm is the only new feature. The remaining bands appear to be due to excess oxidant. All spectra were collected at –60 ° C in DCM.

References

(1) Holm, R. H.; Kennepohl, P.; Solomon, E. I. Structural and Functional Aspects of Metal Sites in Biology. *Chem. Rev.* **1996**, *96*, 2239–2314.

(2) Karlin, K. D. Metalloenzymes, Structural Motifs, and Inorganic Models. *Science.* **1993**, *261*, 701–708.

(3) MacKay, B. A.; Fryzuk, M. D. Dinitrogen Coordination Chemistry: On the Biomimetic Borderlands. *Chem. Rev.* **2004**, *104*, 385–402.

(4) Kurtz, D. M. Oxo- and Hydroxo-Bridged Diiron Complexes: A Chemical Perspective on a Biological Unit. *Chem. Rev.* **1990**, *90*, 585–606.

(5) Schenk, G.; Mitić, N.; Gahan, L. R.; Ollis, D. L.; McGeary, R. P.; Guddat, L. W. Binuclear Metallohydrolases: Complex Mechanistic Strategies for a Simple Chemical Reaction. *Acc. Chem. Res.* **2012**, *45*, 1593–1603.

(6) Jasniewski, A. J.; Que, L. Dioxygen Activation by Nonheme Diiron Enzymes: Diverse Dioxygen Adducts, High-Valent Intermediates, and Related Model Complexes. *Chem. Rev.* **2018**, *118*, 2554–2592.

(7) Lee, S. K.; Nesheim, J. C.; Lipscomb, J. D. Transient Intermediates of the Methane Monooxygenase Catalytic Cycle. *J. Biol. Chem.* **1993**, *26*, 21569–21577.

(8) Rosenzweig, A. C.; Nordlund, P.; Takahara, P. M.; Frederick, C. A.; Lippard, S. J. Geometry of the Soluble Methane Monooxygenase Catalytic Diiron Center in Two Oxidation States. *Chem. Biol.* **1995**, *2*, 409–418.

(9) Lipscomb, J. D.; Que Jr., L. MMO: P450 in Wolf's Clothing? *JBIC, J. Biol. Inorg. Chem.* **1998**, *3*, 331–336.

(10) Merkx, M.; Kopp, D. A.; Sazinsky, M. H.; Blazyk, J. L.; Müller, J.; Lippard, S. J. Dioxygen Activation and Methane Hydroxylation by Soluble Methane Monooxygenase: A Tale of Two Irons and Three Proteins. **2001**, *40*, 2782–2807.

(11) Whittington, D. A.; Lippard, S. J. Crystal Structures of the Soluble Methane Monooxygenase Hydroxylase from *Methylococcus Capsulatus* (Bath) Demonstrating Geometrical Variability at the Dinuclear Iron Active Site. *J. Am. Chem. Soc.* **2001**, *123*, 827–838.

(12) Gherman, B. F.; Dunietz, B. D.; Whittington, D. A.; Lippard, S. J.; Friesner, R. A. Activation of the C-H Bond of Methane by Intermediate Q of Methane Monoozygenase: A Theoretical Study. *J. Am. Chem. Soc.* **2001**, *123*, 3836–3837.

(13) Tinberg, C. E.; Lippard, S. J. Dioxygen Activation in Soluble Methane Monooxygenase. *Acc. Chem. Res.* **2011**, *44*, 280–288.

(14) Koo, C. W.; Rosenzweig, A. C. Biochemistry of Aerobic Biological Methane Oxidation. *Chem. Soc. Rev.* **2021**, *50*, 3424–3436.

(15) Jiang, W.; Yun, D.; Saleh, L.; Barr, E. W.; Xing, G.; Hoffart, L. M.; Maslak, M. A.; Krebs, C.; Bollinger, J. M. A Manganese(IV)/Iron(III) Cofactor in Chlamydia Trachomatis Ribonucleotide Reductase. *Science.* **2007**, *316*, 1188–1191.

(16) Dassama, L. M. K.; Boal, A. K.; Krebs, C.; Rosenzweig, A. C.; Bollinger, J. M. Evidence That the β Subunit of Chlamydia Trachomatis Ribonucleotide Reductase Is Active with the Manganese Ion of Its Manganese(IV)/Iron(III) Cofactor in Site 1. *J. Am. Chem. Soc.* **2012**, *134*, 2520–2523.

(17) Dassama, L. M. K.; Krebs, C.; Bollinger, J. M.; Rosenzweig, A. C.; Boal, A. K. Structural Basis for Assembly of the MnIV/FeIII Cofactor in the Class Ic Ribonucleotide Reductase from Chlamydia Trachomatis. *Biochemistry* **2013**, *52*, 6424–6436..

(18) Yano, J.; Yachandra, V. Mn 4Ca Cluster in Photosynthesis: Where and How Water Is Oxidized to Dioxygen. *Chem. Rev.* **2014**, *114*, 4175–4205.

(19) Wieghardt, K.; Bossek, U.; Nuber, B.; Weiss, J.; Bonvoisin, J.; Corbella, M.; Vitols, S. E.; Girerd, J. J. Synthesis, Crystal Structures, Reactivity, and Magnetochemistry of a Series of Binuclear Complexes of Manganese(II), -(III), and -(IV) of Biological Relevance. The Crystal Structure of [L'MnIV(μ-O)3MnIVL'](PF6)2.H2O Containing an Unprecedented Short Mn…Mn. *J. Am. Chem. Soc.* **1988**, *110* 7398–7411.

(20) Bossek, U.; Hummel, H.; Weyhermüller, T.; Bill, E.; Wieghardt, K. The First *μ*(OH)-Bridged Model Complex for the Mixed-Valent $Fe^{II}Fe^{III}$ Form of Hemerythrin. *Angew. Chem., Int. Ed. Engl.* **1996**, *34*, 2642–2645.

(21) Blakesley, D. W.; Payne, S. C.; Hagen, K. S. Spin-State Variation in Solid State and Solution of Mononuclear Iron(II) 1,4,7-Trimethyl-1,4,7-Triazacyclonane Complexes. *Inorg. Chem.* **2000**.

(22) Lachicotte, R.; Kitaygorodskiy, A.; Hagen, K. S. Distinguishing Hydroxy from Aqua Bridges inParamagnetic Diiron(II) and Dicobalt(II) Models ofReduced Dinuclear Non-Heme Iron Sites in Proteins by 1H, 2H, and 19F NMR of H/D Isotopomers. *J. Am. Chem. Soc.* **1993**, *115*, 8883–8884.

(23) Hagen, K. S.; Armstrong, W. H.; Hope, H. Isolation of a Bis-Oxo-Bridged MnIIIMnIV Intermediate by Regulated Air Oxidation. Synthesis, Structure, and Properties of [Mn2O2(Tren)2](CF3SO3)3. *Inorg. Chem.* **1988**, *27*, 967–969.

(24) Hagen, K. S.; Holm, R. H. Synthesis and Stereochemistry of Metal(II) Thiolates of the Types [M(SR)4]2-, [M2(SR)6]2-,and [M4(SR)10]2- (M = Fe(II), Co(II))+. *Inorg. Chem.* **1984**, *23*, 418–427.

(25) Zhao, N.; Filatov, A. S.; Xie, J.; Hill, E. A.; Rogachev, A. Y.; Anderson, J. S. Generation and Reactivity of a NiIII2(μ-1,2-Peroxo) Complex. *J. Am. Chem. Soc.* **2020**, *142*, 21634–21639.

(26) Zinn, P. J.; Sorrell, T. N.; Powell, D. R.; Day, V. W.; Borovik, A. S. Acetonitrile Hydration and Ethyl Acetate Hydrolysis by Pyrazolate-Bridged Cobalt(II) Dimers Containing Hydrogen-Bond Donors. *Inorg. Chem.* **2007**, *46*, 10120–10132.

(27) Ng, G. K.-Y.; Ziller, J. W.; Borovik, A. S. Preparation and Structures of Dinuclear Complexes Containing MII–OH Centers. *Chem. Commun.* **2012**, *48*, 2546–2548.

(28) Borovik, A. S.; Papaefthymiou, V.; Taylor, L. F.; Anderson, O. P.; Que, L. Models for Iron–Oxo Proteins. Structures and Properties of FeIIFeIII, ZnIIFeIII, and FeIIGaIII Complexes with (μ-Phenoxo)Bis(μ-Carboxylato)Dimetal Cores. *J. Am. Chem. Soc.* **1989**, *111*, 6183–6195.

(29) Reinaud, O. M.; Yap, G. P. A.; Rheingold, A. L.; Theopold, K. H. Novel Binuclear Cobalt Dioxygen Complex - a Step on the Path to Dioxygen Activation. *Angew. Chem., Int. Ed. Engl.* **1995**, *34*, 2051–2052.

(30) Barraclough, C. G.; Lawrance, G. A.; Lay, P. A. Characterization of Binuclear. Mu.-Peroxo and. Mu.-Superoxo Cobalt (III) Amine Complexes from Raman Spectroscopy. *Inorg. Chem.* **1978**, *17*, 3317–3322.

(31) Dalle, K. E.; Meyer, F. Modelling Binuclear Metallobiosites: Insights from Pyrazole-Supported Biomimetic and Bioinspired Complexes. *Eur. J. Inorg. Chem.* **2015**, *21*, 3391–3405.

(32) Solomon, E. I.; Tuczek, F.; Root, D. E.; Brown, C. A. Spectroscopy of Binuclear Dioxygen Complexes. *Chem. Rev.* **1994**, *94*, 827–856.

(33) Song, Y. F.; Berry, J. F.; Bill, E.; Bothe, E.; Weyhermüller, T.; Wieghardt, K. Iron Complexes of New Pentadentate Ligands Containing the 1,4,7-Triazacyclononane-1,4-Diacetate Motif. Spectroscopic, Electro-, and Photochemical Studies. *Inorg. Chem.* **2007**, *46*, 2208–2219.

(34) Wieghardt, K. The Active Sites in Manganese-Containing Metalloproteins and Inorganic Model Complexes. *Angew. Chemie Int. Ed. English* **1989**, *28*, 1153–1172.

(35) Bossek, U.; Nühlen, D.; Bill, E.; Glaser, T.; Krebs, C.; Weyhermüller, T.; Wieghardt, K.; Lengen, M.; Trautwein, A. X. Exchange Coupling in an Isostructural Series of Face-Sharing Bioctahedral Complexes [LMII(μ-X)3MIIIL]BPh4 M = Mn, Fe, Co, Ni, Zn; X = Cl, Br; L = 1,4,7-Trimethyl-1,4,7-Triazacyclononane. *Inorg. Chem.* **1997**, *36*, 2834–2843.

(36) Wu, F.-J.; Kurtz, D. M.; Hagen, K. S.; Nyman, P. D.; Debrunner, P. G.; Vankai, V. A. (*M*-Oxo/Hydroxo)Bis(*μ*-Carboxylato)Diiron(III) and -Dimanganese(III) Complexes with Capping Tris (Imidazol-2-yl)Phosphine Ligands. *Inorg. Chem.* **1990**, *29*, 5174–5183.

(37) Peralta, R. A.; Bortoluzzi, A. J.; De Souza, B.; Jovito, R.; Xavier, F. R.; Couto, R. A. A.; Casellato, A.; Nome, F.; Dick, A.; Gahan, L. R.; Schenk, G.; Hanson, G. R.; De Paula, F. C. S.; Pereira-Maia, E. C.; de P. Machado, S.; Severino, P. C.; Pich, C.; Bortolotto, T.; Terenzi, H.; Castellano, E. E.; Neves, A.; Riley, M. J. Electronic Structure and Spectro-Structural Correlations of Fe IIIZnII Biomimetics for Purple Acid Phosphatases: Relevance to DNA Cleavage and Cytotoxic Activity. *Inorg. Chem.* **2010**, *49*, 11421–11438.

(38) Gu, N. X.; Ung, G.; Peters, J. C. Catalytic Hydrazine Disproportionation Mediated by a Thiolate-Bridged VFe Complex. *Chem. Commun.* **2019**, *55*, 5363–5366.

(39) Krogman, J. P.; Thomas, C. M. Metal–Metal Multiple Bonding in C3-Symmetric Bimetallic Complexes of the First Row Transition Metals. *Chem. Commun.* **2014**, *50*, 5115–5127.

(40) Greenwood, B. P.; Rowe, G. T.; Chen, C.-H.; Foxman, B. M.; Thomas, C. M. Metal-Metal Multiple Bonds in Early/Late Heterobimetallics Support Unusual Trigonal Monopyramidal Geometries at Both Zr and Co. *132*, 44–45.
(41) Zhang, H.; Hatzis, G. P.; Moore, C. E.; Dickie, D. A.; Bezpalko, M. W.; Foxman, B. M.; Thomas, C. M. O2 Activation by a Heterobimetallic Zr/Co Complex. *J. Am. Chem. Soc.* **2019**, *141*, 9516–9520.
(42) Fajardo, J.; Peters, J. C. Tripodal P3XFe−N2 Complexes (X = B, Al, Ga): Effect of the Apical Atom on Bonding, Electronic Structure, and Catalytic N2-to-NH3 Conversion. *Inorg. Chem.* **2021**, *60*, 1220–1227.
(43) Rosenkoetter, K. E.; Ziller, J. W.; Heyduk, A. F. A Heterobimetallic W−Ni Complex Containing a Redox-Active W[SNS]2 Metalloligand. *Inorg. Chem.* **2016**, *55*, 6794–6798.
(44) Wojnar, M. K.; Ziller, J. W.; Heyduk, A. F. Heterobimetallic and Heterotrimetallic Clusters Containing a Redox-Active Metalloligand. *Eur. J. Inorg. Chem.* **2017**, *47*, 5571–5575.
(45) Delgado, M.; Ziegler, J. M.; Seda, T.; Zakharov, L. N.; Gilbertson, J. D. Pyridinediimine Iron Complexes with Pendant Redox-Inactive Metals Located in the Secondary Coordination Sphere. *Inorg. Chem.* **2016**, *55*, 555–557.
(46) Chantarojsiri, T.; Reath, A. H.; Yang, J. Y. Cationic Charges Lead to Inverse Free-Energy Relationship for N–N Bond Formation by MnVI Nitrides. *Angew. Chemie Int. Ed.* **2018**, *57*, 14037–14042.
(47) Cammarota, R. C.; Clouston, L. J.; Lu, C. C. Leveraging Molecular Metal–Support Interactions for H2 and N2 Activation. *Coord. Chem. Rev.* **2017**, *334*, 100–111.
(48) Eisenhart, R. J.; Clouston, L. J.; Lu, C. C. Configuring Bonds between First-Row Transition Metals. *Acc. Chem. Res.* **2015**, *48*, 2885–2894.
(49) Serrano-Plana, J.; Garcia-Bosch, I.; Company, A.; Costas, M. Structural and Reactivity Models for Copper Oxygenases: Cooperative Effects and Novel Reactivities. *Acc. Chem. Res.* **2015**, *48*, 2397–2406.
(50) Schwarz, A. D.; Herbert, K. R.; Paniagua, C.; Mountford, P. Ligand Variations in New Sulfonamide-Supported Group 4 Ring-Opening Polymerization Catalysts. *Organometallics* **2010**, *29*, 4171–4188.
(51) Lacy, D. C.; Park, Y. J.; Ziller, J. W.; Yano, J.; Borovik, A. S. Assembly and Properties of Heterobimetallic Co(II/III)/Ca(II) Complexes with Aquo and Hydroxo Ligands. *J. Am. Chem. Soc.* **2012**, *134*, 17526–17535.
(52) Park, Y. J.; Cook, S. A.; Sickerman, N. S.; Sano, Y.; Ziller, J. W.; Borovik, A. S. Heterobimetallic Complexes with M^{III}-(μ-OH)-M^{II} Cores (M^{III} = Fe, Mn, Ga; M^{II} = Ca, Sr, and Ba): Structural, Kinetic, and Redox Properties. *Chem. Sci.* **2013**, *4*, 717–726.
(53) Sano, Y.; Weitz, A. C.; Ziller, J. W.; Hendrich, M. P.; Borovik, A. S. Unsymmetrical Bimetallic Complexes with M^{II}–(*μ*-OH)–M^{III} Cores ($M^{II}M^{III}$ = $Fe^{II}Fe^{III}$, $Mn^{II}Fe^{III}$, $Mn^{II}Mn^{III}$): Structural, Magnetic, and Redox. *Inorg. Chem.* **2013**, *52*, 10229–10231.
(54) Sano, Y.; Lau, N.; Weitz, A. C.; Ziller, J. W.; Hendrich, M. P.; Borovik, A. S. Models for Unsymmetrical Active Sites in Metalloproteins: Structural, Redox, and Magnetic Properties of Bimetallic Complexes with M^{II}-(*μ*-OH)-Fe^{III} Cores. *Inorg. Chem.* **2017**, *56*, 14118–14128.
(55) Lau, N.; Sano, Y.; Ziller, J. W.; Borovik, A. S. Modular Bimetallic Complexes with a Sulfonamido-Based Ligand. *Dalt. Trans.* **2018**, *47*, 12362–12372.
(56) Cook, S. A.; Ziller, J. W.; Borovik, A. S. Iron(II) Complexes Supported by Sulfonamido Tripodal Ligands: Endogenous versus Exogenous Substrate Oxidation. *Inorg. Chem.* **2014**, *53*, 11029–11035.
(57) Oswald, V. F.; Lee, J. L.; Biswas, S.; Weitz, A. C.; Mittra, K.; Fan, R.; Li, J.; Zhao, J.; Hu, M. Y.; Alp, E. E.; Bominaar, E. L.; Guo, Y.; Green, M. T.; Hendrich, M. P.; Borovik, A. S. Effects of Noncovalent Interactions on High-Spin Fe(IV)–Oxido Complexes. *J. Am. Chem. Soc.* **2020**, *142*, 11804–11817.
(58) Lee, J. L. Synthetic Models for Metalloenzyme Active Sites: Accessing High-Valent Bimetallic Complexes with [M–(μ-OH)–M'] Cores, University of California, Irvine, 2021.
(59) Lee, J. L.; Oswald, V. F.; Biswas, S.; Hill, E. A.; Ziller, J. W.; Hendrich, M. P.; Borovik, A. S. Stepwise Assembly of Heterobimetallic Complexes: Synthesis, Structure, and Physical Properties. *Dalt. Trans.* **2021**, *50*, 8111–8119.
(60) Lee, J. L.; Biswas, S.; Sun, C.; Ziller, J. W.; Hendrich, M. P.; Borovik, A. S. Bioinspired Di-Fe Complexes: Correlating Structure and Proton Transfer over Four Oxidation States. *J. Am. Chem. Soc.* **2022**, *144*, 4559–4571.

(61) Yoshimura, A.; Zhdankin, V. V. Advances in Synthetic Applications of Hypervalent Iodine Compounds. *Chem. Rev.* **2016**, *116*, 3328–3435.
(62) Pfaff, F. F.; Kundu, S.; Risch, M.; Pandian, S.; Heims, F.; Pryjomska-Ray, I.; Haack, P.; Metzinger, R.; Bill, E.; Dau, H.; Comba, P.; Ray, K. An Oxocobalt(IV) Complex Stabilized by Lewis Acid Interactions with Scandium(III) Ions. *Angew. Chemie Int. Ed.* **2010**, *50*, 1711–1715.
(63) Song, W. J.; Seo, M. S.; DeBeer George, S.; Ohta, T.; Song, R.; Kang, M.-J.; Tosha, T.; Kitagawa, T.; Solomon, E. I.; Nam, W. Synthesis, Characterization, and Reactivities of Manganese(V)−Oxo Porphyrin Complexes. *J. Am. Chem. Soc.* **2007**, *129*, 1268–1277.
(64) Song, W. J.; Sun, Y. J.; Choi, S. K.; Nam, W. Mechanistic Insights into the Reversible Formation of Iodosylarene-Iron Porphyrin Complexes in the Reactions of Oxoiron(IV) Porphyrin Pi-Cation Radicals and Iodoarenes: Equilibrium, Epoxidizing Intermediate, and Oxygen Exchange. *Chem. Eur. J.* **2005**, *12*, 130–137.
(65) Nam, W.; Choi, S. K.; Lim, M. H.; Rohde, J.-U.; Kim, I.; Kim, J.; Kim, C.; Que, L. J. Reversible Formation of Iodosylbenzene-Iron Porphyrin Intermediates in the Reaction of Oxoiron(IV) Porphyrin Pi-Cation Radicals and Iodobenzene. **2003**, *42*, 109–111.
(66) Nguyen, A. I.; Hadt, R. G.; Solomon, E. I.; Tilley, T. D. Efficient C–H Bond Activations via O2 Cleavage by a Dianionic Cobalt(II) Complex. *Chem. Sci.* **2014**, *5*, 2874–2878.
(67) McDonald, A. R.; Que Jr., L. High-Valent Nonheme Iron-Oxo Complexes: Synthesis, Structure, and Spectroscopy. *Coord. Chem. Rev.* **2013**, *257*, 414–428.
(68) Wang, B.; Lee, Y.-M.; Tcho, W.-Y.; Tussupbayev, S.; Kim, S.-T.; Kim, Y.; Seo, M. S.; Cho, K.-B.; Dede, Y.; Keegan, B. C.; Ogura, T.; Kim, S. H.; Ohta, T.; Baik, M.-H.; Ray, K.; Shearer, J.; Nam, W. Synthesis and Reactivity of a Mononuclear Non-Haem Cobalt(IV)-Oxo Complex. *Nat. Commun.* **2017**, *8*, 14839.
(69) Hong, S.; Pfaff, F. F.; Kwon, E.; Wang, Y.; Seo, M. S.; Bill, E.; Ray, K.; Nam, W. Spectroscopic Capture and Reactivity of a Low-Spin Cobalt(IV)-Oxo Complex Stabilized by Binding Redox-Inactive Metal Ions. *Angew. Chemie Int. Ed.* **2014**, *53*, 10403–10407.
(70) Hill, E. A.; Kelty, M. L.; Filatov, A. S.; Anderson, J. S. Isolable Iodosylarene and Iodoxyarene Adducts of Co and Their O-Atom Transfer and C–H Activation Reactivity. *Chem. Sci.* **2018**, *9*, 4493–4499.
(71) Groves, J. T.; Nemo, T. E.; Myers, R. S. Hydroxylation and Epoxidation Catalyzed by Iron-Porphine Complexes. Oxygen Transfer from Iodosylbenzene. *J. Am. Chem. Soc.* **1979**, *101*, 1032–1033.
(72) Groves, J. T.; Kruper, W. J. J.; Haushalter, R. C. Hydrocarbon Oxidations with Oxometalloporphinates. Isolation and Reactions of a (Porphinato)Manganese(V) Complex. *J. Am. Chem. Soc.* **1980**, *102*, 6375–6377.
(73) Hong, S.; Wang, B.; Seo, M. S.; Lee, Y.-M.; Kim, M. J.; Kim, H. R.; Ogura, T.; Garcia-Serres, R.; Clémancey, M.; Latour, J.-M.; Nam, W. Highly Reactive Nonheme Iron(III) Iodosylarene Complexes in Alkane Hydroxylation and Sulfoxidation Reactions. *Angew. Chem. Int. Ed.* **2014**, *53*, 6388–6392.
(74) Wang, B.; Lee, Y. M.; Seo, M. S.; Nam, W. Mononuclear Nonheme Iron(III)-Iodosylarene and High-Valent Iron-Oxo Complexes in Olefin Epoxidation Reactions. *Angew. Chemie Int. Ed.* **2015**, *54*, 11740–11744.
(75) Collman, J. P.; Chien, A. S.; Eberspacher, T. A.; Brauman, J. I. Multiple Active Oxidants in Cytochrome P-450 Model Oxidations. *J. Am. Chem. Soc.* **2000**, *122*, 11098–11100.
(76) Leeladee, P.; Goldberg, D. P. Epoxidations Catalyzed by Manganese(V) Oxo and Imido Complexes: Role of the Oxidant-Mn-Oxo (Imido) Intermediate. *Inorg. Chem.* **2010**, *49*, 3083–3085.
(77) Wang, S. H.; Mandimutsira, B. S.; Todd, R.; Ramdhanie, B.; Fox, J. P.; Goldberg, D. P. Catalytic Sulfoxidation and Epoxidation with a Mn(III) Triazacorrole: Evidence for A "Third Oxidant" in High-Valent Porphyrinoid Oxidations. *J. Am. Chem. Soc.* **2004**, *126*, 18–19.
(78) Zdilla, M. J.; Abu-Omar, M. M. Manganese(III) Corrole-Oxidant Adduct as the Active Intermediate in Catalytic Hydrogen Atom Transfer. *Inorg. Chem.* **2008**, *47*, 10718–10722.
(79) Hammes, B. S.; Young, V. G.; Borovik, A. S. Hydrogen-Bonding Cavities about Metal Ions: A Redox Pair of Coordinatively Unsaturated Paramagnetic Co-OH Complexes. *Angew. Chemie Int. Ed.* **1999**, *38*, 666–669.
(80) Jones, J. R.; Ziller, J. W.; Borovik, A. S. Modulating the Primary and Secondary Coordination Spheres within a Series of CoII-OH Complexes. *Inorg. Chem.* **2017**, *56*, 1112–1120.

(81) Lucas, R. L.; Zart, M. K.; Murkerjee, J.; Sorrell, T. N.; Powell, D. R.; Borovik, A. S. A Modular Approach toward Regulating the Secondary Coordination Sphere of Metal Ions: Differential Dioxygen Activation Assisted by Intramolecular Hydrogen Bonds. *J. Am. Chem. Soc.* **2006**, *128*, 15476–15489.
(82) Popescu, D.-L.; Chanda, A.; Stadler, M.; Tiago de Oliveira, F.; Ryabov, A. D.; Muenck, E.; Bominaar, E. L.; Collins, T. J.; de Oliveira, F. T.; Ryabov, A. D.; Munck, E.; Bominaar, E. L.; Collins, T. J. High-Valent First-Row Transition-Metal Complexes of Tetra-Amido (4N) and Diamidodialkoxido or Diamidophenolato (2N/2O) Ligands: Synthesis, Structure, and Magnetochemistry. *Coord. Chem. Rev.* **2008**, *252*, 2050–2071.
(83) Sickerman, N. S. Investigating the Effects of Non-Covalent Interactions in Metal Complexes with Versatile Ligand Scaffolds, University of California, Irvine, 2014.
(84) Ray, M.; Hammes, B. S.; Yap, G. P. A.; Rheingold, A. L.; Borovik, A. S. Structure and Physical Properties of Trigonal Monopyramidal Iron(II), Cobalt(II), Nickel(II), and Zinc(II) Complexes. *Inorg. Chem.* **1998**, *37*, 1527–1532.
(85) Malik, D. D.; Chandra, A.; Seo, M. S.; Lee, Y. M.; Farquhar, E. R.; Mebs, S.; Dau, H.; Ray, K.; Nam, W. Formation of Cobalt–Oxygen Intermediates by Dioxygen Activation at a Mononuclear Nonheme Cobalt(II) Center. *Dalt. Trans.* **2021**, *50*, 11889–11898.
(86) Dori, Z.; Gray, H. B. High-Spin, Five-Coordinate Cobalt(II) Complexes. *Inorg. Chem.* **1968**, *7*, 889–892.
(87) Banci, L.; Benelli, C.; Gatteschi, D.; Mani, F. Unusual Electronic Spectra of the Pseudotetrahedral Complex [Tris((3,5-Dimethyl-1-Pyrazolyl)Ethyl)Amine]Cobalt(II) Bis(Tetraphenylborate). *Inorg. Chem.* **1982**, *21*, 1133–1136.
(88) Searls, C. E.; Kleespies, S. T.; Eppright, M. L.; Schwartz, S. C.; Yap, G. P. A.; Scarrow, R. C. Trigonal Bi- and Monopyramidal Cobalt(II) Complexes of a Novel Guanidine-Based Tripodal Ligand. *Inorg. Chem.* **2010**, *49*, 11261–11263.
(89) Alliger, G. E.; Muller, P.; Cummins, C. C.; Nocera, D. G. Cofacial Dicobalt Complex of a Binucleating Hexacarboxamide Cryptand Ligand. *Inorg. Chem.* **2010**, *49*, 3697–3699.
(90) Blacquiere, J. M.; Pegis, M. L.; Raugei, S.; Kaminsky, W.; Forget, A.; Cook, S. A.; Taguchi, T.; Mayer, J. M. Synthesis and Reactivity of Tripodal Complexes Containing Pendant Bases. *Inorg. Chem.* **2014**, *53*, 9242–9253.
(91) Jones, M. B.; MacBeth, C. E. Tripodal Phenylamine-Based Ligands and Their CoII Complexes. *Inorg. Chem.* **2007**, *46*, 8117–8119.
(92) Banci, L.; Bencini, A.; Benelli, C.; Gatteschi, D.; Zanchini, C. Spectral-Structural Correlations in High-Spin Cobalt(II) Complexes. In *Structure and Bonding*; Springer-Verlag Berlin Heidelberg, 1982; pp 37–86.
(93) Addison, A. W.; Rao, T. N.; Reedijk, J.; van Rijn, J.; Verschoor, G. C. Synthesis, Structure, and Spectroscopic Properties of Copper(II) Compounds Containing Nitrogen-Sulphur Donor Ligands; the Crystal and Molecular Structure of Aqua[1,7-Bis(N-Methylbenzimidazol-2[Prime or Minute]-Yl)-2,6-Dithiaheptane]Copper(II) Perchlorate. *J. Chem. Soc. Dalt. Trans.* **1984**, *7*, 1349–1356..
(94) Kucharski, E. S.; Skelton, B. W.; White, A. H. Crystal Structure of Carbonatohydroxo- (2, 2':6', 2''-Terpyridyl)Cobalt(Iii) Tetrahydrate. *Aust. J. Chem.* **1978**, *31*, 47–51.
(95) Poth, T.; Paulus, H.; Elias, H.; Eldik, R. van; Grohmann, A. Kinetics and Mechanism of Base Hydrolysis in Cobalt(III) Complexes – The Case of a Complex CoLCl2+ Where L Has the Novel Topology of a Square-Pyramidal NN4 Coordination Cap. *Eur. J. Inorg. Chem.* **1999**, *4*, 643–650.
(96) Hana, F.; Lough, A. J.; Lavoie, G. G. Coordinatively- and Electronically-Unsaturated Square Planar Cobalt(III) Complexes of a Pyridine Dianionic Pincer Ligand. *Dalt. Trans.* **2017**, *46*, 16228.
(97) Nurdin, L.; Spasyuk, D. M.; Fairburn, L.; Piers, W. E.; Maron, L. Oxygen–Oxygen Bond Cleavage and Formation in Co(II)-Mediated Stoichiometric O2 Reduction via the Potential Intermediacy of a Co(IV) Oxyl Radical. *J. Am. Chem. Soc.* **2018**, *140*, 16094–16105.
(98) Goetz, M. K.; Hill, E. A.; Filatov, A. S.; Anderson, J. S. Isolation of a Terminal Co(III)-Oxo Complex. *J. Am. Chem. Soc.* **2018**, *140*, 13176–13180.
(99) Connelly, N. G.; Geiger, W. E. Chemical Redox Agents for Organometallic Chemistry. *Chem. Rev.* **1996**, *96*, 877–910.

(100) Schoenfeldt, N. J.; Ni, Z.; Korinda, A. W.; Meyer, R. J.; Notestein, J. M. Manganese Triazacyclononane Oxidation Catalysts Grafted under Reaction Conditions on Solid Cocatalytic Supports. *J. Am. Chem. Soc.* **2011**, *133*, 18684–18695.
(101) Cao, R.; Müller, P.; Lippard, S. J. Tripodal Tris-Tacn and Tris-Dpa Platforms for Assembling Phosphate-Templated Trimetallic Centers. *J. Am. Chem. Soc.* **2010**, *132*, 17366–17369..
(102) Zhdankin, V. V.; Litvinov, D. N.; Koposov, A. Y.; Luu, T.; Ferguson, M. J.; McDonald, R.; Tykwinski, R. R. Preparation and Structure of 2-Iodoxybenzoate Esters: Soluble and Stable Periodinane Oxidizing Reagents. *Chem. Commun.* **2004**, *263*, 106–107.
(103) Zhdankin, V. V.; Koposov, A. Y.; Litvinov, D. N.; Ferguson, M. J.; McDonald, R.; Luu, T.; Tykwinski, R. R. Esters of 2-Iodoxybenzoic Acid: Hypervalent Iodine Oxidizing Reagents with a Pseudobenziodoxole Structure. *J. Org. Chem.* **2005**, *70*, 6484–6491.
(104) Heintz, R. A.; Smith, J. A.; Szalay, P. S.; Weisgerber, A.; Dunbar, K. R. Homoleptic Transition Metal Acetonitrile Cations with Tetrafluoroborate or Trifluoromethanesulfonate Anions. *Inorg. Synth.* **2002**, *33*, 75–83.
(105) Petasis, D. T.; Hendrich, M. P. Quantitative Interpretation of Multifrequency Multimode EPR Spectra of Metal Containing Proteins, Enzymes, and Biomimetic Complexes. *Methods Enzymol.* **2015**, *563*, 171–208.
(106) Bruker AXS Inc, SAINT Version 8.34a. Madison, WI 2013.
(107) Krause, L.; Herbst-Irmer, R.; Sheldrick, G. M.; Stalke, D. Comparison of Silver and Molybdenum Microfocus X-Ray Sources for Single-Crystal Structure Determination. *J. Appl. Crystallogr.* **2015**, *48*, 3–10.
(108) Sheldrick, G. M. A Short History of SHELX. *Acta Crystallogr. Sect. A Found. Crystallogr.* **2008**, *64*, 112–122.
(109) Sheldrick, G. M.; IUCr. Crystal Structure Refinement with SHELXL. *Acta Crystallogr. Sect. A Found. Crystallogr.* **2015**, *71*, 3–8.
(110) Sheldrick, G. M.; IUCr. Crystal Structure Refinement with SHELXL. *Acta Crystallogr., Sect. C Cryst. Struct. Commun.* **2015**, *71*, 3–8.
(111) Kratzert, D. FinalCif.
(112) Hübschle, C. B.; Sheldrick, G. M.; Dittrich, B. ShelXle: A Qt Graphical User Interface for SHELXL. *urn:issn:0021-8898* **2011**, *44*, 1281–1284.
(113) Spek, A. L. PLATON SQUEEZE: A Tool for the Calculation of the Disordered Solvent Contribution to the Calculated Structure Factors. *Acta Crystallogr. Sect. C Struct. Chem.* **2015**, *71*, 9–18.
(114) Spek, A. L.; IUCr. Single-Crystal Structure Validation with the Program PLATON. *J. Appl. Crystallogr.* **2003**, *36*, 7–13.
(115) Spek, A. L. Structure Validation in Chemical Crystallography. *Acta Crystallogr. Sect. D Biol. Crystallogr.* **2009**, *65*, 148–155.

Chapter 4: Modulating magnetic coupling through synthetic control in paramagnetic $Co^{II/III}$–μ-O(H)–Fe^{III} complexes

Introduction

Recent work within the Borovik lab has focused on understanding the chemistry of metal complexes supported by *N,N′,N″*-[nitrilotris(ethane-2,1-diyl)]tris(*P,P*-diphenylphosphinic amido), $[poat]^{3-}$.[1,2] The $[poat]^{3-}$ ligand was designed to have a similar donation strength in the primary (1º) coordination sphere to the ureayl framework $[H_3buea]^{3-}$ to support highly oxidized metal centers.[2–8] The secondary (2º) coordination sphere was engineered to provide hydrogen bond (H–bond) acceptors, similar to the $[RST]^{3-}$ ligand framework(s).[9–12] All three of these ligands share a few key characteristics: local C_3 symmetry, a trianionic ligand field, a tetradentate coordination motif, and a well-defined 2º coordination sphere positioned to form a pocket ideal for hosting and interacting with an exogenous ligand. These features are all supportive of forming high-spin, high valent metal complexes within a rigid ligand field, providing excellent synthetic control. It has become abundantly clear that the P=O units of the phosphinic amido arms of $[poat]^{3-}$ provide a highly effective binding site for a second metal ion and support more highly oxidized metal ions than the $[RST]^{3-}$ sulfonamido groups.[2,4,5,13–17] Indeed, complexes prepared within $[poat]^{3-}$ typically crystallize as $K_x[M^ypoat(L)]$, where one or more of the P=O arms interacts with the K^+ counterion(s).[2,4,5,14–17] Unpublished work within the group has focused considerably on eliminating these P=O···K^+ interactions through metathesis with alkyl ammonium salts. While metathesis may be successful in solution, the P=O···K^+ aggregates are typically the solid product(s) isolated and obtained from X-ray diffraction methods.

The strong interactions the P=O units in $[poat]^{3-}$ exhibit with exogenous metal ion(s) is mirrored in other examples of ligand frameworks that feature similar P=O functionalities. One notable example is the Kläui ligand: $[CpCo^{III}(P(O)RR')_3]^-$, (Fig 4-1).[18] R,R' refers to substituted alkyl, aryl, or alkoxyl groups that are appended from the P=O units. When used to prepare metal complexes, the Kläui complex binds an additional metal through the P=O units in a facial orientation, including main group, transition, and rare earth metal ions (M^x, Fig 4-1).[18–24] The facial coordination motif of the Kläui ligand lends itself to the preparation of bimetallic piano-stool and trimetallic sandwich complexes, based on the stoichiometry of the reagents. In one example, a

trimetallic system was prepared where all metal ions present were Co^{III}. The central Co^{III} ion exhibited spin-crossover behavior between S = 0 and 2 spin states.[19,20] The unusual Co^{III} spin state was achieved due to the strongly donating, but weak field P=O groups from the Kläui ligand. These characteristics are shared by a tripodal phosphinimide ligand developed by Rittle and coworkers, as well as the bistrimetaphosphate complexes described by Stauber *et al.* (Fig 4-1).[25,26] Each of these examples supported formation of high-spin S = 2 Co^{III} complexes, thus indicating that P=O and phosphinimide (P=N–R) moieties may be uniquely suited to supporting high-spin metal centers. In a recent study, the Kläui ligand was used to prepare a series of complexes where the Tc ion coordinated to the P=O groups varied oxidation state between Tc^{I} – Tc^{VII}.[27] This work suggested that P=O groups, in addition to supporting high-spin states, was also supportive of metal ions in a wide variety of oxidation states.

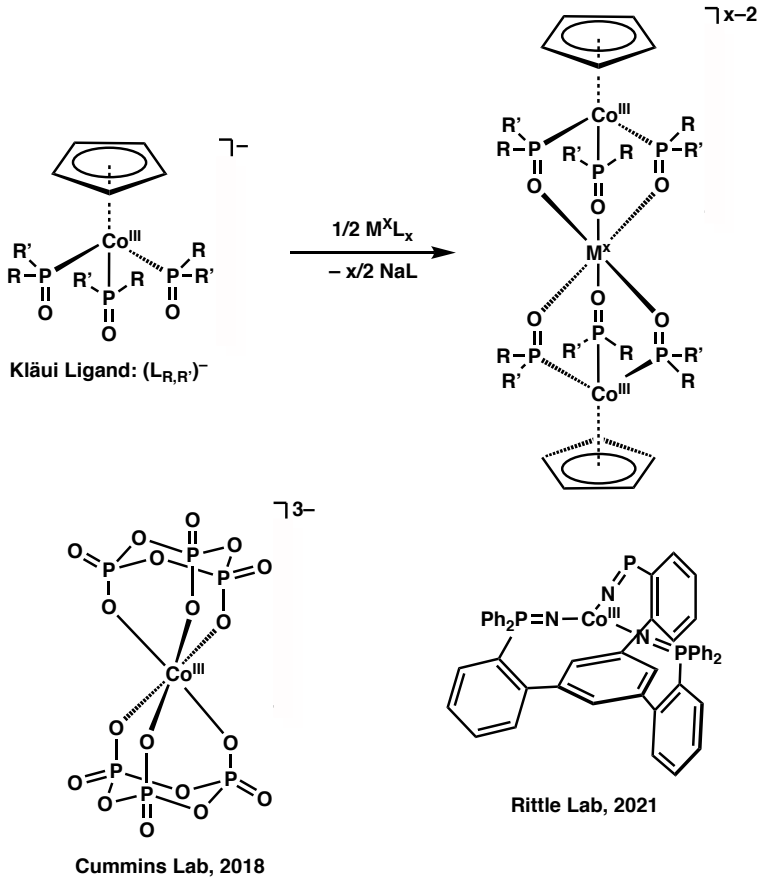

Figure 4-1: Top: Preparation of a trimetallic sandwich complex using the Kläui ligand. The central metal ion, M, has been shown to be main group, rare earth, and transition metal ions. Bottom: S = 2 Co^{III} complexes supported by bistrimetaphosphate and tris(phosphinimide) ligand fields.

Thus far, this dissertation has only discussed metal complexes that featured a redox-inactive metal ion coordinated to the P=O groups. This chapter seeks to explore the chemistry of a Co/Fe system, using K[Co^{II}poat] and [Fe^{II}Me$_3$tacn(OTf)$_2$] to assemble an unsymmetric bimetallic complex. The preparation of the Co/Fe bimetallic system was found to be sensitive and reactive towards O_2, leading to the formation of a μ-OH bridge: [poatCo^{II}–μ-OH–Fe^{III}Me$_3$tacn]OTf. The source of the hydroxido was explored, as well as potential mechanisms of O_2 activation. The data collected suggested that the Co center was not oxidized, but rather [Co^{II}poat]$^-$ primarily provided a site for the Fe^{II} center to dock, while the P=O groups provided a supportive ligand field. It appears that the two systems, K[Co^{II}poat] and [Fe^{II}Me$_3$tacn(OTf)$_2$], act in concert with one another and are both necessary to observe reactivity with O_2 in an example of cooperative bimetallic chemistry. [poatCo^{II}–μ-OH–Fe^{III}Me$_3$tacn]OTf was oxidized using FcOTf. The oxidation was observed on the Co center to form [poatCo^{III}–μ-OH–Fe^{III}Me$_3$tacn](OTf)$_2$. Oxidation of the Co center changed the magnetic coupling between the two metal ions from antiferromagnetic to ferromagnetic coupling. Finally, preliminary deprotonation studies were conducted on [poatCo^{III}–μ-OH–Fe^{III}Me$_3$tacn](OTf)$_2$. The results suggested that the μ-OH bridge could be deprotonated and this deprotonation once again led to a change in the mode of magnetic communication between the two metal centers, from ferromagnetic to antiferromagnetic. Controlling the protonation and oxidation states of the complexes within this series provided a synthetic handle to modify magnetic communication.

Results and Discussion

Reactivity of K[Co^{II}poat] with O_2: mono- versus bimetallic

As discussed in the previous chapter, K[Co^{II}poat] is a trigonal monopyramidal (TMP) coordination complex. For all synthetic details and spectroscopic characterization of K[Co^{II}poat], refer to Chapter 3 of this dissertation. In previous studies from the Borovik lab, the reactivity of Co^{II} complexes in C_3 symmetry with O_2 was studied. It was found that when a starting Co^{II} complex was reacted with O_2 in the presence of H–bond donors, such as ureayl functional groups, a Co^{III}–OH complex was formed or reversible Co^{III}–superoxido generation was observed.[8,28,29] In the absence of H–bond donors, the metal complex did not react with O_2.[28] More recent work from Nam and coworkers indicated that treating [(TMG$_3$tren)Co^{II}OTf]OTf with O_2 in the

presence of a sacrificial H-atom donor resulted in the formation of a Co^{IV}–O complex via a Co^{II}–alkylperoxo intermediate.[30] Given the variety of inorganic products observed following the reaction of C_3-symmetric Co^{II} complexes with O_2, the reactivity of K[Co^{II}poat] with O_2 was of synthetic interest.

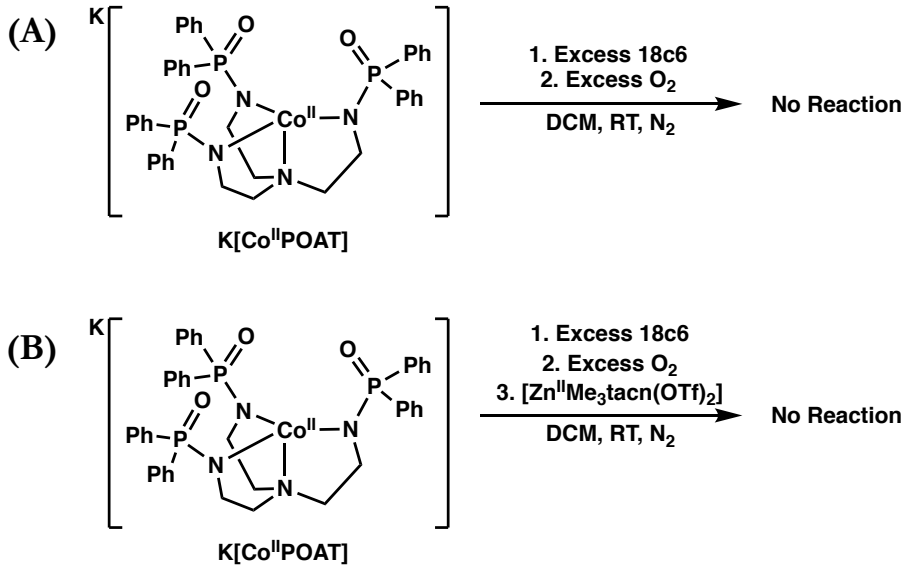

Scheme 4-1: Representation of the lack of reaction between K[Co^{II}poat] and O_2 alone **(A)** and in the presence of [$Zn^{II}Me_3$tacn$(OTf)_2$] **(B)**.

To this end, excess O_2 was added to a solution of K[Co^{II}poat] and the reaction was followed spectroscopically (Scheme 4-1, A). These reactions were carried out in dichloromethane (DCM) in the presence of excess 18-crown-6 ether (18c6). The reaction was monitored by ultraviolet-visible (UV-vis) and ⊥-mode electron paramagnetic resonance (EPR) spectroscopy, but no changes were observed from the starting K[Co^{II}poat] spectra. Even when these reactions were left to stir overnight, no spectroscopic changes here observed. In spite of the relatively low oxidation potential ($Co^{III/II}$, $E_{1/2}$ = –0.495 V versus ferrocenium/ferrocene, $Fc^{+/0}$, DCM, see Chapter 3), which suggested that the Co^{III} oxidation state may be accessible by O_2 ($O_2 \longrightarrow O_2^-$ E°, V versus $Fc^{+/0}$ = –0.22 V, H_2O; +0.08 V, DCM, estimated),[31,32] K[Co^{II}poat] was not reactive towards O_2. While electrochemical potentials play an important role in driving oxidation-reduction (redox) reactions, binding ability/affinity is also important, particularly if O_2 behaves as an inner sphere oxidant.[32,33] In the examples discussed above, intramolecular H–bond donating groups or sacrificial H-atom donors were necessary for O_2 activation to proceed.[28,30] Given that $[poat]^{3-}$ does not provide

intramolecular H–bond donors nor were any H-atom donors added to these reactions, it was unsurprising that K[Co^{II}poat] on its own was not reactive towards O_2.

In Chapter 3 of this dissertation, it was found that the addition of a second metal ion, [Zn^{II}Me$_3$tacn(OTf)$_2$], to [Co^{II}poat]$^-$ in the presence of an external oxidant, isopropyl 2-iodoxybenzoate (IBX-*i*Pr), resulted in the activation of IBX-*i*Pr and the formation of a bimetallic species with a bridging hydroxido ligand. Therefore, [Co^{II}poat]$^-$ was reacted with O_2 in the presence of 18c6 and [Zn^{II}Me$_3$tacn(OTf)$_2$] to determine if the two metals acting together were sufficient to activate O_2 (Scheme 4-1B). The reaction was followed spectroscopically and no changes consistent with oxidation were observed by UV-vis nor EPR spectroscopy. There were subtle differences between the initial K[Co^{II}poat] spectrum and the final spectrum observed, which was preliminarily attributed to an interaction between the Zn^{II} ion and [Co^{II}poat]$^-$ via the P=O groups. This observation is further discussed in Chapter 5.

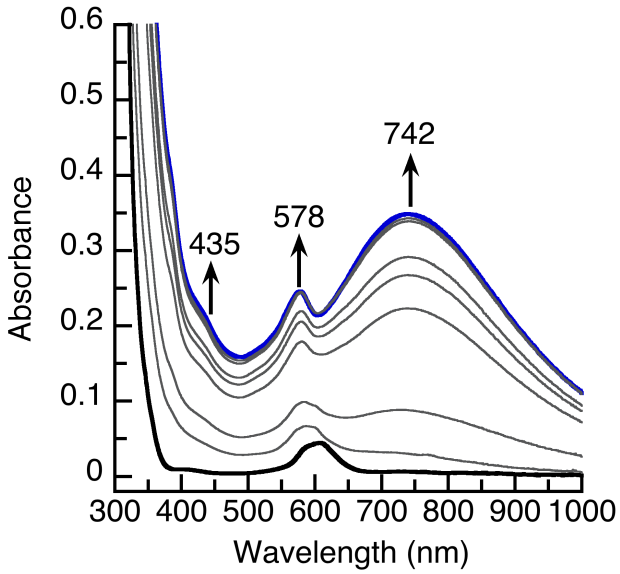

Figure 4-2: UV-vis spectra monitoring the reaction between K[Co^{II}poat] (black trace) with O_2 and [Fe^{II}Me$_3$tacn(OTf)$_2$]. The final product spectrum is shown in blue.

Because there was no reaction observed between [Co^{II}poat]$^-$ and O_2 following addition of a redox-inactive metal, the experiment was modified to incorporate a redox-active metal ion, [Fe^{II}Me$_3$tacn(OTf)$_2$]. When [Fe^{II}Me$_3$tacn(OTf)$_2$] was added to [Co^{II}poat]$^-$ in the presence of dry O_2, an immediate color change occurred (Fig 4-2). A new, deep-blue species formed with features at λ_{max} = 435, 578, 742 nm. This spectrum was unique

to the product of this reaction and was not consistent with either the K[Co^{II}poat] (λ_{max} = 358, 585, 619, 770 nm) or the [Fe^{II}Me$_3$tacn(OTf)$_2$] (featureless, Fig 4-S1B) starting complexes. This reaction was also monitored with ⊥-mode EPR spectroscopy and a silent EPR spectrum was observed. In order to identify the product of this reaction, bulk studies were pursued with a goal of obtaining a molecular structure.

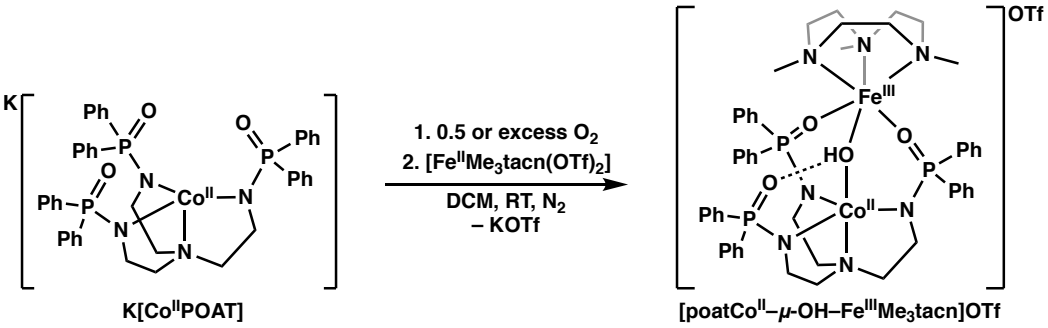

Scheme 4-2: Reaction scheme describing the preparation of [poatCo^{II}–μ-OH–Fe^{III}Me$_3$tacn]OTf.

Synthesis and Structural Details of [poatCo^{II}–μ-OH–Fe^{III}Me$_3$tacn]OTf: Bulk synthetic studies were performed, designed to replicate the reaction observed in the above spectroscopic studies. Following the synthesis outlined in Scheme 4-2, a concentrated solution of K[Co^{II}poat] was prepared in DCM without 18c6 and transferred to a Schlenk flask. [Fe^{II}Me$_3$tacn(OTf)$_2$] was dissolved in DCM in a round bottom flask and sealed. Both solutions were taken out of the dry box and the [Fe^{II}Me$_3$tacn(OTf)$_2$] solution was sparged with N_2. While this solution sparged, dry O_2 was bubbled into the K[Co^{II}poat] solution; addition of O_2 did not result in a color change. The [Fe^{II}Me$_3$tacn(OTf)$_2$] solution was cannulated into the K[Co^{II}poat] and O_2 solution, which resulted in an immediate color change to deep blue, similar to the color observed in the above spectroscopic studies. The resulting solution stirred under a N_2 atmosphere for roughly an hour, at which point the solvent was removed and the resulting solids were dried under vacuum. The solids were transferred to a dry box and redissolved in minimal DCM. The reaction mixture was then filtered to remove any residual solids and layered under *n*-pentane, which resulted in the growth of dark, red-blue dichroic single crystals suitable for single X-ray diffraction (XRD) studies.

The molecular structure revealed a heterobimetallic complex with a single hydroxido bridging ligand, formulated as [poatCo^{II}–μ-OH–Fe^{III}Me$_3$tacn]OTf ([Co^{II}–μ-OH–Fe^{III}]$^+$, Fig 4-3). In addition to the fully refined molecular structure discussed herein, [Co^{II}–μ-OH–Fe^{III}]$^+$ can also be crystallized in a different unit cell (Table 4-S2). A five-coordinate Co^{II} center was bound within the tetradentate backbone of the [poat]$^{3-}$ ligand framework. The fifth coordination site was occupied by the O-atom of a $^-$OH ligand, giving the Co center an overall N_4O coordination environment. The coordination geometry of the Co center is near trigonal bipyramidal, with a τ_5 value of 0.87.[34] The H-atom of the $^-$OH unit was found via a Fourier-difference map, confirming the identity of O1 bridging ligand. In addition to binding to both Co and Fe centers, O1 participated in an intramolecular H–bonding interaction with O2 from one of the P=O groups (O1···O2 = 2.679(2) Å). The Fe center was bound by two O-atom based ligands from the P=O groups of the [poat]$^{3-}$ ligand framework as well as the $^-$OH ligand in a facial orientation. The remaining open coordination sites of the Fe center were occupied with three N-donors from the Me$_3$tacn ligand, also bound in a facial manner. The Fe center had a general N_3O_3 coordination motif, with the ligands arranged in an approximate octahedral geometry. The complex had a +1 charge, with a triflate counterion. The charge provided from the ligands in this molecule was –4; therefore, the charge provided by the two metal centers must add to +5.

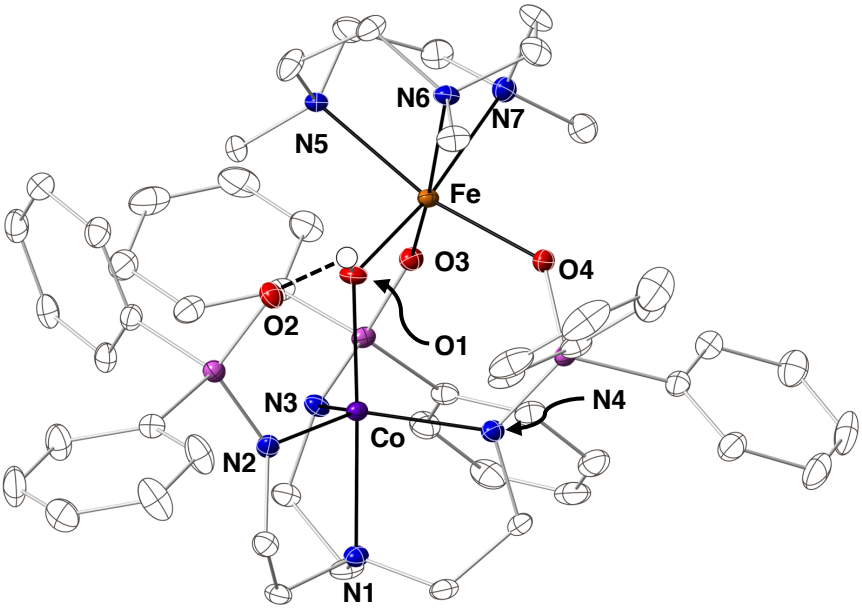

Figure 4-3: Solid state molecular structure of [poatCo^{II}–μ-OH–Fe^{III}Me$_3$tacn]OTf. Only the hydroxido H-atom is shown. All other H-atoms, the counterion, and structural solvent molecules were omitted for clarity. Thermal ellipsoids were drawn at 50% probability.

Table 4-1: Metrical data obtained from the molecular structures of $[Co^{II}–\mu\text{-}OH–Fe^{III}]^{+}$ and $[Co^{III}–\mu\text{-}OH–Fe^{III}]^{2+}$.

Atoms	$[Co^{II}–\mu\text{-}OH–Fe^{III}]^{+}$ Distance, Å	$[Co^{III}–\mu\text{-}OH–Fe^{III}]^{2+}$ Distance, Å
Co–N1	2.172(2)	1.943(3)
Co–N2	2.008(2)	1.924(3)
Co–N3	2.027(2)	1.979(3)
Co–N4	2.029(2)	1.958(3)
Co–O1	2.065(1)	1.935(2)
***N_{eq}···Co**	0.264	0.139
O1···O2	2.679(2)	2.646(3)
Fe–O1	1.848(1)	1.904(2)
Fe–O3	1.994(1)	1.946(2)
Fe–O4	1.995(1)	1.994(3)
Fe–N5	2.218(2)	2.209(3)
Fe–N6	2.226(2)	2.187(3)
Fe–N7	2.238(2)	2.217(3)
Co···Fe	3.3480(4)	3.4001(7)
	Angle, º	**Angle, º**
N1–Co–N2	82.22(6)	84.83(12)
N1–Co–N3	82.51(6)	83.12(12)
N1–Co–N4	82.79(6)	85.48(12)
N1–Co–O1	176.51(6)	176.58(11)
N2–Co–N3	120.05(7)	123.32(13)
N2–Co–N4	124.16(7)	124.83(12)
N3–Co–N4	110.71(7)	109.12(12)
Co–O1–Fe	117.55(7)	124.67(13)
O1–Fe–O3	96.51(6)	92.07(11)
O1–Fe–O4	95.67(6)	91.16(10)
O3–Fe–O4	96.78(5)	99.36(11)
N5–Fe–N6	79.39(6)	80.54(13)
N5–Fe–N7	78.74(6)	78.86(11)
N6–Fe–N7	78.22(6)	79.53(11)
$^{+}\tau_5 = (\beta - \alpha)/60°$	0.87	0.86

* N_{eq}···Co is the distance of the Co atom from the plane formed by the equatorial N–atoms of the $[poat]^{3-}$ backbone.
$^{+}$ τ_5 is the trigonality structural parameter. α and β are the two largest angles in the molecule. $\tau_5 = (\beta - \alpha)/60°$

In order for the two metal centers to provide an overall charge of +5, one metal must have an oxidation state of +2 and the other +3. To determine the oxidation states of the Co and Fe centers, the metal–ligand bond lengths around each metal ion were examined. All of the Co–N/O bond lengths were longer than 2 Å, which is typical of Co^{II} ions in C_3 symmetric ligand fields.[8,12,28,35,36] Crystallographically characterized examples of Co^{II}–OH complexes from the Borovik lab have an average Co–O1 bond length of 2.05 Å (see also Chapter 2),[8,36] while the average Co–O1 bond length contracts to 1.89 Å in structurally characterized Co^{III}–OH complexes (see also Chapters 2, 3).[8,12] Furthermore, the Fe–O bond lengths were all shorter than 2 Å with a noticeably short 1.848(1) Å Fe–O1 bond length. While the Fe–N bond lengths were longer than their Fe–O counterparts, both sets of bond lengths were consistent with known examples of bimetallic Fe^{III} complexes where the Fe^{III} ion was bound to two P=O groups, a bridging $^{-}$OH, and Me_3tacn ligands.[4,5] The bond length analysis supported the assignment of the oxidation states as Co^{II} and Fe^{III} centers.

Discussion of Metal Oxidation States: It was unusual that the Fe ion was more highly oxidized than the Co center in the $[Co^{II}–\mu\text{-}OH–Fe^{III}]^{+}$ complex, based on past work with bimetallic systems in $[poat]^{3-}$. The Co^{II} ion was coordinated in an overall tetra-anionic ligand field, while the Fe^{III} center was supported by a monoanionic ligand field. Because metal complexes within anionic ligand fields are generally more easily oxidized than metal ions in neutral environments, it was expected that the Co^{II} center would be more readily oxidized than the Fe^{II} center. However, there is a large electronegativity difference between the P- and O-atoms of the P=O groups that creates a significant dipole moment (P = 2.19 eV, O = 3.44 eV).[37] The resulting dipole moment between the these atoms imparts significant partial negative character (δ^{-}) to the O, which leads to a buildup of charge around each of the R–P=O O-atoms, to the degree that the P=O groups have also been represented by a resonance structure: $R–^{+}P–O^{-}$.[38–40] The charge buildup creates an electron rich cavity in the 2º coordination sphere (Fig 4-4), incorporating a second, clearly defined ligand field consisting of P=O groups within the $[poat]^{3-}$ ligand. The P=O groups have been previously shown to interact strongly with K^{+} counterion(s), Group II Lewis Acids, and transition metals, while supporting metal centers up to a M^{III} oxidation state [2,4,5,15] Further work with the Kläui ligand also indicated that P=O units were supportive of high-spin, highly oxidized metal centers.[19,20,27] Given that previous work has demonstrated the utility of the P=O ligands towards the preparation

of oxidized metal centers, it was perhaps not surprising in hindsight that the Fe center was oxidized. However, it was unusual that the Co^{II} center did not change oxidation states during this reaction.

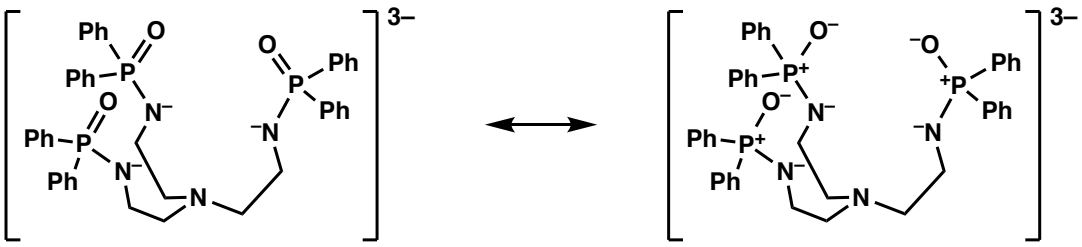

Figure 4-4: Representation of how the R–P=O resonance structure may affect the $[poat]^{3-}$ ligand framework.

As discussed above, $K[Co^{II}poat]$ had a $Co^{III/II}$ couple at –0.495 V versus $Fc^{+/0}$ in DCM. This potential was likely sufficiently reducing that it should be reactive towards O_2 ($O_2 \longrightarrow O_2^-$ E^o, V versus $Fc^{+/0}$ = –0.22 V, H_2O; +0.08 V, DCM).[31,32] However, the Co center was not oxidized in the presence of O_2. While the redox potentials were sufficient for a reaction to occur, the electrochemical potentials are not the only factor that could drive the reaction. The absence of H–bond donating groups in the 2º coordination sphere of $[Co^{II}poat]^-$ likely hinders reactivity towards O_2, as discussed above.[28] Given that the reactivity with O_2 was dramatically different in the presence of a second redox active metal ion, $[Co^{II}poat]^-$ can be viewed as an effective scaffold for the assembly of unsymmetric bimetallic systems, particularly in the presence of O_2. Furthermore, the oxidative load of this reaction appeared to to be borne exclusively by the Fe center in $[Co^{II}–\mu\text{-}OH–Fe^{III}]^+$.

Proposed Mechanisms for the Formation of $[Co^{II}–\mu\text{-}OH–Fe^{III}]^+$: Given that only the Fe center appeared to participate in the redox reaction with O_2, the mechanism of the reaction came into question. Specifically, it was unclear whether this reaction proceeded through an inner or outer sphere oxidation with O_2. If the reaction occurred via an inner sphere mechanism, the O_2 unit would bind first, presumably to the Fe center. O_2 would then be reduced concomitant to the oxidation of the Fe center, likely forming H_2O_2 or H_2O as a byproduct (Scheme 4-3). If an outer sphere mechanism was dominant, the O_2 would not coordinate to either metal center but transfer electronic equivalents through space. The source of the hydroxido O-atom would likely come from

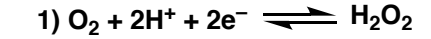

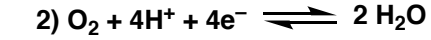

Scheme 4-3: Half reactions involved in the reduction of O_2 to either H_2O_2 (**1**) or H_2O (**2**)

some residual water in solvent or one of the product(s) of O_2 reduction. Regardless of the mechanism, the two metal ions likely pre-assembled in some manner, where the Fe center effectively docked to the P=O units prior to oxidation (Fig 4-5). This would provide a supportive ligand field to the Fe center, perhaps stabilizing it to coordinate to O_2 for an inner sphere mechanism or lowering the redox potential of the Fe center for an outer sphere oxidation by providing a ligand field with significant δ^- character.

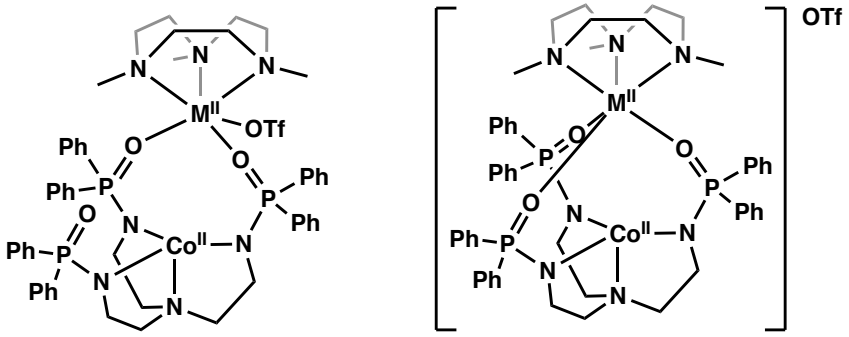

Figure 4-5: Proposed bimetallic species that may pre-assemble prior to oxidation.

To determine if the formation of $[Co^{II}–\mu\text{-}OH–Fe^{III}]^+$ occurred via an outer sphere mechanism, equimolar amounts of $K[Co^{II}poat]$ and $[Fe^{II}Me_3tacn(OTf)_2]$ were mixed and treated with a known outer sphere oxidant, FcOTf. FcOTf was chosen because $[Co^{II}poat\cdots Fe^{II}Me_3tacn]OTf$ has been studied and exhibited a redox event at $E_{1/2}$ = –0.18 V versus $Fc^{+/0}$ in DCM (Fig 4-5, right; for full discussion see Chapter 5). The reaction was monitored by UV-vis spectroscopy to determine if the product of this reaction was $[Co^{II}–\mu\text{-}OH–Fe^{III}]^+$, with the $^-$OH O-atom likely arising from residual water in the solvent. The reaction was followed for 48 hours and there appeared to be a broad increase in the baseline with a weak, low intensity shoulder that grew in. However, the final spectrum was not consistent with was $[Co^{II}–\mu\text{-}OH–Fe^{III}]^+$ (Fig 4-S1A). The bands were significantly different from $[Co^{II}–\mu\text{-}OH–Fe^{III}]^+$, without the diagnostic features at λ = 435, 578, 742 nm. This data further suggested that the oxidation with O_2 did not proceed via an outer sphere mechanism, though the reaction still needs to be studied with $\perp$-mode EPR spectroscopy and replicated in the presence of a small amount of exogenous water to replicate the potential byproduct(s) of O_2 reduction.

The data thus far did not conlcusively support an outer sphere oxidation mechanism driving the formation of $[Co^{II}–\mu\text{-}OH–Fe^{III}]^+$. Therefore, an inner sphere mechanism was considered. Because the Fe center was oxidized in this reaction while the Co ion was not, it was likely that putative O_2 binding occured at the Fe

center in the case of an inner sphere mechanism. Chemical reactions between Fe and O_2 have a long, rich history in both synthetic and biological systems, leading to the formation of different Fe–O(X) species, including Fe–OH complexes, though outer sphere oxidation predomintes in synthetic examples.[4,15,49,41–48] The affinity between O_2 and Fe center(s) is largely due to the energetic requirements of O_2 activation, which could play a role in driving the formation of $[Co^{II}–\mu\text{-}OH–Fe^{III}]^+$ and explain why the oxidation chemistry occurs solely at the Fe center.[31,50]

To better understand the formation of $[Co^{II}–\mu\text{-}OH–Fe^{III}]^+$, $[Fe^{II}Me_3tacn(OTf)_2]$ was treated with excess O_2 in DCM. The reaction was performed without $[Co^{II}poat]^-$ as a control to determine if coordination to the P=O units was necessary to oxidize the Fe^{II} center. As discussed above, a pre-organization $K[Co^{II}poat]$ and $[Fe^{II}Me_3tacn(OTf)_2]$ was proposed, where the Fe^{II} center interacts with the $[Co^{II}poat]^-$ unit through the P=O groups before reacting with O_2 (Fig 4-5). The reaction betwen $[Fe^{II}Me_3tacn(OTf)_2]$ and O_2 was monitored by UV-vis and no immediate color change was apparent. After allowing the solution to stir overnight, a feature centered at λ_{max} = 370 nm appeared. This data suggested that $[Fe^{II}Me_3tacn(OTf)_2]$ on its own reacted slowly with O_2, which was not comparable to the formation of $[Co^{II}–\mu\text{-}OH–Fe^{III}]^+$ (Fig 4-S1B). The sluggish reaction between $[Fe^{II}Me_3tacn(OTf)_2]$ and O_2 compared to generation of $[Co^{II}–\mu\text{-}OH–Fe^{III}]^+$ suggested that the stronger ligand field provided by the P=O groups may help activate the Fe^{II} center towards O_2.[2,4,5,14,15]

To further study the role of the P=O units in supporting oxidation of the Fe center, $[Fe^{II}Me_3tacn(OTf)_2]$ was reacted with O_2 in the presence of $K[Zn^{II}poat]$. $K[Zn^{II}poat]$ was chosen because it is isostructural to $K[Co^{II}poat]$m but features a redox inactive metal ion supported by $[poat]^{3-}$.[51] For a more thorough characterization of $K[Zn^{II}poat]$, see Chapter 5. The reaction was performed in DCM with 18c6 to aid in the dissolution of $K[Zn^{II}poat]$. $K[Zn^{II}poat]$ was treated with O_2, followed by $[Fe^{II}Me_3tacn(OTf)_2]$. Upon addition of O_2 to $[Zn^{II}poat]^-$ (λ_{max} = 325 nm), there was a small jump in the baseline of the spectrum but no new features. Following addition of $[Fe^{II}Me_3tacn(OTf)_2]$, a new high-energy shoulder grew in ~350 nm (Fig 4-6A). The reaction was also followed by ⊥-mode EPR spectroscopy at 77 K and two new species were observed in the spectrum (Fig 4-6B). One species exhibited fatures at g = 4.3, 9.3 consistent with a rhombic, S = 5/2 Fe^{III} center.[4,14,15,46,52] The second species featured a derivative signal at g = 1.9 that appeared axial, perhaps

representing the formation of a small amount of a low spin, $S = 1/2$ Fe^{III} product. The growth in of ⊥-mode EPR active species suggested that the Fe^{II} center was oxidized to some Fe^{III} species in the presence of P=O units. These experiments were preliminary and further study is necessary before any definitive conclusions can be drawn.

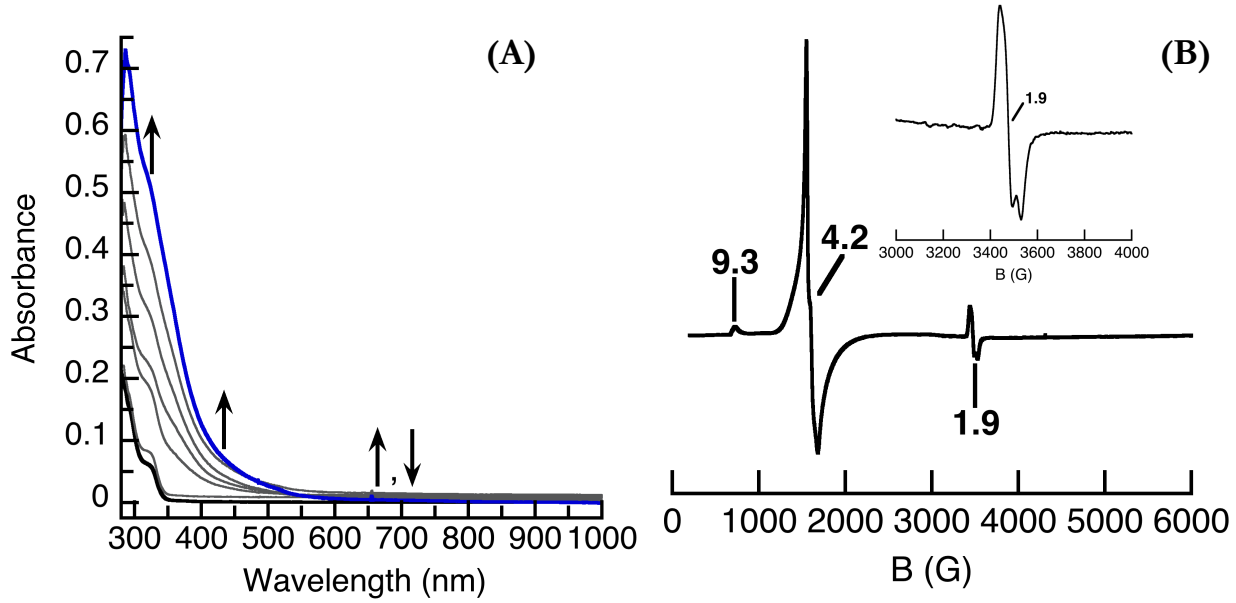

Figure 4-6: (A) UV-vis spectra following the reaction of $[Zn^{II}poat]^-$ (black trace) with O_2 and $[Fe^{II}Me_3tacn(OTf)_2]$ collected in DCM at room temperature. The final spectrum is shown in blue. **(B)** ⊥-mode EPR spectum collected at 77K in DCM:THF following the reaction of $[Zn^{II}poat]^-$, O_2, and $[Fe^{II}Me_3tacn(OTf)_2]$. The inset shows the high field feature.

The experiments discussed above provided evidence that the P=O units played an important role in activating the Fe center towards O_2 , though the data did not definitively support either an inner or outer sphere oxidation mechanism for the formation of $[Co^{II}–\mu\text{-}OHFe^{III}]^+$. Recent studies in the literature suggests that the outer sphere O_2 activation mechanism dominates in synthetic systems, which could be the case in this work.[48,49] Further investigation is necessary to confirm the mechanism. The most helpful experiments would likely involve isotopic labeling studies with $^{18}O_2$, which could give a kinetic isotope effect (KIE) or ^{18}O incoporation in $[Co^{II}–\mu\text{-}OH–Fe^{III}]^+$ by high-resolution mass spectrometry (HRMS).

Spectroscopic and Electrochemical Characterization of [poatCo^{II}–μ-OH–Fe^{III}Me$_3$tacn]OTf: In an effort to further understand the $[Co^{II}–\mu\text{-}OH–Fe^{III}]^+$ system, the complex was characterized using UV-vis, EPR, Attenuated Total Reflectance- Fourier Transform Infrared (ATR-FTIR), and Mössbauer spectroscopies, as well as cyclic voltammetry (CV). Crystalline $[Co^{II}–\mu\text{-}OH–Fe^{III}]^+$ was dissolved in DCM and an electronic absorption

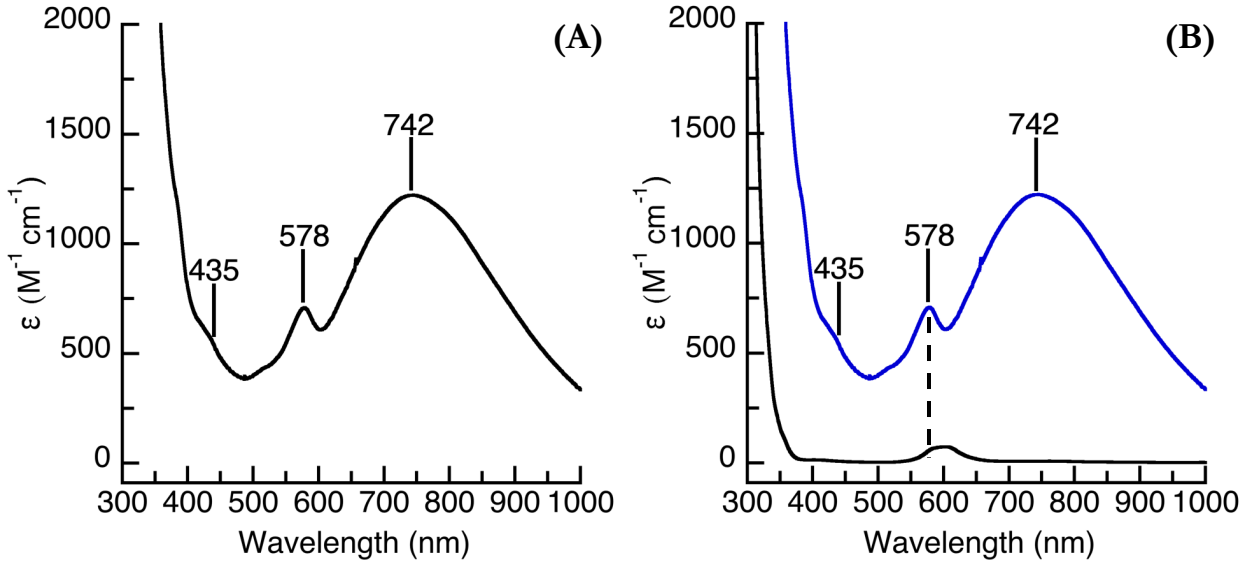

Figure 4-7: (A) Electronic absorbance spectrum of $[Co^{II}–\mu\text{-}OH–Fe^{III}]^+$ collected in DCM at room temperature. **(B)** $[Co^{II}–\mu\text{-}OH–Fe^{III}]^+$ (blue) overlaid with $K[Co^{II}poat]$ (black).

spectrum was collected. The spectrum exhibited features at λ_{max} (molar absorptivity, ε, $M^{-1}cm^{-1}$) = 435 (sh), 578 (708), 742 (1220) nm, (Fig 4-7A) consistent with the spectrum obtained from the *in situ* reaction of $K[Co^{II}poat] + O_2 + [Fe^{II}Me_3tacn(OTf)_2]$. The band at λ_{max} = 578 nm was similar in energy and relative shape to previous examples of Co^{II} complexes in C_3 symmetric ligand environments (Fig 4-7B). It was therefore proposed that the feature at λ = 578 nm could be attributed to the Co^{II} center within the bimetallic complex. However, the molar absorptivity of this feature (ε = 708 $M^{-1}cm^{-1}$) was significantly higher than values associated with typical Co^{II} *d–d* transitions (ε ~10 – 200 $M^{-1}cm^{-1}$). It is likely that the absorbance was intensified due to overlap with the broad, more intense feature at λ_{max} = 742 nm. The lower energy band centered λ_{max} ~ 742 nm (ε = 1220 $M^{-1}cm^{-1}$) was preliminarily proposed to be an intervalence charge-transfer transition (IVCT) between the two different metal centers(Co^{II}, d^7 and Fe^{III}, d^5). This feature was lower in energy and absorbance than expected for charge-transfer transitions, but was also more intensely absorbing than typical *d–d* transitions.[53] IVCT bands are generally broad features found in the visible-near infrared region of the spectrum.[54] The feature centered at λ_{max} = 742 nm was relatively broad, starting ~ 475 nm and tailing off ~ 1000 nm. While the qualitative features of the band at λ_{max} = 742 nm may be consistent with an IVCT transition, further spectroscopic studies and analysis are necessary to confirm this assignment.

The magnetism of [Co^{II}–μ-OH–Fe^{III}]$^{+}$ was studied via EPR spectroscopy. Redissolving crystalline [Co^{II}–μ-OH–Fe^{III}]$^{+}$ resulted in a ⊥-mode silent EPR spectrum, corroborating initial *in situ* studies discussed above and confirming that this complex does not have a half-integer spin ground state. [Co^{II}–μ-OH–Fe^{III}]$^{+}$ was further studied by ∥-mode EPR spectroscopy, which once again resulted in a silent spectrum, likely indicating a spin ground state of S = 1. Initial studies of K[Co^{II}poat] found that the Co^{II} center had a high-spin, S = 3/2 spin state, which is consistent in both TMP and TBP coordination complexes in C_3 symmetric ligand frameworks.[8,12,28,36] Previous work on bimetallic [poat]$^{3-}$ systems found that the Fe^{III} ions coordinated to the P=O groups were high-spin, with S = 5/2 spin states.[4,5] The hydroxido bridging ligand between the Co^{II} and Fe^{III} metal centers likely facilitated antiferromagnetic coupling between the two metal ions, which would lead to a spin ground state of S = 1. Because S = 1 spin systems are difficult to observe with ∥-mode EPR spectroscopy, [Co^{II}–μ-OH–Fe^{III}]$^{+}$ was studied with Evans' Method nuclear magnetic resonance (NMR) spectroscopy to obtain a room temperature effective magnetic moment (μ_{eff}). The Evans' Method spectrum was measured in DCM and the paramagnetically shifted solvent resonance peak was used to calculate a μ_{eff} = 6.18 μ_B. The theoretical spin-only magnetic moment for a S = 1 spin system is μ_S = 2.83 μ_B; the value obtained was between the theoretical spin-only values for S = 5/2 and 3 spin states (μ_S = 5.92 – 6.93 μ_B).

To further corroborate the spin state of [Co^{II}–μ-OH–Fe^{III}]$^{+}$, the complex was studied by Mössbauer spectroscopy. Because [Co^{II}–μ-OH–Fe^{III}]$^{+}$ can be cleanly crystallized in bulk, Mössbauer spectra were measured on natural abundance solid samples. The 4 K Mössbauer spectrum exhibited a doublet, consistent with the formation of an integer spin, S = 1 species (Fig 4-8A). The doublet had an isomer shift (δ) of 0.49 mm s^{-1} and a quadrupole splitting (ΔE_q) of 1.38 mm s^{-1}. These parameters were consistent with a high-spin, S = 5/2 Fe^{III} center supported by N/O ligand donors.[55] This data further supported the assignment of antiferromagnetic coupling between a S = 3/2 Co^{II} center and a S = 5/2 Fe^{III} center.

The low temperature (~10 K) Mössbauer and EPR spectroscopic measurements suggested a spin state of S = 1. The room temperature Evans' Method magnetic moment showed larger spin state value (μ_{eff} = 6.18 μ_B). These variable temperature data points suggested that the metal ions in [Co^{II}–μ-OH–Fe^{III}]$^{+}$ were antiferromagnetically coupled, with a spin ground state of S = 1 and thermally accessible excited spin states.

Further studies are underway to measure the exchange coupling parameter (*J* value) between the two metal ions.

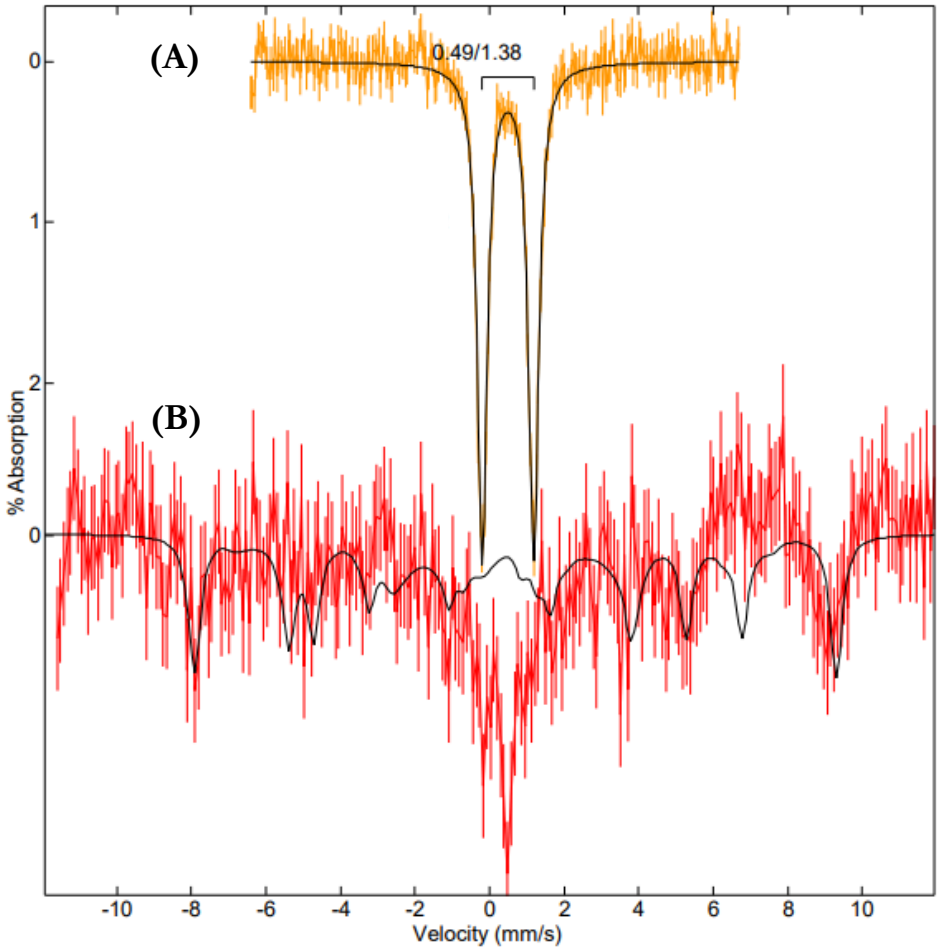

Fig 4-8: Mössbauer spectra measured on crystalline samples $[Co^{II}–\mu\text{-}OH–Fe^{III}]^{+}$ (orange trace, **A**) and $[Co^{III}–\mu\text{-}OH–Fe^{III}]^{2+}$ (red trace, **B**). Simulations are shown as black traces overlaid with the experimental spectra.

$[Co^{II}–\mu\text{-}OH–Fe^{III}]^{+}$ was then investigated using solid state ATR-FTIR spectroscopy. An O–H vibration could not be clearly identified from the spectrum (Fig 4-9, black trace). There was a feature above 3600 cm^{-1} (black trace, +), however the identity of this band was unknown and did not appear consistent with an O–H vibration. In the solid state molecular structure, the $^{-}$OH ligand interacted with the Co^{II} and Fe^{III} centers, and participated in an intramolecular H–bonding interaction with the free P=O unit from the $[poat]^{3-}$ ligand backbone. In literature examples of $M^{II}–\mu\text{-}OH–M^{III}$ complexes, the O–H vibration was typically found between ~3300 – 3100 cm^{-1}, but was not always visible.[5,10–12,15,56–58] Interaction with the two metal centers and the H–bonding interaction with the P=O group likely weakened the O–H bond of the $^{-}$OH ligand, shifting the O–H vibration to lower energies and possibly obscuring it by other vibrational features.

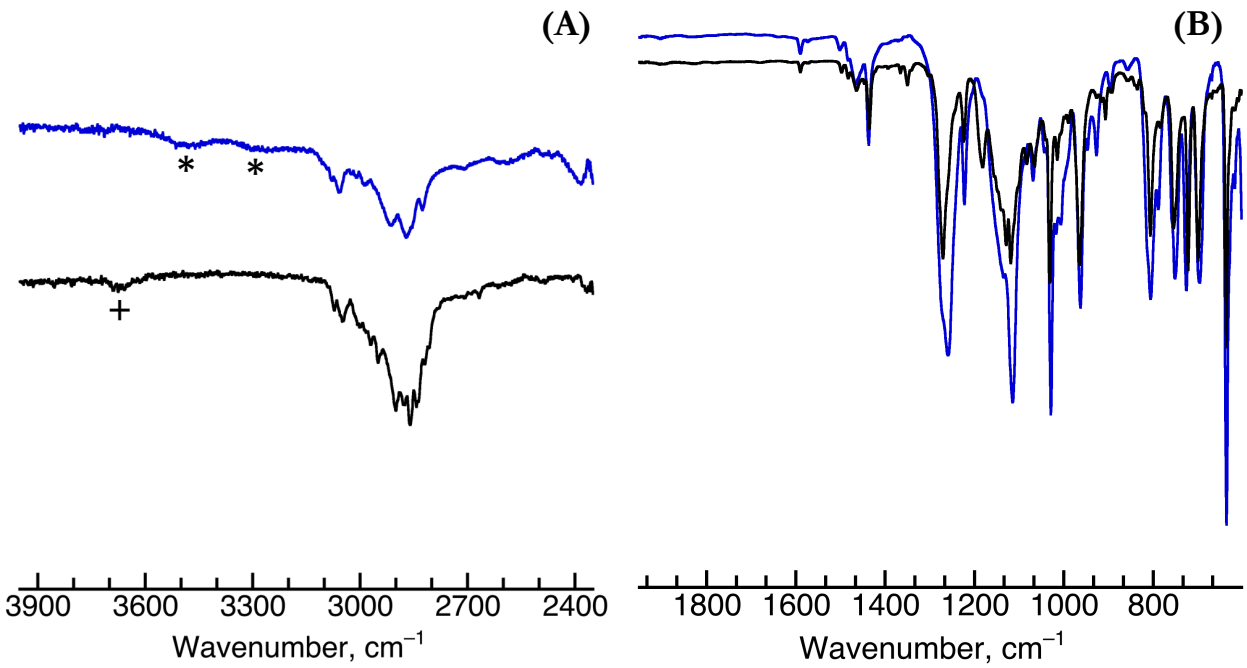

Fig 4-9: Overlay of ATR-FTIR spectra measured of crystalline $[Co^{II}–\mu\text{-}OH–Fe^{III}]^{+}$ (black trace) and $[Co^{III}–\mu\text{-}OH–Fe^{III}]^{2+}$ (blue trace). The high energy region is shown in **(A)** while the lower energy region is shown in **(B).** The + and * symbols represent unidentified vibrational features that are discussed in the body of the document.

The electrochemical behavior of $[Co^{II}–\mu\text{-}OH–Fe^{III}]^{+}$ was studied by CV in DCM. The complex exhibited two reversible redox events at –1.190 and –0.175 V versus $Fc^{+/0}$ (Fig 4-10A, Table 4-2). These events were assigned as the $Co^{II}Fe^{III}/Co^{II}Fe^{II}$ and $Co^{III}Fe^{III}/Co^{II}Fe^{III}$ couples respectively. The reversibility and relatively low potential of the $Co^{III}Fe^{III}/Co^{II}Fe^{III}$ couple (–0.175 V) suggested that $[Co^{II}–\mu\text{-}OH–Fe^{III}]^{+}$ could be oxidized by a mild oxidant, such as Fc^{+}. Each event could be independently isolated and maintained its reversibility (Fig 4-10B, C). When the complex was scanned out to +1.0 V versus $Fc^{+/0}$, new, irreversible electrochemical events appeared in addition to the $Co^{II}Fe^{III}/Co^{II}Fe^{II}$ and $Co^{III}Fe^{III}/Co^{II}Fe^{III}$ couples (Fig 4-10D, new features marked with *). In scanning oxidatively, it is possible that one of the metal ions exhibited a further oxidation to a proposed M^{IV} oxidation state. The final oxidative event (E_{pa} = +1.060 V versus $Fc^{+/0}$) therefore may correspond to a $M^{III}M^{IV}/M^{III}M^{III}$ redox event, however which metal ion may have been oxidized could not be determined from CV alone. It was initially assumed that the Co center, coordinated by the trianionic $[poat]^{3-}$ ligand backbone, would be more easily oxidized. However, there are relatively few examples of discreet metal complexes with Co^{IV} centers,[59,60,69,61–68] and isolation of $[Co^{II}–\mu\text{-}OH–Fe^{III}]^{+}$ demonstrated that a more anionic ligand field was not the sole factor in determining which metal ion was more likely to be oxidized

in a bimetallic system. Furthermore, work from Wieghardt found that the Me_3tacn ligand framework was supportive of a Fe^{IV} center, in a di-Fe system supported by Me_3tacn ligands with μ-carboxylato, μ-oxido core.[70] The Fe^{IV} oxidation state was accessible at +1.48 V versus $Fc^{+/0}$ in MeCN. It is clear that further investigations are necessary to identify the oxidized product at E_{pa} = +1.060 V vs $Fc^{+/0}$.

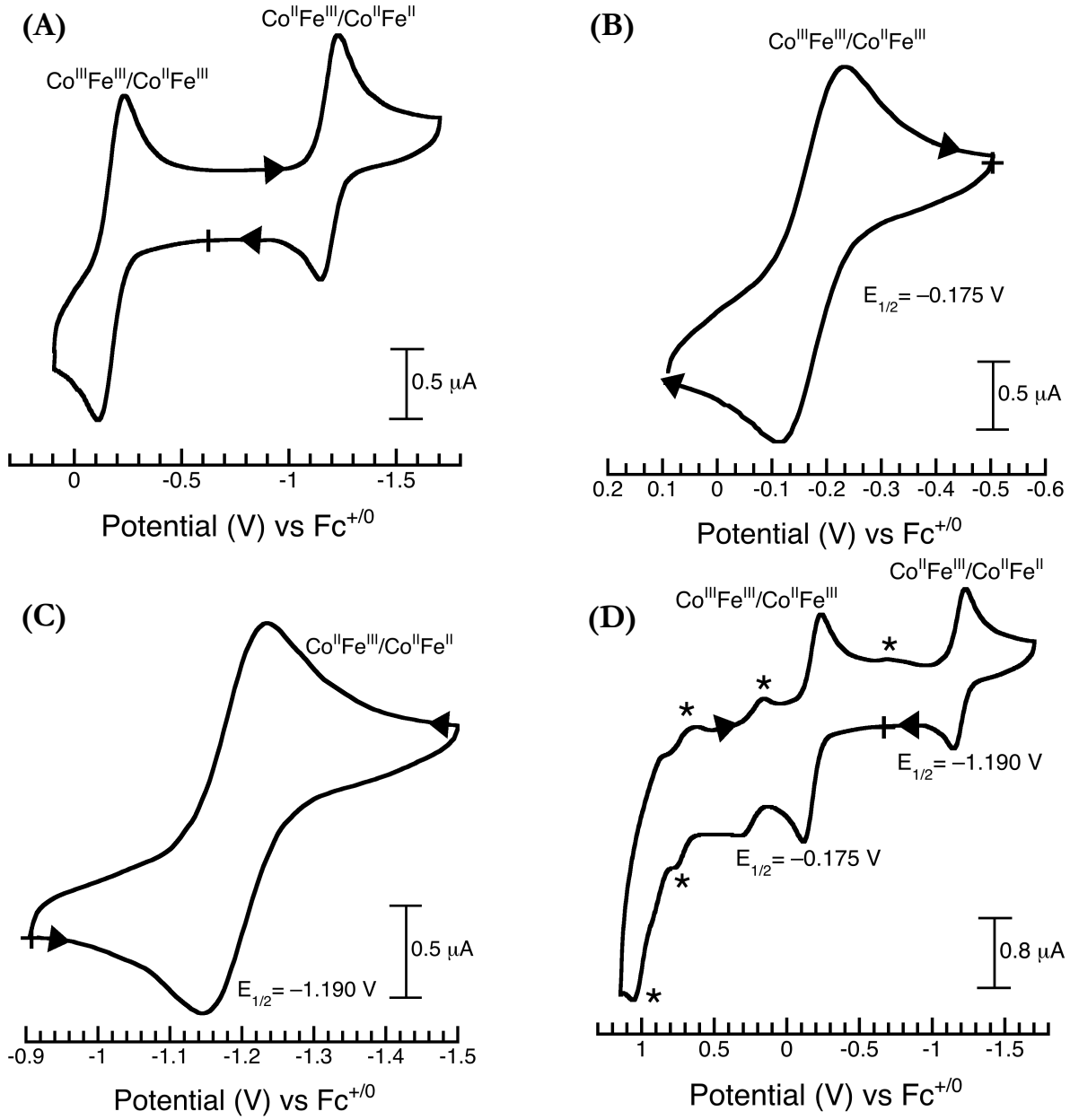

Figure 4-10: (A) $Co^{III}Fe^{III}/Co^{II}Fe^{III}$ (–0.175 V) and $Co^{II}Fe^{III}/Co^{II}Fe^{II}$ (–1.190 V) couples from $[Co^{II}–\mu\text{-}OH–Fe^{III}]^+$ together. The $Co^{III}Fe^{III}/Co^{II}Fe^{III}$ couple was isolated in **(B)** and the $Co^{II}Fe^{III}/Co^{II}Fe^{II}$ was isolated in **(C)**. The full voltammogram swept out past +1 V versus $Fc^{+/0}$ including unidentified electrochemical features, denoted by * is shown in **(D)**.

Table 4-2: Metrical data obtained from CV of $[Co^{II}–\mu\text{-}OH–Fe^{III}]^+$, focused on the reversible couples.

Electrochemical Couple	$Co^{II}Fe^{III}$ / $Co^{II}Fe^{II}$	$Co^{III}Fe^{III}$ / $Co^{II}Fe^{III}$
E_{pa} (V vs $Fc^{+/0}$)	–1.145	–0.110
E_{pc} (V vs $Fc^{+/0}$)	–1.230	–0.235
$E_{1/2}$ (V vs $Fc^{+/0}$)	–1.190	–0.175
ΔE (mV)	90	125
i_{pa}/i_{pc}	1.1	1.1

*$Fc^{+/0}$ reference couple: ΔE = 135 mV, i_{pa}/i_{pc} = 1.5

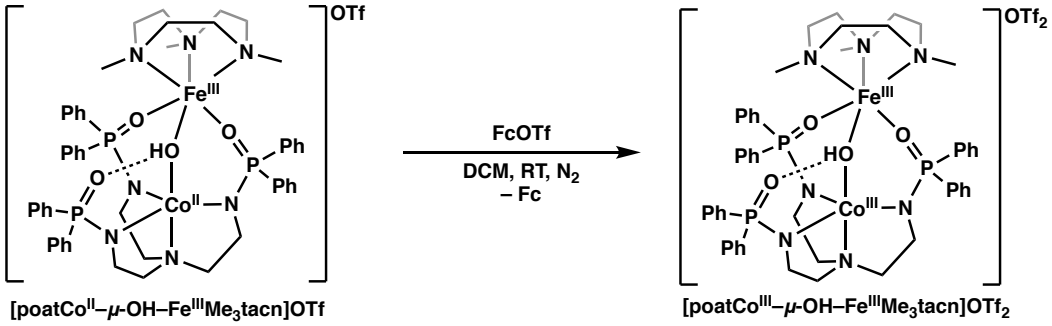

Scheme 4-4: Reaction scheme describing the preparation of $[poatCo^{III}–\mu\text{-}OH–Fe^{III}Me_3tacn](OTf)_2$.

Oxidative Chemistry of $[poatCo^{II}–\mu\text{-}OH–Fe^{III}Me_3tacn]OTf$

Synthesis and Structural Characterization of $[poatCo^{III}–\mu\text{-}OH–Fe^{III}Me_3tacn](OTf)_2$: The CV of $[poatCo^{II}–\mu\text{-}OH–Fe^{III}Me_3tacn]OTf$ exhibited a reversible, one electron event at –0.175 V versus $Fc^{+/0}$ in DCM, assigned as the $Co^{III}Fe^{III}/Co^{II}Fe^{III}$ couple. The potential of this couple suggested that the complex could be oxidized using a Fc^+ salt. Bulk synthesis was undertaken following Scheme 4-4 to investigate the oxidation. To a deep blue solution of $[poatCo^{II}–\mu\text{-}OH–Fe^{III}Me_3tacn]OTf$ in DCM, a solution of FcOTf was added slowly. Addition of FcOTf caused an immediate color change to a deep red-orange solution. After briefly stirring, minimal *n*-hexane was added atop the solution until a slight cloudiness appeared. The was transferred to the glovebox freezer and the vial was stored at –35 ºC. After several days, additional *n*–hexane was added and the vial was returned to the freezer. Roughly a week later, dark-red single crystals single crystals suitable for XRD analysis were grown in a 75% yield.

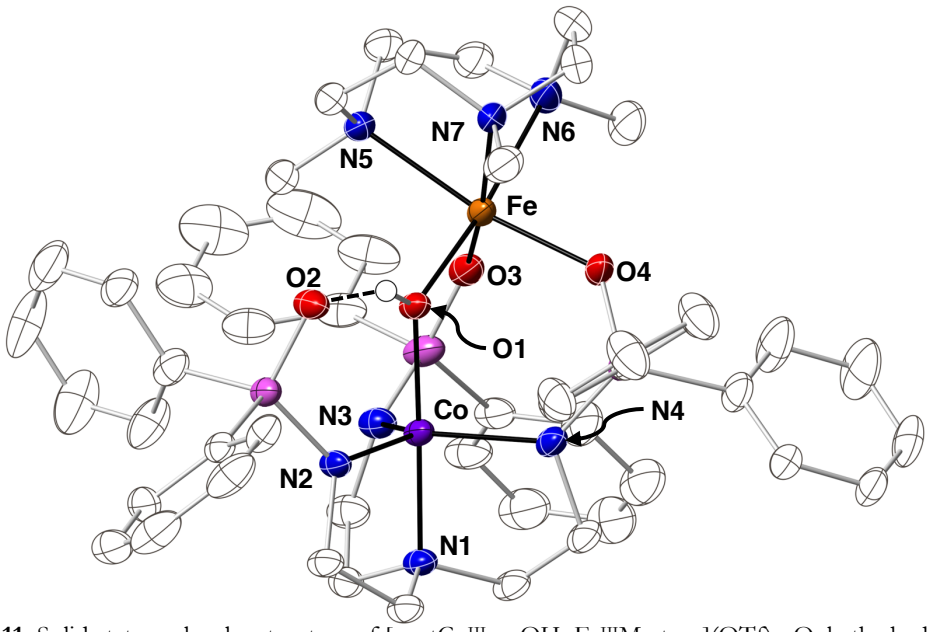

Fig 4-11: Solid state molecular structure of [poatCo^{III}–μ-OH–Fe^{III}Me$_3$tacn](OTf)$_2$. Only the hydroxido H-atom is shown. All other H-atoms, counterions, and structural solvent molecules were omitted for clarity. Thermal ellipsoids were drawn at 50% probability. See Table 4-1 for metrical data (*vide supra*).

The molecular structure shown in Fig 4-11 revealed a bimetallic species: [poatCo^{III}–μ-OH–Fe^{III}Me$_3$tacn](OTf)$_2$, ([Co^{III}–μ-OH–Fe^{III}]$^{2+}$). The 1° coordination environment around each metal ion remained the same as [Co^{II}–μ-OH–Fe^{III}]$^{+}$, with the Co center coordinated to the tren backbone of [poat]$^{3-}$ and the $^{-}$OH ligand in the fifth site, maintaining the TBP coordination geometry (τ_5 = 0.86, Table 4-1). The Fe center interacted with two P=O groups and hydroxido ligand in a facial coordination motif, with the remaining coordination sites saturated by the Me$_3$tacn ligand framework. The hydroxido ligand remained in a H–bonding interaction with the free P=O (O1···O2 = 2.646(3) Å, Table 4-1). The structure also featured two outer sphere OTf^{-} counterions.

The most significant difference between the [Co^{II}–μ-OH–Fe^{III}]$^{+}$ and [Co^{III}–μ-OH–Fe^{III}]$^{2+}$ molecular structures was the contraction in the Co–O/N bond lengths following oxidation. All Co–O/N bond lengths were longer than 2 Å in the [Co^{II}–μ-OH–Fe^{III}]$^{+}$ structure, but were less than 2 Å in the [Co^{III}–μ-OH–Fe^{III}]$^{2+}$ structure, consistent with oxidation of the Co center to Co^{III} (Table 4-1). The Co–N1 bond length contracted the most significantly between the two structures, shortening by 0.23 Å while the remaining Co–N/O bond lengths contracted by an average of 0.08 Å. The bond lengths around the Fe center remained largely unchanged, with average Fe–N$_{avg}$ bond lengths of 2.2 Å and Fe–O$_{avg}$ bond lengths of 2.0 Å, from the P=O groups.

Interestingly, the Fe–O1 bond length increased upon oxidation from 1.848(1) to 1.904(2) Å, possibly due to a complementary shortening of the Co–O1 bond. Finally, it is significant to note that following oxidation of $[Co^{II}–\mu\text{-}OH–Fe^{III}]^{+}$ to $[Co^{III}–\mu\text{-}OH–Fe^{III}]^{2+}$, the $^{-}$OH ligand remained protonated. Thus far, the only other examples of a $[M^{III}–\mu\text{-}OH–M^{III}]^{2+}$ in the $[poat]^{3-}$/Me_3tacn ligand system were $[poatFe^{III}–\mu\text{-}OH–Co^{III}Me_3tacn](OTf)_2$ and $[poatGa^{III}–\mu\text{-}OH–Co^{III}Me_3tacn](OTf)_2$.[4,5,15] In all other M^{III}/M^{III} species within this ligand system, the H^{+} on the $^{-}$OH bridge underwent an intramolecular proton transfer to one of the $[poat]^{3-}$ ligand arms, forming $[(H)poatM^{III}–\mu\text{-}O–M^{III}Me_3tacn](OTf)_2$. It is interesting that it was only the Co/Fe or Co/Ga systems that maintained a μ-OH bridging ligand, regardless of whether each metal was coordinated in the tren backbone or by Me_3tacn.

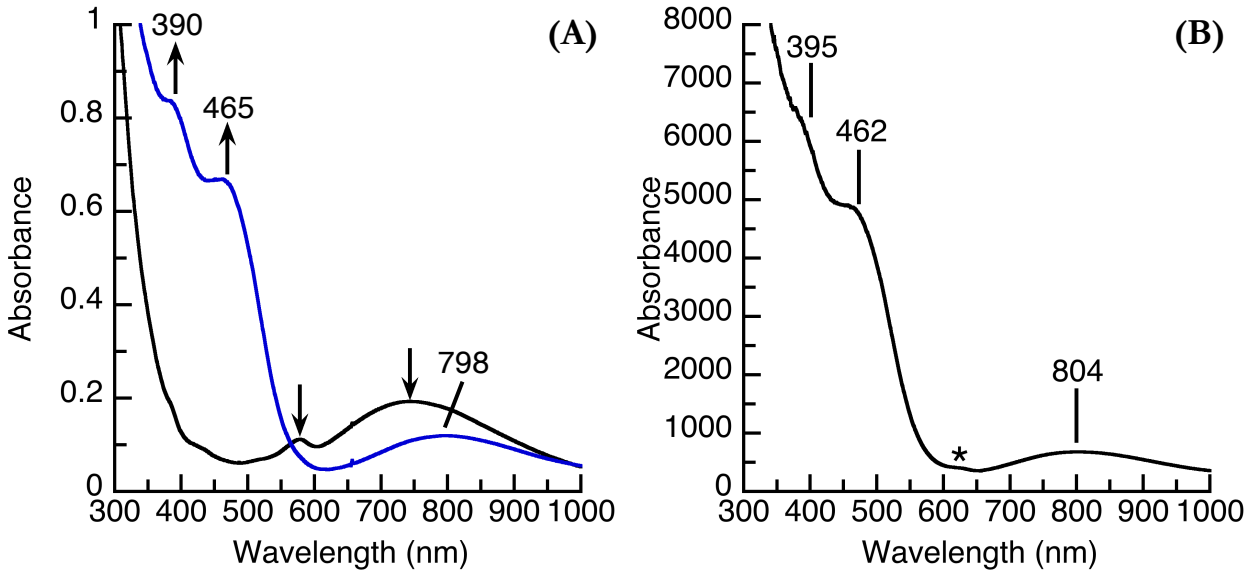

Fig 4-12: (A) Spectra resulting from the reaction of $[Co^{II}–\mu\text{-}OH–Fe^{III}]^{+}$ (black) with FcOTf to form $[Co^{III}–\mu\text{-}OH–Fe^{III}]^{2+}$ (blue). **(B)** Absorbance spectrum from isolated, crystalline $[Co^{III}–\mu\text{-}OH–Fe^{III}]^{2+}$. The * marks a feature that may be due to excess FcOTf.

Spectroscopic and Electrochemical Characterization of $[poatCo^{III}–\mu\text{-}OH–Fe^{III}Me_3tacn](OTf)_2$: The reaction of $[Co^{II}–\mu\text{-}OH–Fe^{III}]^{+}$ with FcOTf resulted in a new absorption spectrum with bands at λ_{max} = 390, 465, 798 nm and a weak feature at 630 nm (Fig 4-12A). Subsequently, crystalline $[Co^{III}–\mu\text{-}OH–Fe^{III}]^{2+}$ was redissolved in DCM and the electronic absorption spectrum was collected, with features once again at λ_{max} = 395, 462, 805 nm (Fig 4-12B). The higher energy feature at 390 nm appeared as a shoulder rather than a more defined feature in the redissolved sample spectrum (Fig 4-12). Additionally, the weak feature at 630 nm (noted with a *) was present.

This feature was presumed to be from excess FcOTf, however solid was $[Co^{III}–\mu\text{-}OH–Fe^{III}]^{2+}$ recrystallized and thoroughly washed and dried before the spectrum was collected. Therefore, it was possible that this feature may have been associated with the metal complex, though its origin and identity was unclear. The shapes and energies of the three dominant features at λ_{max} = 395, 462, and 805 nm were similar to previously characterized Co^{III}–OH species in C_3 symmetric ligand fields; spectra featuring highly absorbing bands ~400 and ~470 nm, with lower energy features ~800 nm are diagnostic of these Co^{III}–OH species.[8,12,28,36] Literature precedent suggests that these features largely arise from transitions around the Co^{III} center. However, the main published examples were primarily mononuclear Co^{III}–OH species and the sole bimetallic example featured electrostatic interaction with a Ca^{2+} ion, rather than a covalent interaction with a second transition metal ion. Perhaps a better comparison for the electronic absorption spectrum of $[Co^{III}–\mu\text{-}OH–Fe^{III}]^{2+}$ was the example discussed in Chapter 3: $[poatCo^{III}–\mu\text{-}OH–Zn^{II}Me_3tacn]^{+}$. In this case, the Co^{III} ion was supported by the $[poat]^{3–}$, and the Zn^{II} center was covalently coordinated to the P=O groups of $[poat]^{3–}$, the hydroxido ligand, and the Me_3tacn framework. $[poatCo^{III}–\mu\text{-}OH–Zn^{II}Me_3tacn]^{+}$ had bands at λ_{max} = 365, 435, 760 nm, similar in shape to $[Co^{III}–\mu\text{-}OH–Fe^{III}]^{2+}$. In comparison to $[poatCo^{III}–\mu\text{-}OH–Zn^{II}Me_3tacn]^{+}$, all bands were shifted to lower energy by ~25 – 40 nm in the $[Co^{III}–\mu\text{-}OH–Fe^{III}]^{2+}$ complex (Fig 4-S2). It is unclear whether this shift was due to the more acidic nature of the Fe^{III} center versus the Zn^{II} ion,[71] or if this shift arose from some transitions originating from the Fe center.

$[Co^{III}–\mu\text{-}OH–Fe^{III}]^{2+}$ was further characterized by solid state ATR-FTIR spectroscopy, (Fig 4-9, blue). Similar to $[Co^{II}–\mu\text{-}OH–Fe^{III}]^{+}$, there did not appear to be an O–H vibration. There were two weak, broad features centered at 3510 and 3300 cm^{-1} (marked by *) but these vibrational frequencies were higher than those typically seen for O–H vibrations of metal complexes (~3100 – 3300 cm^{-1}).[4,5,10–12,15,56–58] Interestingly, a similar system to $[Co^{III}–\mu\text{-}OH–Fe^{III}]^{2+}$ where the ligand fields around each metal ion were switched, $[poatFe^{III}–\mu\text{-}OH–Co^{III}Me_3tacn](OTf)_2$, exhibited similar broad features at 3486 and 3266 cm^{-1}. The origin of these bands in each system was unclear but their overlap suggested that they may be characteristic features of $[poatM^{III}–\mu\text{-}OH–M^{III}Me_3tacn](OTf)_2$ systems. However, this may be difficult to ascertain because only Co/Fe or Co/Ga systems have been prepared with a $[M^{III}–\mu\text{-}OH–M^{III}]^{2+}$ motif.

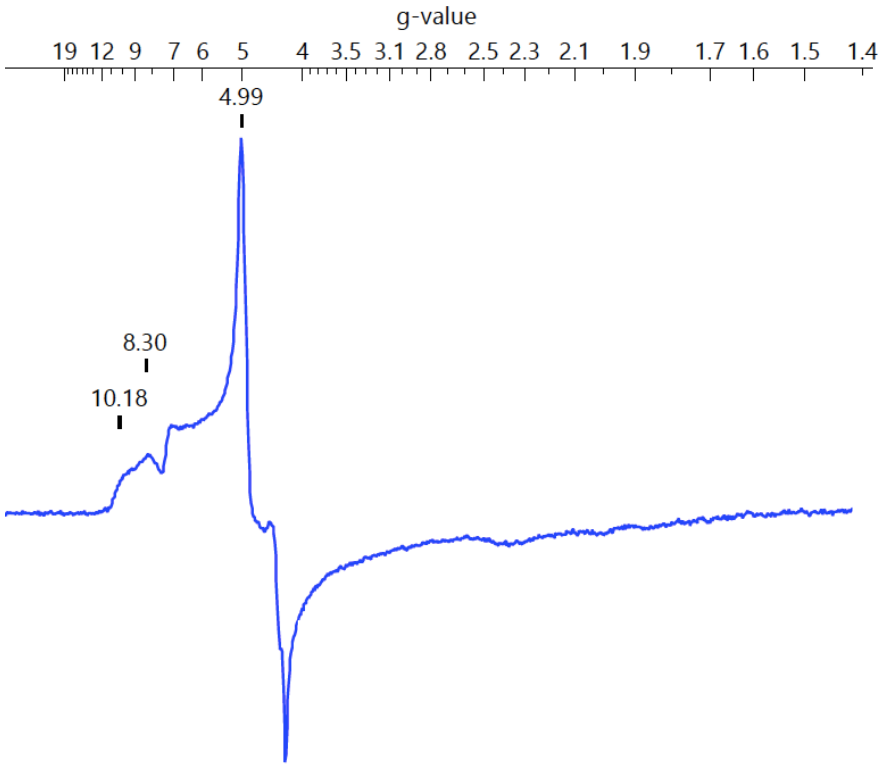

Fig 4-13: ⊥-mode EPR spectrum of $[Co^{III}–\mu\text{-}OH–Fe^{III}]^{2+}$ measured at 7 K in DCM:THF. Simulations of this species to determine rhombicity and other magnetic parameters are still underway.

To determine how the two metal centers magnetically interacted, $[Co^{III}–\mu\text{-}OH–Fe^{III}]^{2+}$ was studied by ⊥-mode EPR spectroscopy. At 77 K, the ⊥-mode EPR spectrum exhibited a broad derivative centered at g ~ 5 and a weak, broad signal around g ~ 2. When the sample was cooled to He temperatures, the signal appeared sharper with a derivative feature at g = 5.0, as well as two lower field features at g = 10.2, 8.3 (Fig 4-13). This signal appears to be from a $S = 7/2$ spin system that can arise from ferromagnetic coupling between a $S = 1$ Co^{III} center and a $S = 5/2$ Fe^{III} center. The ferromagnetic mode of coupling occurred due to oxidation of the Co^{III} center in C_3 symmetry. As discussed in previous chapters, when a Co^{II} ion coordinated in a C_3 symmetric ligand field is oxidized to Co^{III}, the electron configuration changes from a high-spin, $S = 3/2$ spin state to a low-spin, $S = 1$ state. The lost electron is removed from the d_{z^2} orbital localized on the Co center. When this occurs in a bimetallic species, such as $[Co^{III}–\mu\text{-}OH–Fe^{III}]^{2+}$, the loss of this electron disrupts the mode of magnetic communication between the two metal ions. When the d_{z^2} electron was removed, the unpaired electrons localized around the Co ion were now located in orbitals orthogonal to the -OH O-p_z orbital. This

orthogonality gives rise to ferromagnetic interactions between the unpaired electrons on each metal center, per the Goodenough-Kanamori rule.[72,73] Additionally, the spectrum doesn't exhibit any hyperfine features from the ^{59}Co nucleus (I = 7/2), which can be attributed to the loss of the electron in the d_{z^2} orbital. The dominant hyperfine contact was along the z-axis and loss of the electron along the z-axis disrupts the contact between the spin-active nucleus (^{59}Co) and the unpaired electrons.

In addition to low temperature ⊥-mode EPR spectroscopy, the room temperature effective magnetic moment of $[Co^{III}–\mu\text{-}OH–Fe^{III}]^{2+}$ was measured. Using Evans' Method NMR spectroscopy, the paramagnetically shifted solvent resonance was used to calculate a μ_{eff} = 8.36 μ_B. The theoretical spin-only magnetic moment for a S = 7/2 spin system is μ_s = 7.94 μ_B, consistent with the experimentally determined value. The increase in the μ_{eff} value versus the theoretical spin-only magnet moment was likely due to spin-orbit coupling within the molecule.[73] The Evans' Method magnetic data supported a ferromagnetic interaction between the two metal centers.

Mössbauer spectroscopy was further used to study $[Co^{III}–\mu\text{-}OH–Fe^{III}]^{2+}$. The Mössbauer spectrum was measured on a natural abundance solid, crystalline sample of $[Co^{III}–\mu\text{-}OH–Fe^{III}]^{2+}$. The spectrum was weaker in intensity than its $[Co^{II}–\mu\text{-}OH–Fe^{III}]^{+}$ counterpart and could not be definitively commented upon (Fig 4-8B). However, a simulation was proposed where a S = 1 Co^{III} ion was ferromagnetically coupled to a S = 5/2 Fe^{III} center. This simulation appeared to be reasonable when compared to the experimental spectrum and further supported a ferromagnetic mode of interaction between the two metal centers. Note that the more intense feature centered ~0.25 mm s^{-1} may be due to the presence of small amount of excess FcOTf mixed with solid $[Co^{III}–\mu\text{-}OH–Fe^{III}]^{2+}$, exhibiting a deceptively large signal.[4,74]

Finally, the electrochemical profile of $[Co^{III}–\mu\text{-}OH–Fe^{III}]^{2+}$ studied with CV in DCM. The complex exhibited three robust electrochemical events in addition to several less intense unidentified electrochemical events (Fig 4-14). The open circuit potential (OCP) of $[Co^{III}–\mu\text{-}OH–Fe^{III}]^{2+}$ lays ~ 0 V versus $Fc^{+/0}$, a more positive potential than the OCP for $[Co^{II}–\mu\text{-}OH–Fe^{III}]^{+}$ (~ –0.5 V versus $Fc^{+/0}$). The oxidative shift in the OCP was consistent with a more oxidized metal complex. When scanning positively starting at the OCP of $[Co^{III}–\mu\text{-}OH–Fe^{III}]^{2+}$, an irreversible oxidation occurred around +0.9 V versus $Fc^{+/0}$, with a small reduction negative of

this event, at +0.35 V versus $Fc^{+/0}$ (Fig4-14A, Table 4-3). This feature, with an intense, irreversible oxidation event separated by a wide potential window from a less intense return reduction, was similar to features observed in previously characterized bimetallic hydroxido systems.[4,5] In these examples, an intramolecular proton transfer occurred where the hydroxido bridge became sufficiently acidic following oxidation that it led to the protonation of one of the anionic N-groups from $[poat]^{3-}$ and the formation of an oxo bridge. Further study is needed to confirm the identity of the oxidative event and the source of the irreversibility.

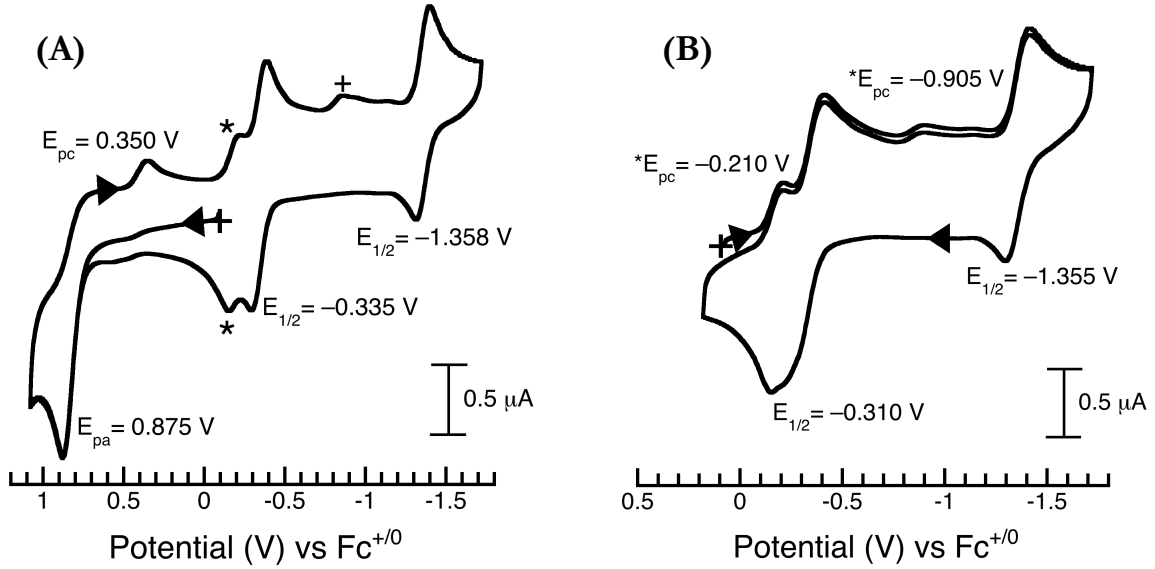

Figure 4-14: Voltammograms obtained from scanning $[Co^{III}–\mu\text{-}OH–Fe^{III}]^{2+}$ oxidatively **(A)** and reductively **(B)**. The * and + mark unidentified electrochemical events that are discussed below.

Table 4-3: Metrical data from marked events from the CV in Figure 4-14A of $[Co^{III}–\mu\text{-}OH–Fe^{III}]^{2+}$.

Electrochemical Event	(V vs $Fc^{+/0}$)
*, E_{pa}	–0.155
*, E_{pc}	–0.195
+, E_{pc}	–0.860

The couple at –0.335 V versus $Fc^{+/0}$ was assigned as the $Co^{III}Fe^{III}/Co^{II}Fe^{III}$ couple based on its potential, which was shifted negatively by –0.16 V than in the voltammogram of $[Co^{II}–\mu\text{-}OH–Fe^{III}]^{+}$. The couple at –1.35 V versus $Fc^{+/0}$, which was assigned as $Co^{II}Fe^{III}/Co^{II}Fe^{II}$ event, was also –0.16 V more negative than the analogous couple in $[Co^{II}–\mu\text{-}OH–Fe^{III}]^{+}$. In addition to the $Co^{III}Fe^{III}/Co^{II}Fe^{III}$ and $Co^{II}Fe^{III}/Co^{II}Fe^{II}$ couples, there were also unidentified electrochemical events, marked with an asterisk and a plus sign (*, + Fig 4-14). The identities of these events are unclear but may be due to some unknown contaminant.

Deprotonation Studies: In the molecular structure of $[Co^{III}–\mu\text{-}OH–Fe^{III}]^{2+}$, the hydroxido ligand participated in a H–bonding interaction with one of the P=O arms from the $[poat]^{3-}$ ligand backbone. Between the H–bonding interaction and its position bridging between two M^{III} ions, the $^{-}$OH ligand was likely acidic and could possibly be deprotonated. To determine this, $[Co^{III}–\mu\text{-}OH–Fe^{III}]^{2+}$ was treated with a series of bases. In a representative experiment, $[Co^{III}–\mu\text{-}OH–Fe^{III}]^{2+}$ was generated *in situ* from $[Co^{II}–\mu\text{-}OH–Fe^{III}]^{+}$ and FcOTf in DCM solutions cooled to –40 °C. The most effective base examined was lithium bis(trimethylsilyl)amide (LiHMDS, pK_a ~ 26, THF).[75] The electronic absorption spectra did not change dramatically, though the low energy feature of λ_{max} = 804 nm of $[Co^{III}–\mu\text{-}OH–Fe^{III}]^{2+}$ shifted to higher energy and slightly increased in intensity (Fig 4-15A). If this reaction was warmed, the spectrum slowly converted to a new species, with features consistent to $[Co^{II}–\mu\text{-}OH–Fe^{III}]^{+}$. This conversion suggested that the proposed product, $[Co^{III}–\mu\text{-}O–Fe^{III}]^{+}$, may be unstable. Indeed, further UV-vis studies indicated that this species was difficult to replicate and identify, due to the subtle spectral changes and the apparent instability.

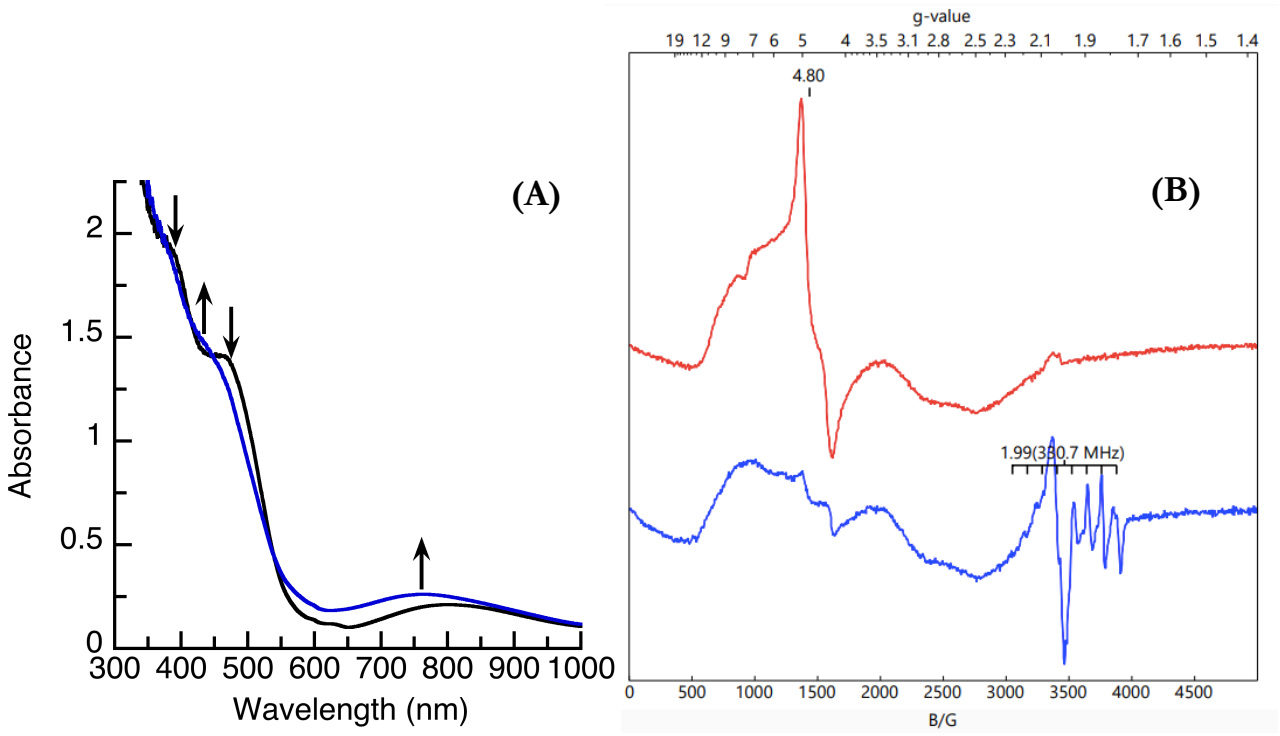

Figure 4-15: (A) UV-vis spectra obtained from reacting $[Co^{III}–\mu\text{-}OH–Fe^{III}]^{2+}$ (black) with LiHMDS (blue), measured at –40 °C in DCM. **(B)** EPR spectra obtained from reacting $[Co^{III}–\mu\text{-}OH–Fe^{III}]^{2+}$ (red) with LiHMDS (blue). Samples were collected at 20 K in DCM:THF.

In addition to the UV-vis studies, this reaction was monitored by ⊥-mode EPR spectroscopy. [Co^{III}–μ-OH–Fe^{III}]$^{2+}$ was generated *in situ* in DCM:THF and cooled to –80 ºC, to slow down the reaction in the more concentrated solution. After the solution equilibrated in the cooling bath, LiHMDS was added and allowed to mix for a few minutes. At this point, the sample was flash frozen in liquid N_2. When the EPR sample was collected at He temperatures, the broad, S = 7/2 signal from [Co^{III}–μ-OH–Fe^{III}]$^{2+}$ (Fig 4-15B, red) began to decrease in intensity, though some of the broader, underlying features appeared to persist, possibly due to excess FcOTf (Fig 4-15B, blue). Concomitant to the loss of the S = 7/2 species, a new signal began to grow in, centered at g = 2. The signal was proposed to arise from an S = 1/2 spin system due to antiferromagnetic coupling between a high-spin S = 5/2 Fe^{III} ion and a now high-spin S = 2 Co^{III} center. The new species exhibited an 8-line hyperfine pattern from the ^{59}Co nucleus, with a hyperfine coupling constant of A_z = 330 MHz. The magnitude of this value was consistent with a strong interaction between the unpaired electrons of the complex with the spin active Co nucleus. Furthermore, the presence of the ^{59}Co hyperfine suggested a rearrangement of the electrons around the Co ion, following a change in the Co spin state. In the ⊥-mode EPR spectrum of [Co^{III}–μ-OH–Fe^{III}]$^{2+}$, no ^{59}Co hyperfine was present because the Co^{III} ion had a spin state of S = 1 and an unoccupied d_{z^2} orbital. If the [Co^{III}–μ-OH–Fe^{III}]$^{2+}$ is deprotonated, the new bridging ligand is an oxido. Incorporation of a μ-O unit leads to a change in the *d*-orbital splitting around the Co^{III} center due to π-bonding with the oxido ligand that raises the d_{xz} and d_{yz} orbitals in energy, making a high-spin, S = 2 spin state now accessible (Fig 4-16). In spite of the useful data obtained in these studies, these results and conclusions are preliminary and more investigation would need to be done to confirm this analysis.

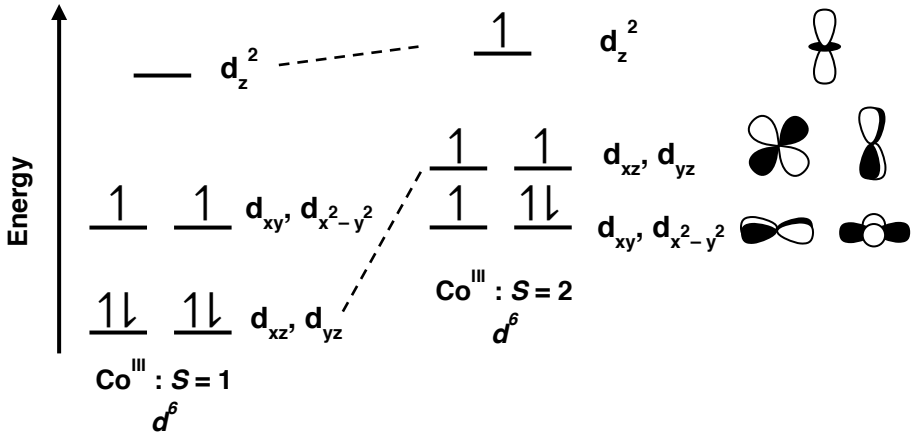

Figure 4-16: Proposed spin state change around the Co^{III} center due to π- donation from an oxido ligand.

Summary and Conclusions

Chapter 4 described an exploration into the reactivity of K[Co^{II}poat] with O_2 in the presence of additional metal ions. K[Co^{II}poat] on its own did not react with O_2, nor did it react in the presence of a redox-inactive metal ion, [$Zn^{II}Me_3$tacn$(OTf)_2$]. When this reaction was explored in the presence of a redox active metal ion, [$Fe^{II}Me_3$tacn$(OTf)_2$], a new species rapidly formed: [poatCo^{II}–μ-OH–$Fe^{III}Me_3$tacn]OTf. The identity of [Co^{II}–μ-OH–Fe^{III}]$^+$ was confirmed through structural and spectroscopic analyses. Interestingly, only the Fe center was oxidized during this reaction and not the Co center. This species exhibited antiferromagnetic coupling between the metal centers and a unique electronic absorption spectrum with a proposed IVCT feature. The compound also exhibited a relatively low potential $Co^{III}Fe^{III}/Co^{II}Fe^{III}$ couple ($E_{1/2}$ = –0.175 V versus $Fc^{+/0}$), suggesting that a [Co^{III}–μ-OH–Fe^{III}]$^{2+}$ species was accessible through oxidation with FcOTf.

Additionally, the mechanism of formation of [poatCo^{II}–μ-OH–$Fe^{III}Me_3$tacn]OTf was examined, as was the oxidation chemistry at the Fe center. It could not be definitively confirmed whether [Co^{II}–μ-OH–Fe^{III}]$^+$ formed via an inner-sphere oxidation mechanism, where the O_2 unit coordinated first likely to the Fe ion before oxidation, or an outer-sphere mechanism. In a control experiment, it was found that [$Fe^{II}Me_3$tacn$(OTf)_2$] on its own did not react with O_2. Therefore, it was clear that the oxidation of the Fe center could be attributed partially to the excellent donorability of the P=O ligands, which provided a strongly donating ligand field. The strong ligand field may have improved the affinity of the Fe center for O_2 aiding in formation of [poatCo^{II}–μ-OH–$Fe^{III}Me_3$tacn]OTf. This is the first example of a bimetallic complex in the [poat]$^{3-}$/Me_3tacn system where the metal ion coordinated by Me_3tacn was in a higher oxidation state than the metal coordinated to the [poat]$^{3-}$ backbone.

Following studies with [Co^{II}–μ-OH–Fe^{III}]$^+$, the complex was oxidized with FcOTf, leading to the formation of [poatCo^{III}–μ-OH–$Fe^{III}Me_3$tacn$(OTf)_2$. The complex was characterized structurally and spectroscopically, which confirmed that the hydroxido ligand remained protonated following oxidation. When [Co^{III}–μ-OH–Fe^{III}]$^{2+}$ was studied by $\perp$-mode EPR spectroscopy, it was observed that the metal ions were now ferromagnetically coupled with a spin state of S = 7/2, due to oxidation of the Co^{III} ion. This oxidation led to

loss of an electron in the d_{z^2} orbital, leading to a ferromagnetic interaction per the Goodenough-Kanamori rules,[72,73] and disruption of hyperfine from the ^{59}Co nucleus.

Finally, spectroscopic studies were carried out to determine if $[Co^{III}–\mu\text{-}OH–Fe^{III}]^{2+}$ could be deprotonated. The UV-vis and ⊥-mode EPR spectra suggested that LiHMDS (pK_a ~ 26, THF)[75] could deprotonate the metal complex, leading to formation of $[Co^{III}–\mu\text{-}O–Fe^{III}]^{+}$. The EPR spectra exhibited a new S = 1/2 spin state due to antiferromagnetic coupling between a high-spin S = 5/2 Fe^{III} center and a high-spin S = 2 Co^{III} ion. The proposed change in the Co^{III} spin state was likely due to π-bonding with the oxido ligand. Further supporting the spin state change was the presence of ^{59}Co hyperfine in the EPR spectrum. The deprotonation studies were promising but more work is needed to confirm these results. The complexes studied in this chapter presented a synthetic handle to modulating metal spin states and magnetic coupling.

Outlook

To best complete this work, the mechanism of formation of $[Co^{II}–\mu\text{-}OH–Fe^{III}]^{+}$ should be studied further. As the data currently stands, an inner- versus outer-sphere oxidation mechanism is unclear. The most efficient way to confirm the mechanism is to pursue ^{18}O labeling studies. $[Co^{II}–\mu\text{-}OH–Fe^{III}]^{+}$ can be readily prepared in good yield in bulk and has already been characterized with HRMS. However, it may be difficult to determine if the isotopic enrichment was due to an inner sphere oxidation with $^{18}O_2$ or if the source of the hydroxido ligand was from ^{18}O-labeled byproduct(s) from reduction of $^{18}O_2$. It may be more informative to follow the formation of $[Co^{II}–\mu\text{-}OH–Fe^{III}]^{+}$ with $^{18}O_2$ to determine if there is a kinetic isotope effect. Finally, a reaction could be carried out where $K[Co^{II}poat]$ is mixed with $[Fe^{II}Me_3tacn(OTf)_2]$ and treated with FcOTf and a small amount of air free water. Additionally, many of the M–OH complexes studied in the Borovik lab have unclear proton sources, which are normally proposed to come from solvent. Some preliminary studies were performed using deuterated DCM to determine if there was a kinetic isotope effect due to the presence of the deuterated solvent. The results of these studies were inconclusive because the deuterated solvent appeared wet and affected the absorption spectra of the starting materials. These studies could be expanded upon using distilled, dried deuterated DCM.

Lastly, deprotonation studies of $[Co^{III}–\mu\text{-}OH–Fe^{III}]^{2+}$ yielded promising initial results. However the experimental conditions may need to be modified to optimize the yield and best stabilize the products. Different bases could further be studied to improve yields and prevent undesired byproducts, given that using an inorganic base such as LiHMDS could result in some interaction of the Li^+ ion with the P=O units from the $[poat]^{3-}$ ligand framework.

Experimental Section

General Procedures

Unless otherwise specified, all reagents were purchased and used from commercially available sources and stored under a N_2 atmosphere in a VAC dry box. Sure-seal bottles of dimethyl acetamide (DMA) were purchased from Honeywell- Burdick & Jackson (99.5% purity). Chloroform ($CHCl_3$) was purchased from Fisher Scientific, distilled under vacuum, and stored under a N_2 atmosphere in a VAC dry box. All other solvents were sparged with argon and purified with a JC Meyer Co. solvent purification system with Q-5 columns and molecular sieves. Potassium hydride (KH) was bought as a 30% suspension in mineral oil, washed on a fine porosity frit with pentane and diethyl ether (Et_2O), dried under vacuum, and stored under N_2. Cobalt (II) acetate ($Co^{II}(OAc)_2$) was purchased from Sigma Aldrich as a pink-purple solid and dried briefly in an oven until a purple powder was obtained. H_3poat,[2] Me_3tacn,[76,77] $[Fe^{II}Me_3tacn(OTf)_2]$,[78] and ferrocenium triflate (FcOTf)[32] were prepared following literature procedures.

Physical Methods

Electronic absorption spectra were collected in a 1 cm quartz cuvette, fitted with a magnetic stir bar. Spectra were recorded on a Cary-60 spectrophotometer or an Agilent UV-vis spectrophotometer fitted with a Unisoku Unispeks cryostat for temperature-controlled spectroscopy. CV was performed with a CHI600C potentiostat. Voltammograms were collected from a ~ 1 mM stock solution of analyte in ~ 100 mM tetrabutylammonium hexafluorophosphate in dry, air-free DCM collected in 4-neck, double-walled cell. A 1 mm glassy carbon electrode acted as the working electrode with a Pt wire counter electrode and a Ag wire reference electrode. All voltammograms were referenced to an internal $Fc^{+/0}$ standard. He-temperature EPR spectra were collected on an X-Band Bruker spectrometer fitted with an Oxford liquid helium cryostat. Signals were referenced and

quantified to a CuEDTA spin standard. The magnetic field was calibrated with an NMR gaussmeter. The microwave frequency of the instrument was calibrated with a frequency counter. 77 K EPR experiments were recorded on a Bruker EMX X-band spectrometer with the following parameters, unless otherwise noted: microwave frequency of 9.64 GHz, a modulation frequency of 100 kHz, a modulation amplitude of 10 G, a microwave power of 2 mW, an attenuation of 20 dB, a time constant of 82 msec, and a conversion time of 41 msec. All EPR samples were prepared under a nitrogen atmosphere in 4 mm quartz EPR tubes, capped with a septum, and flash frozen in liquid nitrogen. Evans' Method NMR spectra were recorded at 500 MHz using a Bruker DRX500 spectrometer with a TCI cryoprobe**.** Mössbauer spectra were recorded with a Janis Research Super-Varietemp Cryostat. Isomer shifts were reported to Fe^0 metal collected at 298 K. Mössbauer and EPR spectra were simulated and fit using SpinCount software.[79] ATR-FTIR spectra were measured on a Thermo Scientific Nicolet iS5 spectrometer fitted with an iD5 ATR attachment. Elemental analyses were measured on a Perkin-Elmer 2400 Series II CHNS elemental analyzer. HRMS measurements were carried out on a Waters Micromass LCT Premier Mass Spectrometer in positive electrospray ionization mode (ES+).

Preparative Methods

K[Co^{II}poat]: 0.1426 g (0.1910 mmol) of H_3poat were dissolved in 4 mL of DMA. To this solution, 0.0280 g (0.698 mmol) KH were added, yielding a bubbling, cloudy solution. The reaction mixture was stirred till bubbling ceased and the solution was clear and colorless. Then, 0.0348 g (0.197 mmol) of $Co^{II}(OAc)_2$ were added as a purple powder suspension in 2 mL of DMA. The reaction mixture was allowed to stir overnight and resulted in formation of a bright, cloudy blue suspension. The reaction mixture was filtered to yield solid blue powder and a bright blue solution. The solid on the frit was washed with minimal DCM, followed by *n*-pentane and Et_2O until the blue color washed away and 0.0345 g of dry, off-white solid remained (92.0% yield; theoretical yield, KOAc = 0.0375 g, 0.382 mmol). The blue filtrate was subsequently dried under vacuum to give bright blue powder. This powder was redissolved in DCM and layered under *n*-pentane to yield 0.1170 g (0.1390 mmol, 72.8% yield) of bright blue, blocky single crystals, suitable for X-ray diffraction analysis. UV-vis (DCM, λ_{max} nm (ε, $M^{-1}cm^{-1}$)) = 410 (13), 585 (67), 610 (71), 770 (8). ATR-FTIR, selected bands (cm^{-1}) = 3050, 2949, 2838, 2342, 1720, 1589, 1481, 1433, 1271, 1232, 1192, 1155, 1118, 1026, 965, 918, 851, 801, 746, 717,

696. EPR (X-Band, ⊥-mode, 20 K, DCM:THF, excess 18c6), g = 4.5, 4.3, 2.0 (A = 262 MHz), E/D = 0.0029, D = +3.6 cm^{-1}. μ_{eff}, Evans Method, DCM = 4.28 μ_B. Cyclic Voltammetry (100 mV/s, DCM, V vs $Fc^{+/0}$) = $E_{1/2}$ = –0.495, E_{pa} = +0.365. Elemental Analysis calculated for $4(C_{42}H_{42}CoKN_4O_3P_3) \cdot C_5H_{12}$; C, 60.42, H, 5.28, N, 6.52; found C, 60.6, H, 4.87, N, 6.71.

[poatCo^{II}–μ-OH–Fe^{III}Me$_3$tacn]OTf: 0.0262 g (0.0499 mmol) [Fe^{II}Me$_3$tacn(OTf)$_2$] was dissolved ~2 mL DCM in a 10 mL round bottom flask and sealed with a septum. This clear, colorless solution was taken out of the glove box and sparged with N_2 on the Schlenk line. While the [Fe^{II}Me$_3$tacn(OTf)$_2$] was sparging, 0.0415 g (0.0493 mmol) K[Co^{II}poat] was dissolved in ~4 mL DCM in a Schlenk flask equipped with a stir bar, sealed, and taken out of the drybox. Dry O_2 (0.600 mL, 0.0268 mmol) was bubbled directly into the clear, blue solution via syringe that did not result in a color change. The Schlenk flask was transferred to the Schlenk line and a small vacuum was applied. The [Fe^{II}Me$_3$tacn(OTf)$_2$] solution was then cannula transferred to the Schlenk flask containing K[Co^{II}poat]. Upon addition of [Fe^{II}Me$_3$tacn(OTf)$_2$], the solution in the Schlenk flask turned a deep, navy blue and the reaction was left to stir. After one hour, the solvent was removed under vacuum, yielding a deep blue solid. The residual solids were left to dry under vacuum. The Schlenk flask was returned to the glovebox and the solid was redissolved in DCM. The deep blue solution was then pipet filtered to remove any excess solids and the filtrate was layered under *n*-pentane, resulting in the growth of 0.0556 g (0.0465 mmol, 94.2% yield) of red-blue dichroic single crystals suitable for X-ray diffraction analysis. UV-vis (DCM, λ_{max} nm (ε, $M^{-1}cm^{-1}$)) = 435 (567, sh), 578 (709), 742 (1220). ATR-FTIR, selected bands (cm^{-1}) = 3687, 3089, 3072, 2951, 2900, 2860, 2843, 2405, 1465, 1436, 1270, 1181, 1129, 1118, 1083, 1065, 1032, 1014, 997, 964, 927, 907, 806, 784, 754, 721, 699. EPR Silent, ⊥- and ∥-modes. μ_{eff}, Evans Method, DCM = 6.18 μ_B. Cyclic Voltammetry (DCM, V vs $Fc^{+/0}$) : Co^{III}Fe^{III}/Co^{II}Fe^{III}, $E_{1/2}$= –0.175, Co^{II}Fe^{III}/Co^{II}Fe^{II}, $E_{1/2}$= –1.190. HRMS (ES+, m/z, z= 1): Exact mass calculated for $C_{51}H_{64}CoFeN_7O_4P_3$: 1046.2915, Found: 1046.2936.

[poatCo^{III}–μ-OH–Fe^{III}Me$_3$tacn](OTf)$_2$: In a scintillation vial, 0.0281 g (0.0235 mmol) of [Co^{II}–μ-OH–Fe^{III}]$^+$ was dissolved in ~1 mL DCM under an inert atmosphere. To this deep blue solution, 0.0090 g (0.027 mmol) FcOTf in ~1 mL DCM was added dropwise, causing an immediate color change to a deep red-orange solution. The reaction was stirred for 10 minutes. After stirring, minimal *n*-hexane was added until slight cloudiness appeared

in the vial. Roughly 1 mL of DCM was added until the solution appeared clear again and the vial was stored at –35 ºC. After 3 days, additional *n*–hexane was added and the vial was returned to the freezer. After 7 days, dark-red single crystals single crystals suitable for X-ray diffraction analysis were grown in a 0.0236 g (0.0175 mmol, 75% yield). UV-vis (DCM, λ_{max} nm (ε, $M^{-1}cm^{-1}$)) = 395 (6150, sh), 462 (4870), 679 (738). ATR-FTIR, selected bands (cm^{-1}) = 3510, 3300, 3078, 2915, 2872, 2826, 2383, 2044, 1590, 1467, 1437, 1259, 1223, 1115, 1069, 1029, 1007, 989, 962, 804, 789, 751, 725, 696, 635, 618. μ_{eff}, Evans Method, DCM = 8.36 μ_B. ⊥- mode EPR: S = 7/2. Cyclic Voltammetry (DCM, V vs $Fc^{+/0}$) : $Co^{III}Fe^{III}/Co^{II}Fe^{III}$ = –0.335, $Co^{II}Fe^{III}/Co^{II}Fe^{II}$ = –1.358. HRMS (ES+, m/z, z= 2): Exact mass calculated for $C_{51}H_{64}CoFeN_7O_4P_3$: 523.1452, Found: 523.1458.

X-ray Crystallographic Methods

[poatCo^{II}–μ-OH–Fe^{III}Me$_3$tacn]OTf: The data for asb647 were collected from a shock-cooled single crystal at 93(2) K on a Bruker SMART APEX II three-circle diffractometer with a sealed X-ray tube using an equatorial mounted graphite as monochromator and a Bruker Apex II CCD detector. The diffractometer was equipped with a low temperature device and used MoK_a radiation (λ = 0.71073 Å). All data were integrated with SAINT and a multi-scan absorption correction using SADABS was applied.[80,81] The structure was solved by direct methods using SHELXS and refined by full-matrix least-squares methods against F^2 by SHELXL-2018/3 using ShelXle.[82–84] All non-hydrogen atoms were refined with anisotropic displacement parameters. All hydrogen atoms were refined with isotropic displacement parameters. Some were refined freely and some on calculated positions using a riding model with their U_{iso} values constrained to 1.5 times the U_{eq} of their pivot atoms for terminal sp^3 carbon atoms and 1.2 times for all other carbon atoms. This report and the CIF file were generated using FinalCif.[85] *Refinement Details:* All non-hydrogen atoms were refined freely without constraints or constraints. For H1, the position and displacement parameter were freely refined. All other hydrogen atoms were refined using a riding model. SQUEEZE,[83] implemented in Platon,[83,86,87] was used to remove residual electron density from two severely disordered partial occupancy dichloromethane molecules.

[poatCo^{III}–μ-OH–Fe^{III}Me$_3$tacn]OTf$_2$: The data for asb726 were collected from a shock-cooled single crystal at 100(2) K on a Bruker APEX-II CCD at the University of California San Diego Crystallography Facility. The diffractometer was equipped with a low temperature device and used Mo K_a radiation (λ = 0.71073 Å). All data

were integrated with SAINT and a multi-scan absorption correction using SADABS was applied.[80,81] The structure was solved by direct methods using SHELXS-97 and refined by full-matrix least-squares methods against F^2 by SHELXL-2018/3 using ShelXle.[82,84,88] All non-hydrogen atoms were refined with anisotropic displacement parameters. All hydrogen atoms were refined with isotropic displacement parameters. Some were refined freely and some on calculated positions using a riding model with their U_{iso} values constrained to 1.5 times the U_{eq} of their pivot atoms for terminal sp^3 carbon atoms and 1.2 times for all other carbon atoms. Disordered moieties were refined using bond lengths restraints and displacement parameter restraints. This report and the CIF file were generated using FinalCif.[85] *Refinement Details:* All non-disordered non-hydrogen atoms were refined freely without restraints or constraints. Disordered occupancies and positions were refined using a free variable. The disordered carbon atoms on the phenyl groups were separately constrained to the corresponding carbons. ADPs of phenyl groups, C7-C12 and C13-C18 were restrained to similar values. ADPs of the carbons directly attached to phosphorus atoms were restrained to more isotropic values. All bond lengths of phenyl groups were restrained to similar values according to their equivalent position around the ring. ADPs for C43 and C43B and ADPs for C44 and C44B were constrained separately to the same values. C43 and C43C required a restraint to maintain a more isotropic shape. The position for H1 was freely refined with the displace parameter constrained to 1.5x O1, and all other hydrogen atoms were refined using a riding model. SQUEEZE,[83] implemented in Platon,[83,86,87] was used to remove electron density of approximately 5.6 heavily disordered chloroform molecules from the unit cell (2.8 per asymmetric unit).

Supplemental Information

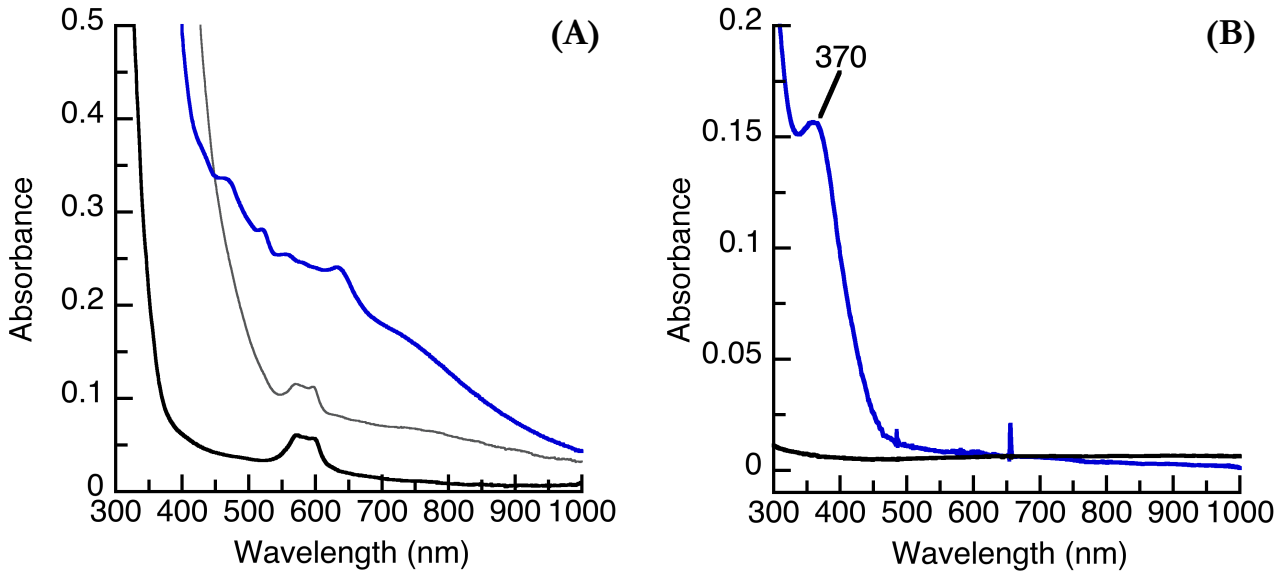

Figure 4-S1: (A) UV-vis spectra following the reaction between K[Co^{II}poat], [Fe^{II}Me$_3$tacn(OTf)$_2$], and FcOTf. The initial spectrum (black) was K[Co^{II}poat], and [Fe^{II}Me$_3$tacn(OTf)$_2$]. The gray trace was after ~15 minutes. The blue trace was after 48 hours. These spectra are not consistent with [Co^{II}–μ-OH–Fe^{III}]$^+$. **(B)** UV-vis spectra following the addition of excess O_2 to [Fe^{II}Me$_3$tacn(OTf)$_2$] (black) after stirring overnight (~15 h, blue) in DCM.

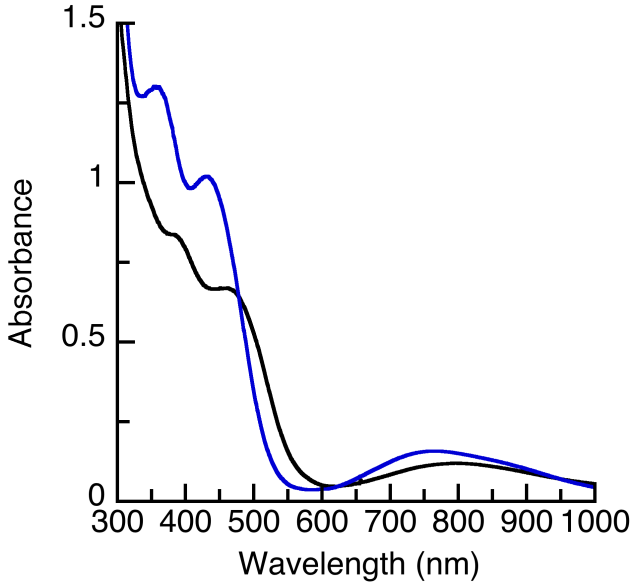

Figure 4-S2: Overlay of [Co^{III}–μ-OH–Fe^{III}]$^{2+}$ (black trace) with [poatCo^{III}–μ-OH–Zn^{II}Me$_3$tacn]OTf (blue). Note that these two samples were not the same concentration. Both were measured at room temperature in DCM.

Table 4-S1: Crystallographic details for [poatCo^{II}–μ-OH–Fe^{III}Me$_3$tacn]OTf (middle column) and [poatCo^{III}–μ-OH–Fe^{III}Me$_3$tacn]OTf$_2$ (right column).

Compound	**[poatCo^{II}–μ-OH–Fe^{III}Me$_3$tacn]OTf · ½ CH$_2$Cl$_2$**	**[poatCo^{III}–μ-OH–Fe^{III}Me$_3$tacn](OTf)$_2$**
Empirical formula	$C_{52.50}H_{65}ClCoF_3FeN_7O_7P_3S$	$C_{53}H_{64}CoF_6FeN_7O_{10}P_3S_2$
Formula weight	1238.31	1344.92
Temperature [K]	93(2)	100(2)
Crystal system	triclinic	triclinic
Space group (number)	$P\bar{1}$ (2)	$P\bar{1}$ (2)
a [Å]	15.0619(16)	14.499(2)
b [Å]	15.2334(17)	14.952(2)
c [Å]	16.2483(18)	16.660(2)
α [°]	107.6255(18)	85.0298(17)
β [°]	101.5360(18)	88.1519(17)
γ [°]	115.4538(16)	87.2756(16)
Volume [Å^3]	2962.7(6)	3592.8(9)
Z	2	2
ϱ_{calc} [gcm^{-3}]	1.388	1.243
Independent reflections	14753	13712
Goodness-of-fit on F^2	1.051	1.029
R_1, [$I \geq 2\sigma(I)$]	0.0386	0.0568
wR_2, [all data]	0.0869	0.1463

$R_1 = \Sigma \mid |F_o| - |F_c| \mid / \Sigma |F_o|$
$wR_2 = [\Sigma[w(F_o^2 - F_c^2)^2] / \Sigma[w(F_o^2)^2]]^{1/2}$

Thermal ellipsoids are shown at 50%

Goof (Goodness-of-fit) = $S = [\Sigma[w(F_o^2 - F_c^2)^2] / (n - p)]^{1/2}$, where n = number of reflections and p = total number of parameters refined.

Table 4-S2: Different unit cells obtained for [poatCo^{II}–μ-OH–Fe^{III}Me$_3$tacn]OTf.

Compound	**asb647**	**asb676, asb684**
Crystal system	Triclinic	Monoclinic
Space group (number)	$P\bar{1}$ (2)	$P2_1/c$
a [Å]	15.0619(16)	14.5919
b [Å]	15.2334(17)	17.7031
c [Å]	16.2483(18)	25.4319
α [°]	107.6255(18)	90.000
β [°]	101.5360(18)	96.370
γ [°]	115.4538(16)	90.000
Volume [Å^3]	2962.7(6)	6569.6

References

(1) Sickerman, N. S. Investigating the Effects of Non-Covalent Interactions in Metal Complexes with Versatile Ligand Scaffolds, University of California, Irvine, 2014.

(2) Oswald, V. F.; Lee, J. L.; Biswas, S.; Weitz, A. C.; Mittra, K.; Fan, R.; Li, J.; Zhao, J.; Hu, M. Y.; Alp, E. E.; Bominaar, E. L.; Guo, Y.; Green, M. T.; Hendrich, M. P.; Borovik, A. S. Effects of Noncovalent Interactions on High-Spin Fe(IV)–Oxido Complexes. *J. Am. Chem. Soc.* **2020**, *142*, 11804–11817.

(3) Oswald, V. F.; Weitz, A. C.; Biswas, S.; Ziller, J. W.; Hendrich, M. P.; Borovik, A. S. Manganese−Hydroxido Complexes Supported by a Urea/Phosphinic Amide Tripodal Ligand. *Inorg. Chem.* **2018**, *57*, 13341–13350.

(4) Lee, J. L. Synthetic Models for Metalloenzyme Active Sites: Accessing High-Valent Bimetallic Complexes with [M–(μ-OH)–M'] Cores, University of California, Irvine, 2021.

(5) Lee, J. L.; Biswas, S.; Sun, C.; Ziller, J. W.; Hendrich, M. P.; Borovik, A. S. Bioinspired Di-Fe Complexes: Correlating Structure and Proton Transfer over Four Oxidation States. *J. Am. Chem. Soc.* **2022**, *144*, 4559–4571.

(6) Taguchi, T.; Gupta, R.; Lassalle-Kaiser, B.; Boyce, D. W.; Yachandra, V. K.; Tolman, W. B.; Yano, J.; Hendrich, M. P.; Borovik, A. S. Preparation and Properties of a Monomeric High-Spin MnV–Oxo Complex. *J. Am. Chem. Soc.* **2012**, *134*, 1996–1999.

(7) Lacy, D. C.; Gupta, R.; Stone, K. L.; Greaves, J.; Ziller, J. W.; Hendrich, M. P.; Borovik, A. S. Formation, Structure, and EPR Detection of a High Spin FeIV—Oxo Species Derived from Either an FeIII—Oxo or FeIII—OH Complex. *J. Am. Chem. Soc.* **2010**, *132*, 12188–12190.

(8) Hammes, B. S.; Young, V. G.; Borovik, A. S. Hydrogen-Bonding Cavities about Metal Ions: A Redox Pair of Coordinatively Unsaturated Paramagnetic Co-OH Complexes. *Angew. Chemie Int. Ed.* **1999**, *38*, 666–669.

(9) Cook, S. A.; Ziller, J. W.; Borovik, A. S. Iron(II) Complexes Supported by Sulfonamido Tripodal Ligands: Endogenous versus Exogenous Substrate Oxidation. *Inorg. Chem.* **2014**, *53*, 11029–11035.

(10) Sano, Y.; Weitz, A. C.; Ziller, J. W.; Hendrich, M. P.; Borovik, A. S. Unsymmetrical Bimetallic Complexes with M^{II}–(μ-OH)–M^{III} Cores ($M^{II}M^{III}$ = $Fe^{II}Fe^{III}$, $Mn^{II}Fe^{III}$, $Mn^{II}Mn^{III}$): Structural, Magnetic, and Redox. *Inorg. Chem.* **2013**, *52*, 10229–10231.

(11) Park, Y. J.; Cook, S. A.; Sickerman, N. S.; Sano, Y.; Ziller, J. W.; Borovik, A. S. Heterobimetallic Complexes with M^{III}-(μ-OH)-M^{II} Cores (M^{III} = Fe, Mn, Ga; M^{II} = Ca, Sr, and Ba): Structural, Kinetic, and Redox Properties. *Chem. Sci.* **2013**, *4*, 717–726.

(12) Lacy, D. C.; Park, Y. J.; Ziller, J. W.; Yano, J.; Borovik, A. S. Assembly and Properties of Heterobimetallic Co(II/III)/Ca(II) Complexes with Aquo and Hydroxo Ligands. *J. Am. Chem. Soc.* **2012**, *134*, 17526–17535.

(13) Ethan A. Hill. Secondary Coordination Sphere Effects on the Properties of High Valent Iron and Manganese Complexes with Oxido and Hydroxido Ligands, University of California, Irvine, Irvine, CA, 2016.

(14) Oswald, V. F. Tripodal Phosphoryl Amide Frameworks: Investigating The Relationship Between High Valent Metal–Oxido And Metal–Hydroxido Complexes, University of California, Irvine, 2018.

(15) Lee, J. L.; Oswald, V. F.; Biswas, S.; Hill, E. A.; Ziller, J. W.; Hendrich, M. P.; Borovik, A. S. Stepwise Assembly of Heterobimetallic Complexes: Synthesis, Structure, and Physical Properties. *Dalt. Trans.* **2021**, *50*, 8111–8119.

(16) Chen Sun. Secondary Coordination Sphere Effects on Properties and Reactivities of Metal Complexes, University of California, Irvine, Irvine, CA, 2021.

(17) Sun, C.; Oswald, V. F.; Hill, E. A.; Ziller, J. W.; Borovik, A. S. Investigation of Iron–Ammine and Amido Complexes within a C3-Symmetrical Phosphinic Amido Tripodal Ligand. *Dalt. Trans.* **2021**, *50*, 11197–11205.

(18) Kläui, W.; Werner, H. Synthesis of Trinuclear Sandwich-Like Cyclopentadienyl Complexes Containing Two Different Metal Atom Centers. *Angew. Chemie Int. Ed. English* **1976**, *15*, 172–173.

(19) Kläui, W.; Eberspach, W.; Gütlich, P. Spin-Crossover Cobalt(III) Complexes: Steric and Electronic Control of Spin State. *Inorg. Chem.* **1987**, *26*, 3977–3982.

(20) Navon, G.; Klaui, W. 59Co NMR of a Cobalt(III) Spin-Crossover Compound. *Inorg. Chem.* **1984**, *23*, 2722–2725.
(21) Kläui, W. The Coordination Chemistry and Organometallic Chemistry of Tridentate Oxygen Ligands with π-Donor Properties. *Angew. Chemie Int. Ed. English* **1990**, *29*, 627–637.
(22) Levitskaia, T. G.; Sinkov, S. I.; Lumetta, G. J. Actinide Binding by Kläui Ligands: REDOX Speciation and Sorption on an Extraction Chromatography Resin. *Radiochim. Acta* **2008**, *96*, 805–815.
(23) Ip, H. F.; So, Y. M.; Lee, H. K.; Williams, I. D.; Leung, W. H. A Stable Iridium(IV) Complex Containing the Kläui Tripodal Ligand [Co(H5-C5H5){P(O)(OEt)2}3]–. *Eur. J. Inorg. Chem.* **2012**, *2012*, 3289–3295.
(24) So, Y. M.; Wong, K. L.; Sung, H. H. Y.; Williams, I. D.; Leung, W. H. Ruthenium Aqua Complexes Supported by the Kläui Tripodal Ligand: Synthesis, Structure, and Application in Catalytic C–H Oxidation in Water. *Eur. J. Inorg. Chem.* **2019**, *2019*, 2368–2374.
(25) Lee, H. B.; Ciolkowski, N.; Winslow, C.; Rittle, J. High Spin Cobalt Complexes Supported by a Trigonal Tris(Phosphinimide) Ligand. *Inorg. Chem.* **2021**, *60*, 11830–11837.
(26) Stauber, J. M.; Zhang, S.; Gvozdik, N.; Jiang, Y.; Avena, L.; Stevenson, K. J.; Cummins, C. C. Cobalt and Vanadium Trimetaphosphate Polyanions: Synthesis, Characterization, and Electrochemical Evaluation for Non-Aqueous Redox-Flow Battery Applications. *J. Am. Chem. Soc.* **2018**, *140*, 538–541.
(27) Grunwald, A. C.; Scholtysik, C.; Hagenbach, A.; Abram, U. One Ligand, One Metal, Seven Oxidation States: Stable Technetium Complexes with the "Kläuii Ligand." *Inorg. Chem* **2020**, *59*, 9396–9405.
(28) Lucas, R. L.; Zart, M. K.; Murkerjee, J.; Sorrell, T. N.; Powell, D. R.; Borovik, A. S. A Modular Approach toward Regulating the Secondary Coordination Sphere of Metal Ions: Differential Dioxygen Activation Assisted by Intramolecular Hydrogen Bonds. *J. Am. Chem. Soc.* **2006**, *128*, 15476–15489.
(29) Sonja M. Peterson. Ligand Design Consideration for the Activation of Small Molecules, University of California, Irvine, Irvine, CA, 2012.
(30) Malik, D. D.; Chandra, A.; Seo, M. S.; Lee, Y. M.; Farquhar, E. R.; Mebs, S.; Dau, H.; Ray, K.; Nam, W. Formation of Cobalt–Oxygen Intermediates by Dioxygen Activation at a Mononuclear Nonheme Cobalt(II) Center. *Dalt. Trans.* **2021**, *50*, 11889–11898.
(31) Huang, X.; Groves, J. T. Oxygen Activation and Radical Transformations in Heme Proteins and Metalloporphyrins. *Chem. Rev.* **2018**, *118*, 2491–2553.
(32) Connelly, N. G.; Geiger, W. E. Chemical Redox Agents for Organometallic Chemistry. *Chem. Rev.* **1996**, *96*, 877–910.
(33) Pegis, M. L.; Wise, C. F.; Martin, D. J.; Mayer, J. M. Oxygen Reduction by Homogeneous Molecular Catalysts and Electrocatalysts. *Chem. Rev.* **2018**, *118*, 2340–2391.
(34) Addison, A. W.; Rao, T. N.; Reedijk, J.; van Rijn, J.; Verschoor, G. C. Synthesis, Structure, and Spectroscopic Properties of Copper(II) Compounds Containing Nitrogen-Sulphur Donor Ligands; the Crystal and Molecular Structure of Aqua[1,7-Bis(N-Methylbenzimidazol-2'-ul)-2,6-dithiaheptane] Copper(II) Perchlorate. *J. Chem. Soc. Dalt. Trans.* **1984**, *7*, 1349–1356.
(35) Ray, M.; Hammes, B. S.; Yap, G. P. A.; Rheingold, A. L.; Borovik, A. S. Structure and Physical Properties of Trigonal Monopyramidal Iron(II), Cobalt(II), Nickel(II), and Zinc(II) Complexes. *Inorg. Chem.* **1998**, *37*, 1527–1532.
(36) Jones, J. R.; Ziller, J. W.; Borovik, A. S. Modulating the Primary and Secondary Coordination Spheres within a Series of CoII-OH Complexes. *Inorg. Chem.* **2017**, *56*, 1112–1120.
(37) Pauling, L. *The Nature of the Chemical Bond and the Structure of Molecules and Crystals: An Introduction to Modern Structural Chemistry*, 3rd ed.; Cornell University Press, 1960.
(38) Kutzelnigg, W. Chemical Bonding in Higher Main Group Elements. *Angew. Chemie Int. Ed.* **1984**, *23*, 272–295.
(39) Reed, A. E.; Von, P.; Schleyer, R. *Chemical Bonding in Hypervalent Molecules. The Dominance of Ionic Bonding and Negative Hyperconjugation over d-Orbital Participation*; John Wiley and Sons, 1990; Vol. 112.
(40) Duvinage, D.; Puylaert, P.; Wieduwilt, E. K.; Malaspina, L. A.; Edwards, A. J.; Lork, E.; Mebs, S.; Hupf, E.; Grabowsky, S.; Beckmann, J. Nickel and Palladium Complexes of a PP(O)P Pincer Ligand Based upon a Peri-Substituted Acenaphthyl Scaffold and a Secondary Phosphine Oxide. *Inorg. Chem* **2022**, *61*, 8406–8418.

(41) Kurtz, D. M. Oxo- and Hydroxo-Bridged Diiron Complexes: A Chemical Perspective on a Biological Unit. *Chem. Rev.* **1990**, *90*, 585–606.
(42) Nam, W. Dioxygen Activation by Metalloenzymes and Models. *Acc. Chem. Res.* **2007**, *40*, 465.
(43) Jasniewski, A. J.; Que, L. Dioxygen Activation by Nonheme Diiron Enzymes: Diverse Dioxygen Adducts, High-Valent Intermediates, and Related Model Complexes. *Chem. Rev.* **2018**, *118*, 2554–2592.
(44) Costas, M.; Mehn, M. P.; Jensen, M. P.; Que, L. Dioxygen Activation at Mononuclear Nonheme Iron Active Sites: Enzymes, Models, and Intermediates. *Chem. Rev.* **2004**, *104*, 939–986.
(45) MacBeth, C. E.; Golombek, A. P.; Young, V. G.; Yang, C.; Kuczera, K.; Hendrich, M. P.; Borovik, A. S. O_2 Activation by Nonheme Iron Complexes: A Monomeric Fe(III)–Oxo Complex Derived From O_2. *Science.* **2000**, *289*, 938–941.
(46) MacBeth, C. E.; Gupta, R.; Mitchell-Koch, K. R.; Young, V. G.; Lushington, G. H.; Thompson, W. H.; Hendrich, M. P.; Borovik, A. S. To Stabilize M−O(H) Units: Synthesis and Properties of Monomeric Iron and Manganese Complexes with Terminal Oxo and Hydroxo Ligands. *J. Am. Chem. Soc.* **2004**, *126*, 2556–2567.
(47) Yadav, V.; Gordon, J. B.; Siegler, M. A.; Goldberg, D. P. Dioxygen-Derived Nonheme Mononuclear Fe^{III}(OH) Complex and Its Reactivity with Carbon Radicals. *J. Am. Chem. Soc.* **2019**, *141*, 10148–10153..
(48) Surendhran, R.; D'Arpino, A. A.; Sciscent, B. Y.; Cannella, A. F.; Friedman, A. E.; MacMillan, S. N.; Gupta, R.; Lacy, D. C. Deciphering the Mechanism of O2reduction with Electronically Tunable Non-Heme Iron Enzyme Model Complexes. *Chem. Sci.* **2018**, *9*, 5773–5780.
(49) Lacy, D. C. Applications of the Marcus Cross Relation to Inner Sphere Reduction of O2: Implications in Small-Molecule Activation. *Inorg. Chem. Front.* **2019**, *6*, 2396.
(50) Kovaleva, E. G.; Lipscomb, J. D. Versatility of Biological Non-Heme Fe(II) Centers in Oxygen Activation Reactions. *Nat. Chem. Biol.* **2008**, *4*, 186–193.
(51) Kálmán, A.; Párkányi, L.; Argay, G. Classification of the Isostructurality of Organic Molecules in the Crystalline State. *Acta Crystallogr. Sect. B Struct. Crystallogr. Cryst. Chem.* **1993**, *49*, 1039–1049.
(52) Cook, S. A.; Borovik, A. S. Molecular Designs for Controlling the Local Environments around Metal Ions. *Acc. Chem. Res.* **2015**, *48*, 2407–2414.
(53) Miessler, G. L.; Fischer, P. J.; Tarr, D. A. *Inorganic Chemistry*, Fifth.; Pearson: Upper Saddle River, NJ, 2014.
(54) Verhoeven, J. W. Glossary of Terms Used in Photochemistry (IUPAC Reconunendations 1996). *Pure Appl. Chem.* **1996**, *68*, 2223–2286.
(55) Münch, E. Aspects of 57Fe Mössbauer Spectroscopy. In *Physical Methods in Bioinorganic Chemistry*; Que Jr., L., Ed.; University Science Books: Sausalito, CA, 2000; pp 287–319.
(56) Sano, Y.; Lau, N.; Weitz, A. C.; Ziller, J. W.; Hendrich, M. P.; Borovik, A. S. Models for Unsymmetrical Active Sites in Metalloproteins: Structural, Redox, and Magnetic Properties of Bimetallic Complexes with M^{II}-(*μ*-OH)-Fe^{III} Cores. *Inorg. Chem.* **2017**, *56*, 14118–14128.
(57) Park, Y. J.; Ziller, J. W.; Borovik, A. S. The Effects of Redox-Inactive Metal Ions on the Activation of Dioxygen: Isolation and Characterization of a Heterobimetallic Complex Containing a MnIII–(μ-OH)–CaII Core. *J. Am. Chem. Soc.* **2011**, *133*, 9258–9261.
(58) Lau, N.; Sano, Y.; Ziller, J. W.; Borovik, A. S. Modular Bimetallic Complexes with a Sulfonamido-Based Ligand. *Dalt. Trans.* **2018**, *47*, 12362–12372.
(59) Nguyen, A. I.; Hadt, R. G.; Solomon, E. I.; Tilley, T. D. Efficient C–H Bond Activations via O2 Cleavage by a Dianionic Cobalt(II) Complex. *Chem. Sci.* **2014**, *5*, 2874–2878.
(60) Nurdin, L.; Spasyuk, D. M.; Fairburn, L.; Piers, W. E.; Maron, L. Oxygen–Oxygen Bond Cleavage and Formation in Co(II)-Mediated Stoichiometric O2 Reduction via the Potential Intermediacy of a Co(IV) Oxyl Radical. *J. Am. Chem. Soc.* **2018**, *140*, 16094–16105.
(61) Pfaff, F. F.; Kundu, S.; Risch, M.; Pandian, S.; Heims, F.; Pryjomska-Ray, I.; Haack, P.; Metzinger, R.; Bill, E.; Dau, H.; Comba, P.; Ray, K. An Oxocobalt(IV) Complex Stabilized by Lewis Acid Interactions with Scandium(III) Ions. *Angew. Chemie Int. Ed.* **2010**, *50*, 1711–1715.
(62) Wang, B.; Lee, Y.-M.; Tcho, W.-Y.; Tussupbayev, S.; Kim, S.-T.; Kim, Y.; Seo, M. S.; Cho, K.-B.; Dede, Y.; Keegan, B. C.; Ogura, T.; Kim, S. H.; Ohta, T.; Baik, M.-H.; Ray, K.; Shearer, J.; Nam, W. Synthesis and Reactivity of a Mononuclear Non-Haem Cobalt(IV)-Oxo Complex. *Nat. Commun.* **2017**, *8*, 14839.

(63) Hong, S.; Pfaff, F. F.; Kwon, E.; Wang, Y.; Seo, M. S.; Bill, E.; Ray, K.; Nam, W. Spectroscopic Capture and Reactivity of a Low-Spin Cobalt(IV)-Oxo Complex Stabilized by Binding Redox-Inactive Metal Ions. *Angew. Chemie Int. Ed.* **2014**, *53*, 10403–10407.
(64) Stich, T. A.; Krzystek, J.; Mercado, B. Q.; McAlpin, J. G.; Ohlin, C. A.; Olmstead, M. M.; Casey, W. H.; David Britt, R. Structural Insights into [Co4O4(C5H 5N)4(CH3CO2)4] +, a Rare Co(IV)-Containing Cuboidal Complex. *Polyhedron* **2013**, *64*, 304–307.
(65) McAlpin, J. G.; Stich, T. A.; Ohlin, C. A.; Surendranath, Y.; Nocera, D. G.; Casey, W. H.; Britt, R. D. Electronic Structure Description of a [Co(III)3Co(IV)O 4] Cluster: A Model for the Paramagnetic Intermediate in Cobalt-Catalyzed Water Oxidation. *J. Am. Chem. Soc.* **2011**, *133*, 15444–15452.
(66) Chakrabarty, R.; Bora, S. J.; Das, B. K. Synthesis, Structure, Spectral and Electrochemical Properties, and Catalytic Use of Cobalt(III)-Oxo Cubane Clusters. *Inorg. Chem.* **2007**, *46*, 9450–9462.
(67) Hadt, R. G.; Hayes, D.; Brodsky, C. N.; Ullman, A. M.; Casa, D. M.; Upton, M. H.; Nocera, D. G.; Chen, L. X. X-Ray Spectroscopic Characterization of Co(IV) and Metal-Metal Interactions in Co4O4: Electronic Structure Contributions to the Formation of High-Valent States Relevant to the Oxygen Evolution Reaction. *J. Am. Chem. Soc.* **2016**, *138*, 11017–11030.
(68) Goetz, M. K.; Schneider, J. E.; Filatov, A. S.; Jesse, K. A.; Anderson, J. S. Enzyme-Like Hydroxylation of Aliphatic C-H Bonds from an Isolable Co-Oxo Complex. *J. Am. Chem. Soc.* **2021**, *143*, 20849–20862.
(69) Zhang, L.; Liu, Y.; Deng, L. Three-Coordinate Cobalt(IV) and Cobalt(V) Imido Complexes with N-Heterocyclic Carbene Ligation: Synthesis, Structure, and Their Distinct Reactivity in C-H Bond Amination. *J. Am. Chem. Soc.* **2014**, *136*, 15525–15528.
(70) Slep, L. D.; Mijovilovich, A.; Meyer-Klaucke, W.; Weyhermüller, T.; Bill, E.; Bothe, E.; Neese, F.; Wieghardt, K. Mixed-Valent $\{Fe^{IV}(\mu\text{-O})(\mu\text{-Carboxylato})_2Fe^{III}\}^{3+}$ Core. *J. Am. Chem. Soc.* **2003**, *125*, 15554–15570.
(71) D. D. Perrin. *Dissociation Constant of Inorganic Acids and Bases in Aqueous Solution*; Pergamon: New York, NY, 1982.
(72) Gordon-Wylie, S. W.; Bominaar, E. L.; Collins, T. J.; Workman, J. M.; Claus, B. L.; Patterson, R. E.; Williams, S. A.; Conklin, B. J.; Yee, G. T.; Weintraub, S. T. Ligand Design for Securing Ferromagnetic Exchange Coupling in Multimetallic Complexes. *Chem.-Eur. J.* **1995**, *1*, 528–537.
(73) Joan Ribas Gispert. *Coordination Chemistry*; Wiley VCH, 2008.
(74) Birchall, T.; Drumond, I. Mössbauer Spectroscopy of Bis(Carbollyl)Iron Anions and Related Molecules. *Inorg. Chem.* **1971**, *10*, 399–401.
(75) Fraser, R. R.; Mansour, T. S.; Savard, S. Acidity Measurements on Pyridines in Tetrahydrofuran Using Lithiated Silylamines. *J. Org. Chem.* **1985**, *50*, 3232–3236.
(76) Schoenfeldt, N. J.; Ni, Z.; Korinda, A. W.; Meyer, R. J.; Notestein, J. M. Manganese Triazacyclononane Oxidation Catalysts Grafted under Reaction Conditions on Solid Cocatalytic Supports. *J. Am. Chem. Soc.* **2011**, *133*, 18684–18695.
(77) Cao, R.; Müller, P.; Lippard, S. J. Tripodal Tris-Tacn and Tris-Dpa Platforms for Assembling Phosphate-Templated Trimetallic Centers. *J. Am. Chem. Soc.* **2010**, *132*, 17366–17369.
(78) Blakesley, D. W.; Payne, S. C.; Hagen, K. S. Spin-State Variation in Solid State and Solution of Mononuclear Iron(II) 1,4,7-Trimethyl-1,4,7-Triazacyclonane Complexes. *Inorg. Chem.* **2000**, *39*, 1979–1989.
(79) Petasis, D. T.; Hendrich, M. P. *Quantitative Interpretation of Multifrequency Multimode EPR Spectra of Metal Containing Proteins, Enzymes, and Biomimetic Complexes*, 1st ed.; Elsevier Inc., 2015; Vol. 563..
(80) Bruker AXS Inc, SAINT Version 8.34a. Madison, WI 2013.
(81) Krause, L.; Herbst-Irmer, R.; Sheldrick, G. M.; Stalke, D. Comparison of Silver and Molybdenum Microfocus X-Ray Sources for Single-Crystal Structure Determination. *J. Appl. Crystallogr.* **2015**, *48*, 3–10.
(82) Sheldrick, G. M. A Short History of SHELX. *Acta Crystallogr. Sect. A Found. Crystallogr.* **2008**, *64*, 112–122.
(83) Spek, A. L. PLATON SQUEEZE: A Tool for the Calculation of the Disordered Solvent Contribution to the Calculated Structure Factors. *Acta Crystallogr. Sect. C Struct. Chem.* **2015**, *71*, 9–18.

(84) Hübschle, C. B.; Sheldrick, G. M.; Dittrich, B. ShelXle: A Qt Graphical User Interface for SHELXL. *J. Appl. Crystallogr.* **2011**, *44*, 1281–1284.
(85) Kratzert, D. FinalCif.
(86) Spek, A. L.; IUCr. Single-Crystal Structure Validation with the Program PLATON. *J. Appl. Crystallogr.* **2003**, *36*, 7–13.
(87) Spek, A. L. Structure Validation in Chemical Crystallography. *Acta Crystallogr. Sect. D Biol. Crystallogr.* **2009**, *65*, 148–155.
(88) Sheldrick, G. M.; IUCr. Crystal Structure Refinement with SHELXL. *Acta Crystallogr., Sect. C Cryst. Struct. Commun.* **2015**, *71*, 3–8.

Chapter 5: Magnetic communication in rigorously C_3 symmetric complexes facilitated by N–P=O bridging units

Introduction

Work from the Borovik lab centers largely on the design of synthetic ligand frameworks that allow for discrete control over both the primary (1°) and secondary (2°) coordination spheres of small molecule metal complexes. This synthetic control has facilitated the isolation of uncommon synthetic species, such as Fe^{III} and Mn^{V} oxido complexes,[1,2] unsymmetric bimetallic systems where the chemistries of each metal ion can be individually examined,[3–10] and allowed for the selective modification of ligand frameworks to tune the pK_a and reactivity of a series of Mn^{III}–OH complexes.[11] These examples were all supported by tripodal ligand frameworks that featured a few key design principles (Fig 5-1). The tripodal ligand systems were designed from a tris(2-aminoethyl)amine (tren) backbone, which was readily modified to incorporate hydrogen bond (H–bond) donors or acceptors in 2° coordination sphere, while providing sufficient steric bulk to isolate mononuclear metal complexes. The tren backbone also served to coordinate metal ions in a tetradentate fashion, which stabilized metal complexes both through the chelate effect[12] and the provision of a rigid ligand scaffold. Furthermore, the tren backbone can be deprotonated to provide a trianionic ligand field that supports high valent, high-spin metal complexes. High-spin metal ions are further favored by the local C_3 symmetry of the tripodal ligand frameworks, which effectively breaks the degeneracy of the t_{2g} *d*-orbital set observed in tetragonal coordination complexes by lowering the symmetry.[13,14] The C_3 symmetry within the tren backbone

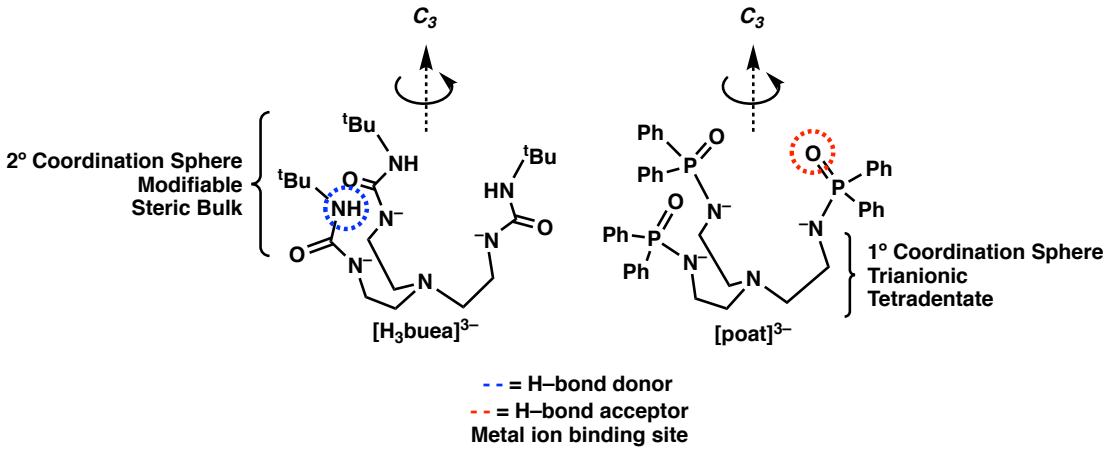

Figure 5-1: Representation of key design principles for C_3 symmetric tripodal ligand frameworks.

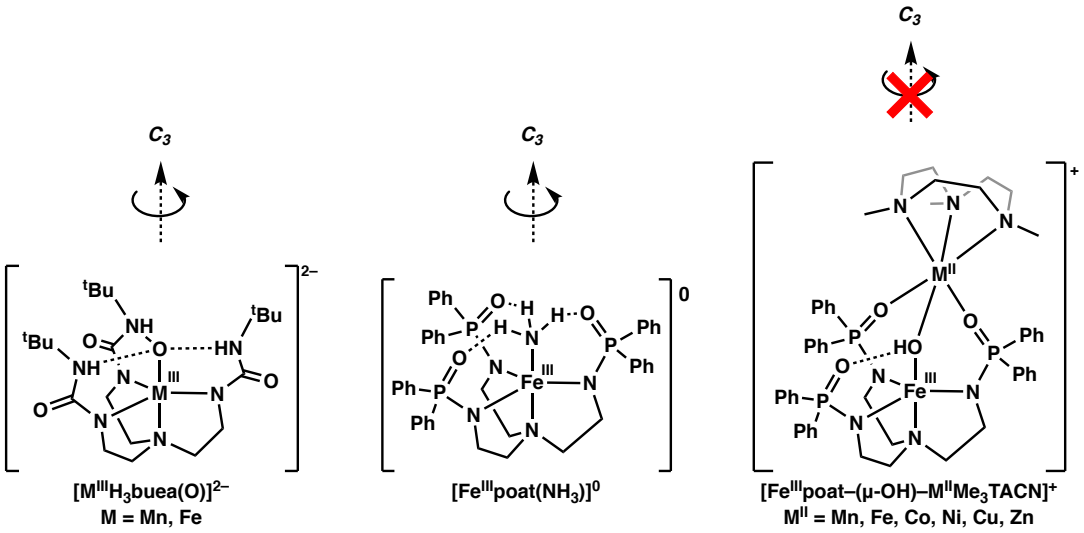

Figure 5-2: Representation of how C_3 symmetry is maintained in mononuclear metal complexes versus disrupted in bimetallic species.

is preserved within the whole ligand framework in the examples shown in Fig 5-1. However, this symmetry is readily disrupted through the introduction of a unique ligand arm, an exogenous ligand that is not C_3 symmetric, or a second metal ion. The overall C_3 symmetry of the complex can be preserved when the exogeneous ligand is also highly symmetric, like an oxido or ammine ligand, but introduction of a second metal ion consistently breaks this symmetry because the auxiliary metal ion interacts with only two of the ligand arms and the fifth ligand (Fig 5-2).[1,3–5,15–17] However, in early studies of the $[poat]^{3-}$ ligand framework, it was found that the P=O units can interact with a metal ion in the absence of an exogenous ligand (Fig 5-3).[18] The P=O groups from two units of a trigonal monopyramidal (TMP) Co^{II} complex, $[Co^{II}poat]^-$, interacted with a Ca^{II} ion forming a trimetallic species. While not rigorously C_3 symmetric, the complex exhibited a rough approximation of three-fold symmetry with all three P=O units of each $[Co^{II}poat]^-$ unit interacting with the Ca^{II} ion. This structure was not the desired product from the reaction, but the molecular structure presented a strategy through which discrete bimetallic complexes could be prepared while maintaining C_3 symmetry.

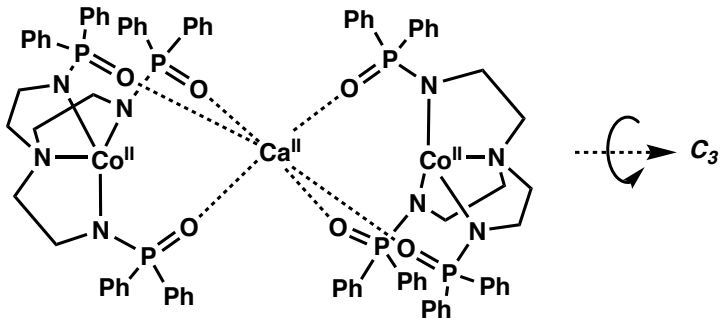

Figure 5-3: Structure of $Ca[Copoat]_2$, with the Ca ion supported only by P=O groups.

My interest in the preparation of C_3 symmetric metal complexes stems from work in the literature that suggested that C_3 symmetry may play a role in enhancing magnetic anisotropy in *3d* transition metal complexes, lending them unique magnetic properties.[19–30] Work by the Dunbar lab focused especially on investigating C_3 symmetric TMP and trigonal bipyramidal (TBP) complexes as candidates for single molecule magnets (SMMs).[23–25] In particular, TMP complexes were observed to exhibit slower magnetic relaxation and larger zero-field splitting (*D*) values than TBP complexes, partly attributed to larger deviations from ideal geometry in the TBP examples.[19,23] SMMs are highly sensitive to coordination environments, where small geometric deviations leads to a decrease in the magnitude of the *D* values and affects magnetic relaxation.[19–21,23–25,27,31,32] To this end, previously characterized TMP complexes from the Borovik lab were studied by others as possible SMMs (Fig 5-4).[6,19,23,33,34] In these examples, distortion from an idealized TMP geometry greatly affected the *D* values and magnetic behavior of the complexes. Notably, the $[Ni^{II}MST]^-$ complex exhibited a large *D*-value of –530 cm^{-1} and rigorous adherence to ideal geometry. Given how greatly geometric deviations affect magnetic behavior, it is desirable to design molecules that rigorously maintain symmetry. To this end, the example discussed in Figure 5-3 is promising because the incorporation of a second metal ion effectively locks the P=O units in place and rigidifies the overall complex, enforcing precise C_3 symmetry.

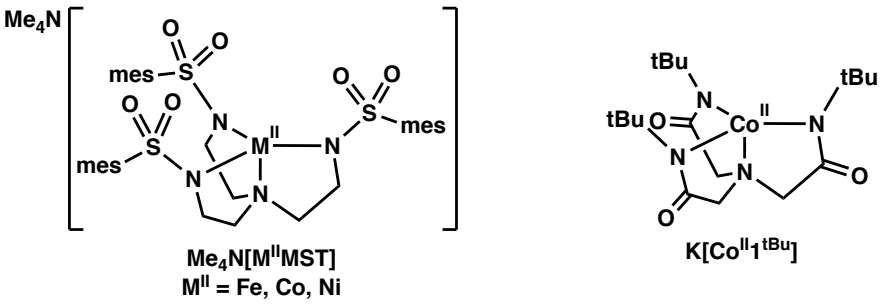

Figure 5-4: Examples of TMP coordination complexes developed by the Borovik lab that have had their magnetic behavior subsequently studied. Note that the $Me_4N[NiMST]$ system was separately prepared and characterized by the Dunbar lab.

Further work focused on the development of SMMs through the design of molecules with large spin states. The earliest example of a SMM was $[Mn_{12}O_{12}(OAc)_{16}(H_2O)_4]$, referred to as Mn12, which had a spin-state of $S = 10$.[35] The trinuclear complex shown in Figure 5-3 demonstrates how multiple metal ions can be incorporated in a single molecule, presenting the opportunity to incorporate additional paramagnetic centers

while maintaining symmetry. This strategy may further improve the magnetization of the complexes by increasing the overall spin (*S*) of the molecule.

This chapter describes the preparation of rigorously C_3 symmetric bimetallic complexes with the following motif: $[M_x^{II}poat\cdots M_y^{II}Me_3tacn]^+$ that crystallize in the highly symmetric $R\bar{3}$ space group. While these bimetallic complexes have been most comprehensively studied in examples where M_x = Co, this motif has been extended to a variety of metal ions where M_x = Mn, Co, and Zn and M_y = Mn, Fe, Co, Cu, and Zn. The preparation of these complexes is straightforward and could likely be adapted for a wider array of *3d* metal ions. In addition to a thorough investigation of the structural properties of $[M_x^{II}poat\cdots M_y^{II}Me_3tacn]^+$ species, these complexes have been studied spectroscopically to evaluate their electronic absorption and magnetic properties, through both electron paramagnetic resonance (EPR), Evans' method, and superconducting quantum interference device (SQUID) magnetometry. The magnetism indicated that the two metal ions are weakly ferromagnetically coupled, which provides insight into how the P=O units may contribute to magnetic coupling. Furthermore, some of the $[Co^{II}poat\cdots M_y^{II}Me_3tacn]^+$ species were investigated for SMM behavior, though preliminary evidence does not suggest that these complexes behave as SMMs.

Results and Discussion

Synthesis and Structural Analysis

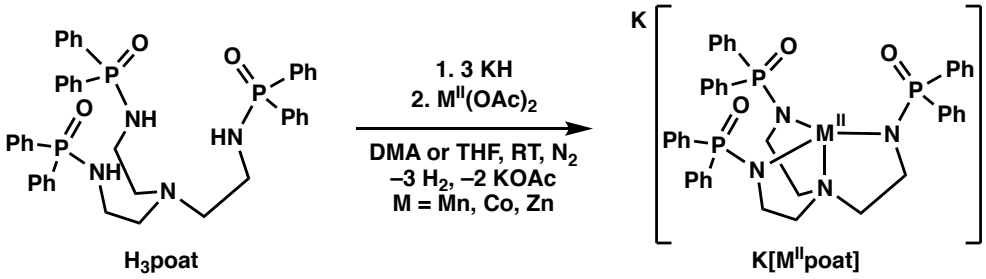

Scheme 5-1: General synthetic procedure for the preparation of trigonal monopyramidal coordination complexes, where M^{II} = Mn, Co, Zn.

Synthesis of mononuclear precursors: A set of trigonal monopyramidal (TMP) coordination complexes were prepared to act as a synthon for the assembly of the C_3-symmetric bimetallic species discussed above (Scheme 5-1). Similar to the synthesis of $K[Co^{II}poat]$ discussed in Chapter 3 of this dissertation, $K[Mn^{II}poat]$ and $K[Zn^{II}poat]$ were prepared. A molecular structure for $K[Mn^{II}poat]$ has not been successfully obtained, therefore any work with this complex was carried out on isolated powder. The purity of powdered $K[Mn^{II}poat]$ was evaluated by

elemental analysis. K[Zn^{II}poat], however, was isolated as crystalline material. X-ray diffraction analysis revealed that K[Zn^{II}poat] was isomorphous to K[Co^{II}poat] (Fig 5-5). K[Zn^{II}poat] also crystallized as a dinuclear unit, where two molecules interacted through the P=O units and K^+ counterions. The $K^+\cdots$O=P interactions effectively shield each Zn^{II} site, ensuring the TMP coordination environment. K[Zn^{II}poat] was more rigorously TMP than K[Co^{II}poat], with the Zn^{II} ion puckered less out of the equatorial plane (0.159 Å) than the Co^{II} center (0.176 Å).

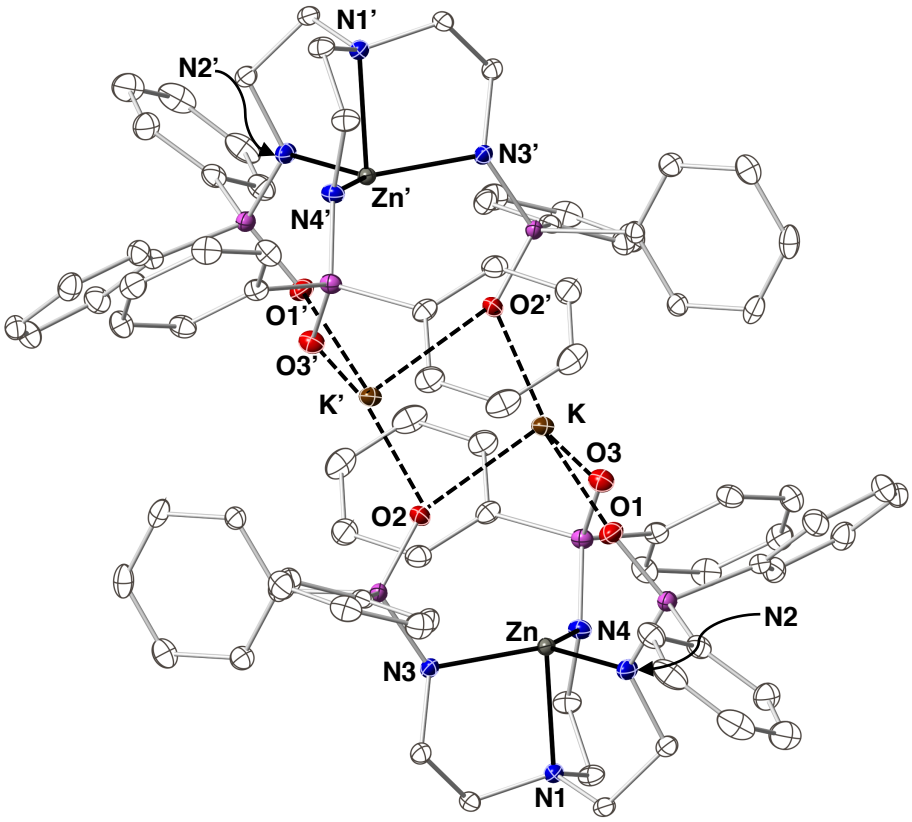

Figure 5-5: Molecular structure of (K[Zn^{II}poat])$_2$ with thermal ellipsoid representation. Thermal ellipsoids are drawn at 50% probability. All H-atoms were omitted for clarity.

Table 5-1: Metrical data obtained from the molecular structure of (K[Zn^{II}poat])$_2$.

Bond	Distance, Å
Zn–N1	2.157(1)
Zn–N2	1.968(2)
Zn–N3	1.990(1)
Zn–N4	1.967(2)
Zn···K	3.8015(5)
Atoms	**Angles, °**
N1–Zn–N2	85.55(6)
N1–Zn–N3	85.03(6)
N1–Zn–N4	85.53(6)
N2–Zn–N3	122.22(6)
N2–Zn–N4	119.94(6)
N3–Zn–N4	115.92(6)
$N_{eq}\cdots$Zn, 0.159 Å	

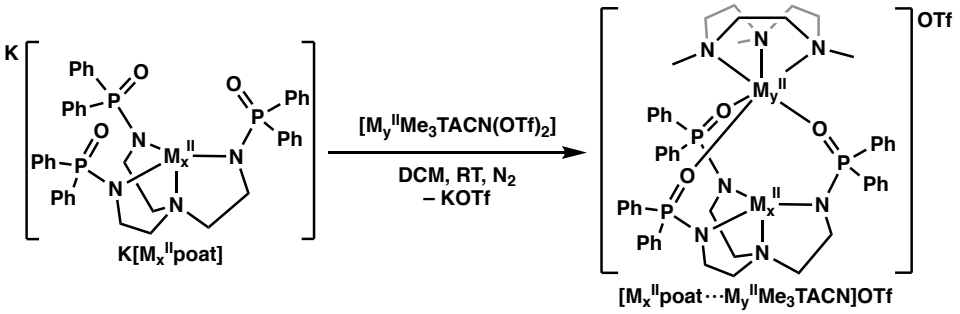

Scheme 5-2: General synthetic procedure for the preparation of *C*$_3$ symmetric bimetallic coordination complexes, where M_x = Mn, Co, Zn and M_y = Mn, Fe, Co, Cu, and Zn.

Synthesis of bimetallic complexes: Following preparation and characterization of the TMP coordination complexes (Scheme 5-1), a series of bimetallic complexes were prepared following the synthetic procedure outlined in Scheme 5-2. In a representative experiment, the TMP starting complex was dissolved in dichloromethane (DCM). An equimolar amount of solid [M_y^{II}Me$_3$tacn(OTf)$_2$] salt was then added slowly as a solution in DCM to the dissolved K[M^{II}poat] to prevent the formation of a trimetallic species, similar to the complex described in Figure 5-3 and products frequently prepared with the Kläui ligand.[18,36–39] When [M^{II}Me$_3$tacn(OTf)$_2$] was added to solutions of K[Co^{II}poat], slight color changes were observed that were not apparent with K[Mn^{II}poat] and K[Zn^{II}poat]. After stirring the reaction for ~30 minutes, the reaction mixture was filtered to remove any residual solids. Finally, the filtrate was recrystallized by vapor diffusion of Et_2O into the DCM mother liquor. These bimetallic species crystallized in good yield, with little color remaining from the mother liquor and yields ranging between ~50 – 90 %. Furthermore, the crystalline products exhibited a unique crystal morphology and appeared feathery in shape (Fig 5-6), as opposed to the blue blocky crystals typically observed for K[Co^{II}poat].

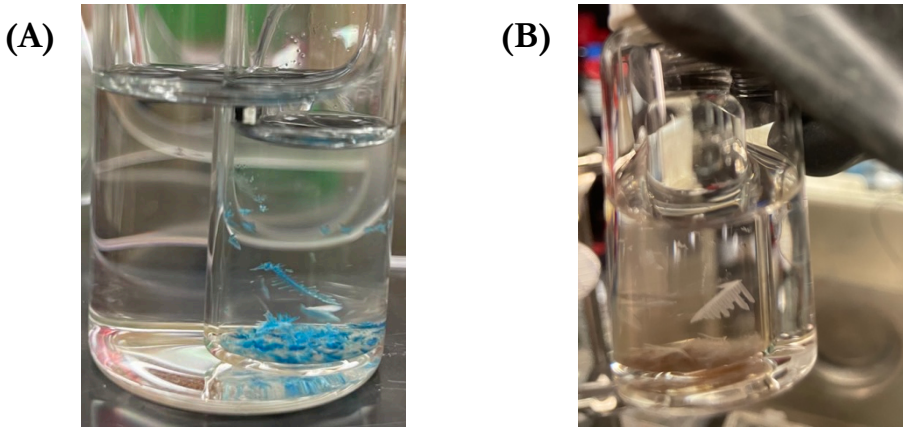

Figure 5-6: Crystalline products obtained from the preparation of [Co^{II}poat···Zn^{II}Me$_3$tacn]OTf **(A)** and [Zn^{II}poat···Zn^{II}Me$_3$tacn]OTf **(B)**.

The molecular structure of these species revealed the formation of a bimetallic complex with the general formulation: $[M_x^{II}poat\cdots M_y^{II}Me_3tacn]^+$. The $[M_x^{II}poat\cdots M_y^{II}Me_3tacn]^+$ complexes, abbreviated $[M_x^{II}\cdots M_y^{II}]^+$, crystallized in the $R\bar{3}$ space group and therefore exhibited trigonal symmetry. The metal ion within the $[poat]^{3-}$ backbone was 4-coordinate with a TMP coordination geometry and an open coordination site in the axial position. The bond lengths between M_x and the N-atoms varied slightly between bimetallic complexes, however the M_x–N1 bond lengths were all above 2.0 Å and the M_x–N2 distance were below 2.0 Å, except when M_x = Mn (Table 5-2). The open axial site, where a fifth ligand would coordinate in a TBP complex, was shielded due to the coordination of the second metal ion, M_y, to the P=O groups of the $[M_x^{II}poat]^-$ unit. The angle between the equatorial N-atoms (N2–M_x–N2) was close ~ 119.5º when M_x = Co or Zn, but was smaller when M_x = Mn (~ 117.6 º; Table 5-2, *vide infra*). The angle formed between the axial and equatorial N-atoms (N1–M_x–N2) varied based on the identity of M_x (Table 5-2, *vide infra*). This angle, accompanied by the puckering of M_x out of the equatorial plane ($M_x\cdots N_{eq}$, Table 5-1), determined the geometric distortion away from an ideal TMP geometry. $[Mn^{II}poat]^-$ was the most distorted away from an ideal TMP geometry ($Mn\cdots N_{eq}$ = 0.325 Å, N1–M_x–N2 = 81.02(5) Å); this distortion may suggest that a TMP geometry is not favored for Mn^{II} ions, which could explain why $K[Mn^{II}poat]$ has not been successfully crystallized. When M_x = Co, the $[Co^{II}poat]^-$ units appeared closer to an ideal TMP geometry ($Co\cdots N_{eq}$, avg = 0.143 Å, N1–M_x–N2, avg = 85.83 Å). In comparison to the $[Co^{II}MST]^-$ analogue studied by the Dunbar lab for SMM behavior, all of the bimetallic complexes where M_x = Co were more rigorously TMP.

For all examples of $[M_x^{II}\cdots M_y^{II}]^+$, M_y was in a 6-coordinate ligand field. M_y was bound in a facial manner to the O-atoms of the P=O groups, forming three triple-atom N–P=O bridge between the two metal centers (M_x, M_y). The coordination of the N–P=O units to M_y shielded the M_x center, which preserved its TMP geometry. The N–P=O bridges provided a limited range of flexibility, constraining the two metal ions to $M_x\cdots M_y$ distances between ~ 3.23 and 3.44 Å (Table 5-1). The remaining M_y coordination sites were occupied by the Me_3tacn ligand, which capped the other octahedral face of M_y. While the ligands around M_y were bound facially, the complex was distorted away from an ideal octahedral arrangement, with the O1–M_y–N3, trans angle considerably less than 180º (~ 165 – 170 Å, Table 5-2).

In comparing $[M_x^{II}poat\cdots M_y^{II}Me_3tacn]^+$ complexes, the coordination motif remained constant, while the bond lengths and angles varied based on the metal ion. All M_y–O1 distances were ~ 2.1 Å. However, the M_y–N3 bond lengths exhibited more variation. Most of the metal ions (M_y = Zn^{II}, Cu^{II}, Co^{II}, Fe^{II}) exhibited M_y–N3 bond lengths ~ 2.2 Å, but when M_x = Mn^{II} the M_y–N3 bond lengths were above 2.3 Å. Furthermore, the N3–M_y–N3 and O1–M_y–N3 bond angles were considerably smaller when M_y = Mn^{II}, suggesting that the Mn^{II} center was also distorted in the 6-coordinate 3 N/3 O donor environment, similar to the geometric deviations observed in $[Mn^{II}poat]^-$. This distortion could be due to the Mn possessing the largest ionic radius of all metal ions studied in this series.[40]

Table 5-2: Metrical data describing relevant bond metrics and atomic distances in the isomorphous molecular structures $[M_x^{II}poat\cdots M_y^{II}Me_3tacn]^+$. $M_x\cdots N_{eq}$ describes the distance between M_x from the plane formed by the equatorial N-atoms, N2.

Compound	**Atomic Distance, Å**					
$[M_x^{II}\cdots M_y^{II}]^+$	**M_x–N1**	**M_x–N2**	**M_y–O1**	**M_y–N3**	**$M_x\cdots M_y$**	**$M_x\cdots N_{eq}$**
$[Co^{II}\cdots Zn^{II}]^+$	2.108(4)	1.962(2)	2.084(2)	2.206(3)	3.4099(8)	0.145
$[Co^{II}\cdots Cu^{II}]^+$	2.102(7)	1.960(4)	2.104(3)	2.176(5)	3.428(2)	0.141
$[Co^{II}\cdots Co^{II}]^+$	2.103(5)	1.959(3)	2.096(2)	2.182(3)	3.423(1)	0.142
$[Co^{II}\cdots Fe^{II}]^+$	2.103(4)	1.960(2)	2.105(2)	2.236(3)	3.3647(9)	0.147
$[Co^{II}\cdots Mn^{II}]^+$	2.095(4)	1.961(3)	2.125(2)	2.316(3)	3.377(1)	0.138
$[Mn^{II}\cdots Mn^{II}]^+$	2.253(3)	2.086(2)	2.131(2)	2.300(2)	3.226(1)	0.325
$[Zn^{II}\cdots Zn^{II}]^+$	2.122(4)	1.978(2)	2.083(2)	2.207(3)	3.440(1)	0.111

Table 5-3: Metrical data describing relevant bond angles in the isomorphous molecular structures $[M_x^{II}poat\cdots M_y^{II}Me_3tacn]^+$. The O1–$M_x$–N3 describes the angle formed between O1 and the N-atom trans to O1 in the Me_3tacn ligand framework

Compound	**Bond Angles, °**				
$[M_x^{II}\cdots M_y^{II}]^+$	**N1–M_x–N2**	**N2–M_x–N2**	**O1–M_y–O1**	**N3–M_y–N3**	**O1–M_y–N3**
$[Co^{II}\cdots Zn^{II}]^+$	85.77(6)	119.46(2)	97.15(7)	80.92(11)	168.53(9)
$[Co^{II}\cdots Cu^{II}]^+$	85.88(13)	119.49(3)	96.48(13)	81.8(2)	169.6(2)
$[Co^{II}\cdots Co^{II}]^+$	85.84(9)	119.48(2)	96.70(9)	81.35(14)	169.15(13)
$[Co^{II}\cdots Fe^{II}]^+$	85.70(7)	119.44(2)	99.06(7)	80.13(12)	166.54(10)
$[Co^{II}\cdots Mn^{II}]^+$	85.96(7)	119.51(2)	99.38(8)	77.44(14)	164.51(11)
$[Mn^{II}\cdots Mn^{II}]^+$	81.02(5)	117.61(3)	96.36(7)	77.88(11)	167.09(8)
$[Zn^{II}\cdots Zn^{II}]^+$	86.77(7)	119.69(1)	96.94(8)	80.89(12)	168.66(11)

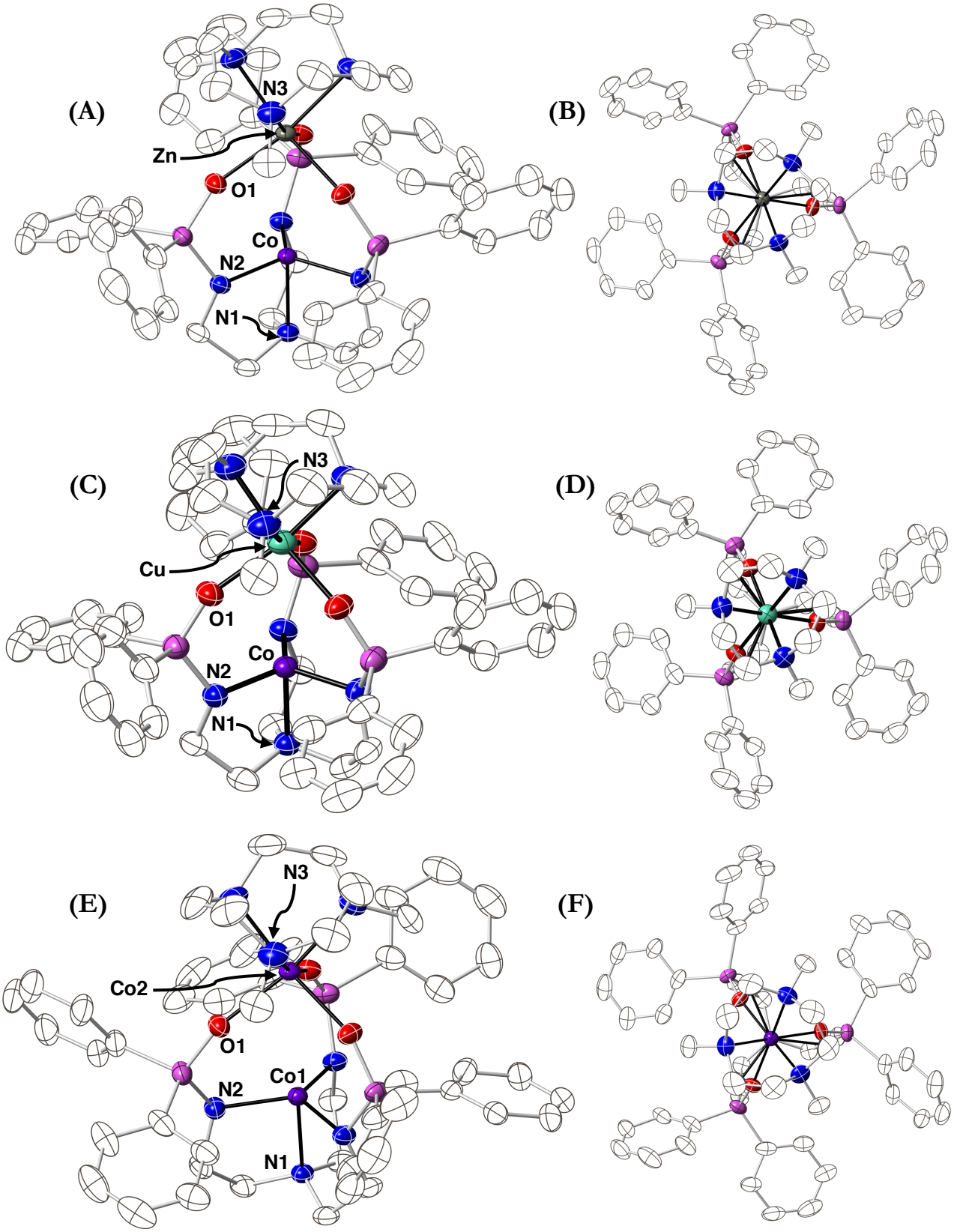

Figure 5-7: (A), (C), (E) show the molecular structures of $[Co^{II}\cdots Zn^{II}]^+$, $[Co^{II}\cdots Cu^{II}]^+$, and $[Co^{II}\cdots Co^{II}]^+$. **(B), (D), (F)** depict the view along the C_3 axis of $[Co^{II}\cdots Zn^{II}]^+$, $[Co^{II}\cdots Cu^{II}]^+$, and $[Co^{II}\cdots Co^{II}]^+$. Thermal ellipsoids are drawn at 50% probability. The ^-OTf ion and H-atoms was omitted for clarity.

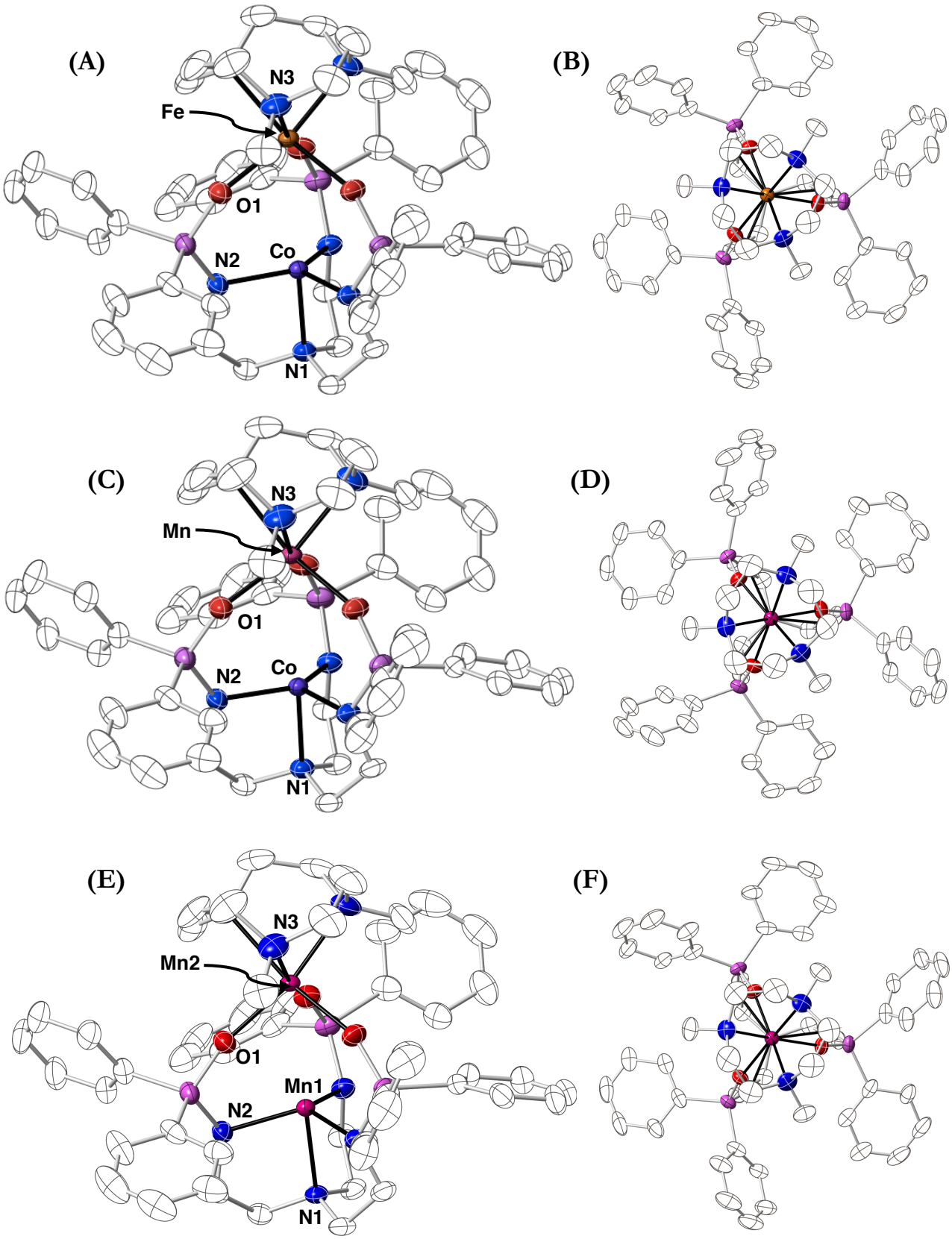

Figure 5-8: (A), (C), (E) show the molecular structures of $[Co^{II}\cdots Fe^{II}]^{+}$, $[Co^{II}\cdots Mn^{II}]^{+}$, and $[Mn^{II}\cdots Mn^{II}]^{+}$. **(B), (D), (F)** depict the view along the C_3 axis of $[Co^{II}\cdots Fe^{II}]^{+}$, $[Co^{II}\cdots Mn^{II}]^{+}$, and $[Mn^{II}\cdots Mn^{II}]^{+}$. Thermal ellipsoids are drawn at 50% probability. The $^{-}$OTf ion and H-atoms were omitted for clarity.

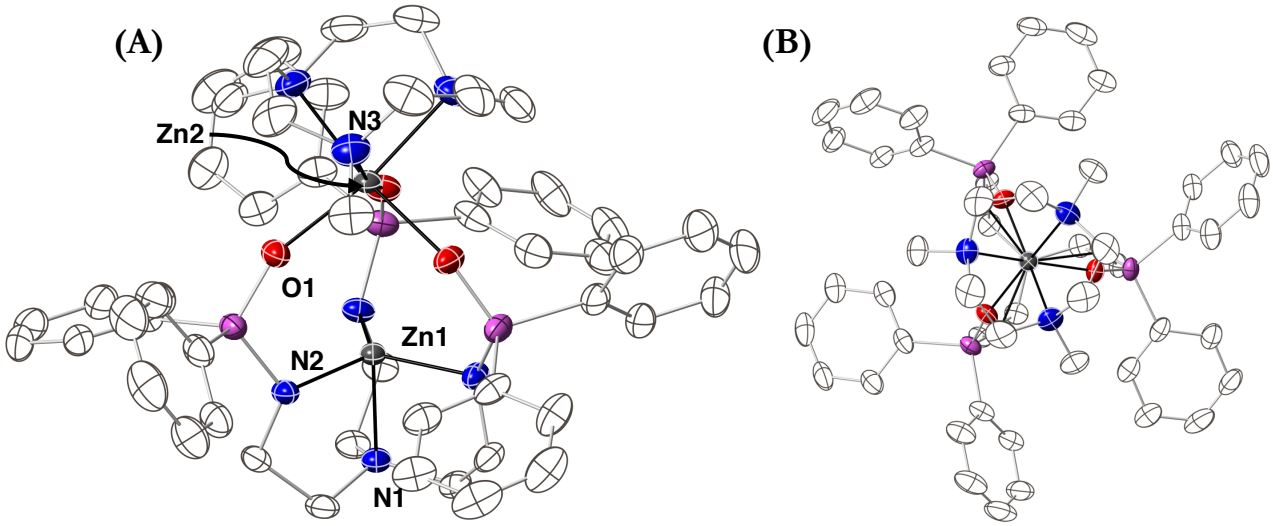

Figure 5-9: (A), show the molecular structures of $[Zn^{II}\cdots Zn^{II}]^{+}$. **(B)** depict the view along the C_3 axis of $[Zn^{II}\cdots Zn^{II}]^{+}$. Thermal ellipsoids are drawn at 50% probability. The OTf ion and H-atoms were omitted for clarity.

Characterization of bimetallic species:

Electronic absorption spectroscopy: UV-vis studies were carried out on the $[M_x^{II}poat\cdots M_y^{II}Me_3tacn]^{+}$ complexes. The absorption spectra of the $[Mn^{II}\cdots Mn^{II}]^{+}$ and $[Zn^{II}\cdots Zn^{II}]^{+}$ complexes were featureless in the visible spectrum, therefore the analysis will focus on the series of complexes where $M_x = Co^{II}$. For the $[Co^{II}\cdots Mn^{II}]^{+}$, $[Co^{II}\cdots Fe^{II}]^{+}$, and $[Co^{II}\cdots Zn^{II}]^{+}$ complexes, the absorption spectra were only subtly different from the absorption features of $K[Co^{II}poat]$ (Fig 5-10). The similarity between the spectral features of $[Co^{II}\cdots Mn^{II}]^{+}$, $[Co^{II}\cdots Fe^{II}]^{+}$, and $[Co^{II}\cdots Zn^{II}]^{+}$ to $K[Co^{II}poat]$ was likely because the starting $[M^{II}Me_3tacn(OTf)_2]$ complexes were added as white or off-white powders, which were colorless in solution and featureless in the UV-vis spectrum.[4,5,41] The more intense absorbance features from $K[Co^{II}poat]$ (λ_{max} = 585, 610 nm) were shifted to slightly higher energies in $[Co^{II}\cdots Mn^{II}]^{+}$, $[Co^{II}\cdots Fe^{II}]^{+}$, and $[Co^{II}\cdots Zn^{II}]^{+}$, by ~ 15 nm (~ 450 cm^{-1}, 0.0558 eV; Fig 5-10). This subtle shift was observed in a similar system, where a Ca^{II} ion was observed to interact with a TMP Co^{II} complex through the sulfonamido oxygen atoms of $[MST]^{3-}$.[6] The spectra obtained by *in situ* generation of $[Co^{II}\cdots M_y^{II}]^{+}$ species were similar in shape to $K[Co^{II}poat]$, however the spectral features appeared sharper when redissolved crystalline material was used. For example, in Fig 5-10 B, the most intense features from redissolved crystalline $[Co^{II}\cdots Zn^{II}]^{+}$ between 500 and 600 nm were notably sharper than *in situ* generated $[Co^{II}\cdots Zn^{II}]^{+}$ (Fig 5-10 A).

When $[Cu^{II}Me_3tacn(OTf)_2]$ · 2 MeCN or $[Co^{II}Me_3tacn(OTf)_2]$ complex was used to prepare a $[Co^{II}\cdots M_y^{II}]^+$ complex, the resulting UV-vis spectra were more complex, with absorption features from both metal centers (Fig 5-11). The $[Co^{II}\cdots Co^{II}]^+$ spectrum exhibited features from each Co^{II} center, which seemed to be additive from the two parent metal complexes. The starting $[Co^{II}Me_3tacn(OTf)_2]$ complex had previously only been characterized from *in situ* preparation,[3] but I have since successfully characterized and crystallized this complex (Fig 5-S2), which formed a dinuclear species in the solid state: $[(Co^{II}Me_3tacn)_2(OTf)_3]OTf$. Each Co^{II} center was coordinated by a Me_3tacn ligand and three triflate anions that bridged between the metal centers. The complex was a +1 salt, with an outer sphere triflate anion. The coordination environment of $[(Co^{II}Me_3tacn)_2(OTf)_3]OTf$ was similar to examples of dinuclear species crystallized by the Wieghardt lab, where each metal ion was coordinated to a Me_3tacn ligand with three bridging anions between the metal centers. An example of these complexes can be found in Chapter 3 (Fig 3-1).[42] In DCM, $[(Co^{II}Me_3tacn)_2(OTf)_3]OTf$ exhibited features at λ_{max} = 370, 480, 517, 543, ~1100 nm (Fig 5-S3). The low energy band ~1100 nm appeared near the detection limit of the spectrophotometer and could not be fully observed, therefore the assignment of this wavelength is tentative. The $[Co^{II}\cdots Co^{II}]^+$ complex exhibited features at λ_{max} = 410, 493, 570, 582, 595, 725, 775, ~1100 (Fig 5-11B). The feature at λ_{max} ~1100 nm was observed in both $[Co^{II}\cdots Co^{II}]^+$ and $[(Co^{II}Me_3tacn)_2(OTf)_3]OTf$. Additionally, the features between 570 – 595 nm were similar to features observed in $K[Co^{II}poat]$ and other $[Co^{II}\cdots M_y^{II}]^+$ complexes. Finally, $[Co^{II}\cdots Cu^{II}]^+$ had bands at λ_{max} = 446, 590, 779 nm (Fig 5-11D). $[Cu^{II}Me_3tacn(OTf)_2]$ · 2 MeCN exhibited a band at λ_{max} = 771 nm,[43] similar to the feature at λ_{max} = 779 nm seen in $[Co^{II}\cdots Cu^{II}]^+$. The feature at λ = 590 nm appeared similar to the starting $K[Co^{II}poat]$ spectrum. The origin of the band at 446 nm is unknown and unique to $[Co^{II}\cdots Cu^{II}]^+$, causing the complex to appear a deep, yellow-green color.

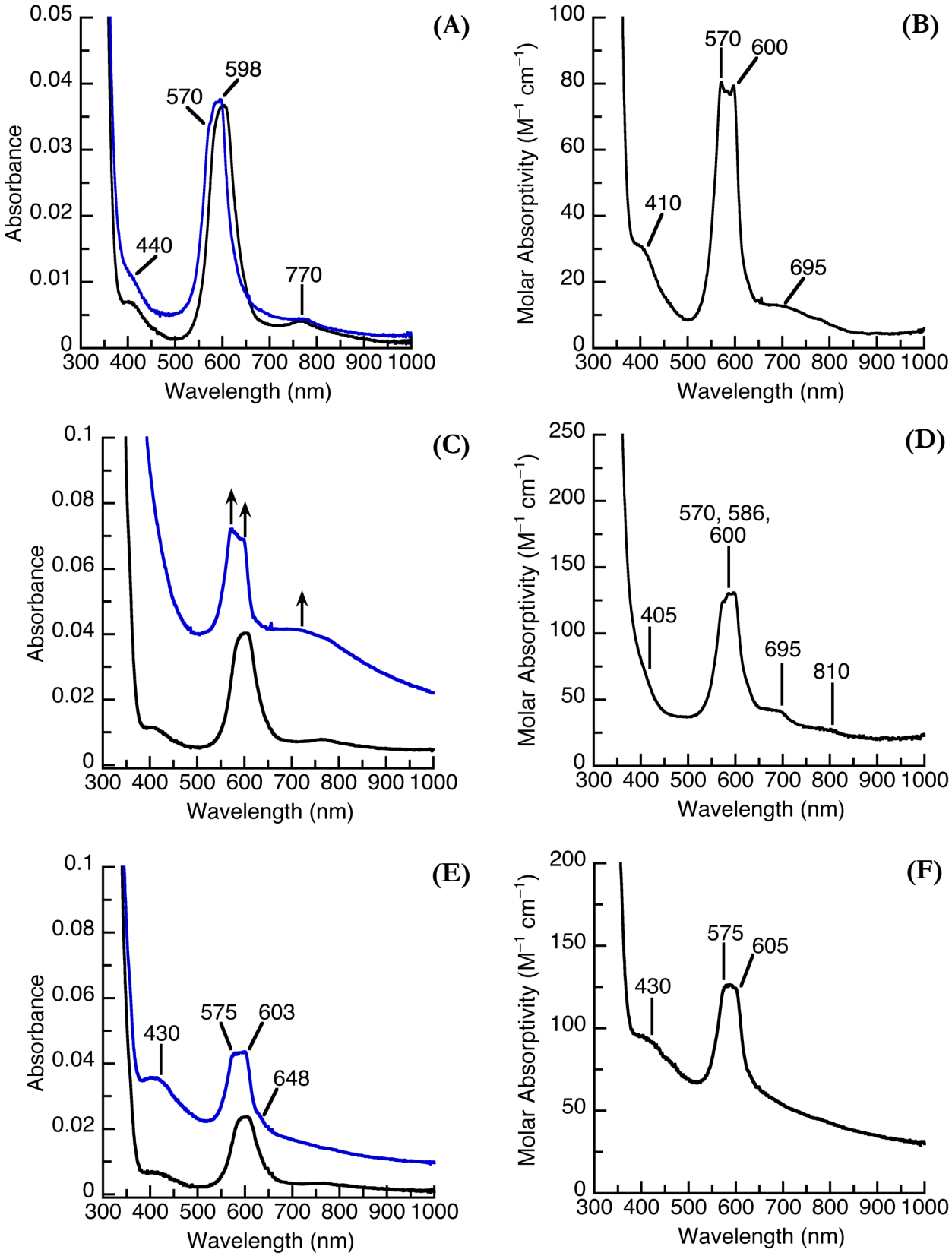

Figure 5-10: UV-vis spectra following the addition of [$Zn^{II}Me_3tacn(OTf)_2$] **(A)**, [$Fe^{II}Me_3tacn(OTf)_2$] **(C)**, and [$Mn^{II}Me_3tacn(OTf)_2$] **(E)** to solutions of K[$Co^{II}poat$]. The baseline jump in **(C)** was likely due to accidental O_2 exposure in the experimental setup. UV-vis spectra obtained from crystalline [$Co^{II}\cdots Zn^{II}]^+$. **(B),** [$Co^{II}\cdots Fe^{II}]^+$ **(D),** and [$Co^{II}\cdots Mn^{II}]^+$ **(F).** The baseline increases in **(E)** and **(F)** were likely due to solubility issues of [$Co^{II}\cdots Mn^{II}]^+$.

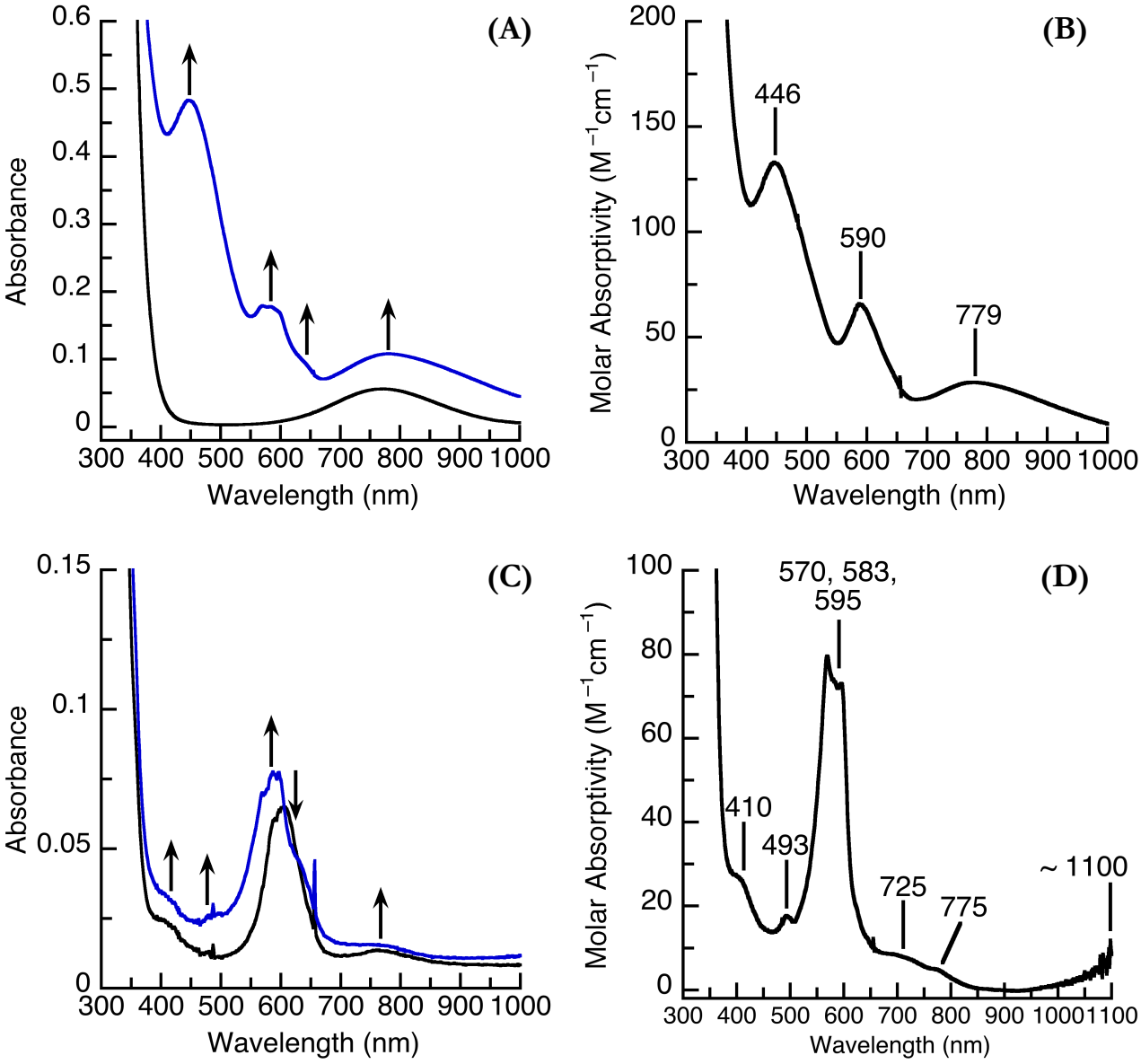

Figure 5-11: (A) UV-vis spectra following the addition of K[Co^{II}poat] to a solution of [Cu^{II}Me$_3$tacn(OTf)$_2$] · 2 MeCN. The blue trace was [Co^{II}···Cu^{II}]$^+$ formed *in situ*. **(B)** Molar absorptivity data measured for [Co^{II}···Cu^{II}]$^+$. **(C)** UV-vis spectra following the addition of [(Co^{II}Me$_3$tacn)$_2$(OTf)$_3$]OTf to a solution of K[Co^{II}poat] (black). **(D)** Molar absorptivity data measured for [Co^{II}···Co^{II}]$^+$. All spectra were measured at room temperature in DCM.

Magnetic Studies: One goal of this project was to better understand the role that N–P=O bridging units play in facilitating magnetic interactions in bimetallic systems supported by [poat]$^{3-}$, as well as investigating how rigorous C_3 symmetry may affect the magnetism of these systems, with an eye towards evaluating their candidacy as SMMs. Therefore, the magnetic behavior of the [M$_x^{II}$poat···M$_y^{II}$Me$_3$tacn]$^+$ complexes was studied through EPR spectroscopy, as well as Evans' method NMR spectroscopy, and SQUID magnetometry. Initial

experiments were carried out with the $[Co^{II}\cdots Zn^{II}]^+$ system. Because Zn^{II} is a d^{10}, diamagnetic metal ion, $[Co^{II}\cdots Zn^{II}]^+$ effectively acts as a control for the remaining $[Co^{II}poat]^-$ based systems, allowing us to understand how the binding of a second metal ion through the N–P=O units affects the Co^{II} center. ⊥-mode EPR spectra were collected on both solid and solution samples of $[Co^{II}\cdots Zn^{II}]^+$. The solid and solution measurements were in good agreement with another, which confirmed that $[Co^{II}\cdots Zn^{II}]^+$ remained intact in solution, though the signal was broader in the solid sample. The ⊥-mode EPR spectra were consistent with a $S = 3/2$ spin system (Fig 5-12). The overall rhombicity of the complex was E/D = 0.0029, which was the same value obtained from the simulation of the starting $K[Co^{II}poat]$ complex. It had been hypothesized, based on the symmetry of $[Co^{II}\cdots Zn^{II}]^+$, that the EPR spectrum would be more axial, with an E/D value closer to 0. However, as discussed in previous chapters, Co^{II} species in C_3 symmetry tend to be relatively insensitive to changes in the ligand field (e.g. TMP versus TBP) and consistently exhibit near axial spectra.[44,45] The simulations did reveal a slight increase in the D-value of $[Co^{II}\cdots Zn^{II}]^+ = +5.6$ cm^{-1}, versus the +3.6 cm^{-1} value obtained from $K[Co^{II}poat]$. Additionally, there was a noticeable increase in the hyperfine coupling constant from the ^{59}Co nucleus, from ~ 260 MHz in $K[Co^{II}poat]$ to 280 MHz in $[Co^{II}\cdots Zn^{II}]^+$. The Evans' method NMR spectrum of $[Co^{II}\cdots Zn^{II}]^+$ exhibited measured μ_{eff} value of 4.89 μ_B (μ_o, $S = 3/2$, 3.87 μ_B). While the effective magnetic moment

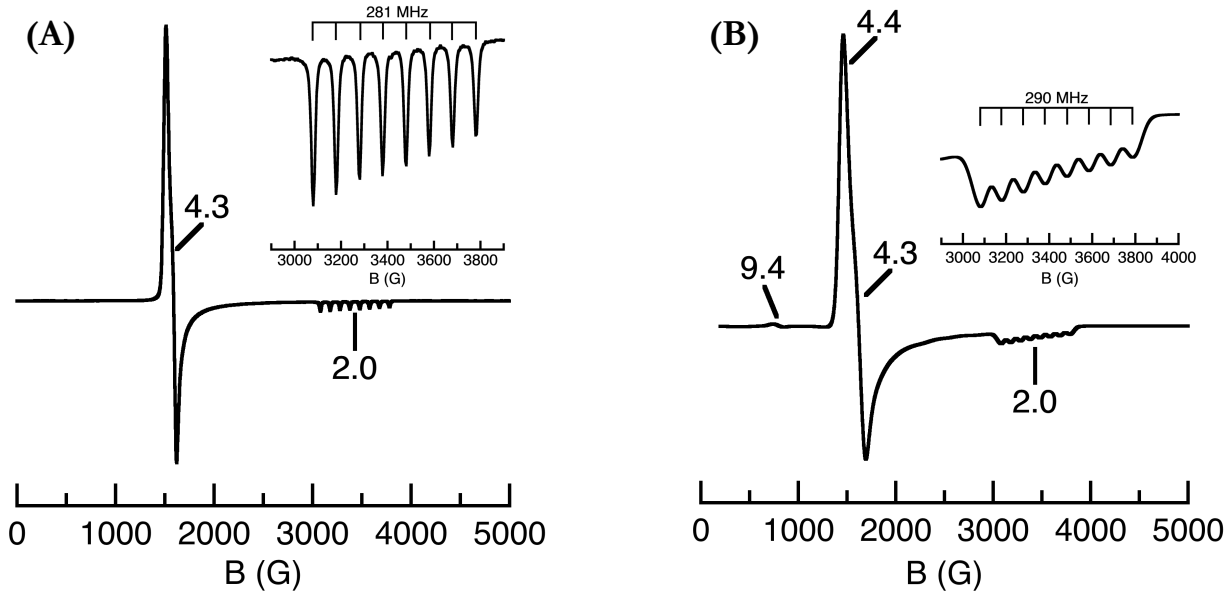

Figure 5-12: (A) ⊥-mode EPR spectrum obtained from $[Co^{II}\cdots Zn^{II}]^+$ measured in DCM:THF at 15 K. **(B)** ⊥-mode EPR spectrum measured from solid, crystalline $[Co^{II}\cdots Zn^{II}]^+$ at 20 K.

was larger than expected for a $S = 3/2$ spin system, this distortion is common for Co^{II} ions due to spin-orbit coupling contributions.[34,46] Finally, $[Co^{II}\cdots Zn^{II}]^{+}$ was studied using SQUID magnetometry in collaboration with the Rinehart lab at UC San Diego (Fig 5-13). The zero-field cooled (ZFC) magnetic susceptibility curve (Fig 5-13 A) exhibited a small slope upwards at lower field, which flattened at higher fields, suggesting that the sloping may have been due to a slight ferromagnetic impurity, possibly due to contamination from some adventitious metal in the dry box environment or during synthesis. Isothermal magnetization plots were collected at 2 and 100 K (Fig 5-13 B). At 2 K, $[Co^{II}\cdots Zn^{II}]^{+}$ exhibited a butterfly shape hysteretic loop which closed at 100 K. The data collected suggested that $[Co^{II}\cdots Zn^{II}]^{+}$ behaved as a typical paramagnet and did not exhibit the independent, permanent magnetization characteristic of SMMs. For SMMs, independent permanent magnetization persists at low temperatures, which can be identified through open hysteresis loops measured from isothermal magnetization plots. Therefore, $[Co^{II}\cdots Zn^{II}]^{+}$ was eliminated as a candidate for SMMs. It is unclear why $[Co^{II}\cdots Zn^{II}]^{+}$ did not act as a SMM, despite its more rigorous C_3 symmetry and lower $Co^{II}\cdots N_{eq}$ puckering versus the $[Co^{II}MST]^{-}$ complex studied by the Dunbar lab, which attributed its magnetic behavior in part to its low geometric distortion.

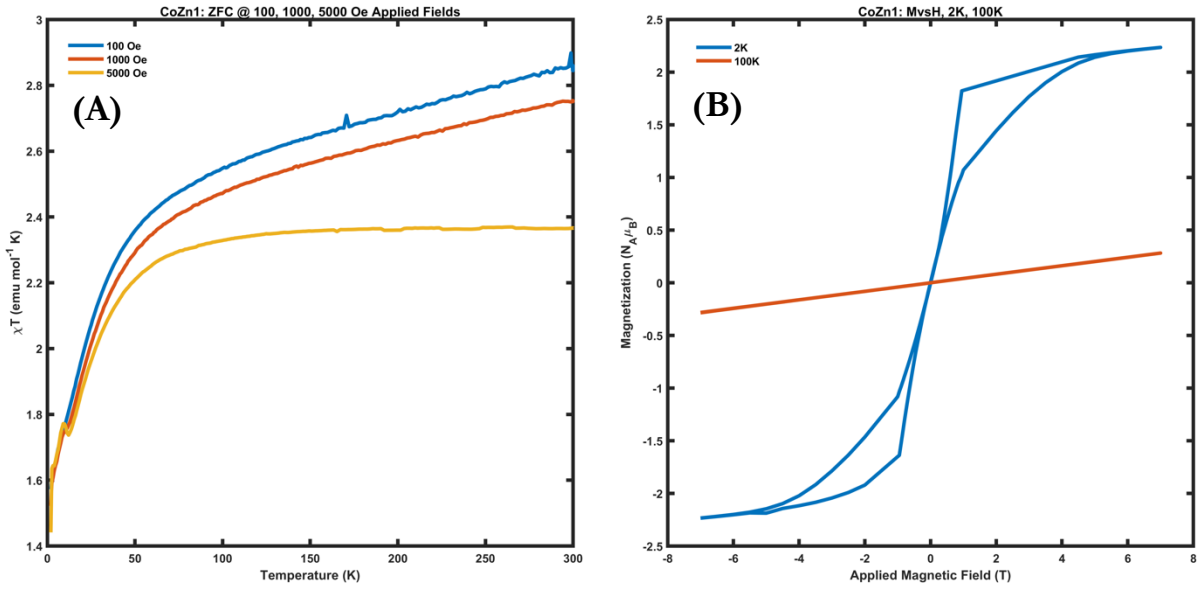

Figure 5-13: (A) ZFC thermal magnetic susceptibility plots of $[Co^{II}\cdots Zn^{II}]^{+}$ collected between 2 – 300 K under varying fields. 100 Oe is shown in blue, 1000 Oe in red, and 5000 Oe in yellow. **(B)** Isothermal magnetization plots shown at 2 K (blue) and 100 K (red).

$[Co^{II}\cdots Cu^{II}]^+$ was also studied by ⊥-mode EPR spectroscopy (Fig 5-14). The data has thus far only been collected at 77 K from *in situ* generated samples. These measurements indicated the formation of a ⊥-mode EPR-silent species, consistent with magnetic interaction between the two half-integer spin metal ions (Cu^{II}: $S = 1/2$; Co^{II}: $S = 3/2$). There were some residual signals at ~ g = 4 and 2, possibly due to incomplete reaction of the starting materials. An overlay of the $[Co^{II}\cdots Cu^{II}]^+$ with the starting $[Cu^{II}Me_3tacn(OTf)_2] \cdot 2$ MeCN is shown in Figure 5-14B, which demonstrates that the residual signal was negligible in comparison to the $[Cu^{II}Me_3tacn(OTf)_2] \cdot 2$ MeCN starting material, suggesting that the majority of the complex had coordinated to $[Co^{II}poat]^-$. Notably, the preparation of $[Co^{II}\cdots Cu^{II}]^+$ was observed to proceed more slowly than the other $[M_x^{II}\cdots M_y^{II}]^+$ complexes and required longer mixing times to see consumption of all starting solids and obtain a clear solution. The slower rate of reaction may have been due to the insertion of the Cu^{II} center into a 6-coordinate ligand environment, when Cu^{II} generally prefers a 4-coordinate, square planar conformation.[12] Therefore, it is feasible that the *in situ* prepared EPR sample was not allowed to mix long enough before it was frozen and the sample was collected.

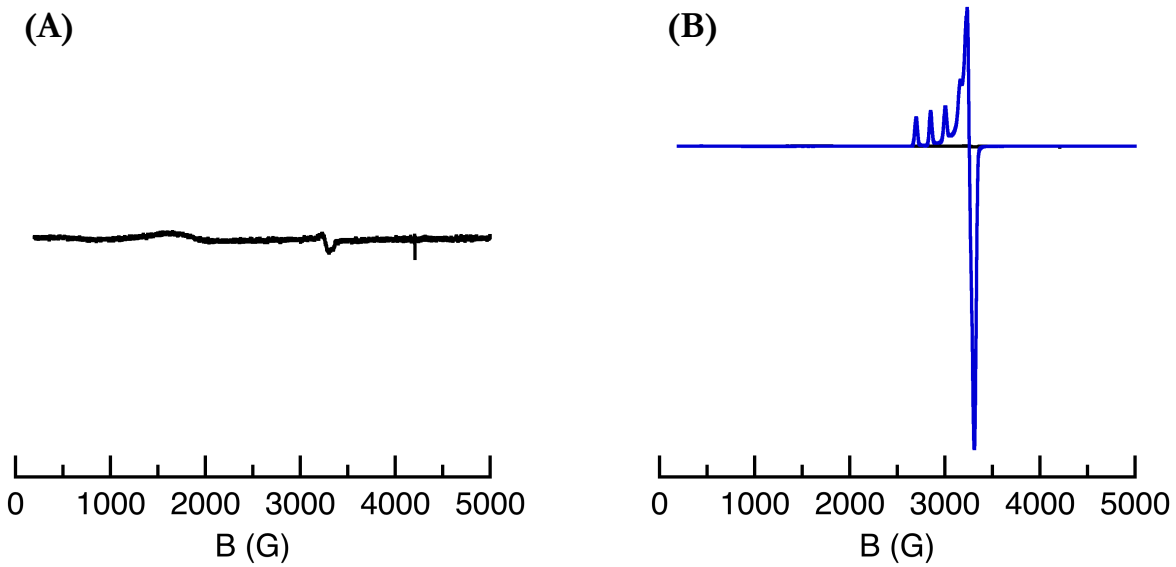

Figure 5-14: (A) ⊥-mode EPR spectrum obtained from $[Co^{II}\cdots Cu^{II}]^+$ measured in DCM:THF at 77 K. The small signals ~ g = 4, 2 were attributed to minimal residual $K[Co^{II}poat]$ and $[Cu^{II}Me_3tacn(OTf)_2] \cdot 2$ MeCN. For reference, **(B)** shows the overlay of ⊥-mode EPR spectra from $[Co^{II}\cdots Cu^{II}]^+$ (black) with $[Cu^{II}Me_3tacn(OTf)_2] \cdot 2$ MeCN (blue) at the same concentrations.

The ⊥-mode EPR spectrum of *in situ* prepared $[Co^{II}\cdots Co^{II}]^{+}$ was measured at 77 K (Fig 5-S4). This complex exhibited a silent ⊥-mode EPR spectrum likely due to an integer spin system, as was expected for a magnetically coupled complex featuring two half-integer spin metal ions. There was a small amount of signal centered ~ g = 4, which may have been due to a small excess of $K[Co^{II}poat]$ or a possible baselining issue. At 77 K, it was difficult to determine what the origin of this signal was and the method of magnetic coupling could not be determined. $[Co^{II}\cdots Co^{II}]^{+}$ was then studied by SQUID magnetometry. The ZFC thermal magnetic susceptibility data was collected at 100, 1000, and 5000 Oe fields. Between 0 – 50 K, the complex exhibited a sharp rise in χT that grew less prominent at lower fields (Fig 5-15 A). The increase in χT values at low temperature was consistent with ferromagnetic coupling between the two magnetic centers. This method of coupling was likely facilitated by the N–P=O bridging units, rather than dipolar interactions that are antiferromagnetic.[47–49] Given the ferromagnetic interaction between the two metal ions, the overall spin state of $[Co^{II}\cdots Co^{II}]^{+}$ was assigned as $S = 6$ ($\mu_S = 6.93\ \mu_B$). This spin state was further supported by the ZFC thermal magnetic susceptibility curves, which converged ~7 emu mol^{-1} K (~7 μ_B). The isothermal magnetization plot at 2 K exhibited a waist-gated hysteresis loop, which closed at 100 K (Fig 5-15 B). Because the hysteresis loop remained closed at all temperatures measured, it was determined that $[Co^{II}\cdots Co^{II}]^{+}$ was not a SMM.

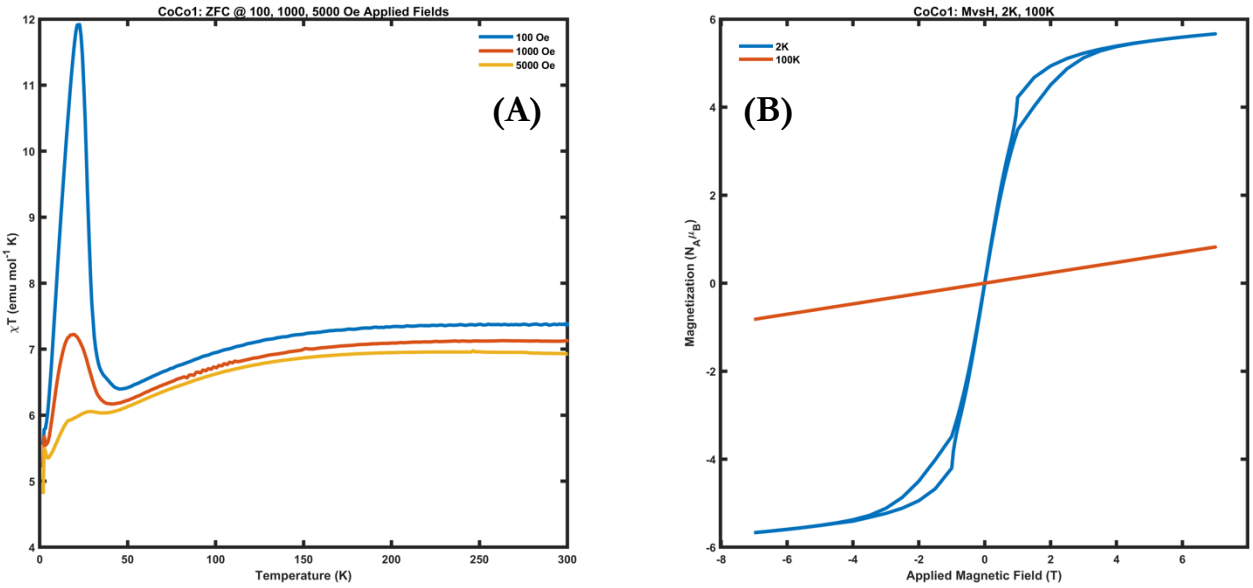

Figure 5-15: (A) ZFC thermal magnetic susceptibility plots of $[Co^{II}\cdots Co^{II}]^{+}$ collected between 2 – 300 K under varying fields. 100 Oe is shown in blue, 1000 Oe in red, and 5000 Oe in yellow. **(B)** Isothermal magnetization plots shown at 2 K (blue) and 100 K (red).

The magnetic behavior of $[Co^{II}\cdots Fe^{II}]^{+}$ was studied. A new signal was observed by ⊥-mode EPR spectroscopy, with a broad derivative signal was centered at g = 6.8 with a peak at g = 9.0 (Fig 5-16). This broad signal was observed initially from an *in situ* preparation of $[Co^{II}\cdots Fe^{II}]^{+}$, as well as from a solid sample measurement. The origin of this signal was assigned as a $S = 7/2$ spin system, arising from ferromagnetic coupling between a $S = 3/2$ Co^{II} center and a $S = 2$ Fe^{II} ion. However, this system was difficult to simulate and the lack of hyperfine from the ^{59}Co nucleus was unusual. To better understand the magnetic behavior of $[Co^{II}\cdots Fe^{II}]^{+}$, the complex was studied with SQUID magnetometry (Fig 5-17). The ZFC thermal magnetic susceptibility curves (Fig 5-17A) exhibited an increase in magnetic susceptibility as the temperature decreased, which supported the assignment of ferromagnetic coupling between the Co^{II} and Fe^{II} centers. Unlike the magnetization plots collected for $[Co^{II}\cdots Zn^{II}]^{+}$ and $[Co^{II}\cdots Co^{II}]^{+}$, the curves collected at different fields did not converge at higher temperatures, though the curves did flatten at higher fields. The isothermal magnetization plot collected at 2 K revealed a waist-closed hysteresis loop, which fully closed at 100 K. Similar to the examples discussed above, $[Co^{II}\cdots Fe^{II}]^{+}$ exhibited standard paramagnetic behavior; none of the data supported that $[Co^{II}\cdots Fe^{II}]^{+}$ acted as a SMM.

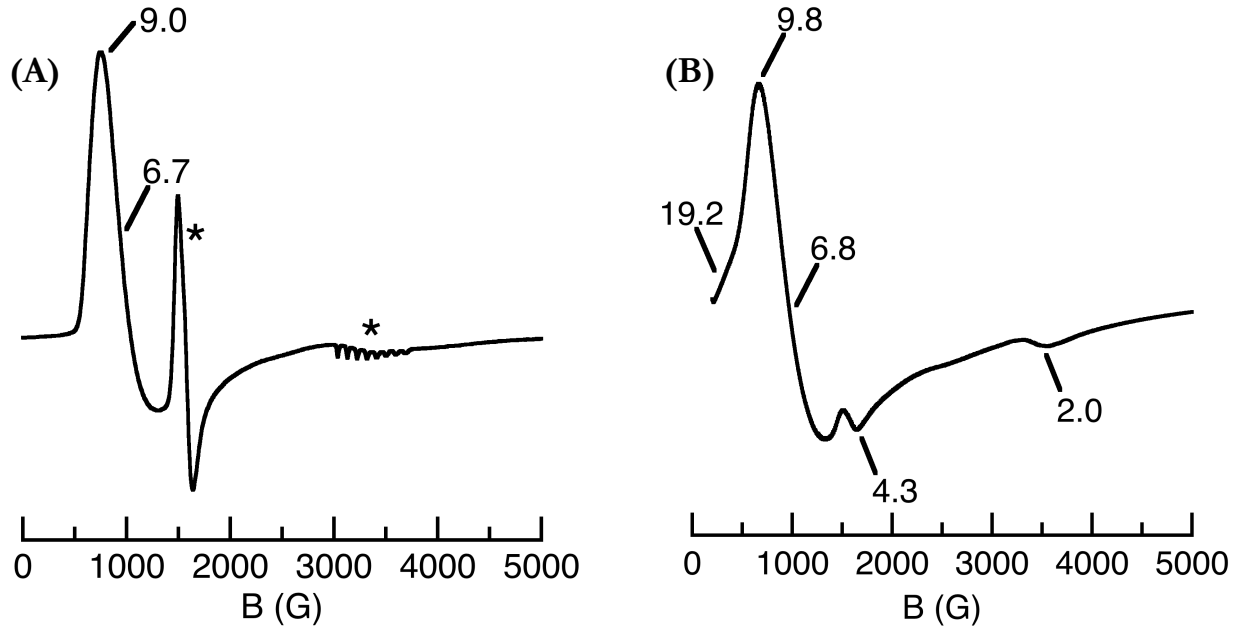

Figure 5-16: (A) ⊥-mode EPR spectrum obtained from *in situ* generated $[Co^{II}\cdots Fe^{II}]^{+}$ measured in DCM:THF. * represents ~14% excess $K[Co^{II}poat]$. **(B)** ⊥-mode EPR spectrum of solid, $[Co^{II}\cdots Fe^{II}]^{+}$.

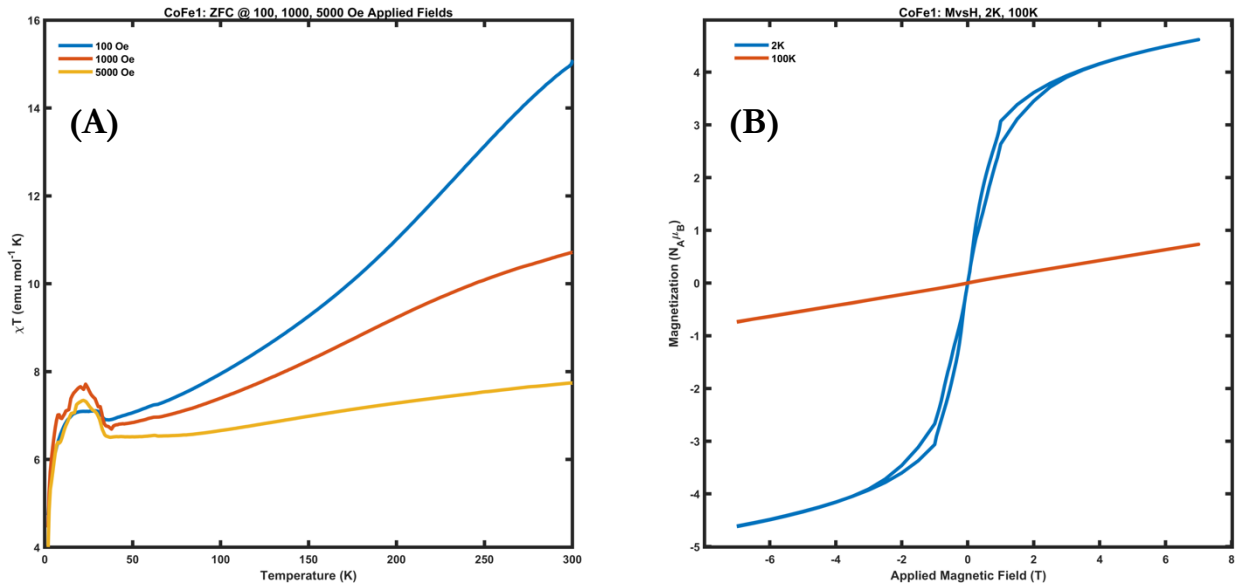

Figure 5-17: (A) ZFC thermal magnetic susceptibility plots of $[Co^{II}\cdots Fe^{II}]^{+}$ collected between 2 – 300 K under varying fields. 100 Oe is shown in blue, 1000 Oe in red, and 5000 Oe in yellow. **(B)** Isothermal magnetization plots shown at 2 K (blue) and 100 K (red).

The $[Co^{II}\cdots Mn^{II}]^{+}$ complex was studied with EPR spectroscopy and predicted to exhibit an overall $S = 4$ spin state due to ferromagnetic coupling between the two metal ions: Co^{II}: $S = 3/2$, Mn^{II}: $S = 5/2$, as was observed in the $[Co^{II}\cdots M_y^{II}]^{+}$ examples discussed above. Therefore, the complex was first examined by ∥-mode EPR spectroscopy and a signal was observed with features at g = 19.6, 16.1, 9.0 (Fig 5-18 A). $[Co^{II}\cdots Mn^{II}]^{+}$ features two metal ions with spin active nucleii (^{55}Mn, $I = 5/2$; ^{59}Co, $I = 7/2$), however no hyperfine features were observed in the ∥-mode EPR spectrum. Interestingly, there was also an EPR signal found in ⊥-mode with features at g = 4.5 and 2.0 (Fig 5-18 B). The feature at g = 4.5 was split by ^{55}Mn hyperfine (A = 412, Fig 5-18 C), while the feature at g = 2.0 was split by both ^{55}Mn and ^{59}Co hyperfine features (A = 254, 224 MHz respectively, Fig 5-18 D). The signals observed in ⊥-mode and the associated hyperfine features were unexpected and the origin of these features are unclear. Furthermore, the lack of hyperfine features observed in the ∥-mode EPR spectrum was unusual. Thus far only solution samples of $[Co^{II}\cdots Mn^{II}]^{+}$ have been measured, but solid state sample measurements are planned to better understand the magnetic behavior of this complex by EPR spectroscopy.

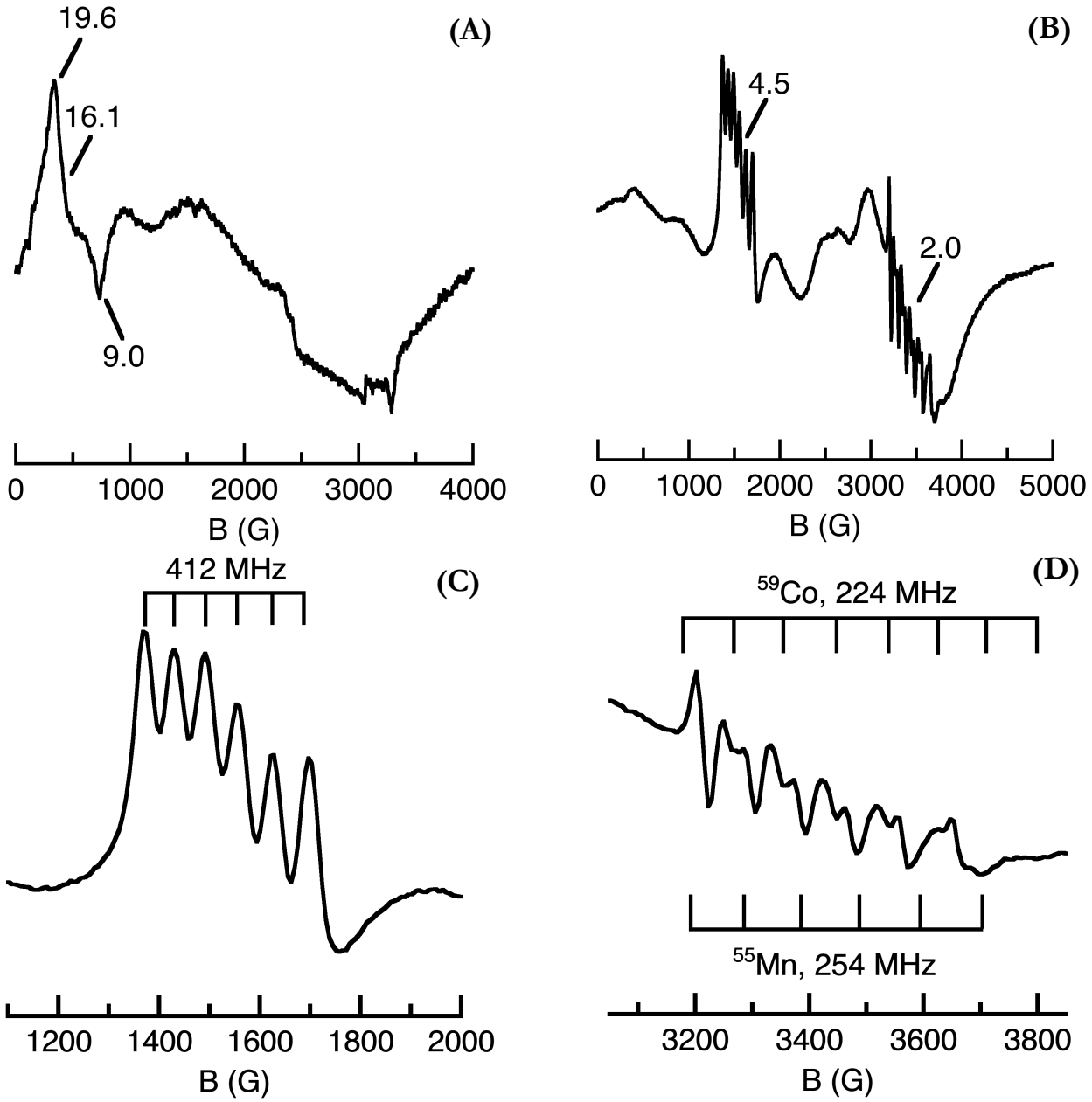

Figure 5-18: EPR spectra obtained from *in situ* prepared $[Co^{II}\cdots Mn^{II}]^{+}$. All spectra were collected at 6 K in DCM:THF. **(A)** The ∥-mode EPR spectrum. **(B)** The full ⊥-mode EPR spectrum of $[Co^{II}\cdots Mn^{II}]^{+}$. **(C)** Low-field region of the ⊥-mode EPR spectrum. **(D)** The high-field region from the ⊥-mode EPR spectrum of $[Co^{II}\cdots Mn^{II}]^{+}$. The signal at g = 2.0 was split by hyperfine from both ^{55}Mn and ^{59}Co nuclei. The ^{59}Co hyperfine was less intense and both sets of hyperfine were close to one another, making individual hyperfine features challenging to identify.

The magnetic properties of $[Co^{II}\cdots Mn^{II}]^{+}$ were also studied using SQUID magnetometry. As observed in the $[Co^{II}\cdots M_y^{II}]^{+}$ examples discussed above, the isothermal magnetization plot of $[Co^{II}\cdots Mn^{II}]^{+}$ collected at 2 K exhibited a waist-gated hysteresis loop, which closed between –2 and +2 T (Fig 5-19 B). When isothermal magnetization was measured at 100 K, the hysteresis loop remained closed. The ZFC thermal magnetic

susceptibility plot was measured at varying fields (Fig 5-19 A). At low temperatures, the magnetic susceptibility plots did not exhibit any increase in χT, as was observed in the other $[Co^{II}\cdots M_y^{II}]^+$ examples where M_y was a paramagnetic metal ion. The relatively flat profile of the magnetic susceptibility plots may suggest that Co^{II} and Mn^{II} ions are either very weakly coupled or are totally uncoupled. To confirm this conclusion, the SQUID experiments should be repeated with a different batch of $[Co^{II}\cdots Mn^{II}]^+$ to accompany the solid state EPR measurements.

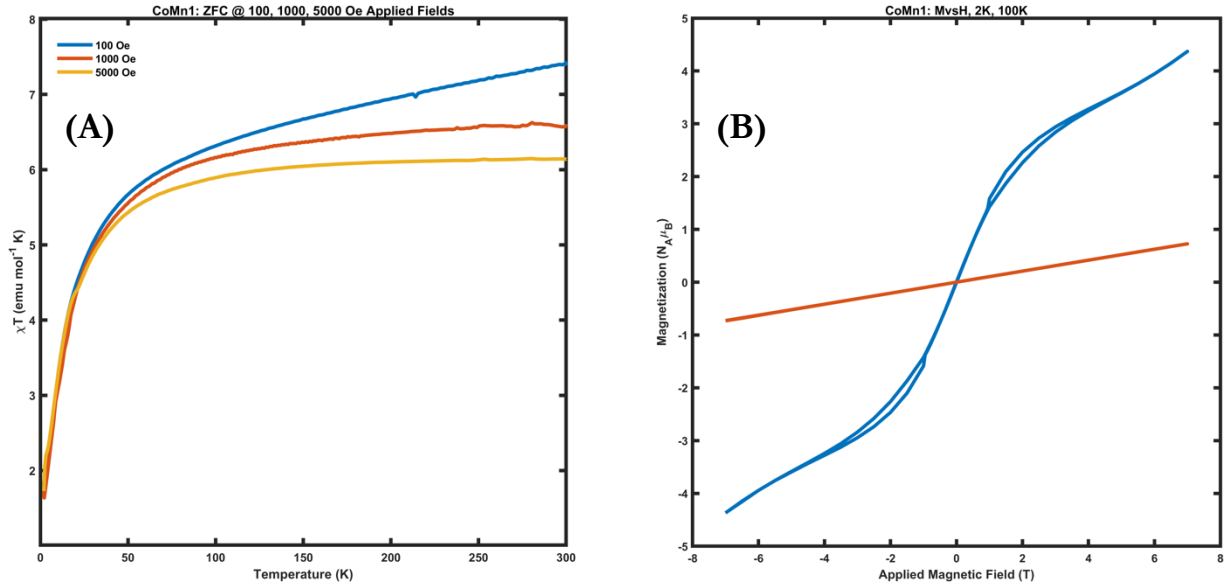

Figure 5-19: (A) ZFC thermal magnetic susceptibility plots of $[Co^{II}\cdots Mn^{II}]^+$ collected between 2 – 300 K under varying fields. 100 Oe is shown in blue, 1000 Oe in red, and 5000 Oe in yellow. **(B)** Isothermal magnetization plots shown at 2 K (blue) and 100 K (red).

Finally, the magnetic data for $[Mn^{II}\cdots Mn^{II}]^+$ was collected. The magnetic behavior of the $[Co^{II}\cdots M_y^{II}]^+$ complexes suggested that the two metal centers were ferromagnetically coupled. Therefore, the $[Mn^{II}\cdots Mn^{II}]^+$ complex was prepared with a goal of accessing a $S = 5$ spin state, the maximum spin state achievable with two *3d* metal ions. Ultimately, the $[Mn^{II}\cdots Mn^{II}]^+$ complex exhibited signals in both ⊥- and ∥-modes, similar to $[Co^{II}\cdots Mn^{II}]^+$ (Fig 5-20 A, B). These spectra were richly featured, with multiple sets of hyperfine. The ⊥- and ∥-mode signals were distinct from one another and did not appear to have significant overlap. From the data collected, it was difficult to assign the spin ground state of this complex or the mode of magnetic coupling, though the current hypothesis is that the two metal centers are ferromagnetically coupled. Additionally, the $[Mn^{II}\cdots Mn^{II}]^+$ spectra are similar to work done by Golombek *et al* on a bimetallic Mn system,

$[(Mn^{II}Me_3tacn)_2(OAc)_3]BPh_4$.[50] In this system, the Mn^{II} centers were weakly coupled and they were studied by both ⊥- and ∥-mode EPR spectroscopy, at Q- and X-bands. The weakly coupled spin system gave rise to signals in both modes and frequencies, due to weak antiferromagnetic coupling ($J = -3.15 \pm 0.25$ cm^{-1}) between the two Mn^{II} ions. $[Mn^{II}\cdots Mn^{II}]^+$ appeared to exhibit weak magnetic coupling, which could give rise to similar signals, though the mode of coupling is still unclear. Furthermore, both $[Mn^{II}\cdots Mn^{II}]^+$ and $[(Mn^{II}Me_3tacn)_2(OAc)_3]BPh_4$ feature three, triple-atom bridges between the two Mn^{II} centers and overall C_3 symmetry, with a threefold rotation axis that runs through the Mn^{II} ions. To fully understand the origins of the different signals observed in the spectra, a deeper analysis is necessary that would involve variable temperature studies at different frequencies, such as X- and Q- or S-band. Finally, solid EPR samples of $[Mn^{II}\cdots Mn^{II}]^+$ were collected (Fig 20 C, D) and the signals were found to be in good agreement with the solution samples, though significantly broadened out, confirming that the bimetallic species remained intact in solution. Much like in the solution sample, a deeper spectral analysis involving variable temperature and frequency measurement as well as simulation studies would be needed to better understand the spectra and the coupling.

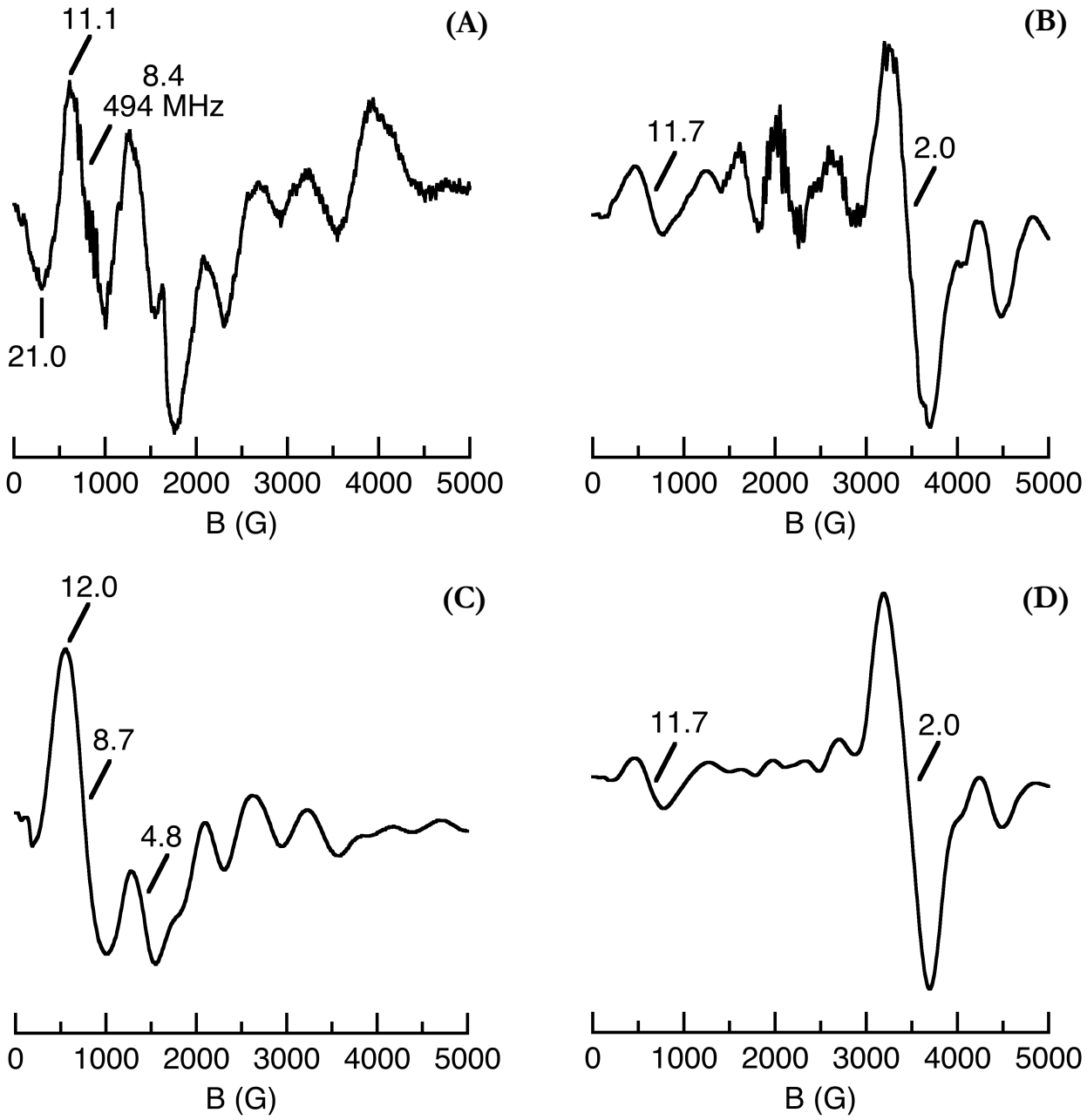

Figure 5-20: ∥-mode **(A)** and ⊥-mode **(B)** EPR spectra obtained from redissolved crystalline $[Mn^{II}\cdots Mn^{II}]^{+}$ in DCM:THF. The ∥-mode EPR spectrum exhibited ^{55}Mn hyperfine on the broad derivative, centered at g = 8.4 (A = 494 MHz). EPR spectra measured from solid $[Mn^{II}\cdots Mn^{II}]^{+}$, collected in ∥-mode **(C)** and ⊥-mode **(D).** The solution and solid samples were in good agreement with one another, though the spectral features were broadened out in the solid samples. ∥-mode EPR spectra were collected at 6 K and ⊥-mode spectra were measured at 20 K.

Summary and Conclusion

This chapter described the preparation and characterization of a series of highly symmetric, $R\bar{3}$ molecular structures with the formulation $[M_x^{II}poat\cdots M_y^{II}Me_3tacn]^+$. These complexes have been prepared with a variety of metal ions, including M_x = Zn, Co, Mn and M_y = Zn, Cu, Co, Fe, Mn. All molecular structures were isomorphous to one another and varied only slightly in bond lengths and angles. They were all rigorously C_3 symmetric, though the metal ion coordinated in $[poat]^{3-}$ remained distorted from ideal TMP geometries due to puckering out of the plane. The $[Co^{II}\cdots M_y^{II}]^+$ complexes have been the most thoroughly studied thus far. The electronic absorption data for these molecules appeared largely dominated by the Co^{II} centers, with only subtle shifts from the starting $[Co^{II}poat]^-$ spectrum. $[Co^{II}\cdots Co^{II}]^+$ appeared to exhibit features from both Co^{II} centers, notably with a low energy band ~ 1100 nm. $[Co^{II}\cdots Cu^{II}]^+$ had the most unique absorption spectrum, with low energy features from both metal centers as well as a higher energy band of unknown origin.

The magnetic properties of the $[M_x^{II}poat\cdots M_y^{II}Me_3tacn]^+$ complexes were also investigated. The $[Co^{II}\cdots Zn^{II}]^+$ complex exhibited a $S = 3/2$ signal by EPR spectroscopy, similar to the starting $K[Co^{II}poat]$ complex. Introduction of a second paramagnetic metal ion to the $[Co^{II}\cdots M_y^{II}]^+$ complexes led to the formation of new EPR signals, which were hypothesized to arise from ferromagnetic coupling between the two metal centers. In addition, $[Co^{II}\cdots Zn^{II}]^+$, $[Co^{II}\cdots Co^{II}]^+$, $[Co^{II}\cdots Fe^{II}]^+$, and $[Co^{II}\cdots Mn^{II}]^+$ were studied by SQUID magnetometry. All complexes studied were found not to exhibit SMM behavior. The proposed ferromagnetic coupling between the two metal centers in $[Co^{II}\cdots Co^{II}]^+$ and $[Co^{II}\cdots Fe^{II}]^+$ was corroborated by the SQUID measurements, though coupling was unclear in the $[Co^{II}\cdots Mn^{II}]^+$ complex. Finally, $[Mn^{II}\cdots Mn^{II}]^+$ was studied in an effort to access a $S = 5$ spin state. $[Mn^{II}\cdots Mn^{II}]^+$ exhibited rich, complicated spectra in both ⊥- and ∥-mode EPR, which require a deeper analysis to better understand the data. Further experiments would involve measurement and analysis of solid samples in ⊥- and ∥-mode EPR spectroscopy, as well as solution measurements at different frequencies and SQUID magnetometry.

Outlook

This chapter described a new method for the preparation of a bimetallic species that interact through N–P=O bridging units provided by the $[poat]^{3-}$ backbone, $[M_x^{II}poat\cdots M_y^{II}Me_3tacn]OTf$. These complexes crystallize reproducibly; the synthetic procedure was effective for a range of *3d* metal ions. Future work could expand the series to a wider selection of metal ions, including *4d* or *5d* transition metal ions, which have not been explored in $[poat]^{3-}$ thus far. The magnetism of the $[M_x^{II}poat\cdots M_y^{II}Me_3tacn]OTf$ complexes were studied with both EPR spectroscopy and SQUID magnetometry, which showed that the N–P=O bridging units supported ferromagnetic coupling between the metal ions, allowing for the development of small molecule complexes with large spin states. The contributions that the N–P=O bridging units have on magnetic coupling has never been specifically studied before and this data provides further insight into the magnetism of bimetallic systems supported by $[poat]^{3-}$. My initial hypothesis was that the $[M_x^{II}poat\cdots M_y^{II}Me_3tacn]^{+}$ molecular systems were good SMM candidates, however none of the complexes exhibited SMM behavior based on the SQUID magnetometry measurements. However, this preparative route may yield magnetically interesting complexes if the series was expanded to include other metal ions.

Experimental Section

General Procedures

Unless otherwise specified, all reagents were purchased and used as received from commercially available sources and stored under an inert atmosphere in a VAC dry box. Sure-seal bottles of DMA were purchased from Honeywell, Burdick, & Jackson (99.5% purity). All other solvents were sparged with argon and purified with a JC Meyer Co. solvent purification system with Q-5 columns and molecular sieves. KH was bought as a 30% suspension in mineral oil, washed on a fine porosity frit 5 times with *n*-pentane and Et_2O, dried under vacuum, and stored under N_2. 18c6 was purchased in 99% purity from Acros Organics, ground with a mortar and pestle to a powder, and dried under vacuum. $Co^{II}(OAc)_2$ was purchased from Sigma Aldrich as a pink-purple solid and dried in an oven until a purple powder was obtained. H_3poat,[51] Me_3tacn,[52,53] $[Zn^{II}Me_3tacn(OTf)_2]$,[4] $[Mn^{II}Me_3tacn(OTf)_2]$,[3] $[Fe^{II}Me_3tacn(OTf)_2]$,[41] $Co^{II}(OTf)_2{\cdot}2MeCN$,[54] and

$[Cu^{II}Me_3tacn(OTf)_2]\cdot 2MeCN$,[43] were prepared following literature procedures. $Zn^{II}(OTf)_2\cdot 2MeCN$[55] was prepared by adapting previous literature reports.

Physical Methods

Electronic absorption spectra were collected in a 1 cm quartz cuvette, fitted with a magnetic stir bar. Spectra were recorded on a Cary-60 spectrophotometer or an 8453E Agilent UV-vis spectrophotometer equipped with a Unisoku Unispeks cryostat for temperature-controlled spectroscopy. Cyclic voltammetry was performed with a CHI600C potentiostat. Voltammograms were measured from a ~1 mM stock solution of analyte in at least 100-fold excess of tetrabutylammonium hexafluorophosphate in dry, air-free DCM collected in 4-neck, double-walled cell. A 1 mm glassy carbon electrode acted as the working electrode with a Pt wire counter electrode and a Ag wire reference electrode. All voltammograms were referenced to an internal $Fc^{+/0}$ standard. He-temperature EPR spectra were collected on an X-Band Bruker spectrometer fitted with an Oxford liquid helium cryostat. Signals were referenced and quantified to a CuEDTA spin standard. The magnetic field was calibrated with an NMR gaussmeter. The microwave frequency of the instrument was calibrated with a frequency counter. 77 K EPR experiments were recorded on a Bruker EMX X-band spectrometer with the following parameters, unless otherwise noted: microwave frequency of 9.64 GHz, a modulation frequency of 100 kHz, a modulation amplitude of 10 G, a microwave power of 2 mW, an attenuation of 20 dB, a time constant of 82 msec, and a conversion time of 41 msec. All EPR samples were prepared under a nitrogen atmosphere in 4 mm quartz EPR tubes, capped with a septum, and flash frozen in liquid nitrogen. EPR spectra were simulated and fit using SpinCount software.[56] Attenuated Total Reflectance-Fourier Transform Infrared (ATR-FTIR) spectra were measured on a Thermo Scientific Nicolet iS5 spectrometer fitted with an iD5 ATR attachment. Evans' Method NMR spectra were recorded at 500 MHz using a Bruker DRX500 spectrometer with a TCI cryoprobe. Chemical shifts were reported in ppm and referenced to an internal trimethylsilane standard in deuterated solvents. Elemental analyses were measured on a Perkin-Elmer 2400 Series II CHNS elemental analyzer. Magnetic data were collected under DC scan modes using a Quantum Design MPMS3 SQUID Magnetometer with equipped AC susceptibility attachment. Crystal samples were finely crushed and loaded in custom quartz tubes (D&G Glassblowing Inc.), layered with eicosane wax, and subsequently flame-sealed under static vacuum. Eicosane

wax was melted within the sealed sample to abate sample torquing and to facilitate thermal conductivity. Diamagnetic corrections for the samples and eicosane wax were calculated using Pascal's constants and subtracted from all static moment data.

Preparative Methods

K[Co^{II}poat]: 0.1426 g (0.1910 mmol) of H_3poat were dissolved in 4 mL of DMA. To this solution, 0.0280 g (0.698 mmol) KH were added, yielding a bubbling, cloudy solution. The reaction mixture was stirred till bubbling ceased and the solution was clear and colorless. Then, 0.0348 g (0.197 mmol) of $Co^{II}(OAc)_2$ were added as a purple powder suspension in 2 mL of DMA. The reaction mixture was allowed to stir overnight and resulted in formation of a bright, cloudy blue suspension. The reaction mixture was filtered to yield solid blue powder and a bright blue solution. The solid on the frit was washed with minimal DCM, followed by *n*-pentane and Et_2O until the blue color washed away and 0.0345 g of dry, off-white solid remained (92.0% yield; theoretical yield, KOAc = 0.0375 g, 0.382 mmol). The blue filtrate was subsequently dried under vacuum to give bright blue powder. This powder was redissolved in DCM and layered under *n*-pentane to yield 0.1170 g (0.1390 mmol, 72.8% yield) of bright blue, blocky single crystals, suitable for X-ray diffraction analysis. UV-vis (DCM, λ_{max} nm (ε, $M^{-1}cm^{-1}$)) = 410 (13), 585 (67), 610 (71), 770 (8). ATR-FTIR, selected bands (cm^{-1}) = 3050, 2949, 2838, 2342, 1720, 1589, 1481, 1433, 1271, 1232, 1192, 1155, 1118, 1026, 965, 918, 851, 801, 746, 717, 696. EPR (X-Band, ⊥-mode, 20 K, DCM:THF, excess 18c6), g = 4.5, 4.3, 2.0 (A = 262 MHz), E/D = 0.0029, D = +3.6 cm^{-1}. μ_{eff}, Evans Method, DCM = 4.28 μ_B. Cyclic Voltammetry (100 mV/s, DCM, V vs $Fc^{+/0}$) = $E_{1/2}$ = –0.495, E_{pa} = +0.365. Elemental Analysis calculated for $4(C_{42}H_{42}CoKN_4O_3P_3) \cdot C_5H_{12}$; C, 60.42, H, 5.28, N, 6.52; found C, 60.6, H, 4.87, N, 6.71.

[Co^{II}poat···Zn^{II}Me$_3$tacn]OTf: In a representative synthesis, 0.2023 g (0.2403 mmol) K[Co^{II}poat] was dissolved in ~ 4 mL DCM. To this clear, bright blue solution, 0.1293 g (0.2418 mmol) ~ 3 mL of $Zn^{II}Me_3TACN(OTf)_2$ in DCM was added dropwise, resulting in a slight color change to a deeper blue solution. After stirring for approximately 30 minutes, this blue solution was recrystallized via vapor diffusion of Et_2O, resulting in feathery, blue single crystals suitable for X-ray diffraction. The crystalline product was isolated via vacuum filtration in 92.86% yield (0.2652 g). UV-vis (DCM, λ_{max} nm (ε, $M^{-1}cm^{-1}$)) = 410 (29), 570 (80), 600 (76), 695 (13). EPR (X-

Band, ⊥-mode, 15 K) Solution, DCM:THF, g = 4.3, 2.0 (A = 281 MHz), E/D = 0.0029, D = +5.6 cm^{-1}. Solid, g = 9.4, 4.4, 4.3, 2.0 (A = 290 MHz). μ_{eff}, Evans Method, DCM = 4.89 μ_B (μ_s, S = 3/2: 3.87 μ_B). Elemental Analysis calculated for 5*([Co^{II}poat···$Zn^{II}Me_3$TACN]OTf) · Et_2O, [5*($C_{52}H_{63}CoF_3N_7O_6P_3SZn$) · $C_4H_{10}O$]; C, 52.71, H, 5.45, N, 8.15; found C, 53.06, H, 5.1, N, 8.34.

[Co^{II}poat···$Cu^{II}Me_3$tacn]OTf: 0.0218 g K[Co^{II}poat] were dissolved in ~1 mL of DCM. This clear blue solution was added slowly to a cloudy, pale-green suspension of [$Cu^{II}Me_3$tacn($OTf)_2$]·2MeCN in ~2 mL DCM (0.0156 g, 0.0254 mmol). The reaction was stirred for roughly an hour and turned cloudy, dark yellow-green in color. This mixture was subsequently pipet filtered and recrystallized via vapor diffusion of Et_2O into the mother liquor. Several yellow-brown crystals grew, suitable for X-ray diffraction analysis. However, a yield could not be obtained. UV-vis (DCM, λ_{max} nm (ε, $M^{-1}cm^{-1}$)) = 446 (133), 590 (66), 779 (29). ⊥-mode EPR silent.

[($Co^{II}Me_3$tacn)$_2$($OTf)_3$]OTf: 0.0356 g (0.0811 mmol) $Co^{II}(OTf)_2$ • 2MeCN were suspended in ~ 3 mL DCM. To this suspension, a small excess of neat Me_3tacn (0.0190 mL, 0.0981 mmol, 1.21 equivalents) was added. The reaction was allowed to stir until all solids were consumed. At this point, the reaction was pipet filtered and recrystallized from vapor diffusion of Et_2O into DCM. This resulted in the growth of single crystals suitable for X-ray diffraction studies, in a 0.0300 g yield (0.0284 mmol, 69.9 % yield). UV-vis (DCM, λ_{max} nm (ε, $M^{-1}cm^{-1}$)) = 370 (30), 480 (39), 517 (35), 543 (30), ~1100 (19). EPR (X-Band, ⊥-mode, 77 K, DCM:THF), g = 2 (broad derivative).

[Co^{II}poat···$Co^{II}Me_3$tacn]OTf: 0.0602 g (0.0715 mmol) of blue, crystalline K[Co^{II}poat] was weighed in a vial. 0.0385 g (0.0364 mmol) of solid, pink [$Co^{II}Me_3$TACN($OTf)_3$]OTf was added and the two solids were dissolved together in ~ 4 mL DCM, resulting in the formation of a bright, purple-blue solution. After roughly 15 min, the reaction mixture was pipet filtered yielding a clear, purple-blue filtrate. The filtrate was then pipet filtered and recrystallized by vapor diffusion of Et_2O into the mother liquor, resulting in single crystals suitable for X-ray diffraction studies (0.0739 g, 0.0624 mmol, 87.4% yield). UV-vis (DCM, λ_{max} nm (ε, $M^{-1}cm^{-1}$)) = 410 (26), 493 (18), 570, 582, 595, 725, 775, ~1000. ⊥-mode EPR silent.

[Co^{II}poat···Fe^{II}Me$_3$tacn]OTf: In a representative synthesis, 0.0642 g (0.0763 mmol) K[Co^{II}poat] was dissolved in ~3 mL DCM. To this clear, bright blue solution, 0.0410 g (0.0781 mmol) Fe^{II}Me$_3$TACN(OTf)$_2$ in ~2 mL DCM was added dropwise, resulting in a slight color change to a deeper blue solution over approximately 30 minutes. The solution was then transferred to 4 mL scintillation vials and recrystallized from vapor diffusion of Et_2O into the mother liquor, resulting in feathery, blue single crystals suitable for X-ray. The blue crystals were isolated via vacuum filtration in diffraction 80.1% yield (0.0799 g, 0.0611 mmol). UV-vis (DCM, λ_{max} nm (ε, $M^{-1}cm^{-1}$)) = 405 (sh), 570 (120), 586 (130), 600 (129), 695 (41), 810 (26). EPR (X-Band, ⊥-mode, 20 K, DCM:THF), g = 9.0, 6.7; solid, g = 19.2, 9.8, 6.8, 4.3, 2.0. μ_{eff}, Evans Method, DCM = 7.53 μ_B (μ_S, S = 7/2: 7.94 μ_B).

[Co^{II}poat···Mn^{II}Me$_3$tacn]OTf: In a representative synthesis, 0.0480 g (0.0570 mmol) K[Co^{II}poat] was weighed with 0.0300 g (0.0572 mmol) Mn^{II}Me$_3$TACN(OTf)$_2$. The two solids were dissolved together in 4 mL DCM and stirred for 15 min, resulting in a blue-green mixture. The mixture was subsequently pipet filtered to remove a faintly yellow solid, yielding a bright blue filtrate. The blue filtrate was diluted to a volume of ~6 mL in DCM and recrystallized by vapor diffusion of Et_2O into the mother liquor, resulting in 0.0394 g of blue single crystals suitable for X-ray diffraction (0.0334 mmol, 52.3% yield). UV-vis (DCM, λ_{max} nm (ε, $M^{-1}cm^{-1}$)) = 430 (88), 575 (124), 605 (118). EPR (X-Band, ⊥-mode, 20 K, DCM:THF), g = 4.5 (A, ^{55}Mn = 412 MHz), 2.0 (A, ^{55}Mn = 254 MHz, ^{59}Co = 224 MHz); (X-Band, ‖-mode, 6 K, DCM:THF), g = 19.6, 16.1, 9.0.

K[Mn^{II}poat]: In a representative experiment, 0.1124 g (0.1505 mmol) of H_3poat was suspended in ~ 2 mL THF. To this suspension, 0.0181 g (0.451 mmol) of KH suspended in ~ 2 mL THF was added. The suspension was allowed to stir until bubbling ceased and the reaction appeared clear and colorless (~ 5 min). Mn^{II}(OAc)$_2$ was added to this solution as a solid (0.0291 g, 0.168 mmol) and stirred for ~ 2 h. At this point, the reaction mixture appeared faintly yellow and slightly cloudy. This mixture was then filtered and 0.0382 mg of white solid were isolated (theoretical yield KOAc = 0.0295 g). The resulting faint yellow filtrate was dried to a solid, then redissolved in ~1 mL THF and triturated with Et_2O until an off-white precipitate formed. 0.0600 g of off-white precipitate was isolated and dried, giving a 50% yield (0.1260 g, 0.1505 mmol theoretical yield). The

identity of the powder was confirmed as K[Mn^{II}poat] by elemental analysis. UV-vis (DCM) = featureless. EPR (X-Band, ⊥-mode, 77 K, DCM:THF), g = 8.9, 4.8, 1.8. Elemental Analysis calculated for 4*(K[Mn^{II}poat]) · *n*-pentane, [5*($C_{42}H_{42}KMnN_4O_4P_3$) · C_5H_{12}]; C, 60.70, H, 5.30, N, 6.55; found C, 60.95, H, 5.02, N, 6.63.

[Mn^{II}poat···$Mn^{II}Me_3$tacn]OTf: In a typical synthesis, 0.1600 g (0.1910 mmol) K[Mn^{II}poat] was dissolved in ~ 3 mL DCM in the presence of excess 18c6 (0.1430 g, 0.5414 mmol, 2.8 equivalents). To this clear colorless solution, 0.1001 g (0.1909 mmol) of [$Mn^{II}Me_3$tacn$(OTf)_2$] was added as a cloudy, faintly yellow suspension in ~ 2 mL DCM. The reaction was stirred until all solids appeared consumed, at which point the reaction was pipet filtered to isolate residual solid materials. The filtrate was subsequently recrystallized by vapor diffusion of Et_2O in DCM, resulting in the growth of faintly brown single crystals suitable for X-ray diffraction studies. The crystals were isolated and subsequently washed with minimal MeCN and Et_2O, resulting in a yield of 0.1483 g of crystalline material (0.1247 mmol, 65.30 % yield). UV-vis (DCM, λ_{max} nm (ε, $M^{-1}cm^{-1}$)) = 420 (48), 505 (sh), 697 (52). EPR (X-Band, ⊥-mode, 20 K, DCM:THF), g = 11.7, 2.0; (X-Band, ‖-mode, 6 K, DCM:THF), g = 21.0, 11.1, 8.4 (A, ^{55}Mn = 494 MHz). Elemental analysis calculated for 4*(Mn^{II}poat···$Mn^{II}Me_3$TACN]OTf) · DCM, [4*($C_{52}H_{63}F_3Mn_2N_7O_6P_3S$) · CH_2Cl_2]; C, 52.51, H, 5.36, N, 8.20; found C, 52.78, H, 5.05, N, 7.90.

K[Zn^{II}poat]: In a representative synthesis, 0.1660 g (0.2223 mmol) H_3poat was dissolved in ~ 3 mL THF with solid KH (0.0265 g, 0.661 mmol) KH. The reaction was stirred until a clear, faint yellow solution persisted and all bubbling ceased. At this point, solid $Zn^{II}(OAc)_2$ was added (0.0417 g, 0.227 mmol) and the reaction was stirred. The reaction was stirred overnight and filtered, resulting in the isolation of 0.0610 g of white solid (theoretical yield, KOAc: 0.0436 g, 0.445 mmol) and the reaction was dried to a faint yellow color. The solid was redissolved in ~ 4 mL DCM and layered under *n*-pentane. The recrystallization resulted in the growth of colorless single crystals suitable for X-ray diffraction study in a 145.3 mg (0.1717 mmol, 77.04% yield). UV-vis (DCM λ_{max}, nm) = 325 (sh). ^{1}H-NMR (600 MHz, CD_2Cl_2, ppm): δ = 2.53 (6 H, t, ethyl), 2.96 (6H, quint., ethyl), 7.25 (12 H, td, *m*-PhH), 7.34 (6 H, td, *p*-PhH), 7.63 (12 H, t, *o*-PhH). ^{31}P-NMR (600 MHz, CD_2Cl_2, ppm): 27.11 (s).

[Zn^{II}poat···Zn^{II}Me$_3$tacn]OTf: In a typical preparation, 0.0312 g (0.0369 mmol) of K[Zn^{II}poat] was dissolved in ~1 mL DCM in the presence of excess 18c6. Then a solution of 0.0198 g (0.0370 mmol) [Zn^{II}Me$_3$tacn(OTf)$_2$] in ~1 mL DCM was added slowly to the K[Zn^{II}poat] solution. The reaction was stirred for ~15 minutes, then pipet filtered, and recrystallized by vapor diffusion of Et_2O into the DCM filtrate. This resulted in the growth of clear, colorless single crystals suitable for X-ray diffraction study in a 0.0098 g (0.0082 mmol, 22% yield). UV-vis (DCM) = featureless.

X-ray Crystallographic Methods

[Co^{II}poat···Zn^{II}Me$_3$tacn]OTf: The data for asb639 were collected from a shock-cooled single crystal at 93(2) K on a Bruker SMART APEX II three-circle diffractometer with a sealed X-ray tube using a equatorial mounted graphite as monochromator and a Bruker Apex II CCD detector. The diffractometer was equipped with a low temperature device and used MoK_a radiation (λ = 0.71073 Å). All data were integrated with SAINT and a multi-scan absorption correction using SADABS was applied.[57,58] The structure was solved by direct methods using SHELXT and refined by full-matrix least-squares methods against F^2 by SHELXL-2018/3 using ShelXle.[59–61] All non-hydrogen atoms were refined with anisotropic displacement parameters. All hydrogen atoms were refined isotropic on calculated positions using a riding model with their U_{iso} values constrained to 1.5 times the U_{eq} of their pivot atoms for terminal sp^3 carbon atoms and 1.2 times for all other carbon atoms. Disordered moieties were refined using bond lengths restraints and displacement parameter restraints. This report and the CIF file were generated using FinalCif.[62] *Refinement Details:* All non-hydrogen atoms in Part 1 were initially freely refined, but a disordered part of the entire molecule (~5%) was found upside down in the trigonal symmetric asymmetric unit. Refinement of the disorder required significant restraints which fixed the M1-M2 (M1 = Co1, M2 = Zn1), N1-M1, P1-C9, P1-C3, P1-N2, N2-C2, C1-C2, N1-C1$, N3-Zn1, N3-C15, N3-C17, C15-C16, O1-M2, N2-M1, and P1-O1 distances of the disordered part to the main part. The bond lengths of the following bonds were fixed to the following distances in parentheses: C15B-C16B (1.54(0.005)), M2B-C15B M2B C15C (2.91(0.005)), M2B-C16B M2B-C16C (3.03(0.005)). The ADPs of O1, P1, M1, M2, N1, C1, C2, C15, C16, and C17 were separately fixed to those of the disordered part. Phenyl rings of the disordered part were fixed to perfect hexagons, and all ADPs of the disordered phenyl carbons were fixed to the same values. Two sixth

triflate ions were found in the asymmetric unit, one sixth is included as disordered across the inversion center and C3 symmetric axis, and the other was removed using SQUEEZE,[60] as an implementation of Platon,[60,63,64] due to major disorder across the C3 symmetric axis and inversion center. All hydrogen atoms were added using a riding model.

[Co^{II}poat···Cu^{II}Me$_3$tacn]OTf: The data for asb729 were collected from a shock-cooled single crystal at 93(2) K on a Bruker X8 Prospector APEX II CCD κ-geometry diffractometer with an IuS microsource using a multi-layer optics as monochromator and a Bruker Apex II CCD detector. The diffractometer was equipped with a low temperature device and used CuK_a radiation (λ = 1.54178 Å). All data were integrated with SAINT and a multi-scan absorption correction using SADABS was applied.[57,58] The structure was solved by direct methods using SHELXT and refined by full-matrix least-squares methods against F^2 by SHELXL-2018/3 using ShelXle.[59,61,65] All non-hydrogen atoms were refined with anisotropic displacement parameters. All hydrogen atoms were refined isotropic on calculated positions using a riding model with their U_{iso} values constrained to 1.5 times the U_{eq} of their pivot atoms for terminal sp^3 carbon atoms and 1.2 times for all other carbon atoms. Disordered moieties were refined using bond lengths restraints and displacement parameter restraints. This report and the CIF file were generated using FinalCif.[62] *Refinement Details:* All non-hydrogen atoms in Part 1 were initially freely refined, but a disordered part of the entire molecule (~5%) was found upside down in the trigonal symmetric asymmetric unit. Refinement of the disorder required significant restraints which fixed the M1-M2 (M1 = Co1, M2 = Cu1), N1-M1, P1-C9, P1-N2, N2-C2, C1-C2, N1-C1$, N3-M1, N3-C15, N3-C17, C15-C16, O1-C15, O1-C16, O1-C17, O1$-C17, O1-M1, O1-M2, N2-M1, and P1-O1 distances of the disordered part to the main part. The bond lengths of the following bonds were fixed to the following distances in parentheses: C15B-C16B (1.54(0.005)), M2B-C15B M2B C15C (2.91(0.005)), M2B-C16B M2B-C16C (3.03(0.005)). The ADPs of O1, P1, M1, M2, N1, N2, N3, C1, C2, C15, C16, and C17 were separately fixed to those of the disordered part. Phenyl rings of the disordered part were fixed to perfect hexagons, and all ADPs of the disordered phenyl carbons were fixed to the corresponding values in Part 1. Two sixth triflate ions were found in the asymmetric unit, one sixth is included as disordered across the inversion center and C3 symmetric axis, and the other was removed using SQUEEZE[60], as an implementation of Platon,[60,63,64] due to major

disorder across the C3 symmetric axis and inversion center. All hydrogen atoms were added using a riding model

[(Co^{II}Me$_3$tacn)$_2$(OTf)$_3$]OTf: The data for asb714t_a_sq were collected from a shock-cooled single crystal at 93(2) K on a Bruker X8 Prospector APEX II CCD κ-geometry diffractometer with an IuS microsource using a multi-layer optics as monochromator and a Bruker Apex II CCD detector. The diffractometer was equipped with a low temperature device and used CuK_a radiation (λ = 1.54178 Å). All data were integrated with SAINT and a multi-scan absorption correction using SADABS was applied.[57,58] The structure was solved by direct methods using SHELXT and refined by full-matrix least-squares methods against F^2 by SHELXL-2018/3 using ShelXle.[59,61,65] All non-hydrogen atoms were refined with anisotropic displacement parameters. All hydrogen atoms were refined isotropic on calculated positions using a riding model with their U_{iso} values constrained to 1.5 times the U_{eq} of their pivot atoms for terminal sp^3 carbon atoms and 1.2 times for all other carbon atoms. Disordered moieties were refined using bond lengths restraints and displacement parameter restraints. This report and the CIF file were generated using FinalCif.[62] *Refinement Details:* Significant constraints and restraints were required to keep this model from becoming chemically unreasonable. Please use this structure for connectivity, only. All equivalent C-N, C-C, and Co-N bond lengths were restrained to similar values. All equivalent N-N distances were restrained to similar values. O3-Co2 and O6-Co2 bond lengths were restrained to similar values. Nearly all atoms were refined with negative part numbers in order to account for disorder across the crystallographic mirror plane. ISOR restraints were applied to the entire molecule. Nitrogen atoms from disordered parts were individually constrained to the same value. Disordered parts of triflate molecules were constrained to the same value. C-C bond lengths were restrained to 1.54A. SQUEEZE,[60] implemented in Platon,[60,63,64] was used to remove what was possibly a heavily disordered chloroform molecule.

[Co^{II}poat···Co^{II}Me$_3$tacn]OTf: The data for asb682 were collected from a shock-cooled single crystal at 93(2) K on a Bruker SMART APEX II three-circle diffractometer with a sealed X-ray tube using a equatorial mounted graphite as monochromator and a Bruker Apex II CCD detector. The diffractometer was equipped with a low temperature device and used MoK_a radiation (λ = 0.71073 Å). All data were integrated with SAINT and a multi-

scan absorption correction using SADABS was applied.[57,58] The structure was solved by direct methods using SHELXT and refined by full-matrix least-squares methods against F^2 by SHELXL-2018/3 using ShelXle.[59,61,65] All non-hydrogen atoms were refined with anisotropic displacement parameters. All hydrogen atoms were refined isotropic on calculated positions using a riding model with their U_{iso} values constrained to 1.5 times the U_{eq} of their pivot atoms for terminal sp^3 carbon atoms and 1.2 times for all other carbon atoms. Disordered moieties were refined using bond lengths restraints and displacement parameter restraints. This report and the CIF file were generated using FinalCif.[62] *Refinement Details:* All non-hydrogen atoms in Part 1 were initially freely refined, but a disordered part of the entire molecule (~5%) was found upside down in the trigonal symmetric asymmetric unit. Refinement of the disorder required significant restraints which fixed the M1-M2 (M1 = Co1, M2 = Co2), N1-M1, P1-C9, P1-N2, N2-C2, C1-C2, N1-C1$, N3-M1, N3-C15, N3-C17, C15-C16, O1-C15, O1-C16, O1-C17, O1$-C17, O1-M1, O1-M2, N2-M1, and P1-O1 distances of the disordered part to the main part. The bond lengths of the following bonds were fixed to the following distances in parentheses: C15B-C16B (1.54(0.005)), M2B-C15B M2B C15C (2.91(0.005)), M2B-C16B M2B-C16C (3.03(0.005)). The ADPs of O1, P1, M1, M2, N1, N2, N3, C1, C2, C15, C16, and C17 were separately fixed to those of the disordered part. Phenyl rings of the disordered part were fixed to perfect hexagons, and all ADPs of the disordered phenyl carbons were fixed to the same values. Two sixth triflate ions were found in the asymmetric unit, one sixth is included as disordered across the inversion center and C3 symmetric axis, and the other was removed using SQUEEZE,[60] as an implementation of Platon,[60,63,64] due to major disorder across the C3 symmetric axis and inversion center. All hydrogen atoms were added using a riding model.

[Co^{II}poat⋯$Fe^{II}Me_3$tacn]OTf: The data for asb645_sq were collected from a shock-cooled single crystal at 93(2) K on a Bruker SMART APEX II three-circle diffractometer with a sealed X-ray tube using a equatorial mounted graphite as monochromator and a Bruker Apex II CCD detector. The diffractometer was equipped with a low temperature device and used MoK_a radiation (λ = 0.71073 Å). All data were integrated with SAINT and a multi-scan absorption correction using SADABS was applied.[57,58] The structure was solved by direct methods using SHELXS and refined by full-matrix least-squares methods against F^2 by SHELXL-2018/3 using ShelXle.[59,61,65] All non-hydrogen atoms were refined with anisotropic displacement parameters. All hydrogen atoms were

refined isotropic on calculated positions using a riding model with their U_{iso} values constrained to 1.5 times the U_{eq} of their pivot atoms for terminal sp^3 carbon atoms and 1.2 times for all other carbon atoms. Disordered moieties were refined using bond lengths restraints and displacement parameter restraints. This report and the CIF file were generated using FinalCif.[62] *Refinement Details:* All non-hydrogen atoms in Part 1 were initially freely refined, but a disordered part of the entire molecule (~5%) was found upside down in the trigonal symmetric asymmetric unit. Refinement of the disorder required significant restraints which fixed the M1-M2 (M1 = Co1, M2 = Fe1), N1-M1, P1-C9, P1-C3, P1-N2, N2-C2, C1-C2, N1-C1$, N3-M1, N3-C15, N3-C17, C15-C16, O1-M2, N2-M1, and P1-O1 distances of the disordered part to the main part. The bond lengths of the following bonds were fixed to the following distances in parentheses: C15B-C16B (1.54(0.005)), M2B-C15B M2B C15C (2.91(0.005)), M2B-C16B M2B-C16C (3.03(0.005)). The ADPs of O1, P1, M1, M2, N1, C1, C2, C15, C16, and C17 were separately fixed to those of the disordered part. Phenyl rings of the disordered part were fixed to perfect hexagons, and all ADPs of the disordered phenyl carbons were fixed to the same values. Two sixth triflate ions were found in the asymmetric unit, one sixth is included as disordered across the inversion center and C3 symmetric axis, and the other was removed using SQUEEZE,[60] as an implementation of Platon,[60,63,64] due to major disorder across the C3 symmetric axis and inversion center. All hydrogen atoms were added using a riding model.

[Co^{II}poat⋯$Mn^{II}Me_3$tacn]OTf: The data for asb664 were collected from a shock-cooled single crystal at 93(2) K on a Bruker SMART APEX II three-circle diffractometer with a sealed X-ray tube using a equatorial mounted graphite as monochromator and a Bruker Apex II CCD detector. The diffractometer was equipped with a low temperature device and used MoK_a radiation (λ = 0.71073 Å). All data were integrated with SAINT and a multi-scan absorption correction using SADABS was applied.[57,58] The structure was solved by direct methods using SHELXS and refined by full-matrix least-squares methods against F^2 by SHELXL-2018/3 using ShelXle.[59,61,65] All non-hydrogen atoms were refined with anisotropic displacement parameters. All hydrogen atoms were refined isotropic on calculated positions using a riding model with their U_{iso} values constrained to 1.5 times the U_{eq} of their pivot atoms for terminal sp^3 carbon atoms and 1.2 times for all other carbon atoms. Disordered moieties were refined using bond lengths restraints and displacement parameter restraints. This report and the

CIF file were generated using FinalCif.[62] *Refinement Details:* All non-hydrogen atoms in Part 1 were initially freely refined, but a disordered part of the entire molecule (~5%) was found upside down in the trigonal symmetric asymmetric unit. Refinement of the disorder required significant restraints which fixed the M1-M2 (M1 = Mn1, M2 = Mn2), N1-M1, P1-C9, P1-C3, P1-N2, N2-C2, C1-C2, N1-C1$, N3-M1, N3-C15, N3-C17, C15-C16, O1-M2, N2-M1, and P1-O1 distances of the disordered part to the main part. The bond lengths of the following bonds were fixed to the following distances in parentheses: C15B-C16B (1.54(0.005)), M2B-C15B M2B C15C (2.91(0.005)), M2B-C16B M2B-C16C (3.03(0.005)). The ADPs of O1, P1, M1, M2, N1, N2, N3, C1, C2, C15, C16, and C17 were separately fixed to those of the disordered part. Phenyl rings of the disordered part were fixed to perfect hexagons, and all ADPs of the disordered phenyl carbons were fixed to the same values with a restraint enforcing a more isotropic ADP. Two sixth triflate ions were found in the asymmetric unit, one sixth is included as disordered across the inversion center and C3 symmetric axis, and the other was removed SQUEEZE,[60] as an implementation of Platon,[60,63,64] due to major disorder across the C3 symmetric axis and inversion center. All hydrogen atoms were added using a riding model.

[Mn^{II}poat···Mn^{II}Me$_3$tacn]OTf: The data for asb664 were collected from a shock-cooled single crystal at 93(2) K on a Bruker SMART APEX II three-circle diffractometer with a sealed X-ray tube using a equatorial mounted graphite as monochromator and a Bruker Apex II CCD detector. The diffractometer was equipped with a low temperature device and used MoK_a radiation (λ = 0.71073 Å). All data were integrated with SAINT and a multi-scan absorption correction using SADABS was applied.[57,58] The structure was solved by direct methods using SHELXS and refined by full-matrix least-squares methods against F^2 by SHELXL-2018/3 using ShelXle. [59,61,65] All non-hydrogen atoms were refined with anisotropic displacement parameters. All hydrogen atoms were refined isotropic on calculated positions using a riding model with their U_{iso} values constrained to 1.5 times the U_{eq} of their pivot atoms for terminal sp^3 carbon atoms and 1.2 times for all other carbon atoms. Disordered moieties were refined using bond lengths restraints and displacement parameter restraints. This report and the CIF file were generated using FinalCif.[62] *Refinement Details:* All non-hydrogen atoms in Part 1 were initially freely refined, but a disordered part of the entire molecule (~5%) was found upside down in the trigonal symmetric asymmetric unit. Refinement of the disorder required significant restraints which fixed the M1-M2 (M1 = Mn1,

M2 = Mn2), N1-M1, P1-C9, P1-C3, P1-N2, N2-C2, C1-C2, N1-C1$, N3-M1, N3-C15, N3-C17, C15-C16, O1-M2, N2-M1, and P1-O1 distances of the disordered part to the main part. The bond lengths of the following bonds were fixed to the following distances in parentheses: C15B-C16B (1.54(0.005)), M2B-C15B M2B C15C (2.91(0.005)), M2B-C16B M2B-C16C (3.03(0.005)). The ADPs of O1, P1, M1, M2, N1, N2, N3, C1, C2, C15, C16, and C17 were separately fixed to those of the disordered part. Phenyl rings of the disordered part were fixed to perfect hexagons, and all ADPs of the disordered phenyl carbons were fixed to the same values with a restraint enforcing a more isotropic ADP. Two sixth triflate ions were found in the asymmetric unit, one sixth is included as disordered across the inversion center and C3 symmetric axis, and the other was removed SQUEEZE,[60] as an implementation of Platon,[60,63,64] due to major disorder across the C3 symmetric axis and inversion center. All hydrogen atoms were added using a riding model.

K[Zn^{II}poat]: The data for asb666 were collected from a shock-cooled single crystal at 93(2) K on a Bruker SMART APEX II three-circle diffractometer with a sealed X-ray tube using a equatorial mounted graphite as monochromator and a Bruker Apex II CCD detector. The diffractometer was equipped with a low temperature device and used MoK_a radiation (λ = 0.71073 Å). All data were integrated with SAINT and a multi-scan absorption correction using SADABS was applied.[57,58] The structure was solved by direct methods using SHELXS and refined by full-matrix least-squares methods against F^2 by SHELXL-2018/3 using ShelXle.[59,61,65] All non-hydrogen atoms were refined with anisotropic displacement parameters. All hydrogen atoms were refined isotropic on calculated positions using a riding model with their U_{iso} values constrained to 1.5 times the U_{eq} of their pivot atoms for terminal sp^3 carbon atoms and 1.2 times for all other carbon atoms. This report and the CIF file were generated using FinalCif.[62] *Refinement Details:* All non-hydrogen atoms were refined freely without constraints or restraints. All hydrogen atoms were refined using a riding model.

[Zn^{II}poat···Zn^{II}Me$_3$tacn]OTf: The data for asb667_sq were collected from a shock-cooled single crystal at 93(2) K on a Bruker SMART APEX II three-circle diffractometer with a sealed X-ray tube using a equatorial mounted graphite as monochromator and a Bruker Apex II CCD detector. The diffractometer was equipped with a low temperature device and used MoK_a radiation (λ = 0.71073 Å). All data were integrated with SAINT and a multi-

scan absorption correction using SADABS was applied.[57,58] The structure was solved by direct methods using SHELXS and refined by full-matrix least-squares methods against F^2 by SHELXL-2018/3 using ShelXle. [59,61,65] All non-hydrogen atoms were refined with anisotropic displacement parameters. All hydrogen atoms were refined isotropic on calculated positions using a riding model with their U_{iso} values constrained to 1.5 times the U_{eq} of their pivot atoms for terminal sp^3 carbon atoms and 1.2 times for all other carbon atoms. Disordered moieties were refined using bond lengths restraints and displacement parameter restraints. This report and the CIF file were generated using FinalCif.[62] *Refinement Details:* All non-hydrogen atoms in Part 1 were initially freely refined, but a disordered part of the entire molecule (~5%) was found upside down in the trigonal symmetric asymmetric unit. Refinement of the disorder required significant restraints which fixed the M1-M2 (M1 = Zn1, M2 = Zn2), N1-M1, P1-C9, P1-C3, P1-N2, N2-C2, C1-C2, N1-C1$, N3-M1, N3-C15, N3-C17, C15-C16, O1-M2, N2-M1, and P1-O1 distances of the disordered part to the main part. The bond lengths of the following bonds were fixed to the following distances in parentheses: C15B-C16B (1.54(0.005)), M2B-C15B M2B C15C (2.91(0.005)), M2B-C16B M2B-C16C (3.03(0.005)). The ADPs of O1, P1, M1, M2, N1, C1, C2, C15, C16, and C17 were separately fixed to those of the disordered part. Phenyl rings of the disordered part were fixed to perfect hexagons, and all ADPs of the disordered phenyl carbons were fixed to the same values. Two sixth triflate ions were found in the asymmetric unit, one sixth is included as disordered across the inversion center and C3 symmetric axis, and the other was removed using SQUEEZE,[60] as an implementation of Platon,[60,63,64] due to major disorder across the C3 symmetric axis and inversion center. All hydrogen atoms were added using a riding model.

Supplemental Information

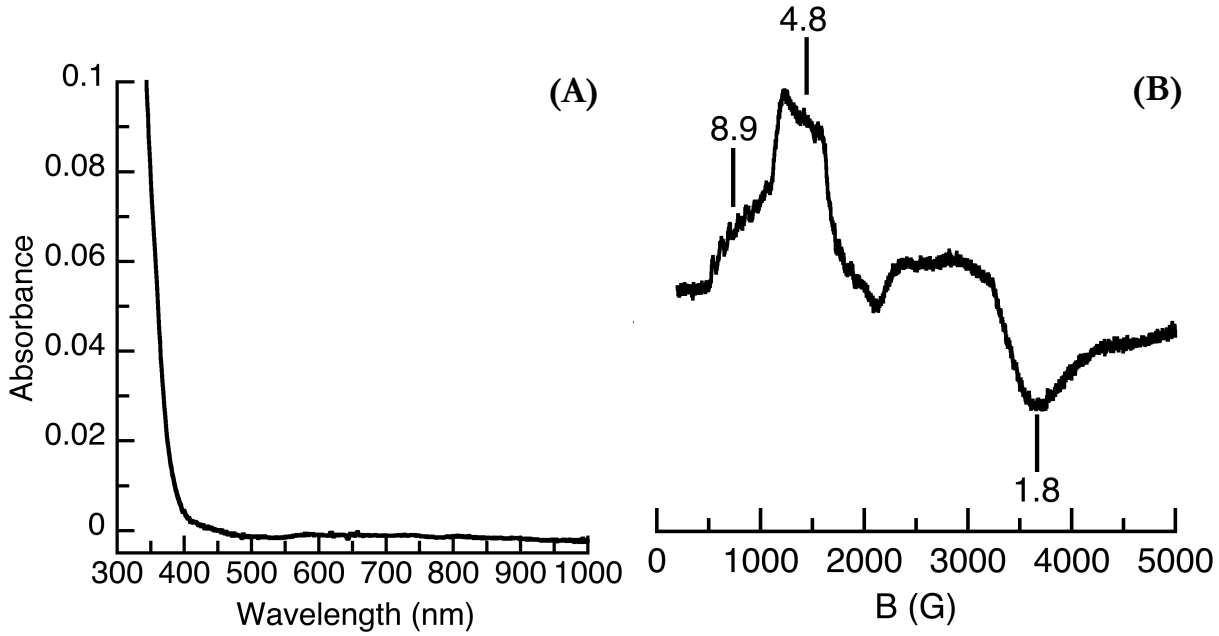

Figure 5-S1: (A) UV-vis spectrum of K[Mn^{II}poat] in DCM at room temperature. **(B)** ⊥-mode EPR spectrum of K[Mn^{II}poat] collected in DCM:THF at 77 K.

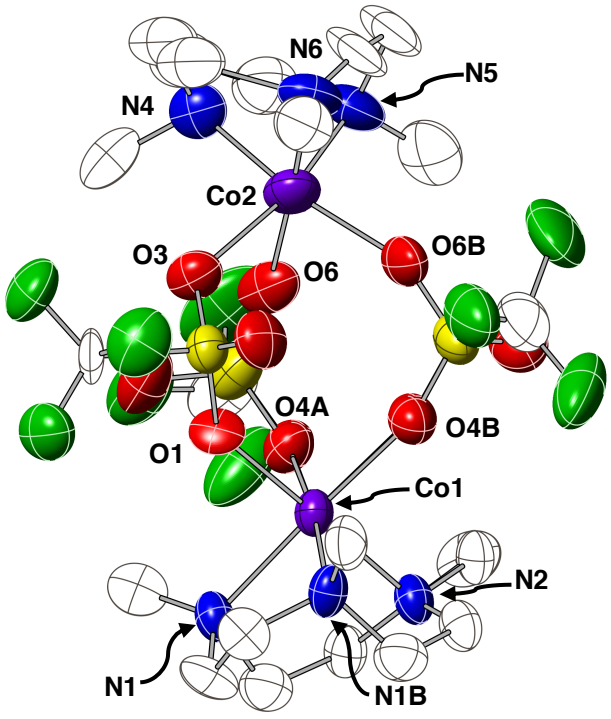

Figure 5-S2: Molecular structure of [(Co^{II}Me$_3$tacn)$_2$(OTf)$_3$]OTf. Thermal ellipsoids were drawn at 50% probability. The outer sphere triflate ion and all H-atoms were omitted for clarity.

Table 5-S1: Metrical data obtained from the molecular structure of [(Co^{II}Me$_3$tacn)$_2$(OTf)$_3$]OTf.

Bond	Distance, Å
Co1–N1	2.082)
Co1–N1B	2.206(18)
Co1–N2	2.136(9)
Co1–O1	2.139(7)
Co1–O4A	2.15(2)
Co1–O4B	2.11(2))
Co2–N4	2.126(9)
Co2–N5	2.126(9)
Co2–N6	2.126(9)
Co2–O3	2.165(9)
Co2–O6	2.194(16)
Co2–O6B	2.38(2)
Co–N$_{avg}$	2.13
Co–O$_{avg}$	2.19
Co···Co	4.897

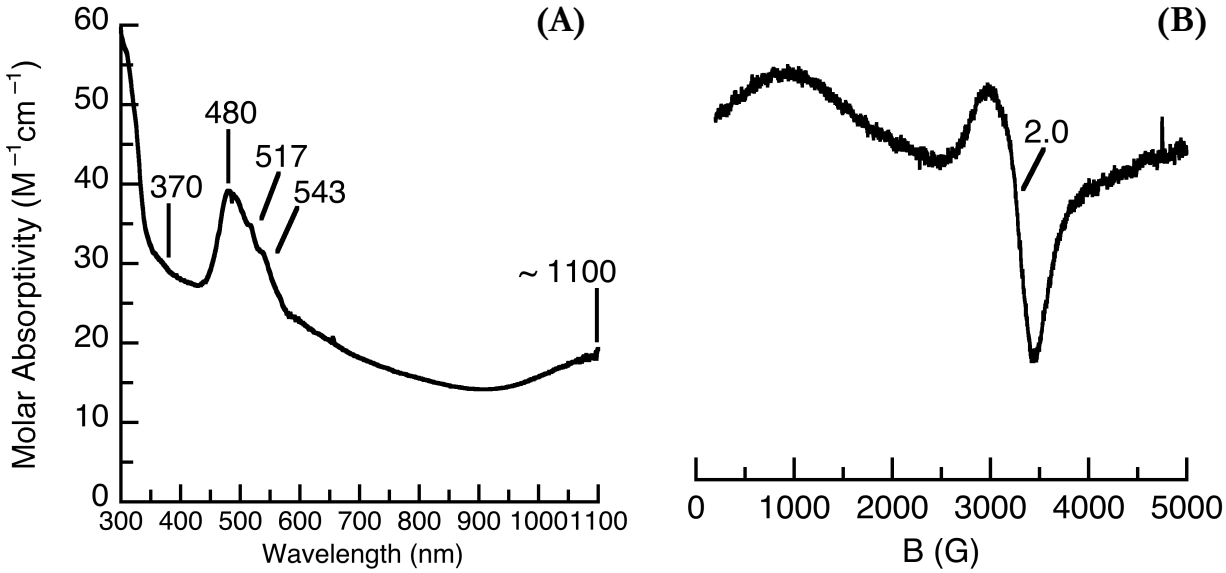

Figure 5-S3: (A) UV-vis spectrum from crystalline [($Co^{II}Me_3tacn)_2(OTf)_3$]OTf in DCM at room temperature. **(B)** ⊥-mode EPR spectrum of [($Co^{II}Me_3tacn)_2(OTf)_3$]OTf collected at 77 K in DCM:THF.

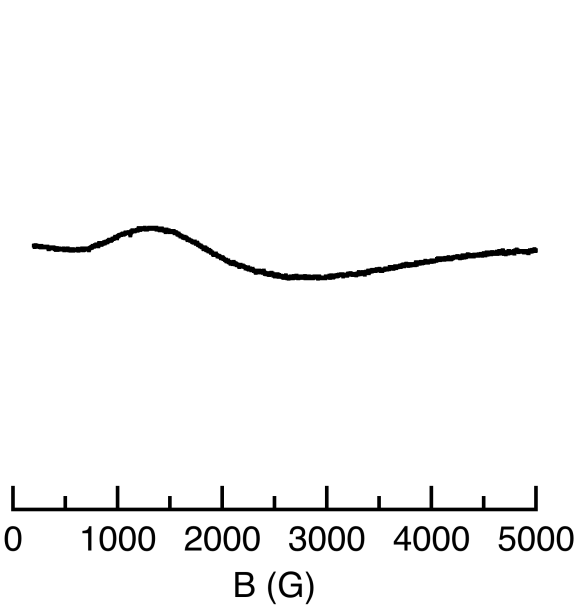

Figure 5-S4: ⊥-mode EPR spectrum of [$Co^{II}\cdots Co^{II}$]$^+$ collected at 77 K in DCM:THF. The signal ~ g = 4 was likely due to a small excess of K[Co^{II}poat].

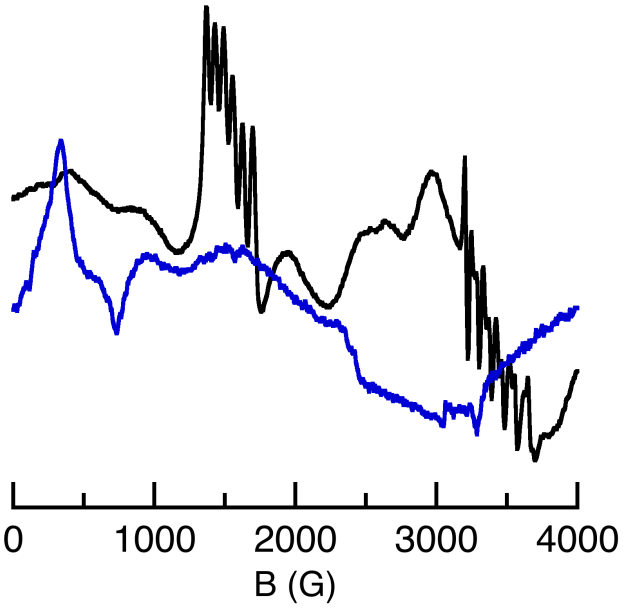

Figure 5-S5: Overlay of ∥-mode EPR spectrum (blue) with ⊥-mode EPR spectrum (black) of [$Co^{II}\cdots Mn^{II}$]$^+$. Both spectra were collected at 6 K.

Table 5-S2: Crystallographic details for [Co^{II}poat···Zn^{II}Me$_3$tacn]OTf (middle column) and [Co^{II}poat···Cu^{II}Me$_3$tacn]OTf (right column).

Compound	**[Co^{II}···Zn^{II}]$^+$**	**[Co^{II}···Cu^{II}]$^+$**
Empirical formula	$C_{51.50}H_{63}CoF_{1.50}N_7O_{4.50}P_3S_{0.50}Zn$	$C_{51.50}H_{63}CoCuF_{1.50}N_7O_{4.50}P_3S_{0.50}$
Formula weight	1113.83	1112.00
Temperature [K]	93(2)	93(2)
Crystal system	trigonal	trigonal
Space group (number)	$R\bar{3}:H$ (148)	$R\bar{3}:H$ (148)
a [Å]	16.3438(8)	16.3442(6)
b [Å]	16.3438(8)	16.3442(6)
c [Å]	34.5412(18)	34.382(2)
α [°]	90	90
β [°]	90	90
γ [°]	120	120
Volume [Å^3]	7990.5(9)	7954.0(8)
Z	6	6
ϱ_{calc} [gcm^{-3}]	1.389	1.393
Independent reflections	5441	3095
Goodness-of-fit on F^2	1.030	1.021
R_1, $[I \geq 2\sigma(I)]$	0.0521	0.0625
wR_2, [all data]	0.1486	0.1788

$R_1 = \Sigma \mid |F_o| - |F_c| \mid / \Sigma |F_o|$
$wR_2 = [\Sigma[w(F_o^2 - F_c^2)^2] / \Sigma[w(F_o^2)^2]]^{1/2}$

Thermal ellipsoids are shown at 50%

Goof (Goodness-of-fit) = S = $[\Sigma[w(F_o^2 - F_c^2)^2] / (n - p)]^{1/2}$, where n = number of reflections and p = total number of parameters refined.

Table 5-S3: Crystallographic details for [(Co^{II}Me$_3$tacn)$_2$(OTf)$_3$]OTf (middle column) and [Co^{II}poat···Co^{II}Me$_3$tacn]OTf (right column).

Compound	**[(Co^{II}Me$_3$tacn)$_2$(OTf)$_3$]OTf**	**[Co^{II}···Co^{II}]$^+$**
Empirical formula	$C_{22}H_{42}Cl_0Co_2F_{12}N_6O_{12}S_4$	$C_{49}H_{63}CoCoF_3N_7O_6P_3S$
Formula weight	1056.71	1145.89
Temperature [K]	93(2)	93(2)
Crystal system	orthorhombic	trigonal
Space group (number)	*Pnma* (62)	$R\bar{3}:H$ (148)
a [Å]	34.267(2)	16.3387(12)
b [Å]	12.6866(10)	16.3387(12)
c [Å]	11.4960(8)	34.492(3)
α [°]	90	90
β [°]	90	90
γ [°]	90	120
Volume [Å^3]	4997.7(6)	7974.1(13)
Z	4	6
ϱ_{calc} [gcm^{-3}]	1.404	1.432
Independent reflections	4830	4428
Goodness-of-fit on F^2	1.060	1.138
R_1, $[I \geq 2\sigma(I)]$	0.0951	0.0576
wR_2, [all data]	0.2853	0.0919

$R_1 = \Sigma \mid |F_o| - |F_c| \mid / \Sigma |F_o|$
$wR_2 = [\Sigma[w(F_o^2 - F_c^2)^2] / \Sigma[w(F_o^2)^2]]^{1/2}$

Thermal ellipsoids are shown at 50%

Goof (Goodness-of-fit) = S = $[\Sigma[w(F_o^2 - F_c^2)^2] / (n - p)]^{1/2}$, where n = number of reflections and p = total number of parameters refined.

Table 5-S4: Crystallographic details for [Co^{II}poat···Fe^{II}Me$_3$tacn]OTf (middle column) and [Co^{II}poat···Mn^{II}Me$_3$tacn]OTf (right column).

Compound	**[Co^{II}···Fe^{II}]$^+$**	**[Co^{II}···Mn^{II}]$^+$**
Empirical formula	$C_{49}H_{63}CoF_3FeN_7O_6P_3S$	$C_{51.50}H_{63}CoF_{1.50}MnN_7O_{4.50}P_3S_{0.50}$
Formula weight	1142.81	1103.40
Temperature [K]	93(2)	93(2)
Crystal system	trigonal	trigonal
Space group (number)	$R\bar{3}:H$ (148)	$R\bar{3}:H$ (148)
a [Å]	16.3608(15)	16.3854(14)
b [Å]	16.3608(15)	16.3854(14)
c [Å]	34.515(3)	34.770(3)
α [°]	90	90
β [°]	90	90
γ [°]	120	120
Volume [Å^3]	8001.1(16)	8084.5(16)
Z	6	6
ϱ_{calc} [gcm^{-3}]	1.423	1.360
Independent reflections	5465	5870
Goodness-of-fit on F^2	1.028	1.054
R_1, $[I \geq 2\sigma(I)]$	0.0575	0.0662
wR_2, [all data]	0.1612	0.1021

$R_1 = \Sigma \mid |F_o| - |F_c| \mid / \Sigma |F_o|$
$wR_2 = [\Sigma[w(F_o^2 - F_c^2)^2] / \Sigma[w(F_o^2)^2]]^{1/2}$

Thermal ellipsoids are shown at 50%

Goof (Goodness-of-fit) = S = $[\Sigma[w(F_o^2 - F_c^2)^2] / (n - p)]^{1/2}$, where n = number of reflections and p = total number of parameters refined.

Table 5-S5: Crystallographic details for [Mn^{II}poat···Mn^{II}Me$_3$tacn]OTf (second column), (K[Zn^{II}poat])$_2$ (third column), and [Zn^{II}poat···Zn^{II}Me$_3$tacn]OTf (fourth column).

Compound	**[Mn^{II}···Mn^{II}]$^+$**	**(K[Zn^{II}poat])$_2$**	**[Zn^{II}···Zn^{II}]$^+$**
Empirical formula	$C_{51.50}H_{63}F_{1.50}MnMnN_7O_{4.50}P_3S_{0.50}$	$C_{84}H_{84}K_2N_8O_6P_6Zn_2$	$C_{51.50}H_{63}F_{1.50}N_7O_{4.50}P_3S_{0.50}Zn_2$
Formula weight	1099.41	1696.35	1120.27
Temperature [K]	93(2)	93(2)	93(2)
Crystal system	trigonal	monoclinic	trigonal
Space group (number)	$R\bar{3}:H$ (148)	$P2_1/n$ (14)	$R\bar{3}:H$ (148)
a [Å]	16.383(6)	14.4882(9)	16.3293(6)
b [Å]	16.383(6)	16.2726(10)	16.3293(6)
c [Å]	34.836(13)	16.8592(11)	34.4706(13)
α [°]	90	90	90
β [°]	90	90.2513(11)	90
γ [°]	120	90	120
Volume [Å^3]	8098(6)	3974.7(4)	7960.0(7)
Z	6	2	6
ϱ_{calc} [gcm^{-3}]	1.353	1.388	1.402
Independent reflections	4487	12815	5776
Goodness-of-fit on F^2	1.042	1.018	1.026
R_1, $[I \geq 2\sigma(I)]$	0.0467	0.0395	0.0519
wR_2, [all data]	0.1242	0.0851	0.1375

$R_1 = \Sigma \mid |F_o| - |F_c| \mid / \Sigma |F_o|$
$wR_2 = [\Sigma[w(F_o^2 - F_c^2)^2] / \Sigma[w(F_o^2)^2]]^{1/2}$

Thermal ellipsoids are shown at 50%

Goof (Goodness-of-fit) = S = $[\Sigma[w(F_o^2 - F_c^2)^2] / (n - p)]^{1/2}$, where n = number of reflections and p = total number of parameters refined.

References

(1) MacBeth, C. E.; Golombek, A. P.; Young, V. G.; Yang, C.; Kuczera, K.; Hendrich, M. P.; Borovik, A. S. O_2 Activation by Nonheme Iron Complexes: A Monomeric Fe(III)–Oxo Complex Derived From O_2. *Science.* **2000**, *289*, 938–941.

(2) Taguchi, T.; Gupta, R.; Lassalle-Kaiser, B.; Boyce, D. W.; Yachandra, V. K.; Tolman, W. B.; Yano, J.; Hendrich, M. P.; Borovik, A. S. Preparation and Properties of a Monomeric High-Spin MnV–Oxo Complex. *J. Am. Chem. Soc.* **2012**, *134*, 1996–1999.

(3) Lee, J. L. Synthetic Models for Metalloenzyme Active Sites: Accessing High-Valent Bimetallic Complexes with [M–(μ-OH)–M'] Cores, University of California, Irvine, 2021.

(4) Lee, J. L.; Oswald, V. F.; Biswas, S.; Hill, E. A.; Ziller, J. W.; Hendrich, M. P.; Borovik, A. S. Stepwise Assembly of Heterobimetallic Complexes: Synthesis, Structure, and Physical Properties. *Dalt. Trans.* **2021**, *50*, 8111–8119.

(5) Lee, J. L.; Biswas, S.; Sun, C.; Ziller, J. W.; Hendrich, M. P.; Borovik, A. S. Bioinspired Di-Fe Complexes: Correlating Structure and Proton Transfer over Four Oxidation States. *J. Am. Chem. Soc.* **2022**, *144*, 4559–4571.

(6) Lacy, D. C.; Park, Y. J.; Ziller, J. W.; Yano, J.; Borovik, A. S. Assembly and Properties of Heterobimetallic Co(II/III)/Ca(II) Complexes with Aquo and Hydroxo Ligands. *J. Am. Chem. Soc.* **2012**, *134*, 17526–17535.

(7) Park, Y. J.; Ziller, J. W.; Borovik, A. S. The Effects of Redox-Inactive Metal Ions on the Activation of Dioxygen: Isolation and Characterization of a Heterobimetallic Complex Containing a MnIII–(μ-OH)–CaII Core. *J. Am. Chem. Soc.* **2011**, *133*, 9258–9261.

(8) Sano, Y.; Lau, N.; Weitz, A. C.; Ziller, J. W.; Hendrich, M. P.; Borovik, A. S. Models for Unsymmetrical Active Sites in Metalloproteins: Structural, Redox, and Magnetic Properties of Bimetallic Complexes with M^{II}-(*μ*-OH)-Fe^{III} Cores. *Inorg. Chem.* **2017**, *56*, 14118–14128.

(9) Park, Y. J.; Cook, S. A.; Sickerman, N. S.; Sano, Y.; Ziller, J. W.; Borovik, A. S. Heterobimetallic Complexes with M^{III}-(μ-OH)-M^{II} Cores (M^{III} = Fe, Mn, Ga; M^{II} = Ca, Sr, and Ba): Structural, Kinetic, and Redox Properties. *Chem. Sci.* **2013**, *4*, 717–726.

(10) Sano, Y.; Weitz, A. C.; Ziller, J. W.; Hendrich, M. P.; Borovik, A. S. Unsymmetrical Bimetallic Complexes with M^{II}–(*μ*-OH)–M^{III} Cores ($M^{II}M^{III}$ = $Fe^{II}Fe^{III}$, $Mn^{II}Fe^{III}$, $Mn^{II}Mn^{III}$): Structural, Magnetic, and Redox. *Inorg. Chem.* **2013**, *52*, 10229–10231.

(11) Barman, S. K.; Jones, J. R.; Sun, C.; Hill, E. A.; Ziller, J. W.; Borovik, A. S. Regulating the Basicity of Metal−Oxido Complexes with a Single Hydrogen Bond and Its Effect on C−H Bond Cleavage. *J. Am. Chem. Soc.* **2019**, *141*, 11142–11150.

(12) Miessler, G. L.; Fischer, P. J.; Tarr, D. A. *Inorganic Chemistry*, Fifth.; Pearson: Upper Saddle River, NJ, 2014.

(13) Mayer, J. M.; Thorn, D. L.; Tulip, T. H. Synthesis, Reactions, and Electronic Structure of Low-Valent Rhenium−oxo Compounds. Crystal and Molecular Structure of $Re(O)I(MeCCMe)_2$. *J. Am. Chem. Soc.* **1985**, *107*, 7454–7462.

(14) Gray, H. B.; Winkler, J. R. Living with Oxygen. *Acc. Chem. Res.* **2018**, *51*, 1850–1857.

(15) Shirin, Z.; Hammes, B. S.; Young, V. G.; Borovik, A. S. Hydrogen Bonding in Metal Oxo Complexes: Synthesis and Structure of a Monomeric Manganese(III)−Oxo Complex and Its Hydroxo Analogue. *J. Am. Chem. Soc.* **2000**, *122*, 1836–1837.

(16) Sun, C.; Oswald, V. F.; Hill, E. A.; Ziller, J. W.; Borovik, A. S. Investigation of Iron–Ammine and Amido Complexes within a C3-Symmetrical Phosphinic Amido Tripodal Ligand. *Dalt. Trans.* **2021**, *50*, 11197–11205.

(17) Sickerman, N. S.; Peterson, S. M.; Ziller, J. W.; Borovik, A. S. Synthesis, Structure and Reactivity of $Fe^{II/III}$–NH3 Complexes Bearing a Tripodal Sulfonamido Ligand. *Chem. Commun.* **2014**, *50*, 2515–2517.

(18) Sickerman, N. S. Investigating the Effects of Non-Covalent Interactions in Metal Complexes with Versatile Ligand Scaffolds, University of California, Irvine, 2014.

(19) Gomez-Coca, S.; Cremades, E.; Aliaga-Alcalde, N.; Ruiz, E. Mononuclear Single-Molecule Magnets: Tailoring the Magnetic Anisotropy of First-Row Transition-Metal Complexes. *J. Am. Chem. Soc.* **2013**, *135*, 7010–7018.

(20) Freedman, D. E.; Harman, W. H.; Harris, T. D.; Long, G. J.; Chang, C. J.; Long, J. R. Slow Magnetic Relaxation in a High-Spin Iron(II) Complex. *J. Am. Chem. Soc.* **2010**, *132*, 1224–1225.
(21) Yao, B.; Singh, M. K.; Deng, Y. F.; Wang, Y. N.; Dunbar, K. R.; Zhang, Y. Z. Trigonal Prismatic Cobalt(II) Single-Ion Magnets: Manipulating the Magnetic Relaxation through Symmetry Control. *Inorg. Chem.* **2020**, *59*, 8505–8513.
(22) Piñero Cruz, D. M.; Woodruff, D. N.; Jeon, I. R.; Bhowmick, I.; Secu, M.; Hillard, E. A.; Dechambenoit, P.; Clérac, R. Switching off the Single-Molecule Magnet Properties of the [CoII(Me6tren)(OH2)]2+ Module by Complexation with Trans-[RuIII(Salen)(CN)2]−. *New J. Chem.* **2014**, *38*, 3443–3448.
(23) Schulte, K. A.; Vignesh, K. R.; Dunbar, K. R. Effects of Coordination Sphere on Unusually Large Zero Field Splitting and Slow Magnetic Relaxation in Trigonally Symmetric Molecules. *Chem. Sci.* **2018**, *9*, 9018–9026.
(24) Pinkowicz, D.; Birk, F. J.; Magott, M.; Schulte, K.; Dunbar, K. R. Systematic Study of Open-Shell Trigonal Pyramidal Transition-Metal Complexes with a Rigid-Ligand Scaffold. *Chem. Eur. J.* **2017**, *23*, 3548–3552.
(25) Woods, T. J.; Ballesteros-Rivas, M. F.; Gómez-Coca, S.; Ruiz, E.; Dunbar, K. R. Relaxation Dynamics of Identical Trigonal Bipyramidal Cobalt Molecules with Different Local Symmetries and Packing Arrangements: Magnetostructural Correlations and Ab Inito Calculations. *J. Am. Chem. Soc.* **2016**, *138*, 16407–16418.
(26) Coste, S. C.; Pearson, T. J.; Altman, A. B.; Klein, R. A.; Finney, B. A.; Hu, M. Y.; Alp, E. E.; Vlaisavljevich, B.; Freedman, D. E. Orbital Energy Mismatch Engenders High-Spin Ground States in Heterobimetallic Complexes. *Chem. Sci.* **2020**, *11*, 9971–9977.
(27) Zadrozny, J. M.; Liu, J.; Piro, N. A.; Chang, C. J.; Hill, S.; Long, J. R. Slow Magnetic Relaxation in a Pseudotetrahedral Cobalt(Ii) Complex with Easy-Plane Anisotropy. *Chem. Commun.* **2012**, *48* .
(28) Ruamps, R.; Batchelor, L. J.; Guillot, R.; Zakhia, G.; Barra, A. L.; Wernsdorfer, W.; Guihéry, N.; Mallah, T. Ising-Type Magnetic Anisotropy and Single Molecule Magnet Behaviour in Mononuclear Trigonal Bipyramidal Co(II) Complexes. *Chem. Sci.* **2014**, *5*, 3927–3929.
(29) Schweinfurth, D.; Sommer, M. G.; Atanasov, M.; Demeshko, S.; Hohloch, S.; Meyer, F.; Neese, F.; Sarkar, B. The Ligand Field of the Azido Ligand: Insights into Bonding Parameters and Magnetic Anisotropy in a Co(II)-Azido Complex. *J. Am. Chem. Soc.* **2015**, *137*, 1993–2005.
(30) Yao, B.; Lu, F.; Gan, D. X.; Liu, S.; Zhang, Y. Q.; Deng, Y. F.; Zhang, Y. Z. Incorporating Trigonal-Prismatic Cobalt(II) Blocks into an Exchange-Coupled [Co2Cu] System. *Inorg. Chem.* **2020**, *59*, 10389–10394.
(31) Deng, Y. F.; Singh, M. K.; Gan, D.; Xiao, T.; Wang, Y.; Liu, S.; Wang, Z.; Ouyang, Z.; Zhang, Y. Z.; Dunbar, K. R. Probing the Axial Distortion Effect on the Magnetic Anisotropy of Octahedral Co(II) Complexes. *Inorg. Chem.* **2020**, *59*, 7622–7630.
(32) Sarkar, A.; Tewary, S.; Sinkar, S.; Rajaraman, G. Magnetic Anisotropy in CoIIX4 (X=O, S, Se) Single-Ion Magnets: Role of Structural Distortions versus Heavy Atom Effect. *Chem. Asian J.* **2019**, *14*, 4696–4704.
(33) Park, Y. J.; Cook, S. A.; Sickerman, N. S.; Sano, Y.; Ziller, J. W.; Borovik, A. S. Heterobimetallic Complexes with M^{III}-(μ-OH)-M^{II} Cores (M^{III} = Fe, Mn, Ga; M^{II} = Ca, Sr, and Ba): Structural, Kinetic, and Redox Properties. *Chem. Sci.* **2013**, *4*, 717–726.
(34) Ray, M.; Hammes, B. S.; Yap, G. P. A.; Rheingold, A. L.; Borovik, A. S. Structure and Physical Properties of Trigonal Monopyramidal Iron(II), Cobalt(II), Nickel(II), and Zinc(II) Complexes. *Inorg. Chem.* **1998**, *37*, 1527–1532.
(35) Sessoli, R.; Gatteschi, D.; Caneschi, A.; Novak, M. A. Magnetic Bistability in a Metal-Ion Cluster. *Nat.* **1993**, *365*, 141–143.
(36) Kläui, W.; Werner, H. Synthesis of Trinuclear Sandwich-Like Cyclopentadienyl Complexes Containing Two Different Metal Atom Centers. *Angew. Chemie Int. Ed.* **1976**, *15*, 172–173.
(37) Navon, G.; Klaui, W. 59Co NMR of a Cobalt(III) Spin-Crossover Compound. *Inorg. Chem.* **1984**, *23*, 2722–2725.
(38) Kläui, W.; Eberspach, W.; Gütlich, P. Spin-Crossover Cobalt(III) Complexes: Steric and Electronic Control of Spin State. *Inorg. Chem.* **1987**, *26*, 3977–3982.

(39) Kläui, W. The Coordination Chemistry and Organometallic Chemistry of Tridentate Oxygen Ligands with π-Donor Properties. *Angew. Chemie Int. Ed. English* **1990**, *29*, 627–637.
(40) Shannon, R. D. Revised Effective Ionic Radii and Systematic Studies of Interatomic Distances in Halides and Chalcogenides. *Acta Crystallogr.* **1976**, *5*, 751–767.
(41) Blakesley, D. W.; Payne, S. C.; Hagen, K. S. Spin-State Variation in Solid State and Solution of Mononuclear Iron(II) 1,4,7-Trimethyl-1,4,7-Triazacyclonane Complexes. *Inorg. Chem.* **2000**, *39*, 1979–1989.
(42) Bossek, U.; Nühlen, D.; Bill, E.; Glaser, T.; Krebs, C.; Weyhermüller, T.; Wieghardt, K.; Lengen, M.; Trautwein, A. X. Exchange Coupling in an Isostructural Series of Face-Sharing Bioctahedral Complexes [LMII(μ-X)3MIIL]BPh4 M = Mn, Fe, Co, Ni, Zn; X = Cl, Br; L = 1,4,7-Trimethyl-1,4,7-Triazacyclononane. *Inorg. Chem.* **1997**, *36*, 2834–2843.
(43) Yang, L.; Tolman, W. B. Type 1 Copper Site Synthetic Model Complexes with Increased Redox Potentials. *J. Biol. Inorg. Chem.* **2012**, *17*, 285–291.
(44) Pfaff, F. F.; Kundu, S.; Risch, M.; Pandian, S.; Heims, F.; Pryjomska-Ray, I.; Haack, P.; Metzinger, R.; Bill, E.; Dau, H.; Comba, P.; Ray, K. An Oxocobalt(IV) Complex Stabilized by Lewis Acid Interactions with Scandium(III) Ions. *Angew. Chemie Int. Ed.* **2010**, *50*, 1711–1715.
(45) Malik, D. D.; Chandra, A.; Seo, M. S.; Lee, Y. M.; Farquhar, E. R.; Mebs, S.; Dau, H.; Ray, K.; Nam, W. Formation of Cobalt–Oxygen Intermediates by Dioxygen Activation at a Mononuclear Nonheme Cobalt(II) Center. *Dalt. Trans.* **2021**, *50*, 11889–11898.
(46) Dori, Z.; Gray, H. B. High-Spin, Five-Coordinate Cobalt(II) Complexes. *Inorg. Chem.* **1968**, *7*, 889–892.
(47) Dormann, J. L.; Fiorani, D.; Tronc, E. Magnetic Relaxation in Fine-Particle Systems; 2007.
(48) Pagels, N.; Albrecht, O.; Görlitz, D.; Rogachev, A. Y.; Prosenc, M. H.; Heck, J. Electronic Coupling through Intramolecular π–π Interactions in Biscobaltocenes: A Structural, Spectroscopic, and Magnetic Study. *Chem. Eur. J.* **2011**, *17*, 4166–4176.
(49) Puhl, S.; orben Steenbock, T.; armen Herrmann, C.; Heck, J. Controlling Through-Space and Through-Bond Exchange Pathways in Bis-Cobaltocenes for Molecular Spintronics. *Angew. Chemie* **2020**, *132*, 2428–2434.
(50) Golombek, A. P.; Hendrich, M. P. Quantitative Analysis of Dinuclear Manganese(II) EPR Spectra. *J. Magn. Reson.* **2003**, *165*, 33–48.
(51) Oswald, V. F.; Lee, J. L.; Biswas, S.; Weitz, A. C.; Mittra, K.; Fan, R.; Li, J.; Zhao, J.; Hu, M. Y.; Alp, E. E.; Bominaar, E. L.; Guo, Y.; Green, M. T.; Hendrich, M. P.; Borovik, A. S. Effects of Noncovalent Interactions on High-Spin Fe(IV)–Oxido Complexes. *J. Am. Chem. Soc.* **2020**, *142*, 11804–11817.
(52) Schoenfeldt, N. J.; Ni, Z.; Korinda, A. W.; Meyer, R. J.; Notestein, J. M. Manganese Triazacyclononane Oxidation Catalysts Grafted under Reaction Conditions on Solid Cocatalytic Supports. *J. Am. Chem. Soc.* **2011**, *133*, 18684–18695.
(53) Cao, R.; Müller, P.; Lippard, S. J. Tripodal Tris-Tacn and Tris-Dpa Platforms for Assembling Phosphate-Templated Trimetallic Centers. *J. Am. Chem. Soc.* **2010**, *132*, 17366–17369.
(54) Chan, S. C.; Ang, Z. Z.; Gupta, P.; Ganguly, R.; Li, Y.; Ye, S.; England, J. Carbodicarbene Ligand Redox Noninnocence in Highly Oxidized Chromium and Cobalt Complexes. *Inorg. Chem.* **2020**, *59*, 4118–4128.
(55) Heintz, R. A.; Smith, J. A.; Szalay, P. S.; Weisgerber, A.; Dunbar, K. R. Homoleptic Transition Metal Acetonitrile Cations with Tetrafluoroborate or Trifluoromethanesulfonate Anions. *Inorg. Synth.* **2002**, *33*, 75–83.
(56) Petasis, D. T.; Hendrich, M. P. Quantitative Interpretation of Multifrequency Multimode EPR Spectra of Metal Containing Proteins, Enzymes, and Biomimetic Complexes. *Methods Enzymol.* **2015**, *563*, 171–208.
(57) Bruker AXS Inc, SAINT Version 8.34a. Madison, WI 2013.
(58) Krause, L.; Herbst-Irmer, R.; Sheldrick, G. M.; Stalke, D. Comparison of Silver and Molybdenum Microfocus X-Ray Sources for Single-Crystal Structure Determination. *J. Appl. Crystallogr.* **2015**, *48*, 3–10.
(59) Sheldrick, G. M.; IUCr. Crystal Structure Refinement with SHELXL. *Acta Crystallogr. Sect. A Found. Crystallogr.* **2015**, *71*, 3–8.

(60) Spek, A. L. PLATON SQUEEZE: A Tool for the Calculation of the Disordered Solvent Contribution to the Calculated Structure Factors. *Acta Crystallogr. Sect. C Struct. Chem.* **2015**, *71*, 9–18.
(61) Hübschle, C. B.; Sheldrick, G. M.; Dittrich, B. ShelXle: A Qt Graphical User Interface for SHELXL. *J. Appl. Crystallogr.* **2011**, *44*, 1281–1284.
(62) Kratzert, D. FinalCif.
(63) Spek, A. L.; IUCr. Single-Crystal Structure Validation with the Program PLATON. *J. Appl. Crystallogr.* **2003**, *36*, 7–13.
(64) Spek, A. L. Structure Validation in Chemical Crystallography. *Acta Crystallogr. Sect. D Biol. Crystallogr.* **2009**, *65*, 148–155.
(65) Sheldrick, G. M.; IUCr. Crystal Structure Refinement with SHELXL. *Acta Crystallogr., Sect. C Cryst. Struct. Commun.* **2015**, *71*, 3–8.